STATISTICAL METHODS FOR COMPOSITIONAL AND PHOTOMETRIC ANALYSIS OF THE LUNAR SURFACE

A thesis approved for the academic degree of

Doktor der Ingenieurwissenschaften (Dr.-Ing.)

at the

Faculty of Electrical Engineering and Information Technology
TU Dortmund University

by

Marcel Hess
Dortmund, 2024

Supervisor:	Prof. Dr. rer. nat. Christian Wöhler
Co-Advisor:	Prof. Dr. rer. nat. Harald Hiesinger
Day of Oral Examination:	15th of April 2024

ABSTRACT

This thesis presents statistical methods and analysis regarding the surface properties and processes of the lunar surface using reflectance spectroscopy. The diurnal variations of OH/H_2O are the first process of interest discussed in this thesis. Closely linked to this are lunar swirls, which are the second major science topic in this work. Thirdly, we need to investigate the mineral composition and space weathering to understand the first two processes.

The solar wind contains protons that form hydroxyl, or possibly water, with the oxygen from the minerals. OH/H_2O on the lunar surface varies with the time of day but persists throughout the day and across all latitudes. We investigate the relationship between the diurnal variations and absolute values of the OH component and the mineralogy for the major lunar minerals for the equatorial regions on the lunar nearside and for local occurrences of Mg-spinel at Theophilus crater and Mare Moscoviense. The plagioclase and TiO_2 abundance are correlated with the OH abundance. High TiO_2 and low plagioclase content correspond to less OH/H_2O at midday and, especially for TiO_2, higher daily variations. Similarly, Mg-spinel-rich regions show reduced OH integrated band depth at lunar midday.

The solar wind is also one of the main drivers of space weathering on the lunar surface. Lunar swirls are particularly interesting because they are not fully understood and local magnetic fields partly shield the surface from the solar wind. This work shows OH/H_2O absorption strength maps at the lunar morning and midday. The absorption is weaker in the morning and noon compared to the surroundings, and the variations across the day are smaller. This suggests that the solar wind influx is reduced at swirls. Furthermore, we analyze spectral trends at the swirls using the compaction significance spectral index (CSSI), which measures the relative importance of space weathering and compaction on the spectra in the visible to near-infrared wavelength range. We validate the CSSI by modeling the influences of compaction and space weathering on the lunar spectra. Not for all locations, the brightness difference comes predominantly from maturity differences, but compaction plays a significant role in the appearance of lunar swirls.

An indicator of the physical properties of the regolith is the photometric behavior. Following, we employ Lunar Reconnaissance Orbiter Camera data to derive the Hapke parameters as a proxy for the physical characteristics at the Reiner Gamma swirl and compare the results to the Chang'e 5 landing site. Landing sites exhibit a reduced opposition effect and roughness because the rocket jet blows away the porous top layer of the regolith. Similarly, the Reiner Gamma swirl also shows a reduced opposition effect, indicating that the explanation of lunar swirls requires compaction as a mechanism. The most consistent theory with the data is that lunar swirls are created by the interaction of a cometary coma and the regolith acting similarly to the landing rocket and subsequent shielding from the solar wind, which is partly responsible for space weathering.

To further investigate the mineral dependency of variations in volatiles across the lunar surface and time-of-day and the origin of swirls, a better characterization of the

mineral abundances and degree of space weathering is necessary. Therefore, we introduce an unmixing framework that considers the effects of space weathering by using the nanophase and microphase particles as endmembers. Consequently, we can also obtain fractional abundances of these small iron particles responsible for spectral reddening and darkening. We validate the unmixing model using immature spectra from the laboratory, synthetically calculated spectra, and mature samples returned from the Moon by the Apollo missions. These spectra can be well characterized using the unmixing model.

Mineral darkening agents like ilmenite further complicate the problem as the spectral effects of several processes are similar. Therefore, the parameters tend to be correlated, so several solutions can explain the observed spectrum. Thus, we propose a Bayesian approach to sample the posterior distribution, which contains information about the uncertainties of the mineral abundances and the best fit. To better constrain the problem, we include prior information about the elemental abundances. These elemental abundances can be obtained independently from external data sources, like gamma-ray spectroscopy. With this information, the uncertainties can be reduced, especially of ilmenite and plagioclase. The grain size is another factor that influences the observed spectra. If the grain size is included as a parameter, the uncertainties of the space weathering agents increase significantly. Finally, we present maps of the major minerals and space weathering agents for the Moon using the unmixing framework.

KURZFASSUNG

In dieser Arbeit werden statistische Methoden und Analysen mit Hilfe von Reflektanzspektroskopie zu den Oberflächeneigenschaften und -prozessen des Mondes vorgestellt. Allgemein werden drei Themen in dieser Arbeit diskutiert. Als erstes werden die tageszeitabhängigen Schwankungen von OH/H_2O auf dem Mond und die damit verbunden Prozesse diskutiert. Eng damit verbunden sind "Lunar Swirls", die das zweite große wissenschaftliche Thema dieser Arbeit darstellen. Drittens muss die Mineralzusammensetzung und die Weltraumverwitterung untersucht werden, um die ersten beiden Prozesse zu verstehen.

Der Sonnenwind enthält Protonen, also ionisierten Wasserstoff, der mit dem Sauerstoff der Minerale Hydroxyl oder möglicherweise Wasser bildet. OH/H_2O auf der Mondoberfläche variiert mit der Tageszeit, bleibt aber den ganzen Tag und über alle Breitengrade bestehen. In dieser Arbeit wird der Zusammenhang zwischen den tageszeitabhängigen Schwankungen und den absoluten Werten der OH-Komponente und der Mineralogie für die wichtigsten Mondminerale für die äquatorialen Bereiche auf der Vorderseite des Mondes und für lokale Vorkommen von Mg-Spinell im Theophilus-Krater und im Mare Moscoviense untersucht. Die Häufigkeiten von Plagioklas und TiO_2 korrelieren mit der OH-Häufigkeit. Hoher TiO_2- und niedriger Plagioklasgehalt entsprechen weniger OH/H_2O zur Mittagszeit und, vor allem bei TiO_2, höheren tageszeitabhängigen Schwankungen. In ähnlicher Weise weisen Mg-Spinell reiche Regionen am Mondmittag eine verringerte OH Bandtiefe auf.

Der Sonnenwind ist auch einer der Haupttreiber der Weltraumverwitterung auf der Mondoberfläche. Lunar Swirls sind besonders interessant, weil sie noch nicht vollständig verstanden sind und in ihrer Umgebung Magnetfelder die Oberfläche teilweise vor dem Sonnenwind abschirmen. Diese Arbeit zeigt Karten der Absorptionsstärke von OH/H_2O am Mondmorgen und -mittag. Die Absorption ist morgens und mittags im Vergleich zur Umgebung schwächer und die Schwankungen über den Tag hinweg sind geringer. Dies deutet darauf hin, dass die Einstrahlung von Sonnenwind bei Lunar Swirls verringert ist. Darüber hinaus werden spektrale Trends an den Lunar Swirls mithilfe des Compaction Significance Spectral Index (CSSI), der den relativen Einfluss von Weltraumverwitterung und Verdichtung auf die Spektren im sichtbaren bis nahinfraroten Wellenlängenbereich beschreibt, analysiert. Der CSSI wird validiert, indem die Einflüsse von Verdichtung und Weltraumverwitterung auf die Mondspektren modelliert werden. Nicht an allen Standorten ist der Helligkeitsunterschied hauptsächlich auf unterschiedliche Grade an Verwitterung zurückzuführen. Vielmehr scheint die Verdichtung eine wichtige Rolle bei der Entstehung von Lunar Swirls zu spielen.

Ein Indikator für die physikalischen Eigenschaften des Regoliths ist das photometrische Verhalten. Daher werden Daten der Lunar Reconnaissance Orbiter-Kamera verwendet, um die Hapke-Parameter als Indikator für die physikalischen Eigenschaften am Reiner-Gamma-Swirl abzuleiten und die Ergebnisse mit dem Landeplatz der Raumsonde Chang'e 5 zu vergleichen. Der Regolith um Landeplätze ist weniger porös und weist eine verringerte Rauhigkeit auf, da der Gasstrahl des Landetriebwerks die poröse

Deckschicht des Regoliths wegbläst. In ähnlicher Weise zeigt auch der Reiner-Gamma-swirl einen verringerten Oppositionseffekt, was darauf hindeutet, dass die Erklärung des photometrischen Verhaltens der Lunar Swirls eine Verdichtung bzw. Verringerung der Porosität des Regoliths als Mechanismus erfordert. Die Theorie, die mit den Daten am besten übereinzustimmen scheint, besagt, dass Lunar Swirls durch die Interaktion zwischen einer Kometenkoma, die ähnlich wie eine Landerakete wirkt, und des Regoliths entstehen. Anschließend wird die Struktur des Swirls durch die Abschirmung vom Sonnenwind, der teilweise für die Weltraumverwitterung verantwortlich ist, über lange Zeiträume erhalten.

Um die Tageszeitabhängigkeit der Schwankungen der flüchtigen Stoffe auf der Mondoberfläche in Abhängigkeit von der Mineralzusammensetzung sowie den Ursprung von Lunar Swirls weiter zu untersuchen, ist eine bessere Charakterisierung der Mineralhäufigkeiten und des Grades der Weltraumverwitterung erforderlich. Daher wird ein Unmixing-Framework vorgestellt, das die Auswirkungen der Weltraumverwitterung berücksichtigt, indem die kleinen Eisenpartikel, die für die spektrale Rötung und Verdunkelung verantwortlich sind, als Endmember verwendet werden. Folglich können auch fraktionale Häufigkeiten dieser kleinen Eisenpartikel ermittelt werden. Anschließend wird das Entmischungs-Modell anhand von Spektren aus dem Labor, synthetisch berechneter Spektren und Gesteinsproben, die von den Apollo-Missionen vom Mond zurück gebracht wurden, validiert. Diese Spektren können mit dem Unmixing-Modell gut charakterisiert werden.

Minerale wie Ilmenit, die das Spektrum verdunkeln, erschweren das Problem zusätzlich, da die spektralen Auswirkungen verschiedener Prozesse ähnlich sind. Daher sind die geschätzten Häufigkeiten miteinander korreliert, sodass mehrere Lösungen das beobachtete Spektrum erklären können. Folglich wird ein Bayes-Ansatz zur Erfassung der Posterior Verteilung vorgeschlagen, mit dem sich Informationen über die Unsicherheiten der Mineralhäufigkeiten und die am besten passende Lösung bestimmen lassen. Um das Problem besser einzugrenzen, können Vorabinformationen über die Elementhäufigkeiten einbezogen werden. Diese Elementhäufigkeiten können auf unabhängige Weise aus externen Datenquellen wie der Gammastrahlenspektroskopie ermittelt werden. Mit diesen Informationen können die Unsicherheiten insbesondere von Ilmenit und Plagioklas verringert werden.

Die Korngröße ist ein weiterer Faktor, der die beobachteten Spektren beeinflusst. Bezieht man die Korngröße als Parameter mit ein, erhöhen sich die Unsicherheiten der Weltraumverwitterungsfaktoren allerdings deutlich. Abschließend werden Karten der wichtigsten Minerale und Weltraumverwitterungsstoffe für den Mond unter Verwendung des in der Arbeit entwickelten Unmixing-Frameworks vorgestellt.

PUBLICATIONS

During the thesis the following papers were published by the author. The thesis is based on these publications.

Peer-reviewed Journal Publications:

Hess, M., T. Wilhelm, C. Wöhler, and K. Wohlfarth (2021a). "Uncertainty Introduced by Darkening Agents in the Lunar Regolith: An Unmixing Perspective." In: *Remote Sensing* 13.22, p. 4702. DOI: 10.3390/rs13224702.

Hess, M., C. Wöhler, A. A. Berezhnoy, J. L. Bishop, and V. V. Shevchenko (2021b). "Dependence of the Hydration of the Lunar Surface on the Concentrations of TiO2, Plagioclase, and Spinel." In: *Remote Sensing* 14.1, p. 47. DOI: 10.3390/rs14010047.

Hess, M., C. Wöhler, M. Bhatt, A. A. Berezhnoy, A. Grumpe, K. Wohlfarth, A. Bhardwaj, and V. V. Shevchenko (2020). "Processes governing the VIS/NIR spectral reflectance behavior of lunar swirls." In: *Astronomy & Astrophysics* 639, A12. DOI: 10.1051/0004-6361/201937299.

Hess, M., C. Wöhler, L. Qiao, and M. Bhatt (2023). "Comparative photometric analysis of the Reiner Gamma swirl and the Chang'e 5 landing site." In: *Astronomy & Astrophysics* 674. DOI: 10.1051/0004-6361/202346098.

Conference Contributions:

Hess, M., T. Wilhelm, M. Arnaut, and C. Wöhler (2021). "Uncertainty-Based Unmixing of Space Weathered Lunar Spectra." In: *52nd Lunar and Planetary Science Conference*. 2548, p. 1048.

Hess, M., C. Wöhler, and J. Bishop (2019a). "Low Abundances of Strongly Bound Hydroxyl in Spinel-rich Areas of the Lunar Crater Theophilus." In: *EPSC-DPS Joint Meeting 2019*. Vol. 13, pp. 1608–1.

Hess, M., C. Wöhler, and L. Qiao (2022). "Photometric Modelling for Chang'e 5 Landing Site and Reiner Gamma Swirl." In: *Europlanet Science Congress 2022*. Vol. 2022, EPSC2022–147. DOI: https://doi.org/10.5194/epsc2022-147.

Hess, M., K. Wohlfarth, and C. Wöhler (2020). "Quantifying Lunar Spinel-Rich Lithologies with Nonlinear Spectral Unmixing Considering Space-Weathering Effects." In: *51st Annual Lunar and Planetary Science Conference*. 2326, p. 1863.

Hess, M., K. Wohlfarth, C. Wöhler, A. A. Berezhnoy, M. Bhatt, and A. Bhardwaj (2019b). "Space Weathering Trends at the Mare Moscoviense Swirl." In: *Europlanet Science Congress 2020*. Vol. 14, EPSC2020–716. DOI: https://doi.org/10.5194/epsc2020-716.

Wöhler, C., M. Bhatt, A. Grumpe, M. Hess, A. Berezhnoy, V. Shevchenko, and A. Bhardwaj (2019). "Regolith Compaction and its Implications for the Formation Mechanism of Lunar Swirls." In: *EPSC-DPS Joint Meeting 2019*. Vol. 13, pp. 1608–1.

Other Publications: The following publications by the author are not part of the thesis but are related to the Master thesis of the author or the author contributed as a co-author.

Hess, M., K. Wohlfarth, A. Grumpe, C. Wöhler, O. Ruesch, and B. Wu (Mar. 2019a). "Overcoming Troublesome Stereo Artifacts: Towards the Perfect Digital Terrain Model of Mars." In: *50th Annual Lunar and Planetary Science Conference*. 2132, p. 2565.

Hess, M., M. Tenthoff, K. Wohlfarth, and C. Wöhler (2022). "Atmospheric Correction for High-Resolution Shape from Shading on Mars." In: *Journal of Imaging* 8.6, p. 158. DOI: https://doi.org/10.3390/jimaging8060158.

Hess, M., K. Wohlfarth, A. Grumpe, C. Wöhler, O. Ruesch, and B. Wu (June 2019b). "Atmospherically compensated shape from shading on the martian surface: Towards the perfect digital terrain model of mars." In: *The International Archives of Photogrammetry, Remote Sensing and Spatial Information Sciences* 42, pp. 1405–1411.

Hess, M., K. Wohlfarth, O. Ruesch, and C. Wöhler (Sept. 2019c). "High Resolution Digital Terrain Model for the Landing Site of the Rosalind Franklin (ExoMars) Rover." In: *EPSC-DPS Joint Meeting 2019*. Vol. 13. Copernicus GmbH, pp. 1533–5.

Qiao, L., M. Hess, L. Xu, C. Wöhler, J. W. Head, J. Chen, Y. Wang, et al. (2023). "Extensive Lunar Surface Disturbance at the Chang'e-5 Mission Landing Site: Implications for Future Lunar Base Design and Construction." In: *Journal of Geophysical Research: Planets* 128, e2022JE007730. DOI: https://doi.org/10.1029/2022JE007730.

Ruesch, O., M. Hess, K. Wohlfarth, T. Heyer, C. Wöhler, T. Bontognali, C. Orgel, E. Sefton-Nash, J.-L. Josset, and J. Vago (2021). "Synthetic topography from the decameter to the centimeter scale on Mars for scientific and rover operations of the ESA-Roscosmos ExoMars mission." In: *Planetary and Space Science* 205, p. 105301.

Ruesch, O., M. Hess, C. Wöhler, V. T. Bickel, R. M. Marshal, M. Patzek, and H. L. F. Huybrighs (2023, submitted, under review). "Discovery of a dust sorting process on boulders near the Reiner Gamma swirl on the Moon." In: *Journal of Geophysical Research: Planets*.

Supervised Theses: The following theses were supervised by the author during his time at TU Dortmund University.

Balamurugan, Medhini R. (2021). "Learning Hyperspectral Unmixing Considering Space Weathering Effects." Master Thesis. Image Analysis Group, TU Dortmund University.

Balamurugan, Monika R. (2023). "Analysis of OH and Mineralogy on the Moon using Machine Learning Techniques." Master Thesis. Image Analysis Group, TU Dortmund University.

Hallmann, D. (2023). "Learning Shape from Shading for the Lunar Surface." Master Thesis. Image Analysis Group, TU Dortmund University.

Liu, S. (2020). "Multiview Shape from Shading on the Martian Surface." Master Thesis. Image Analysis Group, TU Dortmund University.

Motal, T. (2021). "Space Weathering of Lunar Swirls in the NUV." Bachelor Thesis. Image Analysis Group, TU Dortmund University.

Saleh, O. (2020). "GPU Implementation Spectral Unmixing Algorithms." Master Thesis. Image Analysis Group, TU Dortmund University.

Slatosch, J. (2023). "Bayesian Inference of Grain Size for Space Weathered Lunar Spectra." Master Thesis. Image Analysis Group, TU Dortmund University.

ACKNOWLEDGEMENTS

I want to express my heartfelt gratitude to all those who have been by my side on this journey in the past almost 5 years. It has been a challenging yet immensely rewarding one, and I am genuinely thankful for the support, guidance, and encouragement I have received along the way.

I am deeply thankful to my supervisor, Prof. Dr. rer. nat. Christian Wöhler, whose guidance and mentorship have been invaluable throughout this journey. You have always believed in my abilities and provided deep knowledge, experience, discussion, and the freedom to pursue my own ideas. Furthermore, I want to thank Prof. Dr. rer. nat. Harald Hiesinger for his effort and interest in this topic.

My gratitude also extends to my colleagues Mirza Arnaut, Lubaba Migdadi, Tom Sander, Moritz Tenthoff, Thorsten Wilhelm, and Kay Wohlfarth, whose camaraderie and collaborative spirit have provided a supportive academic environment and a great working atmosphere. Furthermore, I am immensely grateful to Tom Sander, Dennis Schmid, Niklas Tötsch, and Kay Wohlfarth for the feedback and the time they took to read through earlier versions of this thesis.

To all my co-authors, and Alexey B. Berezhnoy, Megha Bhatt, Janice Bishop, Le Qiao, and Ottaviano Ruesch in particular, I extend my heartfelt appreciation. For your invaluable feedback, expertise, and support, I am forever grateful. It was an honor to learn from and work together with such accomplished researchers.

I would like to thank all the remarkable students whom I have had the privilege of supervising during their bachelor and master thesis projects, as well as those who were part of the courses I had the honor to teach. Your dedication, enthusiasm, and hard work have been a source of inspiration and pride throughout my academic journey. I wish you all the best for your future careers.

Last, but certainly not least, I would like to thank my friends and family for their support. To my mother Martina, my sister Valerie, and my father Dieter, I am deeply grateful for your encouragement and support throughout my life that has led me to this point.

CONTENTS

LIST OF FIGURES

LIST OF TABLES

ACRONYMS

AUG Augite

AMSA Anisotropic Multiple Scattering Approximation

BD_1 1 µm Band Depth

BD_2 2 µm Band Depth

CBOE Coherent Backscattering Opposition Effect

CCD Charge-Coupled Device

CPX Clino-pyroxene

CSSI Compaction Significance Spectral Index

DEM Digital Elevation Model

DHG Double Henyey Greenstein

DTM Digital Terrain Model

ESA European Space Agency

FMR FerroMagnetic Resonance

FS Ferrosilite

GMM Gaussian Mixture Model

GPU Graphics Processing Unit

GRS Gamma Ray Spectrometer

HMC Hamiltonian Monte Carlo

HCP High Calcium Pyroxene

ILM Ilmenite

KS-test Kolmogorow-Smirnow-test

KDE Kernel Density Estimation

LBD Logarithmic Band Depth

LCP Low Calcium Pyroxene

LMS Lunar Mineralogical Spectrometer

LOLA Lunar Orbiter Laster Altimeter

LRO Lunar Reconnaissance Orbiter

LSCC Lunar Soil Characterization Consortium

M^3 Moon Mineralogy Mapper

mpFe Microphase iron

npFe Nanophase iron

NAC Narrow Angle Camera

NASA National Aeronautics and Space Administration

NIR Near Infrared

NLBD Negative Logarithmic Band Depth

NUTS No-U-Turn Sampler

OHIBD OH Integrated Band Depth

OLV Olivine

OMAT Optical Maturity

OPX Ortho-pyroxene

OTH Other

PCA Principal Component Analysis

PLG Plagioclase

PRG Pargasite

RELAB Reflectance Experiment LABoratory

ROI Region Of Interest

smFe Submicroscropic iron

SfS Shape from Shading

SHOE Shadow Hiding Opposition Effect

SPI Spinel

SPPF Single Particle Phase Function

SELENE Selenological and Engineering Explorer

TC Terrain Camera

TEM Transmission Electron Microscope

UV Ultraviolet

WAC Wide Angle Camera

GLOSSARY

MATHEMATICAL SYMBOLS

x	A scalar.
$\vec{x}$	A vector.
$\mathbf{X}$	A matrix.
$\lvert x \rvert$	The absolute of a scalar.
$\lVert \vec{x} \rVert$	The euclidean norm of a vector.
x_i	The i-th value of a vector.
$\vec{x}^T$, $\mathbf{X}^T$	The transpose.
$\sum_{i=1}^{N} x_i$	The sum from element 1 to N of $\vec{x}$.
$\prod_{i=1}^{N} x_i$	The product of the elements 1 through N of $\vec{x}$.

PROBABILISTIC SYMBOLS

$p(x)$	A probability density function.
$p(A \mid B)$	Conditional probability of A given B.
$F(x)$	A cumulative distribution function.
μ	Location parameter of a probability distribution.
σ^2	Variance.
σ	Standard deviation.
$p(\Theta \mid \mathbf{X})$	Posterior distribution.
$p(\Theta)$	Prior distribution.
$p(\mathbf{X} \mid \Theta)$	Likelihood.
$p(\mathbf{X})$	Evidence.
$\mathcal{N}(x \mid \mu, \sigma^2)$	Normal distribution over x with mean μ and variance σ^2.
$\pi(\Theta_{t-1})$	Proposal distribution.

MODEL PARAMETER SYMBOLS

w	Single scattering albedo.
K	Porosity factor.

B_{CB}	Coherent backscatter opposition effect.
B_{SH}	Shadow hiding opposition effect.
B_{C0}	Coherent backscatter opposition effect amplitude.
B_{S0}	Shadow hiding opposition effect amplitude.
h_c	Coherent backscatter opposition effect width.
h_s	Shadow hiding opposition effect width.
$\bar{\theta}_b$	Macroscopic surface roughness.
λ	Wavelength.
ϕ	Filling factor.
ρ	Density.
b_n	Legendre coefficients.
c_{DHG}	Double Henyey Greenstein function relative forward/backward scattering strength.
b_{DHG}	Double Henyey Greenstein function lobe shape parameter.
Λ	Transport mean free path.
Q_E	Extinction efficiency.
Q_S	Scattering efficiency.
M	Bulk density.
S	Scattering coefficient.
S_E	External surface reflection coefficient.
S_I	Internal surface reflection coefficient.
E	Extinction coefficient.
α	Absorption coefficient.
n	Real index of refraction.
k	Complex index of refraction.
ψ	Azimuth angle.
i	Incidence angle.
e	Emission angle.
μ_0	Cosine of incidence angle.
μ	Cosine of emission angle.
$\mu_{0,e}$	Cosine of effective incidence angle.
μ_e	Cosine of effective emission angle.
$p(g)$	Phase function.
$P_n(x)$	Legendre polynomial of order n.
$H(x)$	Ambertsumian Chandrasekhar H-Function.
$M(\mu, \mu_0)$	Multiple scattering function.
$S(i, e, \psi)$	Surface roughness correction.

1 INTRODUCTION

The Moon holds many important secrets to understanding the history of the solar system and Earth. The current composition and structure of the lunar surface are a product of the eons of geological history and the harsh space environment that the Moon is subject to because, unlike Earth, there is no atmosphere to protect it.

Consequently, the composition is essential to understand the geologic history of the Moon. For example, in some areas, volcanic processes have exposed mantle material on the lunar surface, which is much more mafic than the anorthositic lunar crust (Weitz et al., 1998), which is a glimpse into the lunar interior. However, on the Moon, space weathering has a strong effect on the optical properties of the surface, making it much more difficult to distinguish different materials (Hapke, 2001). The space environment and the solar wind, in particular, lead to a diurnal variation of the OH/H2O abundance (e.g., Bandfield et al., 2016; Grumpe et al., 2019; Wöhler et al., 2017b), but how this may change depending on the mineralogy is still an open question. Lunar swirls are salient as bright patterns and act like a real-world laboratory for the influence of space weathering because here, the local magnetic fields (Hood and Schubert, 1980; Tsunakawa et al., 2015) shield the surface partly from the space environment (e.g., Glotch et al., 2015). Understanding these peculiarities might give new insight into which events led to their creation.

Even though the Moon is the planetary body closest to us, only twelve humans have walked its surface. It is costly and challenging to bring people to the Moon, and we can investigate only small regions this way. It is much more convenient and practical to use remote sensing techniques. However, the challenges of planetary sciences are manifold. We cannot freely conduct experiments to separate the influence of different processes. Most processes, i.e., space-weathering, take a long time and cannot easily be reproduced on Earth. Furthermore, we cannot go back in time to observe the geological history of the Moon directly. We can only investigate the current state and, like a good detective, try to put together the clues to create a comprehensive and consistent story (Anderl, 2017).

The more clues or data we have, the more we can learn, and the higher the chances we will find the correct culprit. Satellites and the sensors they carry map the Moon in various ways. For example, they measure the light reflected from the surface in the visible and near-infrared wavelength range. For longer wavelengths the surface emission becomes dominant. Other devices include radar, lidar, ultra-violet, X-ray, and gamma-ray spectrometers (Bishop et al., 2019). This thesis mainly uses reflectance spectroscopy in the visible and near-infrared, which contains essential features that are diagnostic for the compositional and physical properties of the lunar surface.

However, clues are only helpful if we have a framework of reality to put them together. Where the detective uses common sense and forensics, the planetary scientist employs physical models to simulate the processes. The main physical framework used in this thesis is radiative transfer (Chandrasekhar, 1960) in general and the Hapke (1981)

model specifically. The Hapke model is not entirely physical, but the parameters are derived empirically. However, the agreement with measurements is general enough to be a useful approximation of reality.

So we have data and models that indicate how different processes are connected and what is physically feasible. While the detective can go through all possible options in her or his head, we need computers to simulate possible scenarios and algorithms to find the most likely explanation. We can formulate this as an inversion problem. For example, the model's output is a spectrum, and the inputs are the weights of the constituent minerals. Generally, we want to know for which input the output matches the observed data. In other words, we want to invert the model to obtain the input for a given output. However, while one input corresponds to a specific output, an output can result from several different inputs, so it is essentially an ill-posed problem. For the applications shown in this thesis (e.g., unmixing or photometry), there is rarely a single clear solution to the inversion problem. The parameters of the Hapke model are interrelated, and the spectra of minerals become more and more similar the longer the surface has been subject to the space environment.

Therefore, we want to explore all possible inputs that could have led to our observations. Bayesian inference (e.g., Bishop, 2006; Gelman et al., 2013) provides a framework to obtain not only a single solution but the entire distribution of probable solutions. Additionally, it is convenient to include prior knowledge about the parameters. With the full posterior density, we can make an informed decision of what is the most likely solution.

1.1 CONTRIBUTION

The thesis contributes to three major research areas regarding the lunar surface. Firstly, the variations in the 3-μm absorption band on the Moon are analyzed in relation to the mineralogy and the diurnal variations. This absorption band has been found to be a measure of the abundance of OH/H_2O in the uppermost layer of the lunar regolith. The mineralogy might play a role in to what extent OH is bound to the regolith. Here, the author examines the influence of the major lunar minerals for the equatorial regions of the lunar near side, and the influence of Mg-spinel is assessed for localized occurrences in Mare Moscoviense and Theophilus crater. Regions associated with more TiO_2 or less plagioclase show higher variations of OH integrated band depth over the lunar day but overall smaller values at midday. Similar to TiO_2, regions associated with high Mg-spinel concentrations in Mare Moscoviense and Theophilus crater, exhibit weaker OH absorption bands at lunar midday compared to other compositions. These results have been previously published by the author in Hess et al. (2021c).

Secondly, this thesis contributes to explore the spectral and photometric properties of lunar swirls. Lunar swirls remain enigmatic in that the origin and explanation for their bright appearance are still unclear. In the results published by the author in Hess et al. (2020a), a compaction significance spectral index is defined for on- and off-swirl spectral pairs using Moon Mineralogy Mapper hyperspectral data. The spectral differences due to compaction and space-weathering are modeled, and the OH/H_2O absorption at swirls is analyzed. The results reveal that the spectral differences in the near-infrared are partly due to reduced space-weathering, but differences in compaction are also re-

quired. Furthermore, the photometric analysis of the Reiner Gamma swirl published by the author in Hess et al. (2023) reveals that the swirl and the surrounding maria differ significantly in opposition effect strength, which can be seen as a proxy for porosity. At the on-swirl locations, the opposition effect is less strong, which is consistent with the effects observed at the Chang'e 5 landing site. Bayesian inference is employed to obtain the mean predicted values and the associated uncertainties.

Finally, a new unmixing model is proposed, as published by the author in Hess et al. (2021b). This unmixing model builds upon the commonly used Hapke model (Hapke, 2012b), describing the linear mixing between albedos. It is subsequently combined with a model for space-weathering proposed by Wohlfarth et al. (2019), and the albedos and phase function of the space-weathering particles are mixed with the soil. All parameters of the model are given probabilistic treatment using Bayesian inference. Subsequently, the unmixing model is tested for various real and synthetic spectra, and the uncertainties are evaluated. Furthermore, the model is extended to incorporate the grain size by using the complex indices of refraction to derive the albedos of the endmembers. Moreover, maps of minerals are created using Moon Mineralogy Mapper data.

1.2 OUTLINE

The thesis is structured as follows. After this introduction, Chapter 2 reviews the current knowledge about the Moon with regard to the research topics discussed in this thesis. For example, the composition of the Moon and the presence of OH/H_2O are discussed, as well as space-weathering and the current knowledge about swirls. Additionally, the data sets used in this thesis are explained.

In Chapter 3, the radiative transfer models and their parameters are explained. In particular, the details of the Hapke model (Hapke, 2012b) and the Mie-scattering-based space-weathering framework of Wohlfarth et al. (2019) are discussed. Subsequently, in Chapter 4, the fundamentals of Bayesian inference are reviewed, and Markov Chain Monte Carlo sampling algorithms are briefly compared.

Chapter 5 shows the contributions related to the compositional analysis of the Moon. First, the OH/H_2O variations are analyzed with regard to mineral composition (see Section 5.2). Second, the spectral properties of different swirls with respect to OH/H_2O, compaction, and space-weathering are examined. Third, the unmixing model and the experiments for verification of the model are investigated in Section 5.3. In Section 5.4 the influence of grain size on the unmixing is evaluated. In the following, the unmixing is applied to the global M^3 mosaic at 20 pixels/degree and the Reiner Gamma swirl (see Section 5.5).

In Chapter 6, the photometric model and results for the Reiner Gamma swirl and the Chang'e 5 landing site are analyzed. Finally, the concluding remarks and an outlook on possible future work are given in Chapter 7.

2

RELATED WORK: THE MOON

This chapter is partly adapted or adopted from the introductions of the papers Hess et al. (2020a), Hess et al. (2021b), Hess et al. (2021c), and Hess et al. (2023).

The Moon has inspired humankind's curiosity since the beginning of time and was a key component of ancient rituals. Already approximately 500 B.C. the Greek astronomer Anaxagoras thought of the Moon as a sphere made of rock that reflects the sunlight, and similar theories came up in China and India at the same time. However, the ability to observe our nearest neighbor was very limited until telescopes became available. At the beginning of the 17th century, Galileo Galilei drew the first map of the Moon in his book Sidereus Nuncius using a telescope. After that, it still took until the 19th century to confirm that the Moon has no measurable atmosphere, that the maria are not filled with water, and that the craters are formed by meteorite impacts. The far side of the Moon, however, remained a complete mystery until, in 1959, Luna 3 by the Soviet Union took the first image revealing that there are, except for Mare Moscoviense, no maria on the far side of the Moon. The composition of the lunar surface was still unclear, however. Subsequently, the Surveyor missions unveiled that the top layer of regolith is shallow enough for astronauts to stand on without sinking into the surface, paving the way for the Apollo program.

The Apollo missions returned rock and regolith samples from the Moon to Earth to be analyzed in the laboratory (Adams and McCord, 1970; Adams and Jones, 1970; McCord and Johnson, 1970). Over the six successful Apollo missions (11,12,14,15,16,17), the astronauts returned a total of 381.7 kg of samples to Earth (Heiken et al., 1991). These samples were mainly limited to mare compositions because only Apollo 16 landed close to the highlands. It was the first hard evidence that the maria are filled with basalt containing more pyroxenes, and the highlands contain mainly plagioclase. A selection of samples was later characterized by the lunar Soil Characterization Consortium (LSCC) and is available as the LSCC catalog of highland (Taylor et al., 2001) and mare (Taylor et al., 2003) samples as part of the Reflectance Experiment Laboratory (RELAB) library. The radiometric and exposure ages of the returned samples were shown to be correlated with the impact crater size-frequency distribution (Neukum and Ivanov, 1994; Neukum et al., 2001), such that the geologic ages of homogeneous areas can be determined based on crater statistics (e.g., Hiesinger et al., 2011).

While landers and especially returned samples can provide exact knowledge of the composition, these samples are limited to very small areas. Remote sensing techniques can build on that knowledge and extrapolate it to create maps of the entire surface of the Moon. Before the returned samples could be analyzed, McCord (1969) presented telescopic observations of the Moon measuring the reflectance of the surface in the 0.4-0.8 μm wavelength range. These observations showed that color differences on the Moon go beyond brightness differences (e.g., just highland and maria) and that these could be attributed to compositionally distinct regions.

Whitaker (1972) created false color images with analog techniques to combine an image with an ultraviolet filter and an image with an infrared filter. Bluer regions in these images correspond to high Ti maria, and color differences are likely to correspond to compositional differences.

The main spectral features needed to characterize the mineralogy are the 1-μm and 2-μm absorption bands, which were difficult to acquire remotely until that point. McCord et al. (1981) obtained near-infrared (NIR) spectra of the lunar surface from telescopic observations and could confirm the widespread presence of several pyroxenes, olivine, and plagioclase on the lunar surface. Similarly, Pieters and Mustard (1988) measured spectra with a higher spectral and spatial resolution with a high accuracy to identify mineral species at and around the Copernicus crater using an Earth-based telescope and compared it to Moses Rock in Utah. The interpretation of lunar spectra is, however, more difficult because of the effects of space weathering.

It took until the 1990s when the Clementine and Lunar Prospector missions offered new insights into the composition of the lunar surface by putting sensors into the orbit of the Moon. In 1994, the Clementine spacecraft (Nozette et al., 1994) carried cameras for the ultra-violet (UV) to visible (VIS), NIR, and long-waved infrared wavelength ranges. The radio transmission instruments onboard the Clementine spacecraft were used in the bistatic radar experiment to measure the reflected radio signals on Earth. In the permanently shadowed regions at the poles, the results were interpreted as possible signatures of water ice (Nozette et al., 1996). Hiesinger et al. (2000) and Hiesinger et al. (2003) used Clementine data to divide the main mare basins into spectrally homogenous geologic units and characterized their respective ages based on crater statistics. Furthermore, Lucey et al. (2000a) mapped the FeO and TiO_2 abundance using the UV-VIS camera. Subsequently, building on that work, Lucey (2004) created the first global abundance maps of the major lunar minerals using Clementine UV-VIS data.

The Lunar Prospector revolved around the Moon from 1998 to 1999 and carried, among other instruments, a neutron and a gamma-ray spectrometer (Lawrence et al., 1998). The neutron spectrometer was designed to confirm the presence of water ice in the permanently shadowed regions and found depressions in epithermal neutron flux at the poles, which are a strong indicator for the presence of hydrogen (Feldman et al., 1998). The gamma-ray spectrometer enabled the mapping of elemental abundances in greater detail (e.g., Prettyman et al., 2006).

Because new orbiters in the recent two decades have provided data with higher spectral and spatial resolution, the Moon can be studied in unprecedented detail. The Moon Mineralogy Mapper (M^3) (Pieters et al., 2009) measured NIR spectra almost globally for different local times of day and is used to investigate the mineralogy of the lunar surface. The Lunar Reconnaissance Orbiter (LRO) cameras (Robinson et al., 2010) image the Moon in high spatial resolution under a variety of illumination conditions so that the physical properties can be derived through photometric modeling.

2.1 COMPOSITION

The surface of the Moon is mainly covered by silicate minerals such as clinopyroxene, orthopyroxene, olivine, Ca-rich plagioclase, and smaller amounts of oxide minerals such as ilmenite $FeTiO_3$ and spinel $(Fe, Mg)(Cr, Al, Fe, Ti)_2O_4$ (Papike et al., 1991). According

to spectral modeling studies (Lucey, 2002), the broadly occurring featureless spectra (e.g., Yamamoto et al., 2015) of the lunar highlands can be reproduced by assuming a mineral mixture of more than 90 % plagioclase and less than 10 % pyroxene. The mineral composition of the lunar maria consist of up to about 60% plagioclase, 30–40% pyroxene, up to 10% olivine, and up to about 20% ilmenite (Papike et al., 1991).

Lunar mare areas have high concentrations of different types of pyroxene, exhibiting pronounced absorption bands near 1 μm and 2 μm (e.g., Bhatt et al., 2019; Mustard et al., 2011), as well as contributions from the mineral olivine, displaying a broad and deep absorption band near 1-1.2 μm but no absorption band at 2 μm (e.g., Mustard et al., 2011), and the oxide mineral ilmenite ($FeTiO_3$) with a relatively dark and flat, nearly featureless spectrum in the NIR wavelength range (e.g., Blewett et al., 1997). Typical highland surfaces consist of anorthositic rocks showing no or only very weak absorption bands near 1 μm and 2 μm (e.g., Yamamoto et al., 2015). Minerals of the spinel group are widely distributed on the Moon but usually only appear in small fractions (Prinz et al., 1973). Mg-spinel can be distinguished from other lunar minerals by its deep absorption band at 2 μm and the absence of a 1 μm band (Pieters et al., 2014, 2011). Based on M^3 hyperspectral data, some spatially limited areas were found to contain high Mg-spinel concentrations in several regions of the Moon (Pieters et al., 2014). Other types of spinel (namely Fe- and Cr-spinel) are detected in Sinus Aestuum (Sunshine et al., 2010; Weitz et al., 2017; Yamamoto et al., 2013). Ilmenite and some spinels are opaque minerals that strongly influence the measured reflectance spectra in regolith mixtures. Therefore, these minerals are easier to distinguish, even for low weight percentages (e.g., Cheek and Pieters, 2014).

A significant part of the regolith (for mature surfaces >50%) is made up of agglutinitic glasses produced by micrometeorite impacts that melt the mineral grains (Taylor et al., 1996). Large amounts of submicroscopic iron responsible for the spectral effects of space weathering can be found in the agglutinate glasses. The agglutinates themselves are of a similar composition as the bulk of the mineral fraction (e.g., Baker et al., 2020). The glasses lead to broader absorption bands, but the spectra are dominated by the metallic iron inclusions (Denevi et al., 2021). Additionally, volcanic glasses are abundant in some Mare areas, e.g., in pyroclastic deposits. Taylor et al. (1996) classified the volcanic glasses into Ti-rich orange glasses (mainly from Apollo 17 samples), Fe-Mg-rich green or yellow glasses (from the Apollo 15 landing site), and black glasses that are enriched in Ti and olivine.

2.2 DISTRIBUTION OF OH/H_2O

Near-infrared (NIR) hyperspectral data from the Moon Mineralogy Mapper (M^3) instrument reveal an absorption band near 3 μm that is found all across the Moon under a variety of thermal conditions. The presence and nature of volatile species on the Moon, especially OH/H_2O, has been studied extensively (e.g., Bandfield et al., 2018; Clark et al., 2009; Grumpe et al., 2019; Li and Milliken, 2017; Pieters et al., 2009; Wöhler et al., 2017b), but the different processes leading to the hydration of the surface and their relative importance are still under debate (Schörghofer et al., 2021). Data provided by the M^3 instrument on Chandrayaan-1 (Pieters et al., 2009) yield NIR spectra that cover the Moon nearly globally for different local times of the day. This unique coverage enables

the investigation of diurnal changes on the Moon. These M^3 data show an absorption band near 3 μm that can be found at all latitudes (Bandfield et al., 2018; Li and Milliken, 2017; Wöhler et al., 2017b). This absorption band is indicative of the presence of hydroxyl/water in the uppermost lunar regolith layer. The strength of the feature, however, varies with the local time of day and latitude (e.g., Grumpe et al., 2019; McCord et al., 2011). The results strongly depend on the thermal emission removal (e.g., Bandfield et al., 2018; Clark et al., 2011; Li and Milliken, 2017; Wöhler et al., 2017a; Wohlfarth et al., 2023). The observation of diurnal and latitudinal variations is consistent with independent data obtained from telescopic measurements (Honniball et al., 2020; Honniball et al., 2021). Hendrix et al. (2019) investigated far-ultraviolet data, which are not affected by thermal emission, and also found that OH/H_2O is variable with local time. Other publicly available data sources cannot match the resolution and coverage of M^3 data in the NIR wavelength range, such that the M^3 data set is still a useful tool to investigate the presence of OH/H_2O until hyperspectral data with similar resolution extending beyond 3 μm are available. The primary source of hydroxyl has been commonly attributed to the solar wind, by which protons are implanted into the regolith, where they react with O atoms in the other minerals (e.g., Farrell et al., 2015; Grumpe et al., 2019; Starukhina, 2013; Tucker et al., 2021). However, there is evidence for endogenous OH as well. For instance, Klima et al. (2013) found OH/H_2O signatures at the Bullialdus crater to be of magmatic origin.

The 3 μm absorption band has been found to be strongest in the lunar morning and evening (e.g., Honniball et al., 2020; Li and Milliken, 2017; Wöhler et al., 2017b). Its strength decreases towards lunar midday when sink processes, including diffusive loss and photolysis, become dominant (Grumpe et al., 2019). Because the absorption band persists at lunar midday (Honniball et al., 2020; Li and Milliken, 2017; Wöhler et al., 2017b), Wöhler et al. (2017b) assert the presence of two components, a weakly and a strongly bound component, with different binding energies in the uppermost regolith layer. The modeling of Grumpe et al. (2019) suggested that OH/H_2O with binding energies around 2 eV would be more stable against diffusive loss and photolysis. According to Zhang et al. (1991) and Zhuravlev (2000), such binding sites exist in silicate minerals. We use this as the definition of strongly bound OH/H_2O. In this setting, weakly bound OH/H_2O is estimated to have binding energies of around 0.8 eV and evaporates within several hours at lunar daytime temperatures (Grumpe et al., 2019). At lunar midday, it is expected that only the strongly bound component is left in the upper layers of the regolith (Grumpe et al., 2019; Wöhler et al., 2017b). An extensive review of lunar OH/H_2O is given by Schörghofer et al. (2021). On Earth, mapping the content of OH-bearing minerals is usually performed based on the analysis of satellite NIR spectra as well (see, e.g., Pour et al., 2018).

In this work (see Section 5.2), links between the mineralogy of the surface and the variable OH/H_2O content are investigated, similar to Wöhler et al. (2018), who showed a correlation between TiO_2 abundance and the strength of the 3-μm absorption band.

2.3 SPACE WEATHERING

Due to the lack of an atmosphere, the lunar regolith is subject to the continuous influence of the space environment. Micrometeorite bombardment and solar wind change the

physical and chemical characteristics of the upper layers of the regolith (Hapke, 2001; Pieters and Noble, 2016). These changes include (1) creation of submicroscopic iron particles ($smFe^0$) (Hapke, 2001; Pieters and Noble, 2016), (2) selective comminution of larger grains into smaller grains, (3) melting of grains into agglutinates (Pieters and Noble, 2016) and (4) an increase in porosity creating a 'fairy-castle' structure (Hapke, 2001). The $smFe^0$ particles can be grouped into two categories. Firstly, the smaller nanophase iron ($npFe^0$) particles mostly redden the overall spectrum and dampen the absorption bands but also darken (e.g., Hapke, 2001). These particles are about 2-30 nm in diameter and accumulate in the rims of the mineral grains (Pieters and Noble, 2016). Secondly, the microphase iron ($mpFe^0$) particles darken but do not lead to an increase in spectral slope (Lucey and Riner, 2011).

Space weathering is ubiquitous on the lunar surface and influences and complicates many measurements on the Moon. Therefore, it has been studied extensively (e.g., Hapke, 2001; Housley et al., 1973; Housley et al., 1976; Morris, 1976; Pieters and Noble, 2016). Early transmission electron microscope (TEM) studies showed that the rims of mineral grains contain small inclusions of metallic iron particles of about 5 mm (Keller and McKay, 1993, 1997). More recently, Pieters and Noble (2016) showed TEM images of a sample artificially space-weathered in the laboratory (Noble et al., 2011) and a sample naturally space-weathered by micrometeoroid impacts. Both samples show metallic iron inclusions in the rim and vapor layer of the olivine grain (Pieters and Noble, 2016). Experimental studies that shot samples with lasers melting the outer layers several times showed that larger iron particles are created in the agglutinate glasses by combining smaller particles (Kurahashi et al., 2002; Rout et al., 2008). In these TEM images of natural samples, the larger $mpFe^0$ particles needed to reproduce the effects of space weathering are very rare. Light scattering modeling of clusters of $npFe^0$ particles can reproduce the darkening of $mpFe^0$ particles (e.g., Arnaut et al., 2021). Therefore, the nature of metallic iron particles in lunar soil is more complex than just small and large particles. Nonetheless, models relying on the two types of particles ($npFe^0$ and $mpFe^0$) can reproduce the various spectral effects observed for lunar soils and are thus used in this work. Denevi et al. (2021) found that the $npFe^0$ particles within the agglutinate glass fraction are mainly responsible for the spectral changes by manually sorting out agglutinates.

For laboratory samples, a reliable measure of maturity is the ferromagnetic resonance (FMR) I_S (Morris, 1980). Because the amount of $smFe^0$ that can be created depends on the FeO abundance of the mineral grains, the FMR is commonly normalized by FeO abundance to be able to compare, e.g., mare and highland samples.

To map maturity for the lunar surface using remote sensing data, Lucey et al. (2000b) introduced the optical maturity (OMAT) parameter, which is a measure of the spectral slope (R_{950}/R_{750}) and the overall brightness (R_{750}) and originally intended for clementine data. OMAT is correlated (r=0.68) with I_S/FeO for laboratory samples. However, it has been shown that mineralogy, like pyroxene or the abundance of opaque minerals, can influence that factor (e.g., Staid and Pieters, 2000) such that it has to be used with care. With the introduction of radiative transfer models for $npFe^0$ and $mpFe^0$ particles (Hapke, 2001; Lucey and Riner, 2011; Wohlfarth et al., 2019), the maturity can be represented by the $smFe^0$ abundance. Trang and Lucey (2019) mapped the abundance of $npFe^0$ and $mpFe^0$ using Kaguya Multiband Imager data, and they modeled the host re-

flectance using the FeO and TiO_2 abundance. The contrast between highland and maria is low compared to fresh crater rays in the maps of Trang and Lucey (2019), and swirls do not show an abnormal $mpFe^0$ abundance.

In this work, we aim to create a fully integrated model to estimate the abundance of minerals and space weathering particles for the lunar surface.

2.4 UNMIXING

Unmixing describes the process of determining the abundances of a set of constituent materials (endmembers) for a given spectrum employing radiative transfer modeling to describe the interaction of light with the different endmembers. Here, it must be differentiated between a surface where the endmembers build a macroscopic mixture, such that they are spatially separated like in a checkerboard pattern. This type of mixture can be described by a linear superposition of endmember reflectance spectra. The Moon, however, is covered by a layer of grains from crushed rocks, the so-called regolith. This constitutes a typical intimate mixture, where light interacts with the different particles by multiple scattering inside the medium. Intimate mixtures cannot be described by a linear mixture of reflectance spectra in the near-infrared. It has, however, been shown (e.g., Keshava and Mustard, 2002) that the single scattering albedo (SSA) spectra can be unmixed linearly. Models like the Hapke model (Hapke, 2012b) can be used to calculate the SSA spectra, thus transforming a non-linear problem into a linear unmixing problem.

A major factor contributing to the albedo is the grain size. As briefly reviewed in Section 3.1.6 for typical grain sizes in regolith samples, the larger the grain size, the darker the surface becomes. This relationship, however, is not linear, and also the absorption bands are affected. The unmixing must, therefore, start with the complex refractive indices from which, for a given grain size, the albedo can be derived (Hapke, 1981). The refractive indices of the endmembers need to be obtained by methods discussed later. Based on the refractive indices, the abundance of the constituent minerals and the grain size can be unmixed non-linearly (e.g., Lapotre et al., 2017; Sun and Lucey, 2021).

The vast majority of unmixing approaches rely on classical optimization techniques (e.g., gradient descent or Levenberg Marquardt algorithm) to fit the parameters of the model, like abundances or grain size, to match the measured spectrum. This has been done for several planetary bodies, like on Mars (e.g., Liu et al., 2016; Poulet et al., 2014) or on the Moon (e.g., Li, 2008; Mustard and Pieters, 1987; Rommel et al., 2017; Sun and Lucey, 2021). The endmembers can, for example, be extracted from the image itself such that they span a simplex. Each spectrum in the image can then be calculated as a linear superposition of the edges of the simplex (endmembers) (Keshava and Mustard, 2002). While this has the advantage that this can be applied easily, it has the disadvantage that the composition of these so-called image endmembers might not be known. A different approach is to select endmember spectra from a library of laboratory samples of known composition (Keshava and Mustard, 2002). This way, the composition can be directly determined, but the endmembers must be selected carefully, and some spectra might still lie outside of the resulting simplex.

Spectra obtained under lunar conditions, however, are systematically different compared to laboratory spectra of earth-analogs measured in the laboratory. All the changes caused by space weathering described in Section 2.3 significantly influence the optical

properties of the lunar surface and make it substantially more difficult to distinguish between minerals. For example, Sunshine and Pieters (1998) and Mustard and Pieters (1987) found that due to low spectral resolution and signal-to-noise ratio, multiple solutions might result in similar least squares fits but are physically implausible.

Therefore, unmixing lunar spectra either relies on image endmembers or mature samples returned by the Apollo missions. A catalog that covers a variety of compositions of the maria is the Lunar Soil Characterization Consortium (LSCC) catalog (Taylor et al., 2001, 2010). However, because the simplex is limited only to the main mare compositions and a few highland samples, this catalog cannot cover the entire mineralogy of the lunar surface. E.g., the highlands are dominated by plagioclase (90%) (Papike et al., 1991), and the LSCC catalog cannot accurately describe the typical highland spectra (Hess et al., 2021a). Further, uncommon compositions like the spinel-rich regions detected by Pieters et al. (2011) cannot be explained by unmixing purely based on the LSCC catalog.

Usually, when unmixing a spectrum, only a single best-fit solution is obtained by using one of the optimization techniques mentioned above. Rommel et al. (2017) used a similarity measure between the measured and the modeled spectrum to select the best combination between all possible combinations of endmembers. The differences between the best-fit solution for a particular combination of endmembers and the measured spectra for many combinations are, however, quite similar. Tiny changes in the spectrum could result in an entirely different combination being selected as the best solution. Lapotre et al. (2017) showed with a variety of experiments that the uncertainties of the endmember abundances and grain size are relatively large, and many solutions are equally likely. On the Moon, these uncertainties are likely to be even higher, with the influence of space weathering. In Rommel et al. (2017), the best-fit solution often contained the ilmenite endmember, in contrast to the absence of ilmenite in the actual mixture. Mineral darkening agents like ilmenite, which is abundant in some lunar maria, add another layer of complexity to the unmixing as they are almost featureless and, therefore, mostly darken.

2.5 PHOTOMETRY

Photometry is the measurement of the intensity of light reflected from an object. How much light is received depends on the physical properties of the surface and on the illumination and viewing direction. By inverting models that describe the interaction of light with the surface, we can infer information about the physical and compositional properties of planetary surfaces. However, imagery acquired under a multitude of different illumination and observation geometries is required (e.g., Shkuratov et al., 2011).

Many studies, however, are largely limited to the qualitative assessment of phase ratio images, which are difficult to interpret. To quantitatively evaluate the surface properties, we need to employ knowledge about the topography and a suitable reflectance model. The parameters of semi-physical reflectance models, such as the Hapke (2012b) model, represent physical properties to some extent, but the parameters are oftentimes interrelated (e.g., Helfenstein, 1986; Schmidt and Fernando, 2015) so that effectively there is no unique solution. An entirely probabilistic perspective of the inversion problem, as in the case of Bayesian inference sampling, is well suited to account for these uncertainties and correlated parameters and such approaches have been successfully applied to, for

instance, Mars (Fernando et al., 2013, 2015) or Jupiter's moons (Belgacem et al., 2020, 2021).

Warell (2004) used telescopic observations of the Moon and Mercury for a wide range of phase angles to derive disk-integrated photometric properties of these plants. The Moon, on average, has a low SSA of 0.168 in the visible (550 nm) wavelength range (Warell, 2004) and is mainly backscattering ($c_{DHG} \approx 0.7$, $b_{DHG} \approx 0.21$) (Warell, 2004). Because of the high porosity of the regolith, the opposition effect is strong for most of the lunar surface (Warell, 2004). While the shadow-hiding opposition effect is measurable until larger phase angles, the coherent-backscatter opposition effect is dominant for very small phase angles (<5%) (Shkuratov et al., 1999a). Sato et al. (2014) mapped the Hapke parameters of the Moon in 1×1 degree large tiles for seven wavelength channels in the UV to VIS range. The albedo is strongly wavelength dependent and is influenced by the chemical composition of the surface.

Photometry can give valuable insight into localized features of the lunar surface. For example, irregular mare patches (e.g., Qiao et al., 2020; Surkov et al., 2021) or lunar swirls (e.g., Kaydash et al., 2009; Kreslavsky and Shkuratov, 2003; Pinet et al., 2004), which are briefly reviewed in the following section (Section 2.6).

Another type of local target that is commonly investigated photometrically is landing sites. This decade can be seen as the renaissance of lunar exploration. There have not been as many missions aiming for the Moon since the Apollo era. In 2020, the Chinese lunar sample return mission Chang'e-5 successfully landed in northern Oceanus Procellarum, and the ascending stage lifted off again to return samples to Earth (Zhou et al., 2022). Landing sites of lunar missions have also been studied photometrically. Kreslavsky and Shkuratov (2003) investigated the Apollo 15 landing site and interpreted the less steep phase curve as a result of reduced roughness. Clegg-Watkins et al. (2016) observed similar effects for the Chang'e-3 and Apollo landing sites based on Narrow Angle Camera (NAC) images and concluded that the photometric properties are not significantly altered over the 40-50 years timespan between these missions. Xu et al. (2022) investigated the Chang'e-5 landing site at a very fine spatial scale with the lunar mineralogical spectrometer (LMS) and focused on the analysis of the phase function parameters that indicated a pronounced forward scattering behavior in the sampling zone of Chang'e-5.

2.6 SWIRLS

One of the biggest unsolved mysteries related to our nearest neighbor are lunar swirls. These swirls are characterized by a high-albedo pattern of complex shape, and almost all swirls are located at a magnetic anomaly (e.g., Hood and Schubert, 1980; Hood and Williams, 1989; Tsunakawa et al., 2015). Furthermore, swirls have been found to show a reduced surficial OH/H_2O content (Hendrix et al., 2016; Kramer et al., 2011; Li and Garrick-Bethell, 2019), and the spectral properties appear to be less mature than the surrounding terrain (Blewett et al., 2021; Glotch et al., 2015; Hendrix et al., 2016; Trang and Lucey, 2019). Previously, it was assumed that there is no correlation between topography and the albedo patterns (Denevi et al., 2016; Kramer et al., 2011), but more recent works have suggested that swirls are marginally lower than the surrounding terrain (Domingue et al., 2022). The photometry of swirls has also been observed to be anoma-

lous. Kreslavsky and Shkuratov (2003) and Kaydash et al. (2009) showed that the phase function is less steep at Reiner Gamma and other swirls. Pinet et al. (2004) mapped the Hapke parameters with a genetic algorithm based on Clementine data and found a higher roughness and more forward scattering behavior for the Reiner Gamma swirl. Shkuratov et al. (2007) demonstrated that the Reiner Gamma swirl shows a weaker polarization than the surrounding mare. Bhatt et al. (2023) reported variations within the Reiner Gamma swirl structure from telescopic observations. They found larger grain sizes at the central oval compared to the extended tails but only marginal differences in surface roughness from its surroundings.

Several processes can contribute to the observed anomalies. One of the commonly accepted mechanisms is the shielding of the surface by the local magnetic fields, leading to a reduced solar wind flux (e.g., Lue et al., 2011; Wieser et al., 2010). The solar wind is one of the primary drivers for space weathering (Pieters and Noble, 2016) as well as for the diurnal buildup of OH/H_2O (Grumpe et al., 2019) in the uppermost layer of the regolith. However, the spectral trends at swirls are not entirely consistent with reduced space weathering. In the NIR range, immature regolith is usually associated with a reduced spectral slope, but at swirls, this is not always the case (e.g., Blewett et al., 2021; Pieters et al., 2021). In the ultraviolet (UV) wavelength range, the spectra are less blue (spectrally blue refers to a relatively higher reflectance at a shorter wavelength) than would be expected for immature surfaces of similar composition (e.g., Hendrix et al., 2016). Therefore, additional processes are necessary to fully explain the occurrences of these swirls. It should also be noted that solar wind standoff does not imply a specific formation mechanism. To explain the unexpected spectral differences, a largely wavelength-independent brightening component is needed, where a difference in porosity is one of the possible explanations. Garrick-Bethell et al. (2011) suggested that an electric field generated by the interaction of the magnetic field with the solar wind may sort small electrostatically charged dust particles. Furthermore, if swirls are enriched in feldspathic materials (e.g., Garrick-Bethell et al., 2011) or contain less TiO_2, the higher albedo could also be explained. While Sato et al. (2017) found reduced TiO_2 content on swirls, the authors also noted that this is due to similar effects of maturity and TiO_2 abundances on the 321/415 nm reflectance ratio used for the estimation of TiO_2. Another factor that might contribute to the optical properties of swirls is compaction. Compact soil generally appears brighter but does not change the spectral slope and could possibly also explain the reduced phase curve steepness noted by photometric studies (Kaydash et al., 2009; Kreslavsky and Shkuratov, 2003). Studies have suggested that the swirls have been (at least partly) formed as a result of impacts by a comet or meteoroids (e.g., Hood and Williams, 1989; Schultz and Srnka, 1980). The interaction of the surface with the comet's coma would also lead to the destruction of the highly porous fairy castle structure usually found on the Moon (e.g., Schultz and Srnka, 1980; Shevchenko et al., 1994; Syal and Schultz, 2015). Pinet et al. (2000) proposed a formation of swirls by impacts of fragments from a comet that has been torn apart by tidal forces. To be able to judge the relevance of the different processes, more information about the physical properties of the regolith at swirls is necessary.

2.7 DATA SETS

In this thesis, several different data sets are used. These data sets can be roughly categorized into (multispectral) image data, hyperspectral data, digital elevation models (DEMs), and other derived data sets. In this section, the data sets are introduced and we briefly discuss how and where they were used throughout the thesis. Most image and spectral data are processed with the Integrated Software for Imagers and Spectrometers (ISIS) (Laura et al., 2022) to obtain calibrated radiances map projected to the region of interest (ROI).

(MULTISPECTRAL) IMAGE DATA: The highest-resolution images currently available from orbit for the lunar surface are from the Narrow Angle Camera (NAC) onboard the Lunar Reconnaissance Orbiter (LRO) (Robinson et al., 2010). The two charge-coupled device (CCD) cameras are sensitive to visible light between 400 nm and 760 nm. The LRO first entered a circular orbit at an altitude of 50 km on average, which for a field of view (FOV) of 2.85 degrees and 5000 detector elements for each camera corresponds to a resolution of about 0.5 m/pixel. The two cameras look to the left and to the right and overlap in 135 pixels such that the images can be stitched together. At the nominal altitude, this corresponds to a 5 km swath width. In 2011, the LRO transitioned into an elliptical orbit, reducing the effective resolution for large parts of the Moon.

The Wide Angle Camera (WAC) on the LRO covers a wider swath (57 km in color mode) compared to the NAC and provides seven spectral bands in the VIS and near ultraviolet (NUV) wavelength range between 321 nm and 689 nm (Robinson et al., 2010). The FOV is 60 degrees, and the resolution is approximately 100 m/pixel for the five VIS channels and 400 m/pixel for the two NUV channels. During the primary mission phase, the resolution was about 75 m/pixel for the VIS channels at a spacecraft altitude of 50 km (Scholten et al., 2012). Due to its large FOV, the observation geometry varies strongly within a single image. The sensor operates under the push frame format such that the even and odd images need to be mosaicked into one stripe.

The Multiband Imager onboard the Selenological and Engineering Explorer (SELENE), more commonly called the Kaguya spacecraft, was a multispectral camera with nine spectral bands from the VIS to the NIR (Ohtake et al., 2008). The centers of the spectral bands lie between 415 nm and 1550 nm and could, therefore, be used to characterize the 1 µm absorption band and the spectral slope as an indicator of maturity. The spatial resolution for a nominal altitude of 100 km was approximately 20 m/pixel for the channels in the VIS and 60 m/pixel in the NIR (Lemelin et al., 2015).

HYPERSPECTRAL DATA: The Indian Chandrayaan-1 spacecraft carried the Moon Mineralogy Mapper (M^3) instrument, which was a hyperspectral camera that covers the VIS to NIR wavelength range to characterize the diagnostic 1 µm and 2 µm absorption bands (Pieters et al., 2009). It operated in a *global* mode with a spatial resolution of approx. 140 m/pixel and a *target* mode with higher spatial and spectral resolution. Only a few select locations could be covered in target mode before the premature loss of contact with Chandrayaan-1 on August 29, 2009. Therefore, only data from the global mode will be used. In global mode, 85 spectral channels between 450 nm and 3000 nm are captured.

For wavelengths larger than 2500 nm and the thermal conditions of the Moon, the thermal emission component cannot be neglected. However, the level-2 data set relies on insufficient thermal emission removal (e.g., Bandfield et al., 2018; Li and Milliken, 2017; Wöhler et al., 2017a,b). The method of Clark et al. (2009), which is used for level-2 processing, relies on assumptions about the shape of the spectra and is not physically motivated. Newer models, like Bandfield et al. (2018) and Wöhler et al. (2017b), are based on physical modeling similar to methods that have been applied in the asteroid community for many years and have been proven to be well-suited for estimating the thermal emission of particulate regolith surfaces (see, e.g., Delbo et al., 2015). Recent works on lunar OH/H_2O, e.g., Honniball et al. (2020), also make use of such physically-based methods. Consequently, the level-1 data set is used.

Throughout this work, the level 1B M^3 data are processed with the photometric normalization framework (Grumpe et al., 2015) based on the DEM generation method of Grumpe et al. (2014) to obtain reflectances independent of topography as if all pixels were observed under 30-degree incidence and phase angle, and 0-degree emission angle. In this process, all M^3 images of the ROI are co-registered to the WAC mosaic as a common reference frame so that the different images for different times of the day can be compared. Subsequently, the thermal correction method of Wöhler et al. (2017a) and Wöhler et al. (2017b) is applied.

Hyperspectral data from the laboratory are used for comparisons, experiments, and as endmembers in the unmixing (see Section 5.3). The NASA Reflectance Experiment Laboratory (RELAB) is a public database of reflectance spectra of lunar samples, earth analogs, and synthetic samples, among others. The data are commonly acquired with the RELAB spectrometer at Brown University and publicly available through their website (`https://sites.brown.edu/relab/`, accessed on July 23, 2023). Besides samples from the RELAB, we use reflectance spectra described by Rommel et al. (2017).

DIGITAL ELEVATION MODELS: DEMs are essential tools for many planetary science applications. Applying photometric models, for example, requires precise knowledge about the orientation of the surface facets representing one pixel because the reflectance depends on the incidence and emission angle. The photometric and thermal normalization framework (Grumpe et al., 2015; Wöhler et al., 2014; Wöhler et al., 2017a), which is used extensively (see, e.g., Section 5.1 and Section 5.2) in this work, relies on the generation of an accurate DEM based on the method of Grumpe and Wöhler (2014). In other places, stereo-derived DEMs (e.g., Barker et al., 2016; Scholten et al., 2012) are used.

Fundamentally, DEMs can be created in three ways. (1) Laser altimetry is based on laser pulses and converts the time between sending and receiving the reflection into highly accurate height measurements. (2) Stereo algorithms aim to find matches between two images from different views of the same region to calculate the distance by triangulation. (3) Intensity-based methods, like Shape from Shading (SfS) (e.g., Horn, 1990), use one or more images and reflectance models to estimate the gradient of the surface and infer the absolute heights by integrating over the area.

Scholten et al. (2012) have published the Global Lunar DTM 100 (GLD100), which is photogrammetrically derived. The GLD100 provides almost global (98.2% of the surface) coverage because it is based on LRO WAC imagery acquired between September 2009 and January 2011. The GLD100 is gridded at 100 m/pixel. WAC stereo images from the

primary and early science mission phase (until approx. January 2011) are used so that the average resolution of the images is 75 m/pixel.

Barker et al. (2016) combined SELENE Terrain Camera (TC) stereo data with LRO Lunar Orbiter Laser Altimeter (LOLA) data to create a DEM with a resolution of 512 pixels/degree, which corresponds to approximately 60 m/pixel at the equator. The vertical accuracy was improved compared to the GLD100 and is now 3-4 m.

Shape from Shading can be used to improve the resolution of stereo DEMs and remove artifacts inherent to stereo-matching algorithms, like pixel-locking (Gehrig and Franke, 2016). Consequently, SfS-refined DEMs show improved slopes. Accurate slopes are particularly important for photometric and thermal normalization. Therefore, the SfS framework introduced by Grumpe and Wöhler (2014) is used. Stereo DEMs (like the GLD100 or the SLDEM) are used as constraints in the method of Grumpe and Wöhler (2014). SfS DEMs are inherently aligned to the image data used to create the DEM such that the data can be directly used for photometric calculations.

DERIVED DATA SETS: Several publicly available data sets were created using the spectral imagery listed above.Warell (2004) derived global averages for the Hapke parameters of the Moon from telescopic observations at a wide range of phase angles. In contrast, Sato et al. (2014) calculated resolved maps of Hapke parameters for the Moon based on WAC image data binned into 1-degree $\times$ 1-degree large tiles. Because the phase angles are more limited for imagery obtained by the LRO compared to telescopic observations, Sato et al. (2014) had to make simplifications. For example, the macroscopic roughness is set to a fixed value of 23.4-degree, the values of the phase function are coupled according to the hockey-stick relation (see, e.g., Hapke, 2012a), the opposition effects are combined in the shadow hiding term, and the amplitude of the opposition effect is coupled to the single scattering albedo.

Furthermore, based on WAC imagery, Sato et al. (2017) calculated TiO_2 abundance maps content using the ratio between the NUV channel centered around 321 nm and the VIS channel at 415 nm. For TiO_2 abundances below 2 %, other factors influence the 321/415 ratio more strongly. Therefore, TiO_2 below 2 % cannot be detected. In the highlands, the TiO_2 content is consistently below the detection limit. The highest TiO_2 abundance is found in the western Oceanus Procellarum and Mare Tranquillitatis.

Lemelin et al. (2019) created maps of the major lunar minerals using radiative transfer modeling and Kaguya MI data. Lemelin et al. (2019) used a lookup table, which contained spectra for different maturities and compositions. Map products for orthopyroxene, clinopyroxene, olivine, and plagioclase, as well as plagioclase grain size, optical maturity (OMAT), FeO abundance, submicroscopic iron abundance, and the weighted criteria. The mineral maps will be used in Section 5.2.

Wöhler et al. (2017a) and Wöhler et al. (2017b) have introduced a framework to remove the thermal emission from M^3 data so that the 3-µm absorption as a measure for the OH/H_2O abundance can be characterized. More recently, the maps of the OHIBD parameter at 20 pixels/degree for different times of day and different macroscopic roughness were published on Zenodo (Wöhler et al., 2021). The local OHIBD maps are generated presented in this work (see, e.g., Section 5.1 and Section 5.2) are generated using the same thermal correction framework (Wöhler et al., 2017b) but with manual co-registration and all available images at that location.

3

RELATED WORK: RADIATIVE TRANSFER MODELING

This chapter is partly adapted or adpoted from Hess et al. (2021b) and the Appendix from (Hess et al., 2023). Section 3.2 about the mixing model and Section 3.3 about the implementation of the space weathering model are partly adapted or adopted from Hess et al. (2021b).

To gain information about planetary bodies, we need models for the interaction of light with a nonuniform medium (Hapke, 2012b). These methods fall somewhere on the scale of direct solutions to the Maxwell equations (e.g., Grynko and Shkuratov, 2007; Mishchenko et al., 2006) and approximations using the equation of radiative transfer (e.g., Hapke, 1981; Shkuratov et al., 1999c), which in simple terms, states that light gets absorbed, is added by emission processes, or is scattered while traveling through a medium (Chandrasekhar, 1960). The computational power available to scientists has significantly increased over the last decades. Additionally, specific hardware, like Graphics Processing Units (GPUs), which can execute thousands of instructions in parallel, can be very well suited for these kinds of processing. Nonetheless, solving the electromagnetic equations directly is still a challenging task. Particles with different shapes and sizes have to be modeled to account for the complex nature of particulate planetary surfaces. So inherently, some simplifications are necessary, and these models cannot yet be applied to problems like hyperspectral unmixing.

Mishchenko (2002) showed that for particular media, like atmospheres, where the particles are far apart from each other, the equation of radiative transfer can be derived from electromagnetic theory. While the same has yet to be proven for densely packed particles, like it is the case for the particulate planetary surfaces, the results of the radiative transfer models agree well with measurements (e.g., Hapke, 2012b) and are thus, even though not theoretically correct, at least useful.

Consequently, empirical models, like the Hapke model (see Section 3.1), are commonly used in planetary science applications. In Section 3.2, the mixing model of mineral spectra is described. Moreover, Section 3.3 describes the effects of space weathering and approaches to model the effects.

3.1 HAPKE MODEL

The Hapke model originally formulated by Hapke (1981) was expanded and refined over the years to account for, e.g., effects of surface roughness (Hapke, 1984), opposition effects (Hapke, 1986, 2002), anisotropic multiple scattering (Hapke, 2002), and porosity (Hapke, 2008). The reflected light is dependent on the incidence angle i, the emission angle e, and the phase angle g. The incidence and emission angle are usually used by their cosine value $\mu_0 = \cos(i)$ and $\mu = \cos(e)$, respectively. The bidirectional reflectance according to Hapke (2012b) is then defined as:

$$r(i,e,g) = K\frac{w}{4\pi}\frac{\mu_{0,e}}{\mu_e+\mu_{0,e}}\left[p(g)B_{SH}(g) + M\left(\frac{\mu_e}{K},\frac{\mu_{0,e}}{K}\right)\right]B_{CB}(g)S(i,e,\psi). \quad (1)$$

Where w is the single scattering albedo. K is the porosity factor. $\mu_{0,e}$, μ_e are the cosines of the effective angles corrected for effects of surface roughness. $p(g)$ is the single particle phase function (SPPF). B_{SH} and B_{CB} are the correction factors for the shadow hiding and coherent backscatter opposition effects, respectively. $M\left(\frac{\mu_e}{K},\frac{\mu_{0,e}}{K}\right)$ is the term describing the multiple scattering inside the medium. Following, each of the terms is described in more detail.

3.1.1 *Single Particle Phase Function*

The SPPF depends on the shape and composition of particles inside the medium and is an average over all types of particles. A commonly used approximation for the Fraunhofer diffraction of a particle are the Legendre polynomials (P_n) with the material specific Legendre coefficients b_n (Hapke, 2002):

$$p(g) = 1 + \sum_{n=1}^{\infty} b_n P_n(\cos(g)). \quad (2)$$

For media with closely packed particles, like the lunar regolith, the double lobed Henyey-Greenstein (DHG) function (Henyey and Greenstein, 1941) is suitable (Hapke, 2012a):

$$p(g) = \frac{1+c_{DHG}}{2}\frac{1-b_{DHG}^2}{\left(1-2b_{DHG}\cos(g)+b_{DHG}^2\right)^{3/2}} + \frac{1-c_{DHG}}{2}\frac{1-b_{DHG}^2}{\left(1+2b_{DHG}\cos(g)+b_{DHG}^2\right)^{3/2}} \quad (3)$$

Each of the two lobes is one of the two additive terms. The relative weight of the forward and backward scattering lobes is described by the parameter c_{DHG}. For mostly backscattering scattering particles, as is usually found on the Moon, $c_{DHG} > 0$. For mostly forward scattering particles $c_{DHG} < 0$. The parameter b_{DHG} describes the shape or width of the lobes. The Legendre coefficients for this DHG approximation can be derived from the two parameters accordingly:

$$b_n = \begin{cases} (2n+1){b_{DHG}}^n & \text{if n = even} \\ c_{DHG}(2n+1){b_{DHG}}^n & \text{if n = odd} \end{cases} \quad (4)$$

For the lunar surface the two parameters of the DHG function are strongly correlated (Hapke, 2012a). This correlation follows an exponential form that is often described to have the shape of a hockey-stick and is thus commonly termed hockey-stick-relation. Hapke (2012a) empirically derived the function

$$c_{DHG} = 3.29e^{-17.4b_{DHG}^2} - 0.908 \quad (5)$$

to describe the hockey stick relation. Consequently, it is often reasonable to only estimate one of the parameters and set the other according to this relationship. It should be noted that the parameters of the DHG might be wavelength dependent.

3.1.2 *Multiple Scattering*

To model multiple scattering inside the medium the Ambartsumian–Chandrasekhar H-function (Chandrasekhar, 1960) is used. This function cannot be solved analytically but Hapke (2002) introduced the following approximation:

$$H(x) = \left[1 - wx\left(r_0 + \frac{1-2r_0x}{2}\ln(\frac{1+x}{x})\right)\right]^{-1} \tag{6}$$

with

$$r_0 = \frac{1-\sqrt{1-w}}{1+\sqrt{1-w}}. \tag{7}$$

Initially, Hapke's Isotropic Mutliple Scattering Approximation (IMSA) only accounted for isotropic multiple scattering (Hapke, 1981):

$$M\left(\frac{\mu_e}{K}, \frac{\mu_{0,e}}{K}\right) = H(\frac{\mu_e}{K})H(\frac{\mu_{0,e}}{K}) - 1 \tag{8}$$

For anisotropic scatterers the term:

$$M\left(\frac{\mu_e}{K}, \frac{\mu_{0,e}}{K}\right) = L_1(\mu_{0,e})[H(\frac{\mu_e}{K}) - 1] + L_1(\mu_e)[H(\frac{\mu_{0,e}}{K}) - 1] + L_2[H(\frac{\mu_e}{K}) - 1][H(\frac{\mu_{0,e}}{K}) - 1] \tag{9}$$

is used (Hapke, 2002). Thus, the improved model is termed the Anisotropic Multiple Scattering Approximation (AMSA). The functions L_1 and L_2 are defined as (Hapke, 2002):

$$L_1(x) = 1 + \sum_{n=1}^{\infty} A_n b_n P_n(x), \tag{10}$$

and

$$L_2 = 1 + \sum_{n=1}^{\infty} A_n^2 b_n, \tag{11}$$

with the coefficients b_n according to e.g., Equation 4 and A_n as

$$A_n = \begin{cases} 0 & \text{if n = even} \\ \frac{(-1)^{(n+1)/2}}{n}\frac{1\cdot3\cdot5\cdots n}{2\cdot4\cdot6\cdots(n+1)} & \text{if n = uneven} \end{cases} \tag{12}$$

so that the b_n for even n disappear in case of the multiple scattering term. If not stated otherwise this term is evaluated until $n = 15$, where the Legendre coefficients have become negligible.

3.1.3 *Roughness*

Macroscopic roughness influences the measured signal because it constitutes a superposition of all surface facets that cannot be resolved. It was found that the perceived brightness of the Moon is dependent of latitude and decreases towards the poles (Hapke, 2012b). This effect is particularly pronounced for large phase angles, which could not be explained by the models of the time that did not account for surface roughness. For a rough surface observed under a large phase angle many of the surface facets are shadowed and the brightness decreases strongly. Therefore, the effects of macroscopic surface roughness can best be observed at large phase angles. The roughness of a surface can be characterized by the mean slope angle of the surface facets ($\bar{\theta}_b$). Hapke (2012b) employs a correction for the effective incidence and emission angles (μ_e and $\mu_{0,e}$) and a multiplicative correction term $S(i, e, \psi)$ that accounts for the decrease in brightness the larger $\bar{\theta}_b$ becomes. It must be distinguished between two cases. For $i < e$:

$$\mu_e = \chi(\bar{\theta}_b)\left(\mu + \sin(e)\tan(\bar{\theta}_b)\frac{E_2(e) - \sin^2(\frac{\psi}{2})E_2(i)}{2 - E_1(e) - \frac{\psi}{\pi}E_1(i)}\right), \tag{13}$$

$$\mu_{0,e} = \chi(\bar{\theta}_b)\left(\mu_0 + \sin(i)\tan(\bar{\theta}_b)\frac{\cos(\psi)E_2(e) + \sin^2(\frac{\psi}{2})E_2(i)}{2 - E_1(e) - \frac{\psi}{\pi}E_1(i)}\right), \tag{14}$$

$$S(i, e, \psi) = \frac{\mu_e}{\eta(e)}\frac{\mu_0}{\eta(i)}\frac{\chi(\bar{\theta}_b)}{1 - f(\psi) + f(\psi)\chi(\bar{\theta}_b)\frac{\mu_0}{\eta(i)}}. \tag{15}$$

For $i \geqslant e$:

$$\mu_e = \chi(\bar{\theta}_b)\left(\mu + \sin(e)\tan(\bar{\theta}_b)\frac{E_2(i) - \sin^2(\frac{\psi}{2})E_2(e)}{2 - E_1(i) - \frac{\psi}{\pi}E_1(e)}\right), \tag{16}$$

$$\mu_{0,e} = \chi(\bar{\theta}_b)\left(\mu_0 + \sin(i)\tan(\bar{\theta}_b)\frac{\cos(\psi)E_2(i) + \sin^2(\frac{\psi}{2})E_2(e)}{2 - E_1(i) - \frac{\psi}{\pi}E_1(e)}\right), \tag{17}$$

$$S(i, e, \psi) = \frac{\mu_e}{\eta(e)}\frac{\mu_0}{\eta(i)}\frac{\chi(\bar{\theta}_b)}{1 - f(\psi) + f(\psi)\chi(\bar{\theta}_b)\frac{\mu}{\eta(e)}}. \tag{18}$$

For both cases the helper function χ is:

$$\chi(\bar{\theta}_b) = \frac{1}{\left(1 + \pi\tan^2(\bar{\theta}_b)\right)^2} \tag{19}$$

and η is defined as

$$\eta(y) = \chi(\bar{\theta}_b)\left(\cos(y) + \sin(y)\tan(\bar{\theta}_b)\frac{E_2(y)}{2 - E_1(y)}\right) \tag{20}$$

with

$$E_1 = e^{-\frac{2}{\pi}\cot(\bar{\theta}_b)\cot(y)}, \tag{21}$$

$$E_2 = e^{-\frac{1}{\pi}\cot^2(\bar{\theta}_b)\cot^2(y)}, \tag{22}$$

and

$$f(\psi) = e^{-2\tan(\frac{\psi}{2})}. \tag{23}$$

The azimuth angle ψ can be calculated from the incidence and emission angle as:

$$\psi = \arccos\left(\frac{\cos(g) - \cos(e)\cos(i)}{\sin(e)\sin(i)}\right). \tag{24}$$

3.1.4 *Opposition Effects*

For the Moon in particular, a brightness peak for areas observed under small phase angles can be observed. Similarly, this effect can be seen when taking a picture of the shadow of oneself. The area around the shadow of the head is the brightest, so it looks like a halo. In that area, the phase angle is small so that the illumination and viewing direction are almost identical. When observer, light source, and object are in opposition, small shadows in the microstructure of particulate planetary surfaces disappear so that the regolith on the Moon appears excessively bright. This is called the shadow-hiding opposition effect (SHOE). In the model of Hapke (2012b), this effect is accounted for by multiplying the SPFF with the correction term:

$$B_{SH}(g) = 1 + B_{S0}\frac{1}{1 + \tan(g/2)/h_s}, \tag{25}$$

where B_{S0} denotes the strength or amplitude of this effect and h_s is the angular width. Even for larger phase angles this effect is still noticeable on the Moon. Another contributing factor to the surge of brightness at small phase angles is the coherent backscatter opposition effect (CBOE). The increased brightness is due to constructive inference of waves entering and leaving the medium along the same scattering path. It is modeled by Hapke (2002) as:

$$B_{CB}(g) = 1 + B_{C0}\frac{1 + \frac{1-e^{-(1/h_c)\tan(g/2)}}{(1/h_c)\tan(g/2)}}{2(1 + (1/h_c)\tan(g/2))^2} \tag{26}$$

This effect acts for single scattering and multiple scattering equally, such that the correction term is applied to both (see Equation 1). For the CBOE the angular width can be determined for a certain wavelength (λ) and the mean length of the path a proton takes before it interacts with another particle (Λ).

$$h_c = \frac{\lambda}{4\pi\Lambda}. \tag{27}$$

In applications trying to derive photometric properties of the lunar regolith from orbital or telescopic imagery it is practically impossible to distinguish between SHOE and CBOE contributions. Therefore, both effects are combined in the SHOE term. Only if there is information about the width of the opposition effect at different wavelength SHOE and CBOE contributions can be distinguished. Sato et al. (2014) mapped the Hapke parameters for the lunar surface and found that the strength of the opposition effect is strongly correlated with the SSA. For the wavelengths of the WAC channels Sato et al. (2014) empirically derived the parameters s and t describing this correlation. So that an expected B_{S0} can be predicted based on the albedo:

$$B_{S0,\text{predicted}}(w) = \frac{s + wt}{wp(0)} \tag{28}$$

For the WAC channel at 604 nm $s = 2.438$ and $t = 0.096$ (Sato et al., 2014). When inverting the Hapke model to infer the photometric parameters from multi-view imagery the estimated opposition effect amplitude ($B_{S0,\text{estimated}}$) can be divided by the predicted value.

$$B_{S0,\text{corrected}} = \frac{B_{S0,\text{estimated}}}{B_{S0,\text{predicted}}(w)} \tag{29}$$

If this so corrected value $B_{S0,\text{corrected}}$ can be used to estimate whether the estimated value is abnormal compared to typical lunar regolith.

3.1.5 *Compaction*

The lunar surface is covered by a very porous layer of regolith, thus sometimes referred to as the "fairy castle". When this fairy castle is destroyed, for example when a rocket lands, the surface becomes brighter. Hapke (2008) discusses this effect and introduces the porosity factor K as follows:

$$K = -\ln(1 - EL)/EL \tag{30}$$

with the mean distance between particles (L) and the extinction coefficients

$$E = \sum_i N_i \sigma_i Q_{E,i}. \tag{31}$$

If the volume and area diameter of the particles are equal and the wavelength is small compared to the particle size so that the extinction efficiencies $Q_{E,i} = 1$ the approximation

$$EL \approx 1.209\phi^{2/3} \tag{32}$$

can be used for determining the porosity factor. Where ϕ denotes the filling factor that is defined as:

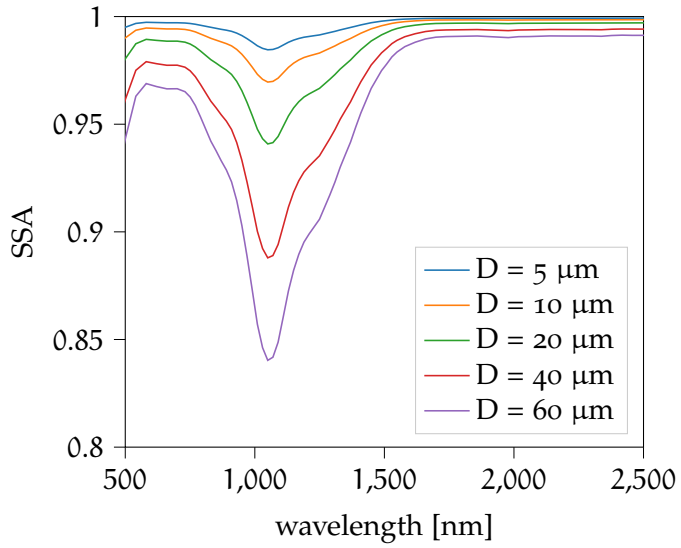

Figure 3.1: The refractive indices are derived from the RELAB sample with the ID PO-EAC-056 based on the method described by Lucey (1998). Using these complex refractive indices the SSA spectra are calculated for different grain sizes.

$$\phi = \sum_i N_i v_i, \tag{33}$$

with N_i denoting the number of particles per unit volume and v_i the volume of the particle. So that the filling factor represents the part of the unit volume occupied by particles. A higher compaction (smaller porosity) is described by a higher filling factor and thus leads to a higher reflectance (up to $\phi = 0.752$, when the porosity factors starts to decrease again). The top layer of the regolith has a small filling factor $\phi \approx 0.3$ that increases quickly with depth (Carrier III et al., 1991).

3.1.6 *Grain Size*

Another parameter that has a strong effect on the measured reflectance spectra is the grain size. The SSA changes depending on the grain size of the sample. Therefore, a correction factor like it was used for the other effects is not sufficient so that we need to derive the SSA directly from the refractive indices. The complex refractive indices m are defined as:

$$m = n + ik. \tag{34}$$

The imaginary part of the refractive indices k represents the extinction coefficients and n is the real index of refraction. For closely packed particles $Q_E = 1$ and, therefore, w can be derived as (Hapke, 1981):

$$w = Q_S = S_E + \frac{(1 - S_E)(1 - S_I)\left[r_i + e^{-2(\alpha(\alpha+s))^{1/2}D/3}\right]}{1 - r_i S_I + (r_i - S_I)e^{-2(\alpha(\alpha+s))^{1/2}D/3}}. \tag{35}$$

where D denotes the grain size (diameter of the particle) and s the internal scattering efficiency, which could be determined based on several reflectance spectra converted to albedo for different grain sizes. The value for s is typically very small for mineral grains. In this work we usually set $s = 0$, meaning no internal scattering, because there is not enough data to determine s and because the samples used in this work correspond to mineral samples and not glasses, following the argumentation of Lucey (1998). The external surface reflection coefficient is defined as:

$$S_E = \frac{(n-1)^2}{(n+1)^2} \tag{36}$$

and the approximation for the internal surface reflection coefficient, where Lucey (1998) added 0.014 to fit better with the exact solution:

$$S_I = 1.014 + \frac{4}{n(n+1)^2}. \tag{37}$$

The bihemispherical reflectance r_l is defined as (Lucey, 1998):

$$r_l = \frac{1 - \sqrt{\frac{\alpha}{\alpha+s}}}{1 + \sqrt{\frac{\alpha}{\alpha+s}}} \tag{38}$$

and the internal absorption coefficient:

$$\alpha = \frac{4\pi nk}{\lambda}. \tag{39}$$

Figure 3.1 shows the albedo spectra derived from the complex refractive indices for several grain sizes. The smaller the grain size the brighter the spectrum but the absorption bands are also less pronounced. Lucey (1998) derived the refractive indices based on an empirical relationship between Magnesium number (Mg#) and n under the assumption that n is independent of wavelength. The problem is underdetermined because we only have one equation to solve for n and k but if we set n according to Lucey (1998) k can be determined based on the measured reflectance and the Hapke model.

3.2 MIXING MODEL

According to Hapke (2012b) the single scattering albedo of a mixture (w_{mix}) is defined as the scattering coefficients (S) divided by the extinction coefficient (E) of the mixture,

$$w_{mix} = \frac{S}{E} = \frac{\sum_i N_i \sigma_i Q_{S,i}}{\sum_i N_i \sigma_i Q_{E,i}} \tag{40}$$

with N_i as the number of particles of particle type i per unit volume and $\sigma_i = \pi a_i^2$ as the cross-sectional area, where a_i denotes the radius of the corresponding particle type (Hapke, 2012b). The scattering efficiency is $Q_{S,i} = Q_{E,i} w_i$ such that the mixing formula becomes:

$$\vec{w}_{mix} = \frac{\sum_i \frac{M_i Q_{E,i}}{\rho_i D_i} \vec{w}_{em,i}}{\sum_i \frac{M_i Q_{E,i}}{\rho_i D_i}}. \tag{41}$$

The bulk density of particle type i is denoted M_i and the average particle diameter D_i. Assuming that the endmembers have the same average grain size D_i and the same extinction efficiencies $Q_{E,i}$ the fraction can be reduced. The albedo of the mixture can then be expressed as a linear superposition of the endmember SSA spectra $w_{em,i}$ weighted with the Hapke coefficients $\theta_{em,i}$

$$\vec{w}_{med}(\vec{\theta}_{em}) = \sum_i \theta_{em,i} \vec{w}_{em,i}. \tag{42}$$

For a mixture of typical lunar minerals the extinction efficiencies, grain size, and density are constant and approximately equal among the endmembers, therefore, these simplifications will be used to calculate the SSA spectrum of the mixed mineral endmembers (see Section 5.3). This spectrum is then subsequently used as the input to the space weathering framework (described in Section 3.3) to calculate the reflectance spectra of the mixture.

When the mixture directly results from the particular known endmembers used in the unmixing, the sum of the weights should be equal to one ($\sum_i \theta_{em,i} = 1$). In this work we are not enforcing this constraint, but prefer solutions where the sum is close to one. By not enforcing the sum-to-one constraint for the fractional abundances $\theta_{em,i}$ the sum can be seen as a "catch-all" parameter for all linear, wavelength independent, differences among the endmembers and compared to the examined sample. However, it is physically implausible to have endmembers with a negative contribution. Therefore, all endmember weights must be larger than zero, i.e., $\theta_{em,i} > 0$.

The porosity or compactness (Hapke, 2008) of a sample changes the brightness of a sample almost without introducing a change to the continuum slope. Therefore, this parameter introduces a scaling factor on the weights of the endmembers depending on the compactness of the sample. Depending on the laboratory setup other factors might influence the measured spectra. E.g., the gain of the sensor might be different such that a linear offset is introduced, when comparing the measurements of the same mineral for different laboratories.

3.3 SPACE WEATHERING MODELS

Space weathering poses a major challenge, e.g., for unmixing mineral abundances on the lunar surface. In addition to the darkening and reddening, the diagnostic absorption features are obscured by the optical influence of the space weathering particles (e.g., Lucey and Riner, 2011). This makes it harder to differentiate between the different minerals. While the band position remains constant the depth of the absorption that could normally be used to estimate the fraction of the constituent minerals is less clear. Submicroscopic metallic iron particles (smFe) accumulate in the rim of the grains and

Table 3.1: Material parameters

Parameter	$npFe^0$	$mpFe^0$	Medium
ρ [g/cm^3]	7.568	7.568	3.5
D [nm]	10	150	30 µm
$\vec{Q}_E(\lambda)$	Fig. 3.2a	Fig. 3.2a	2.1

agglutinates, which cause the optical effects observed for mature lunar regolith (Britt and Pieters, 1994; Hapke, 2001; Lucey and Riner, 2011).

Hapke (2001) introduced a framework that models the effects of these metallic iron particles in the regolith based on Maxwell-Garnett effective medium theory. The model predicts a darkening and reddening in the NIR and a dampening of the absorption bands. Lucey and Noble, 2008 found that the model diverges from measurements when the smFe particles inside the examined sample become larger. Hapke (2001) does only account for nanophase metallic iron particles ($npFe^0$), which are only a few nanometers small. However, transmission election microscope studies revealed that agglutinates contain much larger iron particles with tens of nanometers radius (e.g., Pieters and Noble, 2016). These particles are termed microphase iron ($mpFe^0$) or sometimes Britt-Pieters particles (Britt and Pieters, 1994; Lucey and Riner, 2011).

To model the influence of these larger particles, Lucey and Riner (2011) proposed to replace the size independent absorption term from Hapke (2001) with a term derived from Mie-theory. Lucey and Riner (2011) then implemented a mixture of the two types of particles with the medium to simulate the effects of space weathering. The particle size required to reproduce the darkening effect of mpFe particles was found to be 200 nm, which is larger than the sizes found by experiments (Lucey and Riner, 2011).

Wohlfarth et al. (2019) defined a framework based on ab-initio Mie modeling to characterize the effects of the space weathering particles. The extinction and scattering efficiencies, the albedo, and the phase function parameters for the iron particles of two different sizes and those of the host medium are calculated based on Mie-theory. These parameters are then used to calculate the mixture. If not stated otherwise particle sizes of 5 nm and 75 nm radius or 10 nm and 150 nm diameter, for $npFe^0$ and $mpFe^0$ respectively, were used throughout this work. The model worked best for an $mpFe^0$ particle size of 75 nm radius.

It is important to note that extinction efficiencies are not constant over the wavelength and are very different for the mineral endmembers and for each of the iron particles (see Figure 3.2a). As a result, the fraction in Equation 42 cannot be reduced. The SSA spectrum of the mixed mineral endmembers (w_{med}) according to Equation 42 is then used as the starting value for the mixture with the iron particles. It is here assumed that all endmembers have a similar grain size distribution, density and extinction efficiencies. The values are adapted from Wohlfarth et al. (2019) and listed in Table 3.1. The mixture of the iron particles and the medium is then defined as:

$$\vec{w}_{total}(\vec{w}_{med}(\vec{\theta}_{em}), M_{npFe}, M_{mpFe}) = \frac{(1 - M_{npFe} - M_{mpFe})F_{med}\vec{w}_{med} + M_{npFe}\vec{w}_{npFe}F_{npFe} + M_{mpFe}\vec{w}_{mpFe}F_{mpFe}}{(1 - M_{npFe} - M_{mpFe})F_{med} + M_{npFe}F_{npFe} + M_{mpFe}F_{mpFe}}. \quad (43)$$

using the factor F_x with x referring to either the medium (med), npFe^0 particles (npFe), or mpFe^0 particles (mpFe).

$$F_x = \frac{\vec{Q}_{E,x}}{\rho_x D_x} \quad (44)$$

The phase function of a mixture is also defined by the weighted sum of the phase functions of the components. The phase functions of the soil and the small npFe^0 particles are independent of wavelength, but the larger mpFe^0 particles have a wavelength dependent phase function (see also Figure 3.3), which is, therefore, given as a vector.

$$\vec{p}_{total}(g, M_{npFe}, M_{mpFe}) = \frac{(1 - M_{npFe} - M_{mpFe})F_{med}\vec{w}_{med}p_{med}(g)}{(1 - M_{npFe} - M_{mpFe})F_{med}\vec{w}_{med} + M_{npFe}F_{npFe}\vec{w}_{npFe} + M_{mpFe}F_{mpFe}\vec{w}_{mpFe}} + \frac{M_{npFe}\vec{w}_{npFe}F_{npFe}p_{npFe}(g) + M_{mpFe}\vec{w}_{mpFe}F_{mpFe}p_{mpFe}(g)}{(1 - M_{npFe} - M_{mpFe})F_{med}\vec{w}_{med} + M_{npFe}F_{npFe}\vec{w}_{npFe} + M_{mpFe}F_{mpFe}\vec{w}_{mpFe}}. \quad (45)$$

The phase functions are defined by the Legendre coefficients as in Equation 2. These b_n are calculated based on the refractive indices, grain size, and the Legendre expansion of the Mie phase function from Fowler (1983). By equating the coefficients it can be shown that the b_n of the mixture are also the weighted b_n of the soil, npFe^0, and mpFe^0 particles. The Legendre coefficients of the mixture are then used to calculate the wavelength dependent phase function of the mixture and are additionally used in the multiple scattering term $M(\mu, \mu_0)$. Finally, we obtain reflectance spectra of the mixture, according to Equation 1.

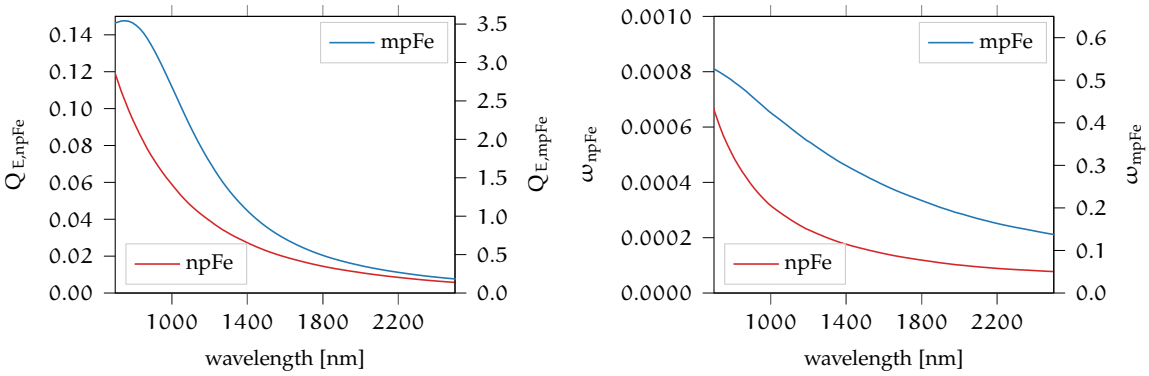

(a) Extinction efficiencies Q_E (b) SSA

Figure 3.2: Extinction efficiencies and SSA spectra of the space weathering components npFe^0 and mpFe^0 calculated according to Wohlfarth et al. (2019).

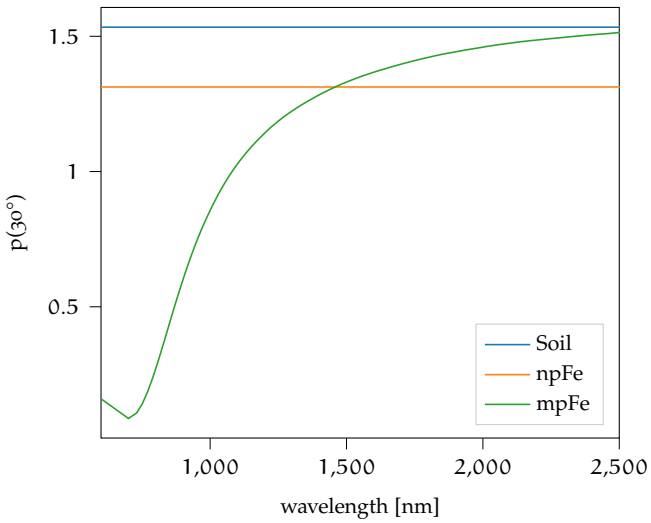

Figure 3.3: Phase function values for 30° phase angle. The soil and the npFe^0 particles phase functions are independent of the wavelength in contrast to the mpFe^0 particles.

4

RELATED WORK: BAYESIAN INFERENCE

The fundamentals about Bayesian inference and sampling algorithms in this chapter are partly adapted or adopted from Hess et al. (2021b).

The Moon as a research object poses many challenges. We cannot conduct experiments by changing parameters individually to separate their influences. We observe the Moon as it is and try to create models that describe our observations. However, the parameters of the models are oftentimes interrelated so that multiple solutions are possible. Inherent to the process are uncertainties due to measurement noise and the limited size of the data set. The frequentist approach is to see uncertainty mainly as measurement noise so that experiments are repeated in order to estimate the error bars on the data. For example, the expectation when rolling a die is 3.5, and the standard deviation is approximately 1.71, which can be estimated by repeating the die roll. As established, on the Moon, we are unable to repeat experiments. From the Bayesian perspective, the uncertainty stems from the limited size of the data set. For example, suppose we observe the Moon from several different directions and we have knowledge of how light is scattered depending on the material properties. In that case, we still have multiple solutions that describe our observations because we cannot acquire data from all directions independently of each other. Then, our data set is limited by the number of times and the way the spacecraft passes over that particular surface element. We are, therefore, much more interested in the uncertainties of the parameters, and we can update that uncertainty when more data becomes available.

With Bayesian inference (see, e.g., Gelman et al., 2013) we can estimate the probability distributions of parameters of a model based on a set of data and additional assumptions about the data. All parameters of the model are described as probability distributions. The goal, therefore, is to estimate the probability densities of the parameters Θ given some data $\mathbf{X}$. This is called the posterior distribution $p(\Theta \mid \mathbf{X})$. According to Bayes' rule, the posterior density can be written as

$$p(\Theta \mid \mathbf{X}) = \frac{p(\Theta)p(\mathbf{X} \mid \Theta)}{p(\mathbf{X})}. \tag{46}$$

For a given data set, the evidence $p(\mathbf{X})$ is constant and can be neglected during inference. Consequently, we can define the unnormalized posterior density (Gelman et al., 2013) as

$$p(\Theta \mid \mathbf{X}) \sim p(\Theta)p(\mathbf{X} \mid \Theta). \tag{47}$$

The prior $p(\Theta)$ expresses our assumptions and knowledge about the parameters previous to the experiment. It can introduce already known information about the distribution of the parameters into the procedure, or it can be uninformative (see Section 4.1). The probability of the data given a set of parameters Θ is denoted by the likelihood

($p(\mathbf{X} \mid \Theta)$). The likelihood is evaluated as a function of Θ and gives us an estimate of how likely the observed data are to occur given the current parameters.

This unnormalized posterior distribution can be calculated analytically if the probability distributions are chosen in a specific way, which might be limiting in practice. With the advancement of computer technology and the introduction of Markov Chain Monte Carlo (MCMC) methods (Neal, 1993), like the Metropolis algorithm (Metropolis et al., 1953), it is possible to estimate complex probability distributions numerically. The algorithm used in this work to sample from the posterior density distribution is described in Section 4.2.

4.1 PRIORS

Priors are one of the major components of the Bayesian approach to parameter estimation. All parameters of a model should be treated probabilistically. This knowledge about what parameters are realistic can be informative or non-informative or somewhere in between. An example of a non-informative prior is the beta distribution with $\alpha = \beta = 1$ for a parameter that is physically limited to the interval [0,1], like the single scattering albedo (see orange line in Figure A.1). The non-informative prior would then correspond to a uniform distribution in the physically plausible interval.

A more informative prior, or weakly informative prior, might include that the albedo on the Moon is, on average, about 0.22 at 400 nm (Sato et al., 2014) but still, a broad range of values is possible so that we could set the mode of the Beta distribution to 0.22 with a large variance.

An informative prior represents precise knowledge about a parameter. In this work, for example, we know the elemental abundance of the mineral mixture so that we can choose a small variance for the prior and every mineral combination, for which the elemental abundance diverges from that composition is considered to be an unlikely solution.

In Bayesian inference, the prior is updated when new evidence or data is available to build the posterior. The more data is available, the less important the prior becomes. However, if the data contains little information the influence of the prior can still be significant. For example, if our observations of the Moon are limited to a small phase angle interval (e.g., 30-70 degree), we have little information about the relative strength of the forward scattering lobe. Therefore, the posterior of the phase function parameters closely follows the prior. The subjectivity of the prior should be added with care, and a poor choice of priors, which for example, contradict each other, can lead to poor estimates of the posterior density. However, priors can also be beneficial when they help decide, in the case of large regions where the likelihood is flat, which solution is more plausible according to the experience from similar data sets.

4.2 SAMPLING ALGORITHMS

The goal of the Monte Carlo simulation is to approximate the posterior distribution. Most of the sampling algorithms as well as our approach, are based on the Metropolis algorithm (Metropolis et al., 1953), which was subsequently generalized to non-symmetrical proposal distributions and is then called the Metropolis-Hastings algorithm

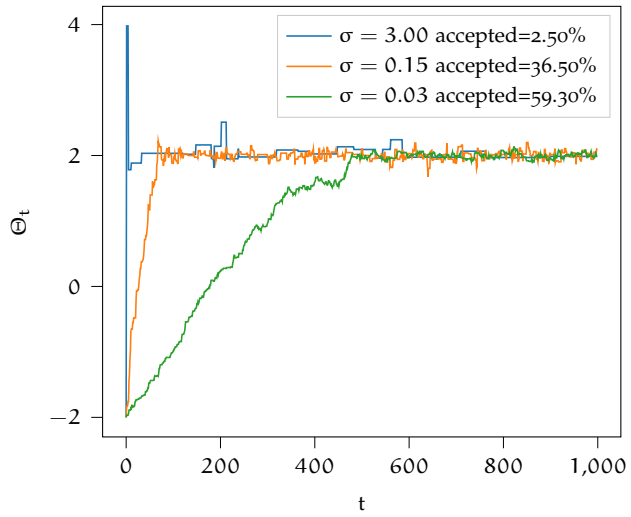

Figure 4.1: Three chains for the proposals generated from $\mathcal{N}(\mu = \Theta_{t-1}, \sigma)$ with σ according to the legend entry. If σ is chosen too large many proposals are rejected so that the posterior is not sampled efficiently (blue line). If σ is chosen too small the convergences towards the high posterior density region is slow (green line).

(Hastings, 1970). This algorithm describes a random walk through the posterior space such that for a large number of samples, the samples converge to the posterior distribution. Generally, at each step of the Markov chain, a proposal ($\Theta_t \sim \pi(\Theta_{t-1})$) is randomly generated based on the current location in parameter space. This proposal is then either accepted or rejected, and the current parameters are consequently used for the next proposal. If the proposal is more probable than the current sample, then the proposal is always accepted. If the proposal is less likely than the current sample, it is accepted with a certain probability. Therefore, also less probable solutions are sometimes accepted, but the regions of high posterior density are sampled more often.

Depending on the starting value and the chosen proposal distribution, the algorithm first samples from an area of low posterior density and then moves towards the region of higher posterior density. The first phase is called burnin, and the samples should be omitted. Figure 4.1 shows the sampled chains trying to find the mean of $\mathcal{N}(\mu = 2, \sigma = 0.1)$ using three different proposal distributions π. The proposals are generated from a Normal distribution of the form $\pi \sim \mathcal{N}(\mu = \Theta_{t-1}, \sigma)$ where σ is either 3, 0.15, or 0.03. This example illustrates the importance of selecting suitable proposal distributions that are sometimes not trivial to find.

The random walk behavior of the Metropolis algorithm can lead to slow convergence because a majority of the proposals are rejected (e.g., Gelman et al., 2013), and correlated parameters can make the algorithm much less efficient (Hoffman and Gelman, 2014). Modified versions of the Metropolis algorithm improve the proposals by, e.g., estimating the covariance matrix on the previous examples and scaling the proposal distribution accordingly (e.g., Haario et al., 2001) or by additionally proposing an alternative step that is chosen based on the rejection of the first proposal (Haario et al., 2006). However, it still remains that these methods tend to be less efficient for non-linearly correlated parameters due to their inherent random walk behavior (Hoffman and Gelman, 2014).

Hamiltonian Monte Carlo (HMC) borrows ideas from Hamiltonian dynamics (Neal et al., 2011) and introduces a 'momentum' variable. As in Hamiltonian dynamics, the momentum variable and the position are building a dynamic system. The entire sampling process is subdivided into simulations of L leapfrog steps, each of length ϵ. To calculate the momentum at a position in posterior space, we need to calculate the derivative of the posterior density for the local environment numerically or analytically. With the advances in automatic differentiation in tools like, e.g., Theano (Bastien et al., 2012), which is used in the pymc3 framework (Salvatier et al., 2016), it is possible to quickly calculate the analytical derivatives of more complex functions. If the derivative cannot be calculated automatically by Theano, the numerical calculation is very time-consuming.

The two parameters of HMC (L and ϵ), however, must be tuned by hand and strongly influence the performance of the algorithm. The parameter L determines the length of one simulation of Hamiltonian dynamics, and if chosen too large, the leapfrog steps tend to do a U-turn and return to the starting location (Gelman et al., 2013). The No U-Turn Sampler (NUTS) (Hoffman and Gelman, 2014) is an extension to HMC that automatically stops one simulation of Hamiltonian dynamics when the leapfrog step would not increase the distance to the starting location and, therefore, removes the need to tune the L parameter by hand (Hoffman and Gelman, 2014). This way, the NUTS sampler can effectively explore the posterior space.

This algorithm is likely the best choice for the problems discussed in this thesis because it can effectively sample from a posterior distribution where we expect some parameters to be correlated, and the target distribution might be multimodal.

5 COMPOSITIONAL ANALYSIS

5.1 CONTRIBUTION: PROCESSES GOVERNING THE VIS-NIR SPECTRAL BEHAVIOR OF LUNAR SWIRLS

This section and subsections herein are adapted or adopted from Hess et al. (2020a). The author's contribution is the modeling of the influence of space weathering and compaction on the spectral pairs, data analysis, illustrations, writing, and correspondence with the journal editor.

We investigated six bright swirls associated with magnetic anomalies of variable strength using Chandrayaan-1 Moon Mineralogy Mapper (M^3) hyperspectral image data. We examined the 3 μm absorption band generally ascribed to solar wind-induced OH/H_2O and spectral trends in the near-infrared wavelength range at on-swirl and off-swirl locations. We found that the 3 μm absorption band is weaker at on-swirl than at off-swirl locations and shows only weak variations with time-of-day. This result is consistent with magnetic anomaly shielding that reduces solar wind interaction with the surface. For a small swirl structure in Mare Moscoviense, we found the 3 μm absorption band to be similar to that of its surroundings due to the absence of strong magnetic shielding. Our spectral analysis results at on-swirl and off-swirl locations suggest that the spectral trends at on-swirl and off-swirl locations cannot always be explained by reduced space weathering alone. We propose that a combination of soil compaction possibly resulting from the interaction between the surface and cometary gas and subsequent magnetic shielding is able to explain all observed on-swirl vs. off-swirl spectral trends including the absorption band depth near 3 μm. Our results suggest that an external mechanism of interaction between a comet and the uppermost regolith layer might play a significant role in lunar swirl formation.

5.1.1 *Definition of the Compaction-Significance Spectral Index*

Spectral pairs are selected by taking a swirl pixel and the closest pixel that is of approximately similar brightness as the mare background. Some example locations are shown in Figure 5.1. This method ensures that pixel pairs do not exhibit significant compositional differences. In the VIS to NIR space weathering leads to an increased spectral slope (reddening) and strong suppression of the mineral absorption bands (Hapke, 2001). In contrast, Figure 5.2 illustrates that soil compaction leads to a changed overall brightness but the spectral slope is practically unchanged (Hapke, 2008) as emphasized by the plots normalized to the reflectance at 1.579 μm. By this distinction we can define a measure for the relative spectral significance of each of the two factors based on the difference between on-swirl and off-swirl pixels.

The modulation at 1.579 μm wavelength between a dark off-swirl spectrum (index d) and a brighter on-swirl spectrum (index b) is given by:

$$M_{1579} = \frac{R^{b}_{1579} - R^{d}_{1579}}{R^{b}_{1579} + R^{d}_{1579}}, \tag{48}$$

the root square deviation between the normalized dark spectrum $S_d(\lambda)$ and the normalized bright spectrum $S_b(\lambda)$ by:

$$RSE = \sqrt{\int_{661nm}^{2577nm} [S_b(\lambda) - S_d(\lambda)]^2 \, d\lambda}. \tag{49}$$

The integral in Eq. 49 covers the wavelength range from 661 nm to 2577 nm corresponding to M^3 channels 6 to 75. Larger wavelengths are neglected in order to exclude the 3-μm absorption band, which exhibits systematic differences between on-swirl and off-swirl material. We found the RSE to increase with modulation M_{1579}. For a given M_{1579}, small RSE values were found for the soil compaction trend predicted by the Hapke (2008) model and large values for a spectral trend due to reduced space weathering. Hence, we defined the compaction-significance spectral index (CSSI) as:

$$CSSI = \frac{M_{1579}}{RSE}, \tag{50}$$

where small values of CSSI indicate similarity to a spectral trend due to reduced space weathering and large values similarity to the modeled soil compaction trend. Hence, the value of the CSSI provides direct information about the relative importance of reduced space weathering and soil compaction, given a pair of on-swirl vs. off-swirl spectra.

In the case of pure compaction and in the absence of noise, the model from Hapke (2008) yields a CSSI of ~0.7 that is largely independent of the modulation M_{1579}. Adding noise to the reflectance spectra decreases the CSSI because the RSE value increases. When Gaussian noise with a standard deviation of 0.5 % is added to the reflectance spectra, which is a realistic value, the CSSI decreases to ~0.4 for pure compaction.

5.1.2 *Results*

5.1.2.1 *Behavior of the 3-μm band depth*

For all examined magnetic anomalies (Table 5.1), 3-μm band depth maps are provided for as many local times of day as possible, where "morning", "midday" and "afternoon" maps were assembled from M^3 data acquired at local times between 07:00-08:00, 10:00-14:00 and 16:00-17:00 hours local time, respectively. The 3-μm band depth is given as the average relative absorption depth across the wavelength range 2.697-2.936 μm (Wöhler et al., 2017b). Maps of the mare swirl Reiner Gamma and the highland swirl near Dufay (the latter not being very prominent at visible and NIR wavelengths but distinguishable at UV wavelengths, see Denevi et al., 2016) are shown in Figures 5.3-5.4 and maps of the other examined swirls in Figures 5.5-5.8. To the east of the swirl near Dufay, a bright region is apparent (see also Denevi et al., 2016) which shows up as an area of strongly increased 3-μm band depth (see Wöhler et al., 2019, for details). On the surface around

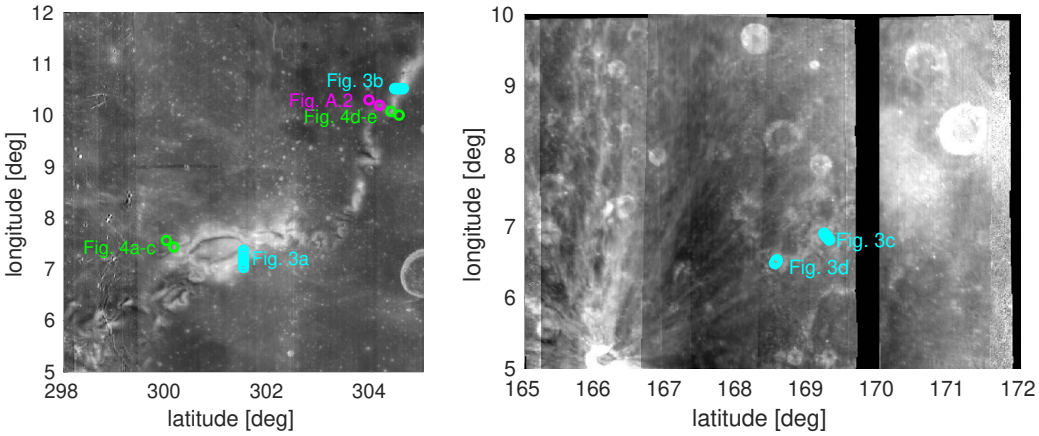

(a) Reiner Gamma (b) Dufay

Figure 5.1: Positions of the spectra selected to illustrate the spectral differences of compaction and space weathering in Figures 5.9 and 5.10 from the Reiner Gamma and Dufay Swirls.

the magnetic anomalies, the 3-µm band depth is weaker at midday than in the morning and afternoon, which is the general behavior in the lunar maria and highlands (Wöhler et al., 2017b). On the swirls, the 3-µm band is typically weaker than in their surroundings and shows only slight variations during the lunar day. All examined swirls except the swirl in Mare Moscoviense exhibit a negative anomaly in 3-µm band depth with respect to the surrounding surface (i.e., the 3-µm band is weaker on-swirl than off-swirl). Similar to Li and Garrick-Bethell (2019), our results indicate a weaker 3-µm band inside than outside the magnetic anomalies for the Reiner Gamma and Gerasimovich swirls. Our time-of-day-dependent analysis reveals that for Reiner Gamma and the highland swirls near Gerasimovich and Hayford E, the decrease in 3-µm band depth between morning and midday is much weaker for the swirl than for the surrounding surface. For the swirls in Mare Ingenii and near Dufay only M^3 data acquired at local midday are available. The small swirl in Mare Moscoviense (Figure 5.5) does not exhibit a 3-µm band depth anomaly but behaves like the surrounding mare surface. Furthermore, another high-albedo pattern corresponds to a unique strongly positive 3-µm band depth anomaly located slightly off the center of the associated magnetic anomaly (i.e., the 3-µm band is stronger on than off the bright structure, see Figure 5.4). The special nature of this structure has been subject of a previous study (Wöhler et al., 2019).

5.1.2.2 *On-swirl vs. off-swirl spectral trends*

For a large number of locations on each swirl, we manually defined pairs of points at on-swirl and nearest off-swirl locations, respectively. Similar series of spectra from on-swirl to off-swirl locations were analyzed by Pieters and Noble (2016) and Bhatt et al. (2018). For each pair of points, the CSSI was computed as shown in Figures 5.3e, 5.4d and 5.5e. For Reiner Gamma, the same was done for various small fresh craters in the surrounding mare region to check if a similar spectral behavior can be observed. Typical on-swirl vs. off-swirl spectral trends are shown in Figure 5.9 and the corresponding locations and CSSI values are listed in Table 5.2.

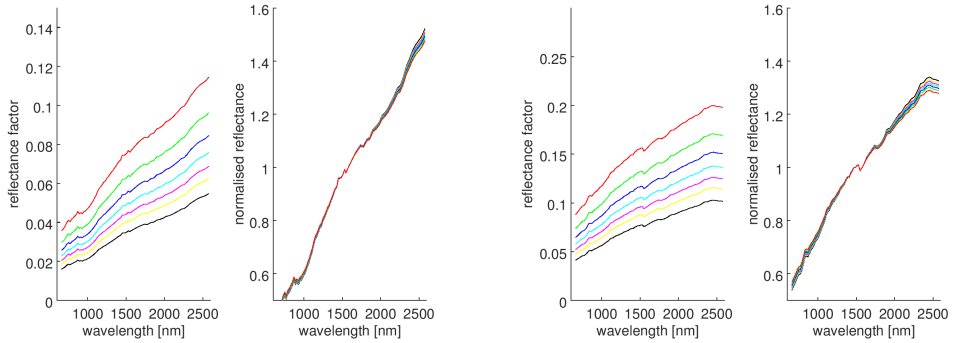

Figure 5.2: Spectral trend due to soil compaction computed based on the model by Hapke (2008). The darkest line in each plot corresponds to the measured spectrum. The brighter spectra are modelled based on the filling factor of the model by Hapke (2008) with increasing soil compaction. (a) Mature mare spectrum (average of 1 km^2 area at 14.167° E, 21.700° N). (b) Mature highland spectrum (average of 1 km^2 area at 182.400° E, 2.233° N). The filling factor ranges from 0 (bottom curve) to 0.6 (top curve) in steps of 0.1.

Swirl	**Longitude**	**Latitude**	**Max. magnetic flux density [nT]**
Reiner Gamma	302.0° E	7.4° N	508.2
Mare Ingenii	163.4° E	36.2° S	300.5
Mare Moscoviense	144.8° E	26.8° N	11.4
Dufay	169.4° E	7.2° N	72.2
Gerasimovich	236.6° E	23.0° S	587.0
Hayford E	189.0° E	13.6° N	62.7

Table 5.1: Locations of magnetic anomalies and maximum modelled magnetic flux density at the surface from (Tsunakawa et al., 2015).

Figure	**Longitude**	**Latitude**	**Type**	**CSSI**
5.9a	301.647° E	7.480° N	Mare swirl, SW trend	0.036
5.9b	304.603° E	10.637° N	Mare swirl, compaction trend	0.208
5.9c	169.227° E	6.903° N	Highland swirl, SW trend	0.031
5.9d	168.560° E	6.527° N	Highland swirl, compaction trend	0.275

Table 5.2: Information about the extracted spectra in Figure 5.9. High CSSI values indicate a spectral trend dissimilar to space weathering. Low CSSI values imply a trend consistent with reduced space weathering. The mare spectra are from the Reiner Gamma swirl and the highland representatives are from the Dufay swirl.

To further illustrate the difference of the spectral trends due to space weathering and compaction, we used the model of Hapke (2008) to examine the influence of the filling factor, and we employed the Mie-scattering based technique by Wohlfarth et al. (2019) to model the effects of space weathering. If the on-swirl and off-swirl spectral difference can be best explained by space weathering, we expect that we will be able to reproduce

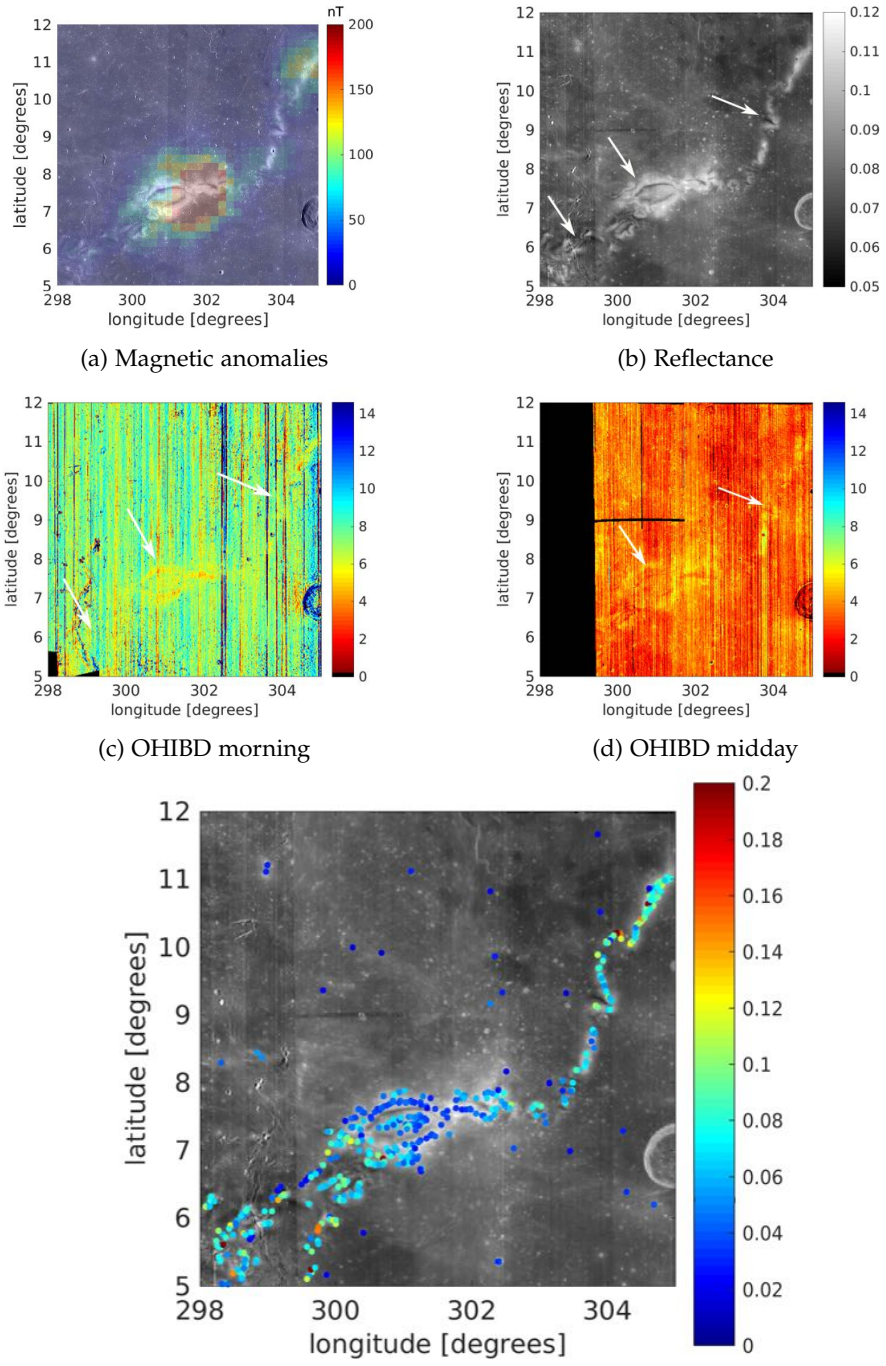

(a) Magnetic anomalies

(b) Reflectance

(c) OHIBD morning

(d) OHIBD midday

(e) Compaction

Figure 5.3: Mare swirl Reiner Gamma. White arrows indicate swirl structures, black pixels denote missing data. (a) Images from the Lunar Reconnaissance Orbiter Camera Wide Angle Camera (LROC WAC) (Robinson et al., 2010) mosaic (Wagner et al., 2015) (available online: `https://astrogeology.usgs.gov/search/map/Moon/LRO/LROC_WAC/Lunar_LRO_LROC-WAC_Mosaic_global_100m_June2013`) with Kaguya magnetic flux density maps at surface level (Tsunakawa et al., 2015) as overlay. (b) M^3 reflectance at 1.579 µm. (c),(d) Integrated 3-µm band depth (OHIBD). (e) CSSI.

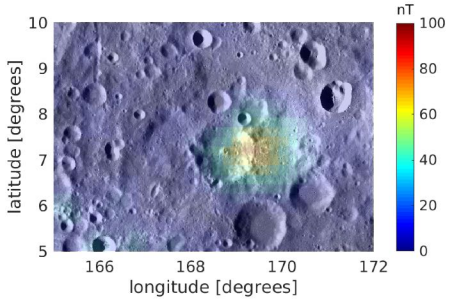

(a) Magnetic anomalies

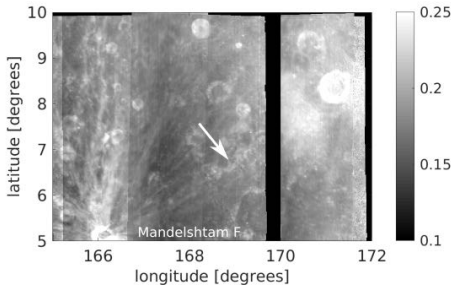

(b) Reflectance

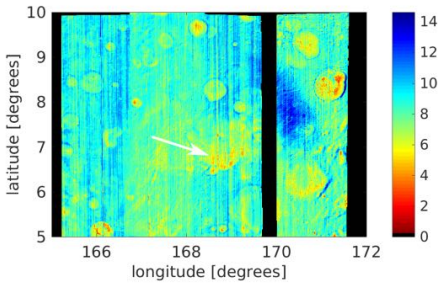

(c) OHIBD midday

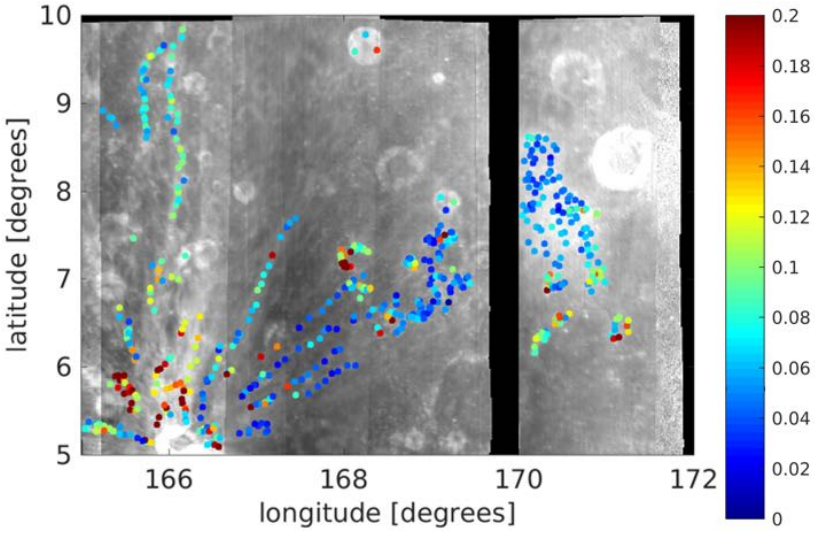

(d) Compaction

Figure 5.4: Swirl near Dufay. White arrows indicate swirl structures, black pixels denote missing data. (a) LROC WAC mosaic (Wagner et al., 2015) with Kaguya magnetic flux density maps at surface level (Tsunakawa et al., 2015) as overlay. (b) M^3 reflectance at 1.579 µm. (c) 3-µm band depth. (d) CSSI.

the off-swirl spectrum by artificial space weathering of the on-swirl spectrum relatively precisely. The artificially compacted off-swirl spectrum should then be less similar to the on-swirl spectrum, and the other way round for a spectral difference best explained by compaction. We selected two typical pairs of off-swirl and on-swirl locations at Reiner

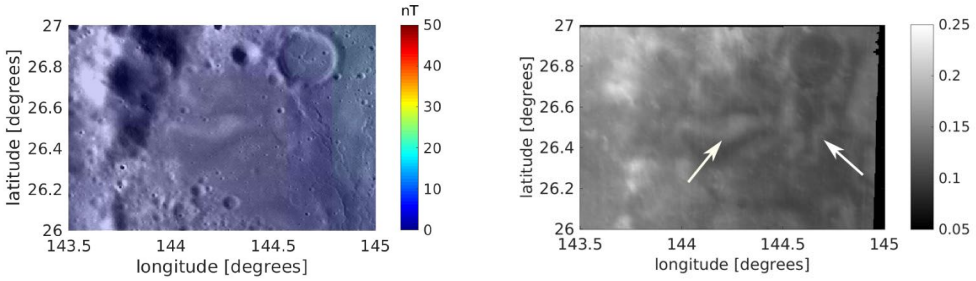

(a) Magnetic anomalies

(b) Reflectance

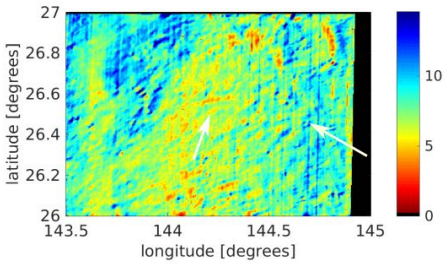

(c) OHIBD morning

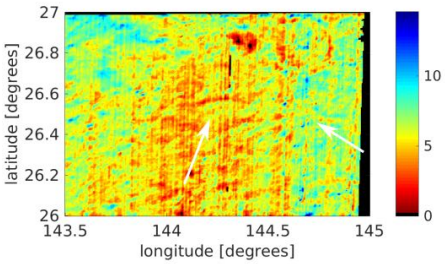

(d) OHIBD midday

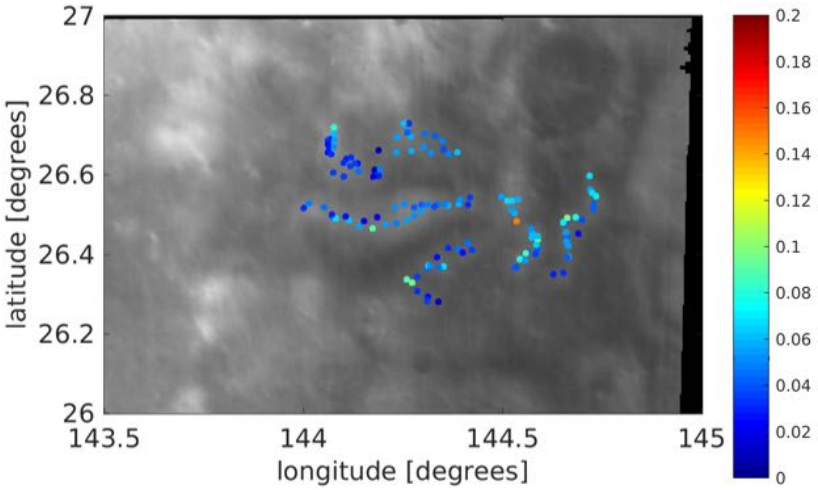

(e) Compaction

Figure 5.5: Swirl in Mare Moscoviense. White arrows indicate swirl structures, black pixels denote missing data. (a) LROC WAC mosaic (Wagner et al., 2015) with Kaguya magnetic flux density maps at surface level (Tsunakawa et al., 2015) as overlay. (b) M^3 reflectance at 1.579 µm. (c), (d) 3-µm band depth (morning, midday). (e) CSSI.

Gamma, one with high and another with a low CSSI. The measured on-swirl and off-swirl spectra with their respective space-weathered and compacted spectra are shown in Figure 5.10.

We expect the magnetic field to be effective in reducing the space weathering, but we do not expect it to alter the entire nature of space weathering. On the Moon, space

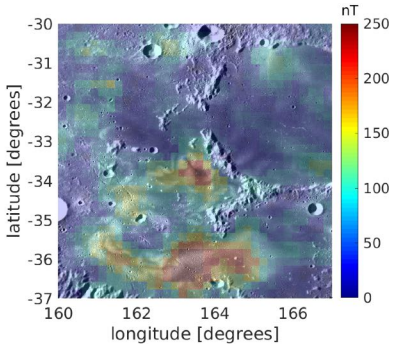

(a) Magnetic anomalies

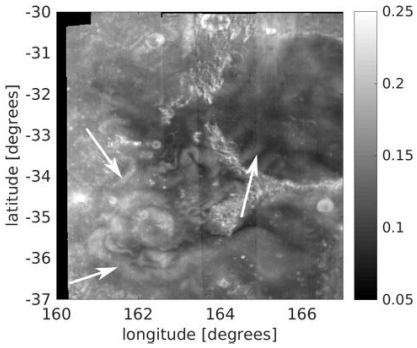

(b) Reflectance

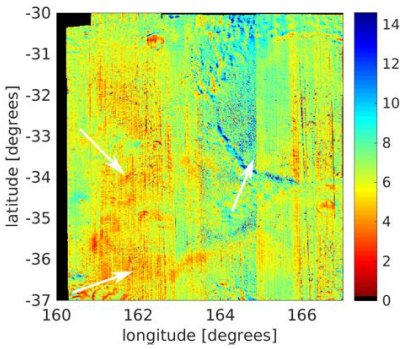

(c) OHIBD midday

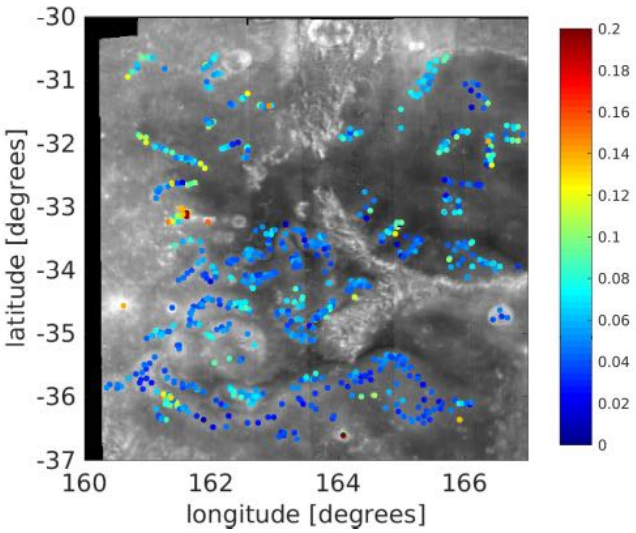

(d) Compaction

Figure 5.6: Swirl in Mare Ingenii. White arrows indicate swirl structures, black pixels denote missing data. (a) LROC WAC mosaic (Wagner et al., 2015) with Kaguya magnetic flux density maps at surface level (Tsunakawa et al., 2015) as overlay. (b) M^3 reflectance at 1.579 µm. (c) 3-µm band depth. (d) CSSI.

weathering is always associated with reddening of the spectral continuum and dampening of the absorption bands due to submicroscopic iron particles being formed. Besides solar wind particles, meteoroid impacts may produce nanophase iron (npFe) particles (e.g., Markley and Kletetschka, 2016; Thompson et al., 2017). The npFe particles

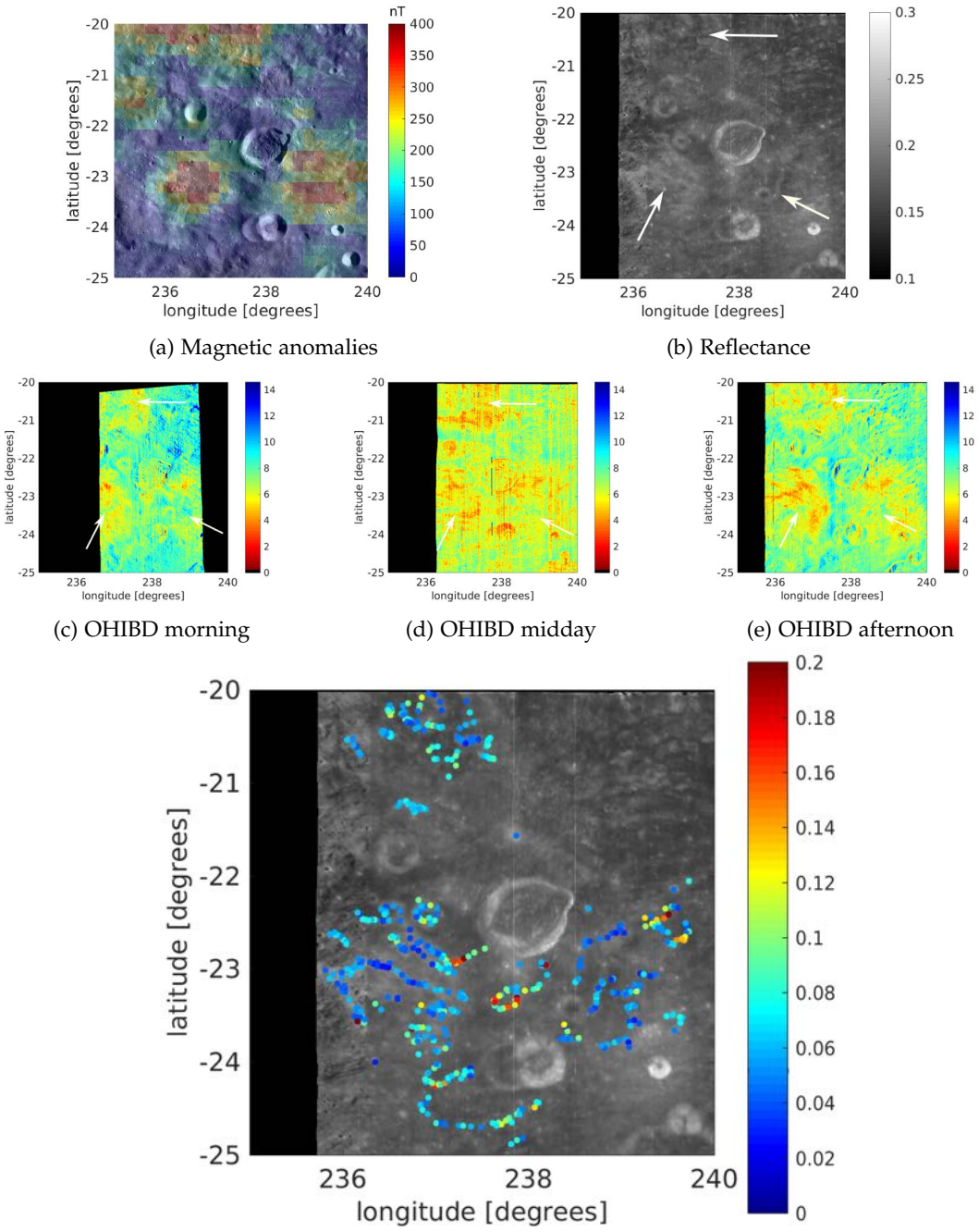

(a) Magnetic anomalies

(b) Reflectance

(c) OHIBD morning

(d) OHIBD midday

(e) OHIBD afternoon

(f) Compaction

Figure 5.7: Swirl near Gerasimovich. White arrows indicate swirl structures, black pixels denote missing data. (a) LROC WAC mosaic (Wagner et al., 2015) with Kaguya magnetic flux density maps at surface level (Tsunakawa et al., 2015) as overlay. (b) M^3 reflectance at 1.579 µm. (c)–(e) 3-µm band depth. (morning, midday afternoon) (f) CSSI.

(< 100 nm diameter) are mainly responsible for the spectral reddening, whereas the larger microphase iron (mpFe) particles (> 100 nm diameter) are mainly responsible for the darkening (Britt and Pieters, 1994; Lucey and Riner, 2011).

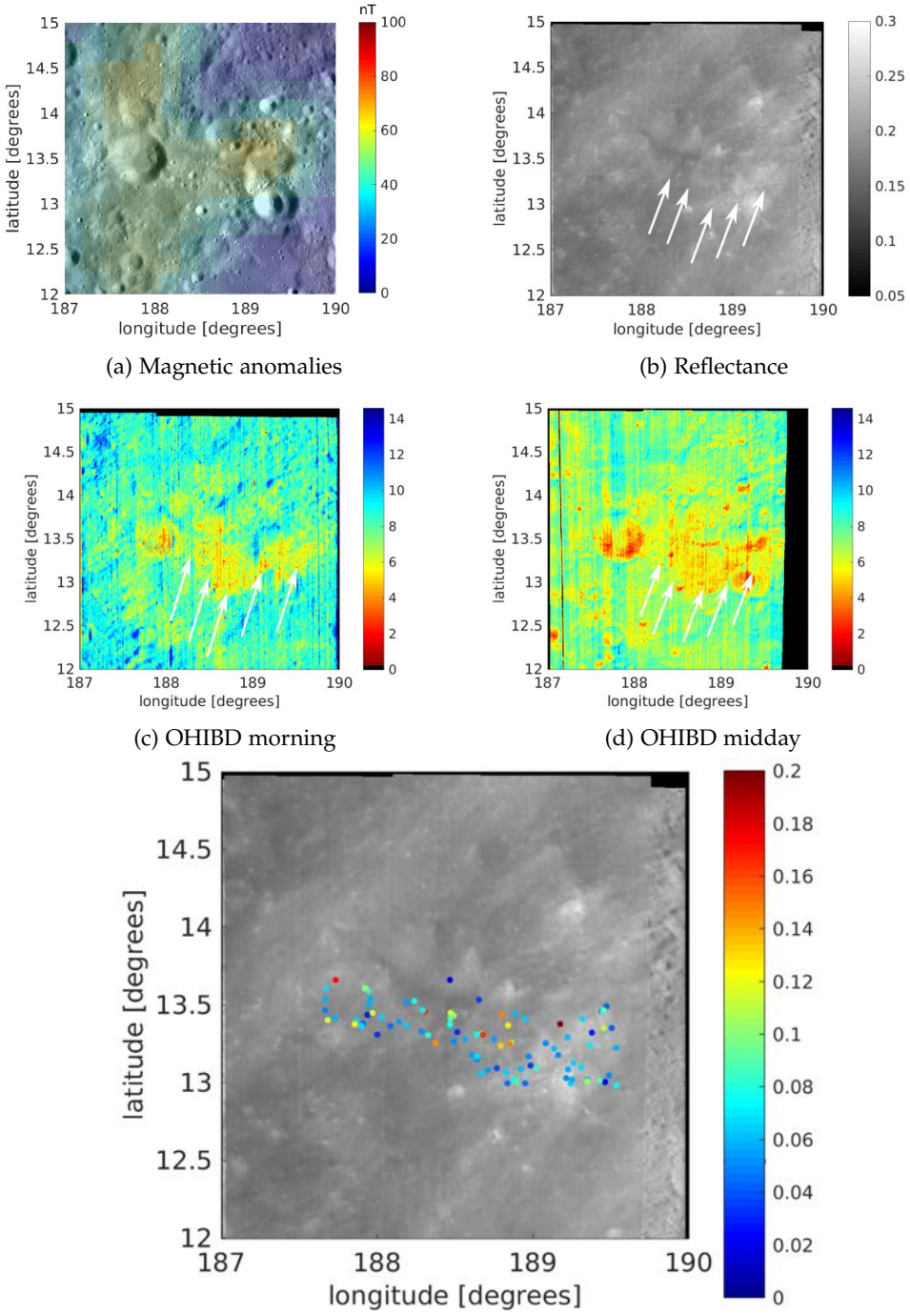

(a) Magnetic anomalies

(b) Reflectance

(c) OHIBD morning

(d) OHIBD midday

(e) Compaction

Figure 5.8: Swirl near Hayford E. White arrows indicate swirl structures, black pixels denote missing data. (a) LROC WAC mosaic (Wagner et al., 2015) with Kaguya magnetic flux density maps at surface level (Tsunakawa et al., 2015) as overlay. (b) M^3 reflectance at 1.579 µm. (c) 3-µm band depth at lunar morning and (d) at lunar midday. (e) CSSI.

In principle, the space weathering model by Wohlfarth et al. (2019) used in this work is able to account for very large mpFe particles with radii of up to 115 nm that may compensate for the reddening effect, whereas traditional models (e.g., Hapke, 2001) only

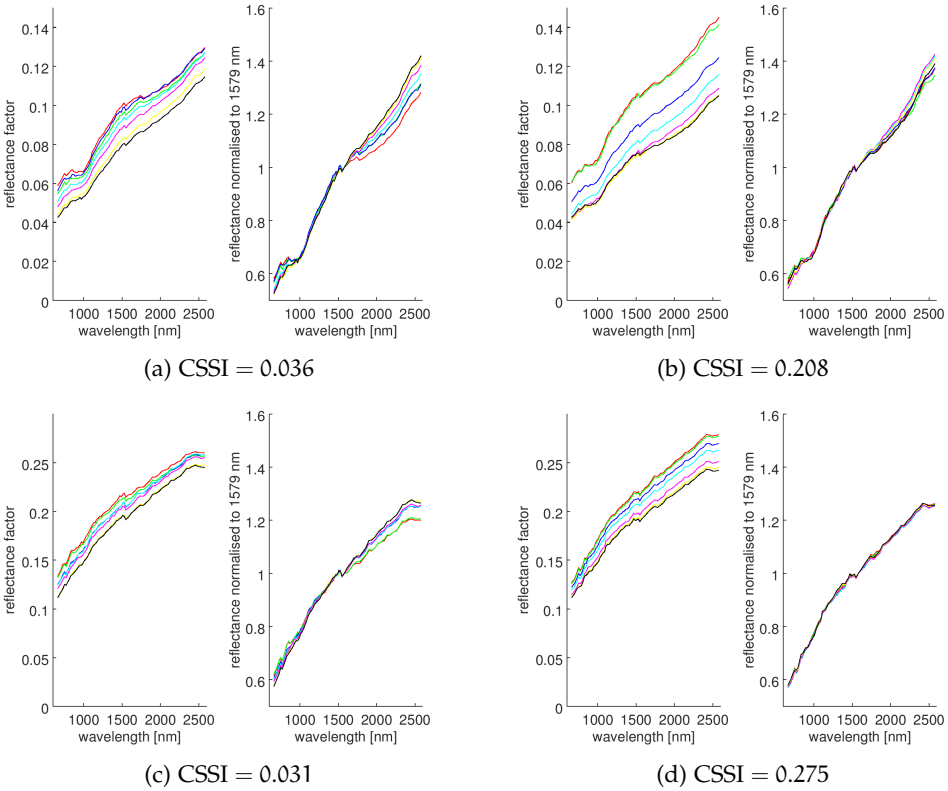

(a) CSSI = 0.036

(b) CSSI = 0.208

(c) CSSI = 0.031

(d) CSSI = 0.275

Figure 5.9: Measured spectral trends from on-swirl to off-swirl locations for spectral pairs representing a spectral trend consistent with reduced space weathering and increased soil compaction, respectively. (a), (b) Mare swirl Reiner Gamma. (c), (d) Highland swirl near Dufay. The footprint size of the spectra is 700×700 m. Each series of spectra was extracted at seven equidistant points on the straight line connecting the on-swirl location with the corresponding off-swirl location. The spectra which are brightest and darkest at 1.579 µm, respectively, were used to compute the compaction-significance spectral index (see section 5.1.1). The wavelength range is 0.661 µm to 2.577 µm.

consider the smaller npFe particles. Transmission electron microscopy measurements conducted by Pieters and Noble (2016), though, have not shown iron particles in mature lunar samples as large as the mpFe particles required by our model to compensate for the reddening effect.

Therefore, we expect the mpFe weight percentage of areas where the CSSI is low, corresponding to a difference mainly in maturity, to be representative for the region around a swirl. When modeling all location pairs at Reiner Gamma with a relatively low CSSI (CSSI < 0.04), also including a few fresh mare craters, we obtained a mean weight percentage of mpFe of 0.17 wt%. This value is consequently used in all our modeled spectra. Not applying this constraint would mean that the mpFe content is variable by a factor of three to four across the mature soil around the swirl (where the magnetic shielding is absent and thus cannot influence the space weathering), which is not plausible as the intensity and composition of the solar wind are supposed to be uniform outside the magnetic field.

Additionally, it should be noted that the npFe and mpFe weight percentages are only a relative measure for the difference in space weathering between on-swirl and off-swirl

spectra and do not necessarily represent the absolute weight percentage of npFe and mpFe particles in each of the measured spectra. Consequently, pairs with a low CSSI correspond to the highest difference in maturity and, therefore, the actual difference in mpFe for pairs with high CSSI values is probably even lower than the default value used.

The mpFe maps created by Trang and Lucey (2019) with the Lucey and Riner (2011) model using Kaguya Multiband Imager data illustrate that there are only minor differences in mpFe between locations on the swirl and next to it. Their maps furthermore show that the npFe weight percentage is strongly different between on-swirl and off-swirl locations and also varies between the locations of our selected spectral pairs. While the model of Lucey and Riner (2011) and the model of Wohlfarth et al. (2019), which is used in this work, are different, both use npFe und mpFe particles to reproduce the spectral trends observed due to space weathering. Using the fixed mpFe weight percentage of 0.17 wt% for the complete region and optimizing only for the best-fit npFe weight percentage, we obtained the following results.

Figure 5.10 shows that the first pair of spectra (Figure 5.10a–c) can be best explained by a difference in maturity. Figure 5.10a indicates that the compacted off-swirl spectrum does not fit the on-swirl spectrum well, but rather the space-weathered on-swirl spectrum fits the off-swirl spectrum as seen in Figure 5.10b. The other pair (Figure 5.10d–e) corresponds to a high CSSI of about 0.09. This spectral pair can best be modeled with compacting the off-swirl spectrum by increasing the filling factor (see Figure 5.10d). The space-weathered on-swirl spectrum cannot accurately describe the mature off-swirl spectrum, because there is no reddening of its continuum slope and its absorption bands are not less pronounced than in the on-swirl spectrum. While this effect could in principle be modeled by adding large amounts of mpFe (about three to four times the default value used), this would require a different process contradicting the common assumptions made about the spectral effects of lunar space weathering. As can be seen in the normalized spectra (Figure 5.10c and 5.10f), the compacted on-swirl spectra have the same normalized spectral slope and, therefore, can hardly be distinguished from the corresponding off-swirl spectra in normalized reflectance, see also the modeling result for a pair with a very high CSSI of 0.34 shown in Figure 5.11. A similar spectral trend has been found by Pieters and Noble (2016) for a location on Reiner Gamma. This modeling illustrates that the CSSI is a tradeoff factor between the spectral trends of space weathering and compaction modeled with the filling factor. Both processes are likely to be present, but either one might be more dominant, depending on the location.

As shown in Figure 5.3e, in the central bright oval part of the mare swirl Reiner Gamma the CSSI obtains values of ~0.03, comparable to the surrounding small fresh craters. However, in the southwestern part of the central oval, the small "flower" structures southwest of it and in the northern part of the "tail," moderately large values of CSSI in the range 0.1–0.2 and in some places even very large values exceeding 0.2 are found. The central oval of Reiner Gamma is strongly shielded by the magnetic field, which reaches magnetic flux density of 508.18 nT, and, therefore, we assume that here the shielding from the solar wind is the main factor for the explanation of the high albedo. This is consistent with the mainly small values of the CSSI. In the tail of Reiner Gamma magnetic shielding is also present, but here the high values of the CSSI suggest that the dominant process leading to increased albedo appears to be a difference in

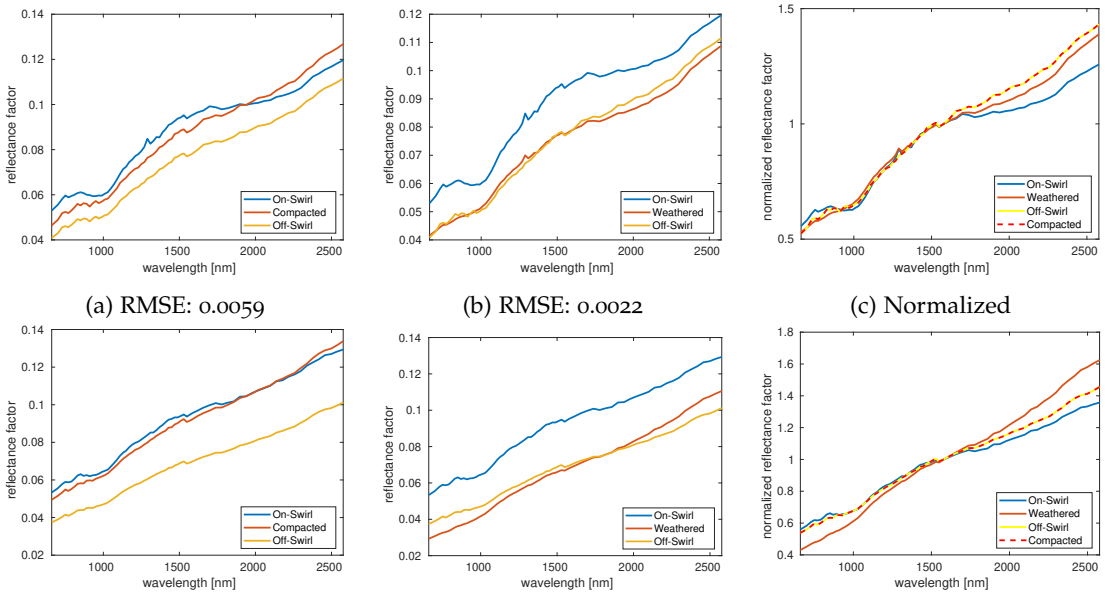

(a) RMSE: 0.0059 (b) RMSE: 0.0022 (c) Normalized

(d) RMSE: 0.0040 (e) RMSE: 0.0059 (f) Normalized

Figure 5.10: Illustration of the different spectral trends for two on-swirl and off-swirl pairs of spectra from Reiner Gamma. (a)–(c) Pair of spectra with a low CSSI, where the space weathering model provides a better fit. (d)–(e) Pair of spectra with a high CSSI, where the soil compaction model provides a better fit. The best-fit spectra for a compacted off-swirl spectrum are shown in (a) and (d). On-swirl spectra that have been artificially space-weathered according to Wohlfarth et al. (2019) to obtain a best fit to the measured off-swirl spectrum are shown in (b) and (e). The locations of the spectra are displayed in Figure 5.1a. The exact locations, best-fit model parameter values and CSSI values are listed in Table 5.3. The best-fit root mean squared errors (RMSE) are listed in the captions of the individual diagrams.

Description	**(a)–(c) on-swirl**	**(a)–(c) off-swirl**	**(d)–(f) on-swirl**	**(d)–(f) off-swirl**
Latitude	7.432° N	7.558° N	10.078° N	10.005° N
Longitude	300.138° E	299.995° E	304.375° E	304.535° E
Difference in mpFe [wt%]	0.170			
Difference in npFe [wt%]	0.870		1.535	
Difference in filling factor	0.083		0.223	
Difference in CSSI	0.027		0.09	

Table 5.3: Results of the modeling runs shown in Figure 5.10. The first set of spectra (a)–(c) constitutes a spectral difference similar to reduced space weathering. The second set (d)–(f) is consistent with a difference in albedo due to increased soil compaction.

compaction. The magnetic shielding in the tail is significantly weaker with a maximum magnetic flux density of only 132.14 nT.

As an independent verification of the spectral differences between the "oval" and the "tail" of Reiner Gamma, we performed a principal component analysis (PCA) (Marsland, 2015), similar to Chrbolková et al. (2019). Figure 5.12e shows the mean spectrum of the region. The eigenvectors of the covariance matrix, the so-called principal components, contain information about trends in the data but are usually difficult to interpret in an

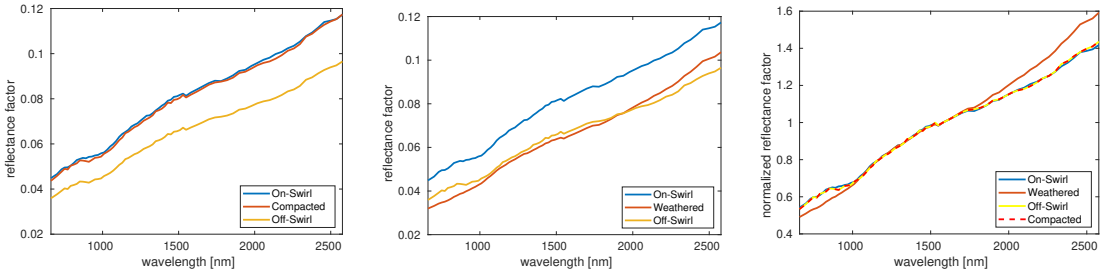

(a) RMSE: 0.0016 (b) RMSE: 0.0039 (c) Normalized at 1579 nm

Figure 5.11: Spectral pair with a high CSSI of 0.34. The compacted off-swirl spectrum with a filling factor of 0.144 can almost perfectly describe and recreate the on-swirl spectrum. The space-weathered on-swirl spectrum with a respective npFe 1.217 wt % and mpFe 0.17 wt % does not recreate the off-swirl spectrum accurately. The position of the spectral pair is marked in Figure 5.1. The on-swirl location is: 10.198 °N, 304.152 °E and the off-swirl location is: 10.302 °N, Lon: 303.945° E. The root mean squared errors (RMSE) of the modeled with respect to the measured spectra are listed in the corresponding captions.

intuitive way. However, in this special case the first component, describing most of the variance in the data, can be interpreted to contain information about the 1-µm and 2-µm absorption bands (Figure 5.12f). The second component indicates a "bluening" of the spectrum occurring in the transition from mature to immature soils (Figure 5.12g). The score maps of the second and the third principal component show systematic differences between the "oval" and the "tail" (Figure 5.12. In the score map of principal component 2 (Figure 5.12b) the bright "tail" is hardly distinguishable from the surrounding mare surface, confirming that the spectral properties of the "tail" systematically differ from those of the "oval".

At the Dufay swirl, the CSSI is lowest where the magnetic shielding is strongest (Figure 5.4d), similar to Reiner Gamma. No clear trends are apparent at the Moscoviense, Ingenii, Gerasimovich and Hayford E swirls (Figures 5.6d, 5.7f and 5.8e). Large values of CSSI are observed in small areas of all examined swirls, that is, in the western part of the Dufay highland swirl and the southern part of the bright structure to the east (Figure 5.4d), the Mare Ingenii swirl (Figure 5.6d), the central, southern and eastern part of the Gerasimovich swirl (Figure 5.7f), and the central-eastern part of the Hayford E swirl (Figure 5.8e). For the small swirl in Mare Moscoviense, the CSSI is generally lower but also reaches values larger than 0.1 (Figure 5.5e). Interestingly, also the rays close to the fresh crater Mandelshtam F southwest of the Dufay swirl exhibit large values of the CSSI (Figure 5.4d).

5.1.3 *Discussion*

The flux of solar wind protons is modulated by magnetic fields on small to large spatial scales (Hemingway and Tikoo, 2018; Kallio et al., 2019). In principle, the occurrence of negative 3-µm band depth anomalies in association with magnetic anomalies for all examined swirls except the Mare Moscoviense swirl is consistent with the common assumption that inside the magnetic anomaly the solar wind proton flux at the surface is lower than outside (e.g., Blewett et al., 2011; Kramer et al., 2011) or prevents their

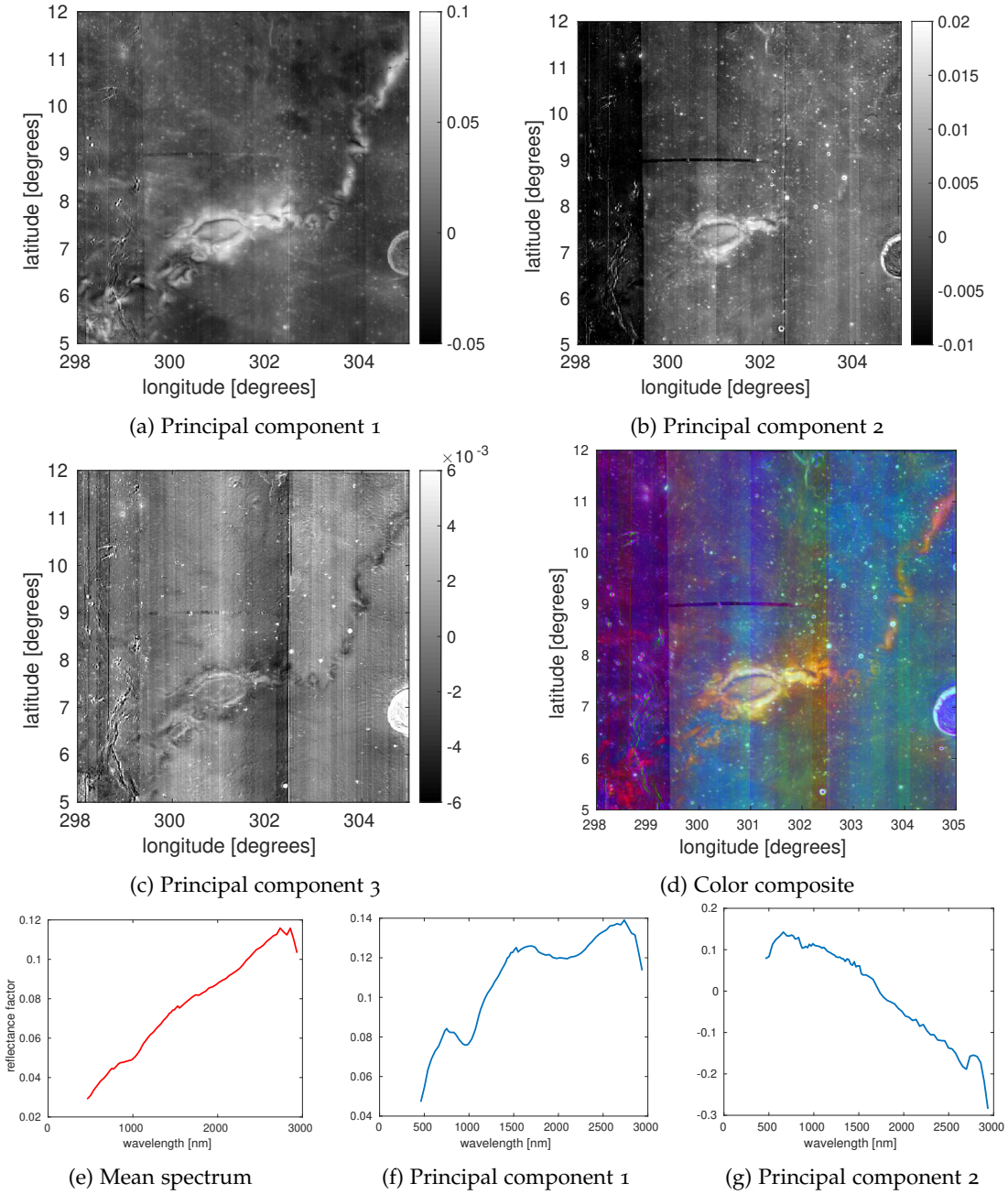

(a) Principal component 1

(b) Principal component 2

(c) Principal component 3

(d) Color composite

(e) Mean spectrum

(f) Principal component 1

(g) Principal component 2

Figure 5.12: Maps of the scores of the first three principal components for the Reiner Gamma region.

deep penetration into the regolith by reducing their velocity (Farrell et al., 2017), thus reducing the rate of subsequent reactions with surface-bound oxygen.

The Mare Moscoviense swirl, which is associated with a weak maximum magnetic field at surface level of only 11.44 nT (Table 5.1, Figure 5.5a), does not exhibit a 3-µm band depth anomaly. This behavior is consistent with the probable lack of magnetic shielding.

Our observations indicate that outside the magnetic anomalies the difference between the morning or afternoon and the midday 3-µm band depth values is smaller than about

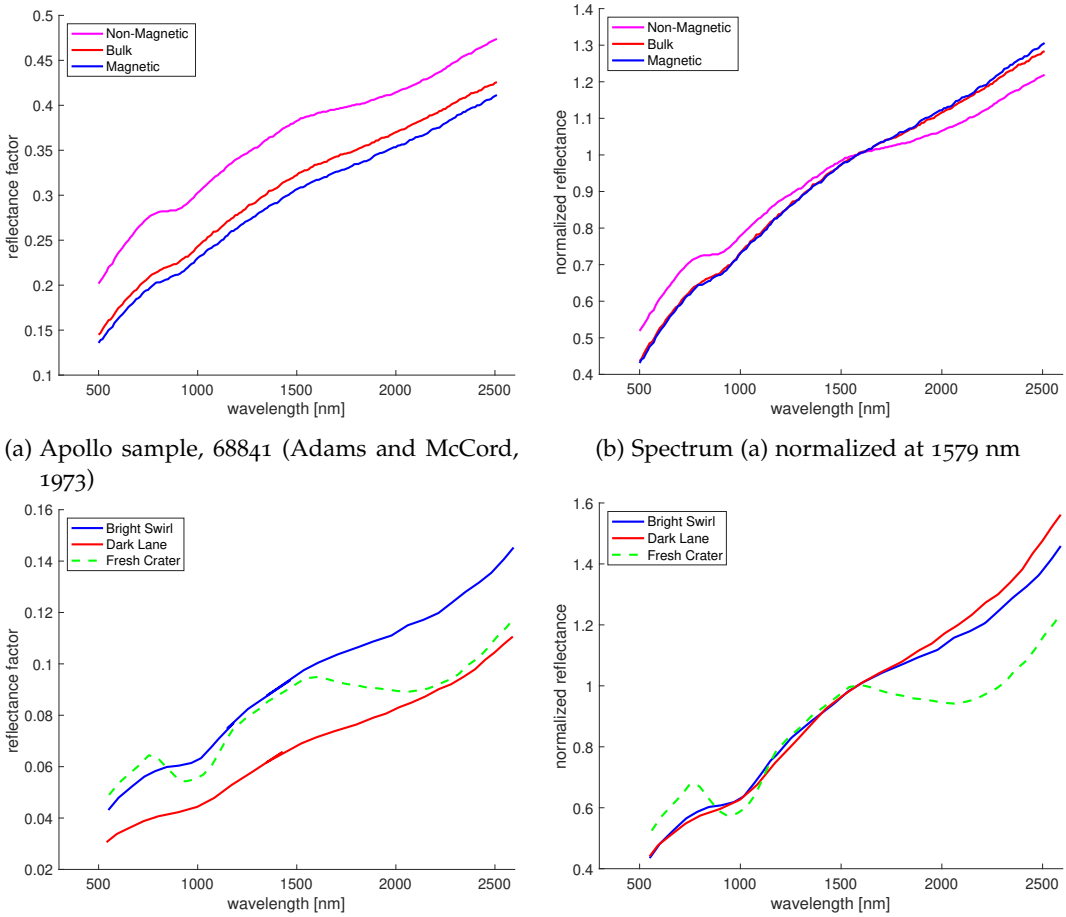

(a) Apollo sample, 68841 (Adams and McCord, 1973)

(b) Spectrum (a) normalized at 1579 nm

(c) M^3 spectral pair (Pieters, 2018).

(d) Spectrum (c) normalized at 1579 nm

Figure 5.13: Comparison of spectral trends described by (Pieters, 2018, see Figure 2 therein). The magnetic separates in (a) are taken from RELAB database (http://planetary.brown.edu/relab), with Sample-IDs LS-JBA-180-M, LS-JBA-180-N and LS-JBA-180-P for magnetic, non-magnetic and bulk samples, respectively. These laboratory spectra were originally acquired by Adams and McCord (1973). The CSSI for the spectra of magnetic vs. non-magnetic material corresponds to 0.044. The bright swirl, dark lane and fresh crater spectra were derived from M^3 data by Pieters (2018), we extracted the spectra shown in (c) manually from Figure 2B of Pieters (2018). The CSSI value for the spectral pair of bright swirl and dark lane corresponds to 0.108.

30%. In contrast, surficial H column densities about ten to one hundred times higher in the morning and afternoon than at midday are predicted by the model of Farrell et al. (2017) for the low-latitude range in which the examined magnetic anomalies are located. This discrepancy might be explained by the presence of a more strongly bound OH/H_2O component (e.g., Bandfield et al., 2016; Li and Milliken, 2017), which may be quenched in agglutinates (Li and Milliken, 2017). This component is not subject to diffusive loss and photolysis. The observed 3 µm band depth then corresponds to an additive combination of the strongly bound component and the weakly bound, time-of-day-dependent component (Grumpe et al., 2019; Li and Milliken, 2017; Wöhler et al., 2017b).

The reduced 3-μm band depth at on-swirl vs. off-swirl locations is also detectable at midday. This observation suggests that also the strongly bound OH/H_2O component is less abundant inside than outside the magnetic anomalies and is thus dependent on the solar wind flux. Consequently, the strongly bound component is not completely due to hydrated minerals. Rather, it might consist of OH/H_2O induced by solar wind protons that underwent diffusion into binding states of sufficiently high energy in the surface mineral that it is not susceptible to diffusive loss and photolysis on time scales comparable to the lunar day. It has been shown that due to the presence of darkening agents, such as ilmenite, the 3-μm absorption band depth is expected to decrease with decreasing albedo (Milliken and Mustard, 2007). To explain our observation that the 3-μm band is weaker inside than outside a magnetic anomaly, the abundance of the darkening agent would have to be higher on-swirl than off-swirl. In contrast, to explain the high swirl albedo, the abundance of the darkening agent would have to be lower on-swirl than off-swirl. Hence, variations in the abundance of darkening agents are not able to explain both the albedo and the behavior of the 3-μm band depth. Furthermore, as pointed out by Kramer et al. (2011) there is no plausible process that is able to explain how the darkening agent should have been removed from the on-swirl location. Therefore, we assume that this effect has no significant influence on the estimation of the 3-μm band depth.

On the one hand, the mechanism of magnetic shielding is thus consistent with the observation of reduced space weathering at the swirls, corresponding to the small CSSI values smaller than 0.05 exhibited by all swirls examined in this study. On the other hand, this mechanism alone cannot explain the observed peculiar spectral signatures showing nearly no variation in normalized reflectance between on-swirl and off-swirl surfaces, as indicated by large CSSI values in the range 0.1–0.2 and even higher in some parts of all examined swirls. Of course, a possible explanation for compacted soil is that magnetic shielding may also able to prevent the surface from becoming as porous as the surrounding soil. Highly porous and fine-grained regolith often referred to as "fairy castle" (Hapke and Horn, 1963) is created by gardening of the regolith by micrometeorites and solar radiation (e.g., Hapke and Horn, 1963). This would, however, suggest that the magnetic field shields the surface also from micrometeorite impact, which is generally assumed to be not the case (e.g., Chrbolková et al., 2019), or that the high porosity of mature regolith is mainly caused by charged particles of the solar wind rather than by micrometeorites, which would be physically unintuitive.

Consequently, the peculiar spectral signatures indicating compacted soil provide evidence for the occurrence of an additional physical process beyond magnetic shielding. As a possible external mechanism, the interaction between the regolith and cometary gas has been suggested (e.g., Gold and Soter, 1976; Pinet et al., 2000; Shevchenko, 1993), which might be similar to the effect of a landing rocket jet (e.g., Shevchenko, 1993). This mechanism can explain the observed on-swirl vs. off-swirl spectral trends in the following ways:

It has been proposed that the magnetic field is also relevant to explaining the origin of swirls. The separation between magnetic and non-magnetic grains has been proposed to be an explanation for the spectral signatures on and around swirls (Pieters, 2018; Pieters and Garrick-Bethell, 2015). Magnetic materials are darker than non-magnetic materials (Adams and McCord, 1973), so that a removal of the magnetic components from the

swirl would lead to a difference in albedo. Furthermore, the normalized spectral slope of magnetic samples is larger than that of non-magnetic samples, resulting in a relatively low CSSI of 0.044 (Figure 5.13b). The pair of spectra for a dark lane and an on-swirl spectrum from Pieters (2018) shown in Figure 5.13c, and 5.13d corresponds to a CSSI of 0.108, a similarity that suggests a difference in compaction rather than a difference in maturity. The spectral difference of non-magnetic and magnetic grains is similar to the space weathering trend described in Section 5.1.2.2. The process of magnetic separation is thus able to explain spectral trends with low CSSI values, but not the occurrence of spectral trends associated with large CSSI values attributed to soil compaction in Section 5.1.2.2.

The spectral signatures of reduced space weathering observed for all examined swirls can be explained by the removal of an uppermost very thin, strongly mature regolith layer by the cometary gas, where the newly exposed regolith will undergo reduced space weathering due to the presence of localized magnetic shielding. A similar process is described by Wu and Hapke (2018) in their analysis of reflectance spectra of the regolith near the Chang'e-3 lander affected by the landing rocket jet, which were acquired by the VNIS instrument on-board the Yutu rover. Their series of spectra exhibit a clear space weathering trend. This will preferentially happen when the gas moves approximately parallel to the surface. Wu and Hapke (2018) point out that the gas jet of the landing rocket removed only a very thin layer of regolith and did not change the surface roughness. This would support the finding of Glotch et al. (2015) that the surface roughness is not altered at swirls. Wu and Hapke (2018) also assumed that only the finest regolith fraction might be removed by the gas jet. However, a difference between on-swirl and off-swirl material in average grain size alone would not be able to explain the difference in albedo. Immature soils are known to be more coarsely grained than mature soils (e.g., Dollfus, 1999), and coarsely grained regolith always has a lower albedo than finely-grained regolith of the same composition (e.g., Kramer et al., 2011), so that the coarse grain size supposedly associated with the immature on-swirl locations cannot explain their high albedo. Garrick-Bethell et al. (2011) suggested the opposite effect as an explanation for the albedo difference, meaning that, in their model, the finely grained regolith fraction is transported to the swirl locations by electric fields generated by separation of charged solar wind particles due to the local magnetic field. This requires a systematic sorting of the grains over long periods of time as a consequence of periodically recurrent differential grain motion during lifting of the regolith at sunrise and sunset. Furthermore, to explain the spectral behavior of swirls that deviates from reduced space weathering, their model requires an increased component of highland material at on-swirl relative to off-swirl locations, whose origin is not obvious.

Depending on its direction of motion, the cometary gas may also lead to compaction of the regolith. To explain the increase in swirl albedo (which is at most a factor of 1.5 relative to a "normal" surface) by regolith compaction alone, that is, without changing the maturity, the Hapke (2008) model indicates that the filling factor of the regolith would have to be increased from its typical value of 0.3 (Hapke, 2008) to about 0.5–0.6 (Figure 5.2a). The uppermost centimeters of the regolith determine its thermal properties (Vasavada et al., 1999). Hence, compression of a very thin regolith layer of only a few grains thickness would explain the observed reflectance properties due to the limited penetration depth of NIR photons of at most several microns, while in agreement with

the findings by Glotch et al. (2015) this compression would not change the bulk thermal properties of the regolith. It is also consistent with the finding by Neish et al. (2011) that swirls are very thin.

Here, the mechanism of complete or partial magnetic shielding continues to be of essential importance to explain the current appearance of the swirl patterns, because it maintains the observed high-albedo structures and negative 3-µm band depth anomalies over long periods. The existence of the Mare Moscoviense swirl, where magnetic shielding is supposedly absent or much weaker than for the other examined swirls, may be explained by interaction with cometary gas that happened so recently that no significant space weathering effects could occur since then.

The occurrence of large CSSI values (> 0.2) on the ejecta blanket of the fresh ~15 km diameter crater Mandelshtam F at distances from the center of up to two to three crater diameters (Figure 5.4) can be explained in the way that in the vicinity of the crater the bright structures are due to localized strong compaction of the immature continuous ejecta deposits near the crater. At larger distances from the crater, the rays oriented in the north-eastern direction show a spectral trend that is more similar to reduced space weathering (CSSI < 0.05) compared to the rays oriented in northern direction (CSSI ≈ 0.1). This behavior may be due to an asymmetric distribution of the crater ejecta, where a broad streak of bright ejecta material extends from the crater to the north. Assuming that this immature material is overlaid by narrow bright filaments of similarly immature but compacted material would explain the large CSSI values inferred for the northern ray. In contrast, the northwestern rays were deposited directly on relatively dark and thus mature highland material, so that the inferred small CSSI values reflect the difference in maturity between the northeastern rays and the surrounding surface.

Shevchenko (1993) estimated the age of Reiner gamma formation to be about 40 million years and stated that within the last 40 million years about 40 swirl-forming events could have occurred. This estimate, however, did not consider the magnetic shielding of the surface, which is supposed to extend the lifetime of the swirl structures substantially. The size of a comet responsible for the formation of Reiner gamma is estimated to be three to four km by Pinet et al. (2000). Hydrodynamic modeling of the origin of swirls due to interaction between cometary coma and the lunar surface shows that the impact of 1 km large comets can explain the properties of the observed swirls (Syal and Schultz, 2015). In this work, the frequency of 1 km large comet impacts with the Moon is estimated to be one impact per 29 million years. For more accurate estimates of the size of swirl-forming comets, one needs to better know the properties of the lunar regolith. The estimated dynamic pressure of the gas for Apollo exhaust events is about 6890 $\mathrm{N\,m^{-2}}$ and it was large enough to decrease the porosity and to change reflectance properties of the regolith near the landing site (Hinners and El-Baz, 1972). Additional studies of the influence of the interaction of cometary gas with the surface on porosity and reflectance properties of the lunar surface are needed. To further quantify and validate the presented model, it would be necessary to know the age of the swirls and how long magnetic shielding can preserve the albedo markings. If these parameters were known, they could be compared to the influx of comets and how frequently such interaction events occur.

5.2 CONTRIBUTION: DEPENDENCE OF THE HYDRATION OF THE LUNAR SURFACE ON THE MINERALOGY

This section and subsections herein are adapted or adopted from (Hess et al., 2021c), and also partly from Hess et al. (2020b), and Hess et al. (2019a). The contribution is motivated by the observations of reduced OH/H_2O at spinel-rich regions.

We investigate the interrelation between the hydration of the lunar regolith and the mineral composition of the surface of the Moon with respect to the concentrations of plagioclase and TiO_2, highly correlated with the oxide mineral ilmenite, and Mg-spinel. The spectral properties of lunar regions with a low concentration of plagioclase or a high concentration of TiO_2 or Mg-spinel show a strong reduction in hydration at lunar midday compared to other compositions. This suggests that these oxide minerals contain less of the strongly bound OH component, which is not removed at lunar midday. The time-of-day-dependent variation of the 3-μm band depth is greater in TiO_2-rich areas compared to other mare regions. The TiO_2-rich regions, therefore, appear to have a strong tendency to adsorb solar wind induced hydrogen into binding states of low energy that can more readily desorb and readsorb OH/H_2O on a daily basis.

5.2.1 *Parameter Definitions*

The studies carried out in this work are based on the level 1B data set acquired by M^3 (Pieters et al., 2009), which is subsequently photometrically calibrated and the thermal emission component is removed. We used M^3 images that were resampled to 300 pixels/degree for regional analysis and to 20 pixels/degree to construct a nearly global mosaic. The spectral radiance values were then converted to normalized spectral reflectance values using Hapke's anisotropic multiple scattering approximation (Hapke, 2002) and the topography of the surface, which is represented by a high-resolution Digital Terrain Model (DTM) constructed with the method of Grumpe et al. (2014). All M^3 images are carefully co-registered to the reference WAC mosaic (Speyerer et al., 2011) such that all pixels correspond to the same location on the ground. Absorption features near 3 μm for estimating the amount of OH/H_2O are affected by thermal emission, requiring the thermal emission component to be removed from the measured spectral radiance. We used the thermal correction framework described by Wöhler et al. (2017a), Wöhler et al. (2017b) and Grumpe et al. (2019), which corresponds to an iterative extension of the thermal equilibrium method of Shkuratov et al. (2011). Our method accounts for the influence of surface roughness (see also, Bandfield et al., 2018) and yields an effective surface temperature (see, Grumpe et al., 2019, for details). The thermally corrected spectra are then used to determine the OH integrated band depth (OHIBD) parameter of the 3 μm band, which is a measure of the amount of hydroxyl/water in the uppermost layer of the regolith (Wöhler et al., 2017a,b), according to

$$\mathrm{OHIBD} = 100 \times \frac{\int_{\lambda_{min}}^{\lambda_{max}} \left(1 - \frac{R(\lambda)}{c(\lambda)}\right) d\lambda}{\lambda_{max} - \lambda_{min}}, \tag{51}$$

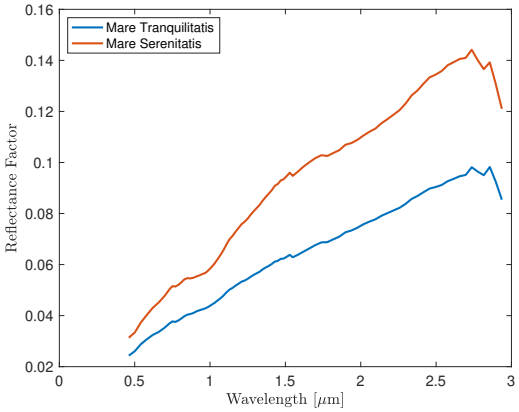

(a) Mare spectra

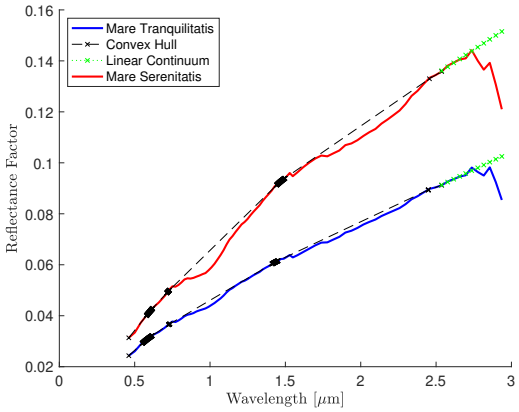

(b) Mare spectra, with continuum

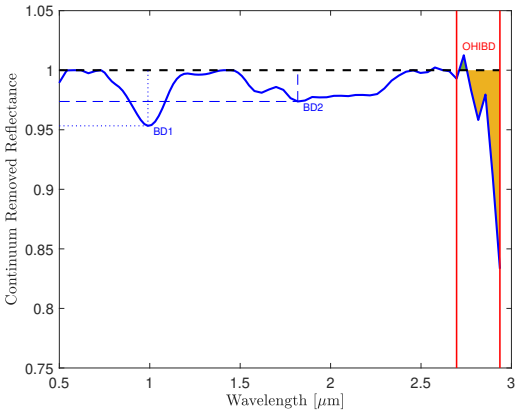

(c) Mare Tranquilitatis

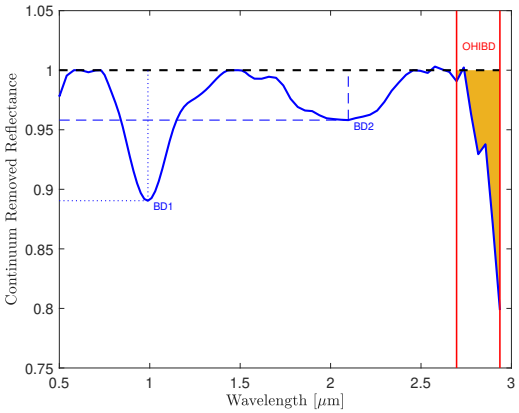

(d) Mare Serenitatis

Figure 5.14: Example spectra of high-TiO_2 mare (blue curve) and low-TiO_2 mare area (red curve), reflectance factor (Figure 5.14a) and with continuum (Figure 5.14b). The blue curve spectrum was taken from Mare Tranquillitatis as an average spectrum of a $4° \times 4°$ area centered around (9° N, 34° E). The red curve spectrum was extracted from Mare Serenitatis as an average spectrum of a $4° \times 4°$ area centered around (24° N, 18° E). The continuum removed spectra are shown in Figures 5.14c and 5.14d for Mare Tranquillitatis and Mare Serenitatis, respectively. For BD1 and BD2 the continuum is defined as the convex hull of the spectrum. For the 3 µm range the continuum is a linear function fitted to the values between 2.537 and 2.657 µm marked in green in Figure 5.14b.

where $R(\lambda)$ is the thermally corrected reflectance spectrum (see, e.g., Figure 5.14a) and $c(\lambda)$ the linear continuum fitted to the reflectance values between 2.537 and 2.657 μm (see green lines in Figure 5.14b). The OHIBD parameter can be interpreted as the mean relative absorption across the wavelength interval $[\lambda_{min}, \lambda_{max}]$ with $\lambda_{min} = 2.697$ μm and $\lambda_{max} = 2.936$ μm. The part over which the integral is calculated is marked in Figures 5.14c and 5.14d, for a weak and strong absorption, respectively. Differences in gain between M^3 observations does not influence the measured OHIBD.

The other spectral parameters used for this work, characterizing the absorption bands near 1 μm and 2 μm, are inferred with the framework described by Wöhler et al. (2014) and Bhatt et al. (2015). First, the spectra are smoothed by applying an optimization scheme that minimizes the deviation from the reflectance values and the second derivative (Marsland, 2015). The continuum is removed according to the convex hull method (Fu et al., 2007). The continuum-removed spectra are then used to calculate the spectral parameters BD1 and BD2 as shown in Figures 5.14c and 5.14d with BD1 referring to the band depth of the 1 μm band and BD2 to the 2 μm band, respectively.

In this study we specifically use the negative logarithmic band depth ratio of BD1 and BD2 (NLBD) parameter, corresponding to the negative value of the logarithmic band depth ratio (LBD) parameter defined by Bhatt et al. (2015):

$$\mathrm{NLBD} = \log_{10} \frac{\mathrm{BD2}}{\mathrm{BD1}} = -\log_{10} \frac{\mathrm{BD1}}{\mathrm{BD2}} = -\mathrm{LBD} \tag{52}$$

Hence, a high NLBD value occurs when the 2 μm band is strong and the 1 μm band is weak, which is the case when Mg-spinels are present. However, this is only a qualitative description of the mineral abundance – a quantitative analysis is planned to be conducted in future studies, e.g., based on the spectral unmixing framework of Rommel et al. (2017). Areas found to exhibit a high spinel abundance according to the NLBD parameter are very similar to the findings of previous studies relying on other methods (e.g., Dhingra et al., 2011; Pieters et al., 2014, 2011).

To study a possible dependence of the NLBD values on photometric conditions of observations we compare NLBD, BD1, BD2, and OHIBD values for morning and midday observations (see Figure 5.15). The measured BD1 parameter changes slightly between morning and midday observations despite the photometric corrections. In the range of the 1 μm band the radiometric corrections due to the detector temperatures are the strongest (Green et al., 2011), which might introduce systematic errors in this wavelength range. In contrast, the BD2 parameter is stable between morning and midday (see Figure 5.15d). The NLBD parameter slightly varies mainly because the BD1 parameter exhibits slight differences between morning and midday observations. This bevavior may well be due to the fact that the correction for detector temperature applied to the M^3 spectral radiances by the science team is strongest in the 1-μm range (Isaacson et al., 2011). However, the correlation between morning and midday NLBD is high, such that higher NLBD values in the morning also correspond to higher NLBD values at midday. Therefore, when determining the NLBD value we always use spectra that are optimized with the Hapke model (Hapke, 2002) to best fit all available observations from the same location. OHIBD on the other hand is systematically lower at midday than it is in the morning. Therefore, we use the spectra of all individual observations to be able to compare different times of day.

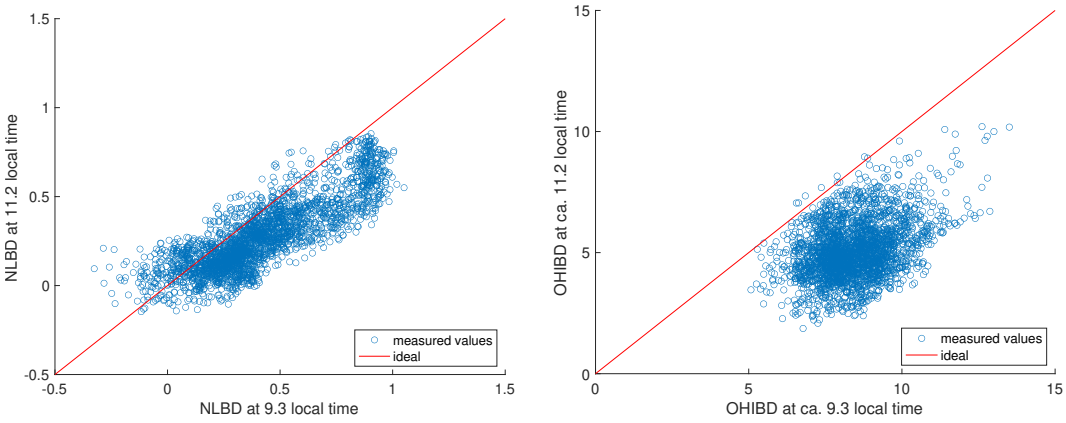

(a) NLBD (b) OHIBD

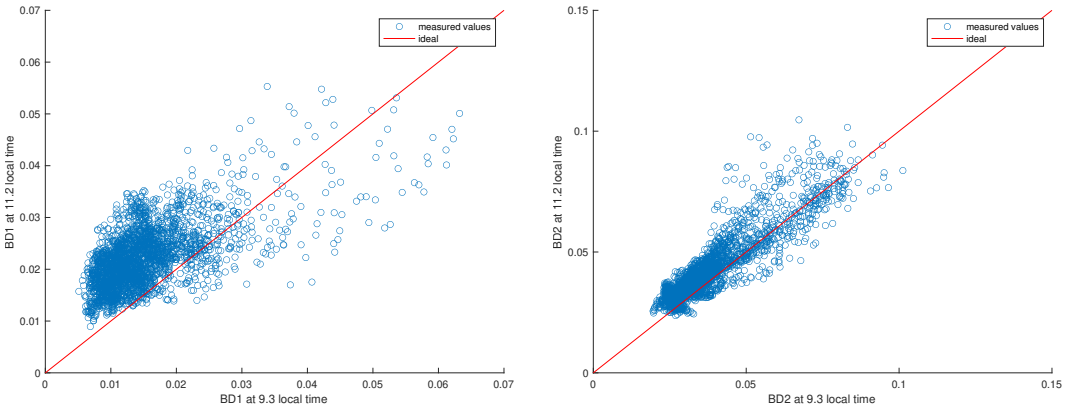

(c) BD1 (d) BD2

Figure 5.15: NLBD and OHIBD parameter for the two images at morning and midday of the region near Mare Moscoviense examined in this study (see Section 5.2.3.2).

Ti, with an abundance highly correlated with the abundance of opaque minerals (Lucey et al., 2000a) whose most important representative is ilmenite (Papike et al., 1991), is distinguished in the NIR wavelength range by a low albedo and continuum slope towards 2.5 μm (Nash and Conel, 1974) and a high LBD (low NLBD) value due to partial suppression of the 2 μm pyroxene band (Bhatt et al., 2015). In the UV wavelength range the TiO_2 abundance is linearly correlated with the 321 nm and 415 nm reflectance ratio. This parameter was used by Sato et al. (2017) to derive a TiO_2 abundance map from the global WAC mosaic. These abundance maps will be used in this work to find relations to the hydration of the regolith. Further, we will employ the mineral maps of Lemelin et al. (2016) based on Kaguya MI images for the minerals plagioclase, olivine, orthopyroxene and clinopyroxene.

5.2.2 *Abundant Minerals*

First, we use the TiO_2 maps of Sato et al. (2017) and the mineral maps of Lemelin et al. (2016) to find correspondences between the composition and the OHIBD parameter.

Regional OHIBD maps illustrate time-of-day-dependent changes in hydration (Figure 5.16). The M^3 images were divided into morning and midday images and a global mosaic was created by Wöhler et al. (2017b). Images taken between 7 AM and 8 AM local time were defined as morning values, and images taken between noon and 2 PM were defined as midday images. The OHIBD maps show artifacts in the form of vertical lines. This variance of OHIBD does not result from an actual change in OHIBD, but most likely from inaccuracies of the detector that may be caused by temperature effects inside the sensor and inaccuracies of the flat-field corrections (Wöhler et al., 2017b). At latitudes beyond 30° the time-of-day-dependent variations of the 3-μm band depth are higher than at lower latitudes, leading to systematic latitude-dependent differences. In order to reduce the influence of latitude in our analysis, we omit the higher latitudes as well as the areas west of 120° W and east of 60° E, because there is only very limited M^3 coverage at different times of day. Figure 5.16a shows the OHIBD map of the lunar morning, where the OHIBD values are higher compared to the midday values, but the location-dependent variations are small. At midday (Figure 5.16b) the OHIBD difference between different mare areas is much more pronounced. The ilmenite-rich mare areas in Mare Tranquillitatis and the western part of Oceanus Procellarum show OH/H_2O abundances of approximately 60 % less compared to the surrounding mare regions. The data in Figure 5.16c depicting the difference values are noisier than the OHIBD maps for morning and midday because errors are enhanced through subtraction of uncertain quantities. Additionally, some areas lack data for morning or midday values.

Ilmenite shows large abundances in Ti-rich regions, while minor carriers of Ti are rare forms of the pyroxene augite ($(Ca,Na)(Mg,Fe,Al,Ti)(Si,Al)_2O_6$) or the oxide minerals rutile (TiO_2) and Ti-rich spinels (e.g. ulvöspinel Fe_2TiO_4) (Papike et al., 1991). In the following, we will use the notation of TiO_2 following the nomenclature of Sato et al. (2017), referring to minerals where a cation is Ti^{+4} and the anions are O_2^{2-} in the crystal structure. Note that we do not refer to rutile, which is very rare on the lunar surface. In the finest fraction of the lunar mare soils ($\leqslant$ 45 μm in size), 40-60% of the TiO_2 is in the form of ilmenite, 20-40% in agglutinitic glasses, 15-20% in volcanic glasses and less than 3% in plagioclase, olivine, and pyroxene (Taylor et al., 2001). A similar relationship was

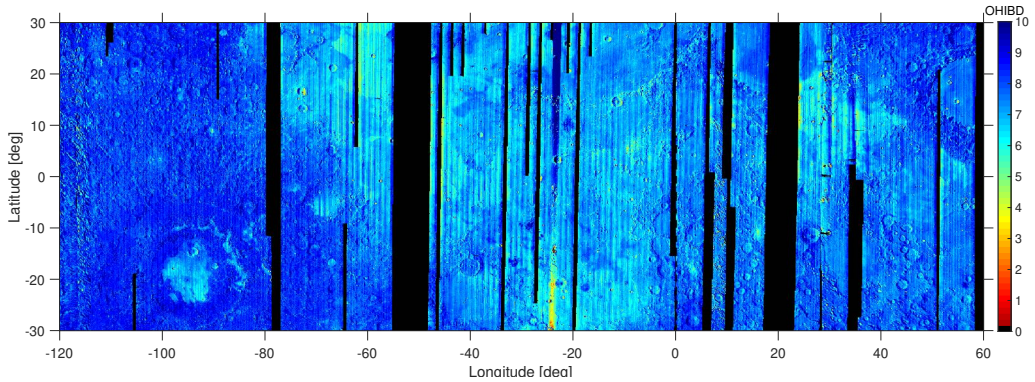

(a) OHIBD in the morning.

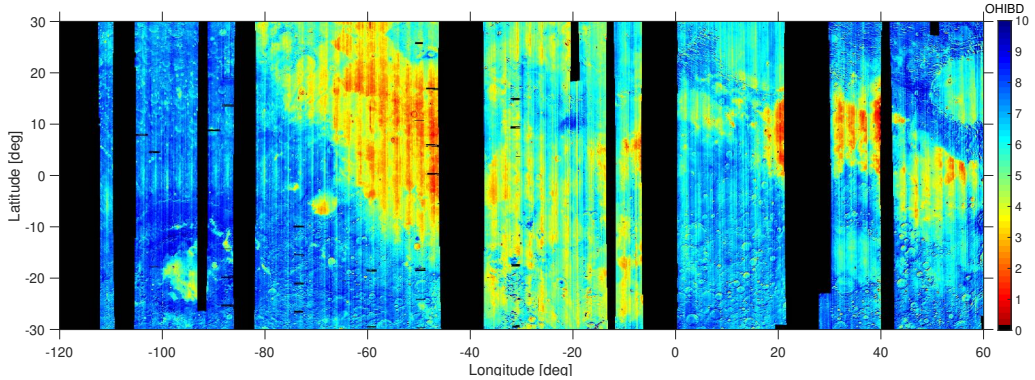

(b) OHIBD at midday.

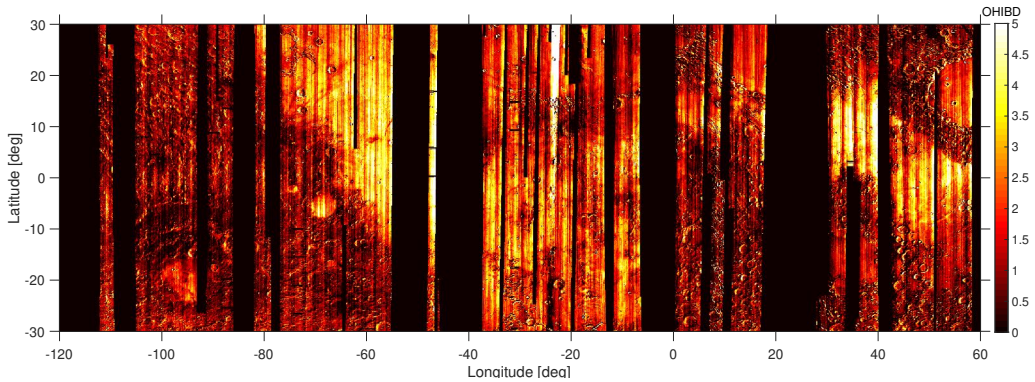

(c) OHIBD morning-midday difference.

Figure 5.16: (a) Map of OHIBD values determined from the morning M^3 data. (b) Map of OHIBD values determined from the midday M^3 data. (c) Map of OHIBD difference between morning and midday.

found by Coman et al. (2018) where it is noted that 1/3 to 2/3 of the TiO_2 content in lunar samples is attributed to ilmenite with an average of 52.6 wt.%. Ilmenite is widely assumed to be responsible for the overall remotely sensed TiO_2 abundance based on spectral parameters in the UV and NIR wavelength range (e.g. Bhatt et al., 2015; Blewett et al., 1997; Coman et al., 2018; Pieters et al., 2002; Sato et al., 2017). The ilmenite abundance is also found to be strongly correlated with the TiO_2 concentration ($r = 0.933$) of the lunar mare returned samples (Pieters et al., 2002). In the mare areas the TiO_2 abundance is dominantly above 2 wt.%. In conclusion, we will use a TiO_2 map as a proxy to investigate the relationship between ilmenite and OHIBD.

Since the lunar highlands uniformly contain only negligible amounts of TiO_2, we focus on the mare areas to calculate the correlation between TiO_2 abundance and OHIBD. To differentiate between mare and highland regions, we use the map by Nelson et al. (2014) converted to a binary map and scaled to 20 pixels per degree. Figure 5.17 shows the TiO_2 map for our study site from Sato et al. (2017), illustrating that minerals containing TiO_2 can be found in high abundances in some mare areas, like Mare Tranquillitatis and the western part of Oceanus Procellarum. In Figure 5.14 selected average M^3 spectra of two $4° \times 4°$ regions of mare areas with high (Mare Tranquillitatis) and low (Mare Serenitatis) TiO_2 concentrations are shown. These spectra illustrate the trend that areas rich in TiO_2, and consequently ilmenite, have less pronounced absorption bands at 1 µm, 2 µm, and 3 µm (blue curve in Figure 5.14). Even though, the absorption band depths are dependent on the overall composition, the pyroxene absorption bands are dampened by the flat ilmenite spectrum. Overall ilmenite-rich areas are darker compared to the surrounding mare areas.

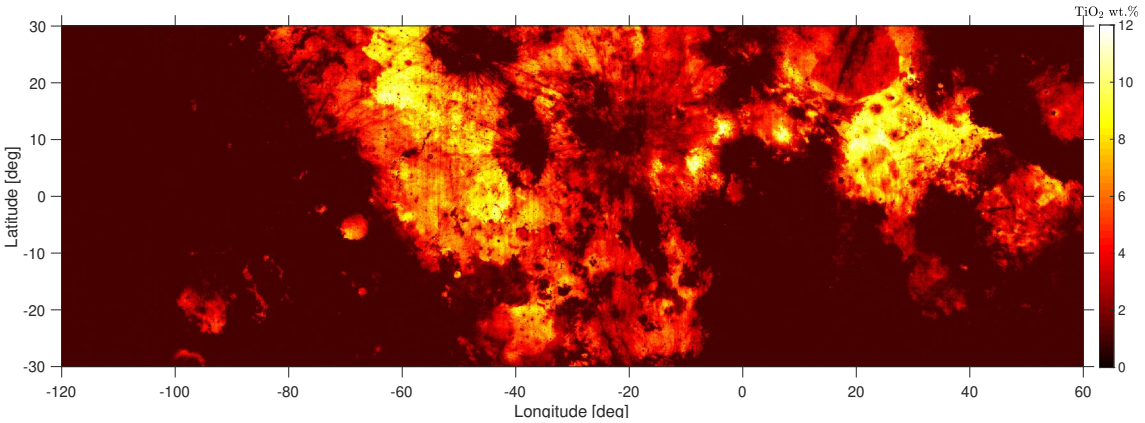

Figure 5.17: TiO_2 content in the equatorial mare regions from Sato et al. (2017).

In this study we always use the correlation coefficient r rather than its square r^2, in order to be able to distinguish between positive and negative correlations. The correlation coefficients for all minerals are listed in Table 5.4. For TiO_2 in the morning, the correlation coefficient is only $r = -0.30$, effectively corresponding to the absence of correlation (see Figure 5.18a). In the morning hours, the range of OHIBD values is from 5.5% at the lowest and 9% at the maximum. This means that the variance of OHIBD in the morning is relatively small (Figure 5.18a) compared to midday. At midday, the strongly bound component is the dominating factor, because the weakly bound component has mostly evaporated. The inverse correlation between midday OHIBD and TiO_2 abundance is clearly visible (Figure 5.18b). Here, the correlation coefficient r corresponds to -0.71.

Table 5.4: Correlation coefficients r for the dependence of OHIBD on the abundances of the major minerals on the surface of the Moon.

	mare			highland		
Mineral	morning	midday	difference	morning	midday	difference
TiO_2 (Ilmenite)	-0.30	-0.71	0.43	––	––	––
Plagioclase	0.20	0.65	-0.54	0.49	0.65	-0.34
Olivine	-0.08	-0.33	0.29	––	––	––
Orthopyroxene	-0.07	-0.36	0.33	-0.55	-0.67	0.30
Clinopyroxene	-0.22	-0.50	0.37	-0.34	-0.46	0.24

Both correlation coefficients are negative, suggesting that the OHIBD values increase in general with a decrease in TiO_2 abundance. Figure 5.18c shows that the OHIBD difference between morning and midday, in contrast to the absolute values, increases with increasing TiO_2 abundance. The OHIBD difference values, however, are relatively noisy as a consequence of the propagation of uncertainty due to the subtraction of two uncertain quantities. E.g., both OHIBD morning and OHIBD midday values are subject to uncertainties which are enhanced in the difference values. This uncertainty is also apparent in the correlation coefficients of the difference values, which show a positive correlation of $r = 0.43$ visible in the density plot in Figure 5.18c.

To make sure that temperature does not affect the observed correlations we need to investigate whether the temperature changes significantly between high-Ti and low-Ti mare. Figure 5.19 depicts the temperature at the borders between highland and mare and between high-Ti and low-Ti mare. While there is a small difference in temperature between highland and mare areas (see Figure 5.19a), there is no significant difference between the temperatures of high-Ti and low-Ti maria (see Figure 5.19b). The dependence on the latitude is visibly the strongest, such that we have to compare high-Ti and low-Ti maria at similar latitudes. The variance in the mare areas amounts to about 1 K. Therefore, we can rule out that the trends of TiO_2 and OHIBD can be attributed to temperature alone.

Let us consider correlations of the OHIBD values with the abundances of other minerals on the surface of the Moon. Plagioclase is the most abundant mineral for the majority of the lunar surface. For the lunar nearside in the equatorial region between 30° S to 30° N and 120° W to 60° E, that relationship is shown in Figure 5.20. The plagioclase abundance as determined by Lemelin et al. (2019) is shown in Figure 5.21. In Figure 5.22 the density plots of the correlation between plagioclase abundance and OHIBD are shown for mare and highland areas separately. According to Figure 5.22 plagioclase rich rocks contain more OH/H_2O than other areas. Plagioclase is positively correlated with the OHIBD values at midday in both highland and mare areas, $r = 0.65$ and $r = 0.65$, respectively. In the morning, only in the highlands a moderate correlation ($r = 0.49$) can be observed, while the difference values are correlated in the mare areas ($r = -0.54$).

Compositional maps by Lemelin et al. (2019) of orthopyroxene, clinopyroxene and olivine show only weak correlations with the OHIBD values at different times of the day (see Figures 5.23, 5.24 and 5.25 for orthopyroxene, clinopyroxene and olivine, respec-

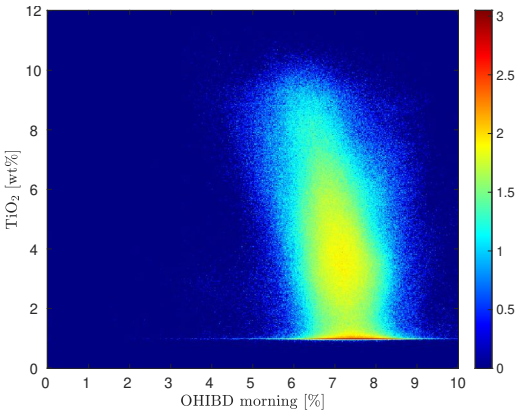

(a) Morning OHIBD (r = −0.30)

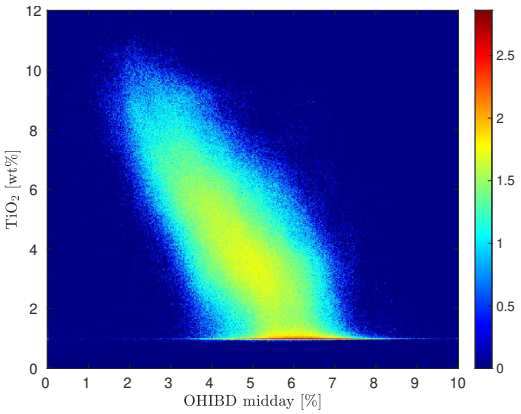

(b) Midday OHIBD (r = −0.71)

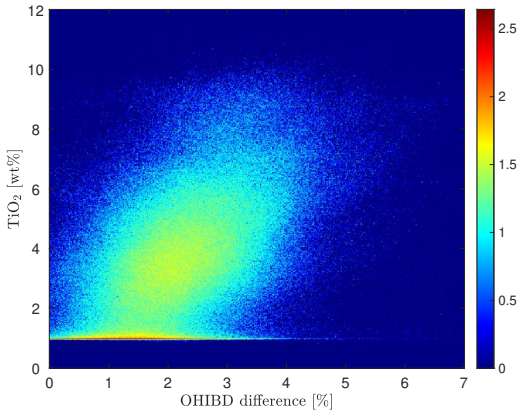

(c) OHIBD difference (r = 0.43)

Figure 5.18: Density plots for TiO_2 abundance vs. morning OHIBD, midday OHIBD and difference between morning and midday OHIBD. The color bar represents the decadal logarithm of the number of examples at a discrete pixel in parameter space.

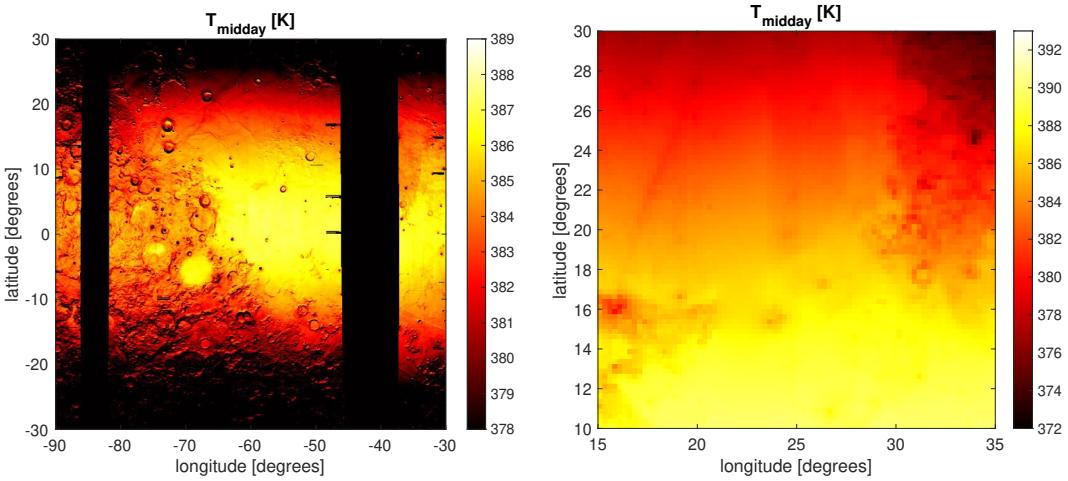

(a) Western part of Oceanus Procellarum.

(b) Mare Tranquilitatis and Mare Serenitatis.

Figure 5.19: Temperature maps of the borders between mare and highland and high-Ti and low-Ti maria at midday. The edge of Oceanus Procellarum is visible, but there is no visible difference between high-Ti basalt in the western part and low-Ti basalts in the eastern part of Oceanus Procellarum (see also Figure 5.17). At the border between the low-Ti Mare Serenitatis (north) and the high-Ti Mare Tranquillitatis (south), the major factor driving temperatures is the latitude. For the high-Ti mare basalt in the very east of Mare Serenitatis and the low-Ti western part of Mare Serenitatis the temperature differences are around 1 K.

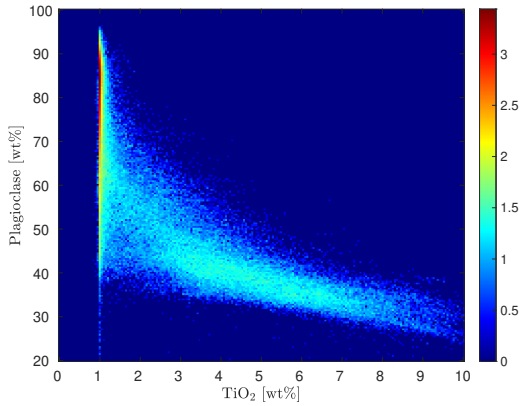

Figure 5.20: Density plot of plagioclase and TiO_2 abundance. The trend corresponds to a correlation coefficient of $r = -0.80$.

tively). Orthopyroxenes are essentially uncorrelated in the mare areas, but a relatively flat correlation can be observed in the highlands for morning and midday values. In the highlands the abundance is usually quite low compared to the mare areas, where a correlation is almost absent.

5.2.3 *Spinel*

Spinel is the name of a group of cubic oxide minerals with the general formula $A^{2+}D_2^{3+}O_4^{2-}$, where A is typically a divalent metal cation and D is a trivalent metal cation. Most spinels in returned lunar samples belong to chromite ($FeCr_2O_4$), ulvöspinel (Fe_2TiO_4)

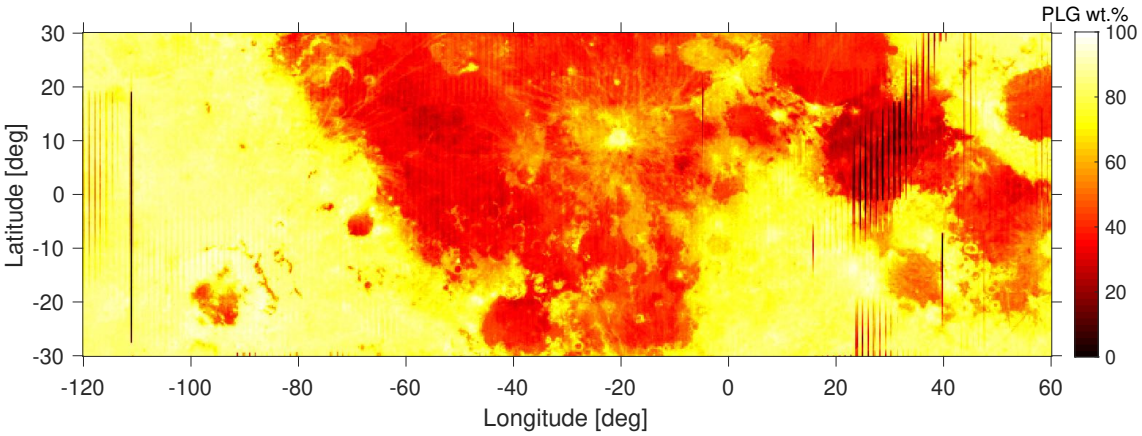

Figure 5.21: Plagioclase content in the equatorial regions (data from Lemelin et al., 2019)

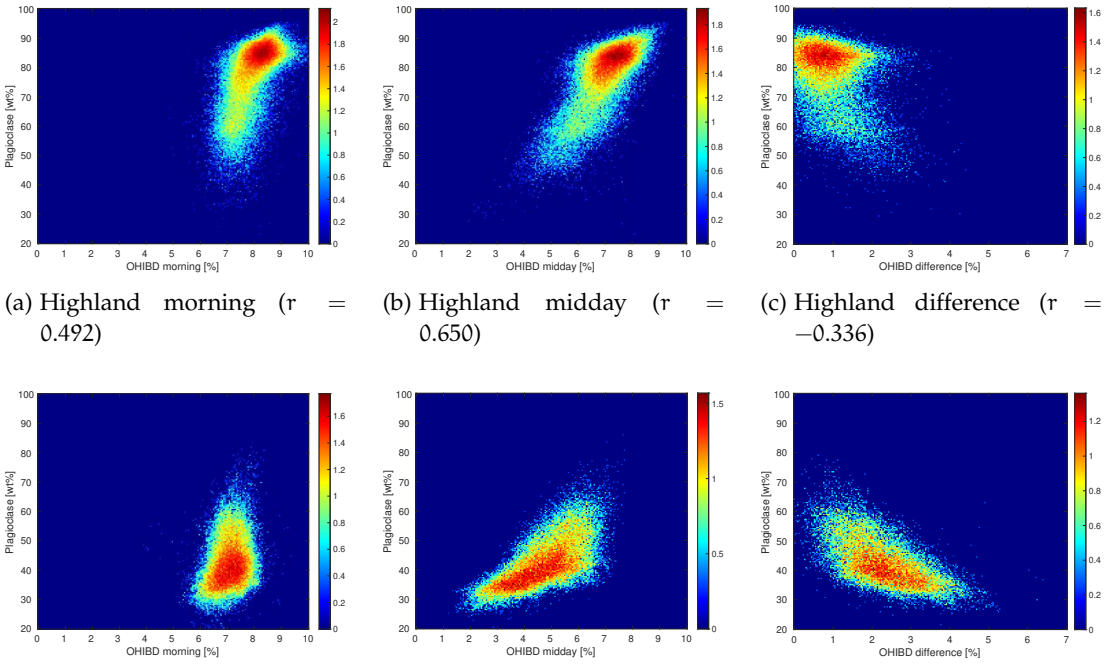

(a) Highland morning (r = 0.492)

(b) Highland midday (r = 0.650)

(c) Highland difference (r = −0.336)

(d) Mare morning (r = 0.204)

(e) Mare midday (r = 0.649)

(f) Mare difference (r = −0.538)

Figure 5.22: Density plots of plagioclase and OHIBD correlations based on the plagioclase abundance map of Lemelin et al. (2019) and the OHIBD maps of Wöhler et al. (2017b) for mare and highland soil separately. The color bar represents the decadal logarithm of the number of examples at a discrete pixel in parameter space.

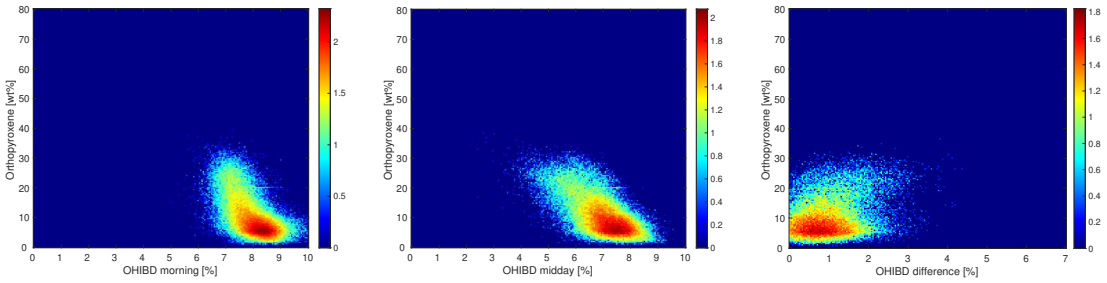

(a) Highland morning (r = −0.553) (b) Highland midday (r = −0.666) (c) Highland difference (r = 0.303)

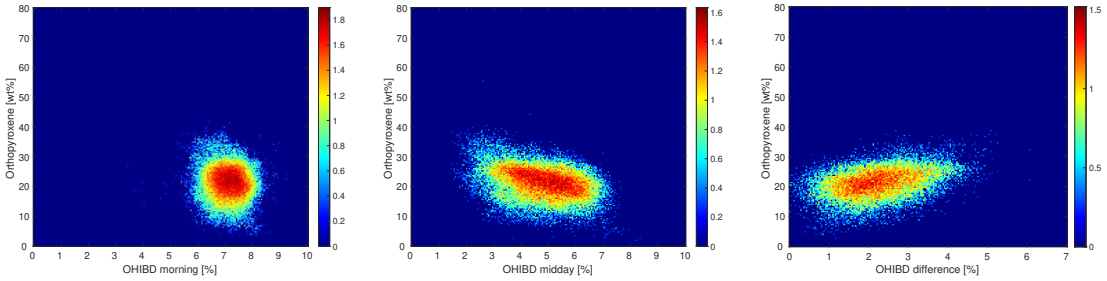

(d) Mare morning (r = −0.071) (e) Mare midday (r = −0.360) (f) Mare difference (r = 0.328)

Figure 5.23: Density plots for the orthopyroxene weight percentage of Lemelin et al., 2019 plotted against the OHIBD values at different times of day. The comparison is carried out in the equatorial mare and highland regions on the lunar near-side.

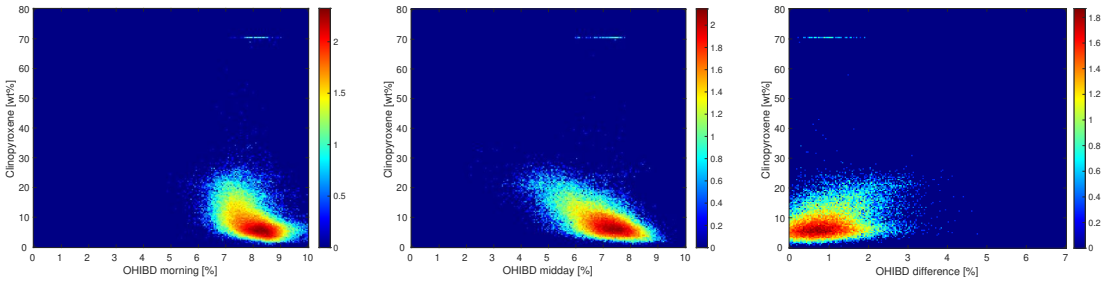

(a) Highland morning (r = −0.345) (b) Highland midday (r = −0.455) (c) Highland difference (r = 0.235)

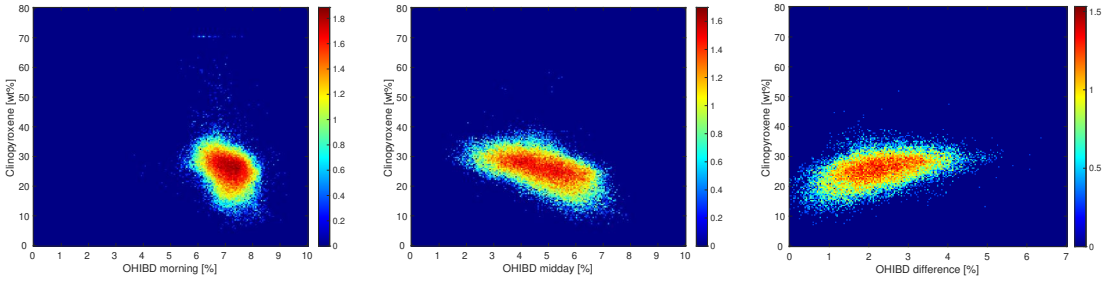

(d) Mare morning (r = −0.217) (e) Mare midday (r = −0.500) (f) Mare difference (r = 0.372)

Figure 5.24: Density plots for the clinopyroxene weight percentage of Lemelin et al., 2019 plotted against the OHIBD values at different times of day. The comparison is carried out in the equatorial mare and highland regions on the lunar near-side.

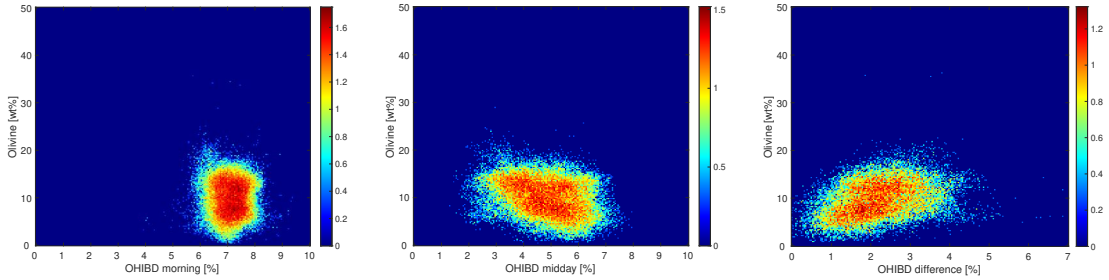

(a) Mare morning ($r = -0.079$) (b) Mare midday ($r = -0.332$) (c) Mare difference ($r = 0.293$)

Figure 5.25: Density plots for the olivine weight percentage of Lemelin et al., 2019 plotted against the OHIBD values at different times of day. The comparison is limited to the equatorial mare regions on the lunar near-side, because the abundance of olivine in the highlands is negligible.

and hercynite ($FeAl_2O_4$) (Papike et al., 1991). Spinel minerals are found in mare basalt (mainly titanium chromites and chromian ulvöspinel) as well as in highland rocks (chromite and pleonaste spinel) (Papike et al., 1991). Using M^3 data, minerals of the spinel group have been found in high concentrations at several locations on the Moon (Pieters et al., 2014). The first region that has been identified to have abundant spinel occurrences is the highland immediately west of Mare Moscoviense (Pieters et al., 2011). Another region showing similar spectral signatures is the Theophilus crater (Dhingra et al., 2011). In the regions of interest, previous studies identified Mg-spinel ($MgAl_2O_4$) as the most likely mineral (Dhingra et al., 2011; Pieters et al., 2011). The spectral signature of spinel appears most clearly in the two areas selected for this study, we will use these areas for evaluating the relationship between the parameters NLBD, indicating the presence of spinel, and OHIBD, indicating the integrated 3-µm band depth. The spectral properties of spinel can be seen in Figure 5.26, that shows laboratory spectra from the RELAB database (`https://pds-geosciences.wustl.edu/spectrallibrary/default.htm`) (Pieters et al., 2004) of nearly pure spinels from terrestrial samples alongside a nearly pure ilmenite spectrum inferred from lunar rocks. The Mg-spinel spectrum exhibits a strong absorption band around 2 µm and no absorption band at 1 µm, which is characteristic for low-Fe spinel (Cloutis et al., 2004). For studies of hercynite, chromite and ulvöspinel the reflectance maximum around 1.5 µm should be investigated. The spectral difference between (Fe/Cr)-spinel and the surrounding mare surface as shown by Weitz et al. (2017) is less pronounced than the spectral difference between Mg-spinel and the surrounding highland areas examined by Pieters et al. (2011) and Dhingra et al. (2011). Furthermore, it has been found that spinels exhibit a broad 2.6-3 µm absorption band in an almost anhydrous state (Rossman and Smyth, 1990) or a narrow 2.8-µm absorption band (Cloutis et al., 2004). These features are explained by the presence of Fe^{2+} (Rossman and Smyth, 1990) and O-H stretching (Cloutis et al., 2004). Hence, even small amounts of hydroxyl (and possibly also Fe^{2+}) might lead to a more pronounced absorption at around 3-µm.

In this section, we examine regions in the Theophilus crater and west of Mare Moscoviense because they show the spatially most extended lunar areas with a high content of Mg-spinel (Dhingra et al., 2011; Pieters et al., 2014, 2011). Regions containing Fe,Cr-spinels are planned to be investigated in the future.

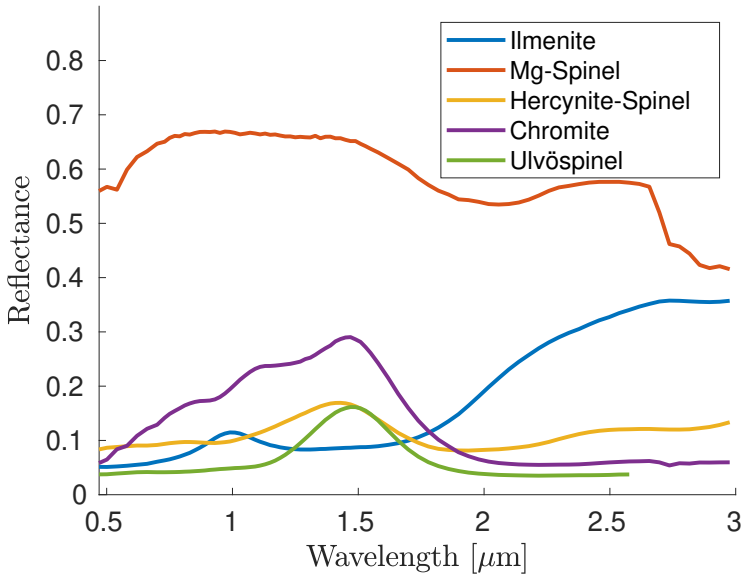

Figure 5.26: Blue curve: mineral separate of ilmenite sample (spectral ID: LR-CMP-222). Red curve: Mg-spinel ($MgAl_2O_4$) with low iron content (spectral ID: SP-EAC-021). Yellow curve: hercynite ($FeAl_2O_4$) (spectral ID: SP-EAC-074). Violet curve: chromite ($FeCr_2O_4$) (spectral ID: CR-EAC-017). The spinel spectra are from terrestrial analogue materials, they were taken from Cloutis et al. (2004) and downloaded from the RELAB spectral library. Green curve: ulvöspinel ($FeFeTiO_4$) (RELAB database, spectral ID: MR-MSR-004, synthetically created sample).

5.2.3.1 *Theophilus Crater*

The first region of interest is selected from the Theophilus crater located on the lunar near-side at the northwestern border of Mare Nectaris. The mineralogy of the central peak of the Theophilus crater is quite diverse with occurrences of plagioclase, pyroxene, spinel and olivine, but the most common compositions are mafic-free anorthosites (Dhingra et al., 2011). The M^3 image available for this region was taken at 08:45 local time, or about 81 hours after sunrise. This crater is located near the equator, so that we expect that about half of the weakly bound OH/H_2O component has already been removed at this time of day (see Grumpe et al. (2019), compare Figures S1h and S1g for regions 7 and 8 therein). Therefore, we assume that the behavior can be interpreted to be intermediate between morning and midday. There are several areas in Theophilus crater

Table 5.5: Correlation coefficients r for the spinel-rich regions. Dependence of the OHIBD value on the different factors.

	Theophilus	Mare Moscoviense	
	08:45 local time	09:20 local time	11:15 local time
NLBD > 0.3 (spinel)	-0.436	-0.295	-0.563
NLBD < 0.3 (no spinel)	-0.385	0.043	-0.195
Phase ratio	0.126	0.043	0.096
Plagioclase	0.022	0.055	0.019

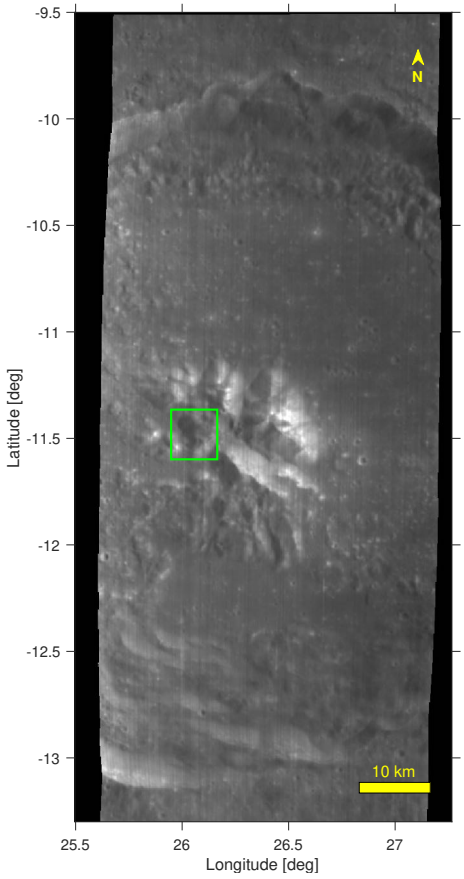

Figure 5.27: M^3 radiance image M3G20090203T160452 at 1.579 µm. The region of interest at the central peak of Theophilus crater is marked by a green rectangle.

with high Mg-spinel abundances, and we have chosen the region with the strongest Mg-spinel signature whose position is shown in Figure 5.27. The NLBD and OHIBD parameters were then calculated according to the procedure described in Section 5.2.1. Figure 5.28 shows an overview of the radiance, NLBD and OHIBD maps along with the estimated surface temperature as a reference. The strongest NLBD values correspond to low OHIBD values. The estimated effective temperature does not correlate with the NLBD values, suggesting that temperature variations in the scene are not associated with mineralogy. The strong temperature variations are due to the uneven terrain and the relatively low elevation of the sun. Therefore, a small moderate positive correlation between temperature and OHIBD is visible in Figure 5.29.

The analysis of spinel-rich areas differs from the analysis of the other minerals in one significant way. While the other minerals are contained to a certain extent in nearly each mare region, spectrally detectable abundances of spinel are only found in spatially limited areas. This implies that there are two distinct classes, one containing spinel and one (the surrounding terrain) containing no or an undetectable amount of spinel. To distinguish between these two classes, we assume that all pixels having an NLBD parameter higher than 0.3, corresponding to a twice as deep 2 µm band depth compared to the 1 µm band depth, contain spinel (in spectra of mature areas without spinel the 1 µm band is deeper than the 2 µm band). In Figure 5.30 areas containing spinel (magenta points), show a correlation, but for the areas that are assumed to contain negligible

amounts of spinel (blue points) the values are effectively uncorrelated. For reference, the mean spectra of the two clusters at Theophilus crater are shown in Figure 5.31. In general, high NLBD values correspond to lower OH/H_2O abundances. This is apparent in Figure 5.32 as well, which shows some example spectra and the locations where they have been extracted. In the still darker and cold spinel-rich areas, the correlation between NLBD and OHIBD is less pronounced.

Another important factor that might contribute to the measured OHIBD values is the surface roughness on sub-pixel scales. Shkuratov et al. (1994) proposed that phase-ratio images can be used to investigate the surface roughness. Because the influence of the albedo is significantly reduced in phase-ratio images, they are mostly correlated with the small-scale surface roughness (Shkuratov et al., 2010). For the area in Theophilus crater, the phase-ratio image is shown in Figure 5.33. It can be seen that in the region of interest there are no anomalies correlated to the OHIBD values except for a small part to the northeast where higher phase-ratio values (which are presumably due to topography) correspond to lower OHIBD values. The correlation coefficient describing the relationship between the phase ratio values and the OHIBD values at Theophilus is only $r = 0.126$ (Figure 5.34a). All correlation coefficients for the spinel-rich regions are listed in Table 5.5. The plagioclase abundance in this area (Figure 5.35) is also uncorrelated with the OHIBD values (Figure 5.34b).

Spectra 1–3 and 6 indicate the presence of Mg-spinel, but the spinel-specific signature in spectrum 6 is not nearly as clear as in the other three examples. Spectra 4 and 5 show a deep absorption at 3 μm, while the spinel-rich spectra are comparably flat. The continuum-removed spectrum of location 2 is shown in Figure 5.32c as a representative of a high spinel abundance region and the continuum-removed spectrum of location 5 is shown in Figure 5.32d as an example of a region with low spinel concentration. The OHIBD parameter is high for spectrum 5 and low for spectrum 2 with spinel signature. This region at the central peak of Theophilus shows that spinel-rich areas correspond to a reduced OH/H_2O integrated band depth when the surface temperatures are so high that large amounts of the weakly bound OH/H_2O component have been removed. Unfortunately, there is no M^3 image of this region available for early morning or late midday.

5.2.3.2 *Mare Moscoviense*

High concentrations of spinel were found for the first time in two small areas to the west of Mare Moscoviense (Pieters et al., 2011). In this section, we examine the larger southern occurrence at the rim of the basin as shown in Figure 5.36. The surrounding surface is typical anorthositic highland. For this region, images from two different times of day are available. In the late lunar morning, at 09:20 (image M3G20090125T172601) local time, it can be assumed due to the moderately high latitude that the weakly bound OH/H_2O component is still partially present (see Grumpe et al. (2019), compare Figures 22 and 23 for region 17 therein). At the acquisition time of the second image, lunar midday at around 11:15 (image M3G20081229T101650), Grumpe et al. (2019) argued that the weakly bound OH/H_2O component is diminished and only the strongly bound OH/H_2O component remains.

The NLBD values are not dependent on the time of day, allowing this parameter to be calculated based on all available M^3 spectral radiance data simultaneously (see Fig-

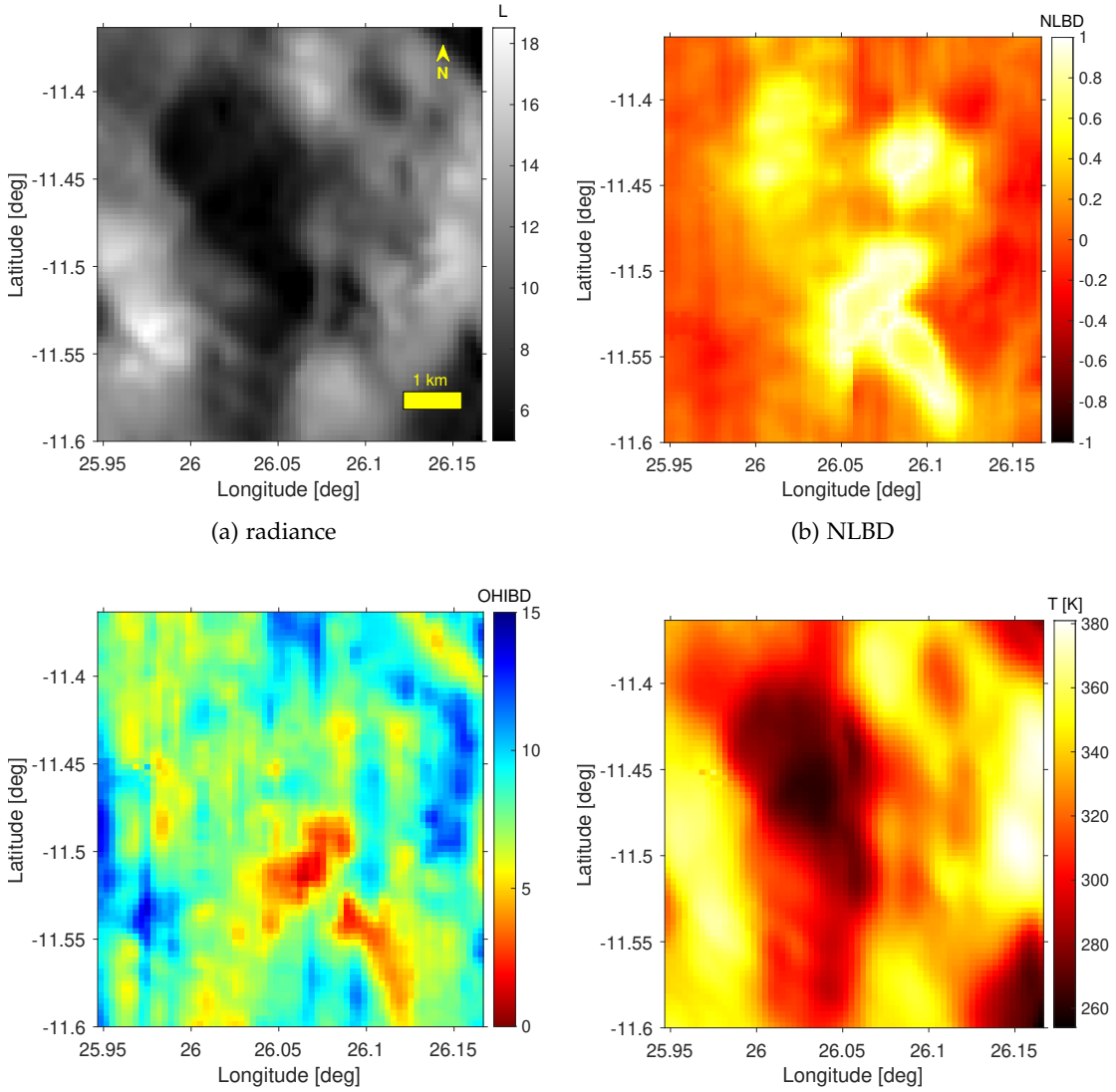

(a) radiance

(b) NLBD

(c) OHIBD [percent]

(d) Temperature [K]

Figure 5.28: Selected part of the central peak region of the Theophilus crater. The image was taken at 08:45 local time.

ure 5.37b). The OHIBD parameter maps were constructed separately for both available times of day (see Figures 5.37c and 5.37e). At midday, the region with the lowest OHIBD lies in the center of the region characterized by the highest NLBD values, but its immediate surroundings that also show elevated NLBD values are not as strongly deprived in OHIBD. For this OHIBD depleted region, temperature variations are only minor ($\leqslant$ 3 K). This area also appears to be rather flat in the radiance image, making it unlikely to be influenced by artifacts due to thermal emission removal. In the lunar morning, the high-NLBD areas in part also show lower OHIBD values, but the difference is not as significant. This trend is illustrated in the scatter plots in Figure 5.38, where the morning values are nearly uncorrelated, but at lunar midday high NLBD values correspond to low OHIBD values. The correlation coefficients are listed in Table 5.5. For the cluster of pixels that are likely to contain spinel (NLBD values > 0.3), we found a correlation coefficient of $r = -0.295$ at lunar morning and $r = -0.563$ at lunar midday. Corresponding

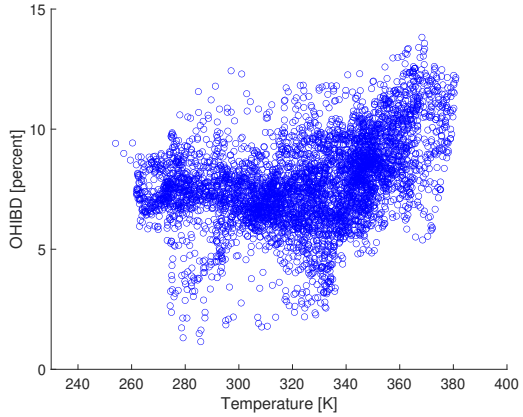

Figure 5.29: The temperature and the OHIBD value at the Theophilus region show a moderate correlation of $r = 0.4$.

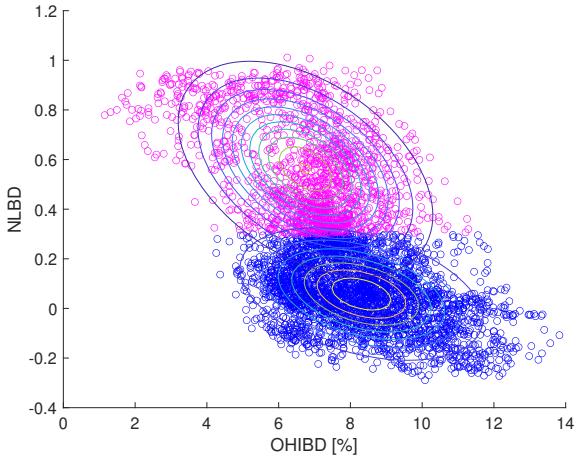

Figure 5.30: Scatter plot of NLBD vs. OHIBD for the region at Theophilus crater. The correlation coefficient for all pixels with an NLBD value larger than 0.3 (magenta circles) is $r = -0.436$. For the pixels with a NLBD value below 0.3 (blue circles) it is $r = -0.385$.

values for regions with low spinel content (NLBD values below 0.3) are $r = 0.043$ and $r = -0.195$, respectively. For reference, the phase-ratio image is shown in Figure 5.39. In general, the surface is relatively smooth when compared to the Theophilus crater. In Figures 5.40a and 5.40b the correlation between the phase-ratio values and the OHIBD parameter is depicted. There appears to be no correlation in the region of interest between phase-ratio and OHIBD, so that we can relatively safely rule out that the surface roughness influences the observed correlation between OHIBD and spinel. The plagioclase abundance is also uncorrelated with the OHIBD values (Figures 5.41, 5.40c and 5.40d).

Figure 5.42 shows some example spectra and their positions in the NLBD map. These spectra indicate that in the lunar morning the OHIBD values are generally higher than at midday, but at both times of day the selected spectra 1 and 2 show the typical 2-µm absorption band of Mg-spinel and a relatively weak 3-µm absorption band. Spectrum 4 is possibly overcompensated in thermal emission due to small-scale localized inaccuracies in the DEM leading to an inaccurate estimate of the incidence angle at that specific location.

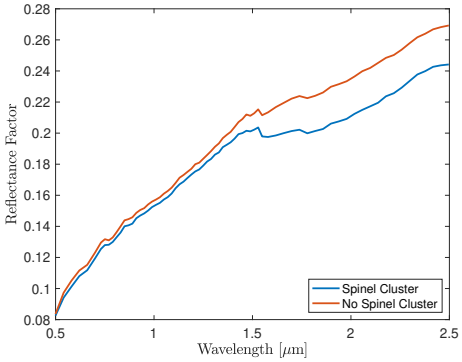

Figure 5.31: Mean spectra for the pixels with an NLBD value above 0.3 and below 0.3 representing the spinel and no spinel clusters, respectively (see Figure 5.30). These spectra are taken from the Theophilus crater region of interest.

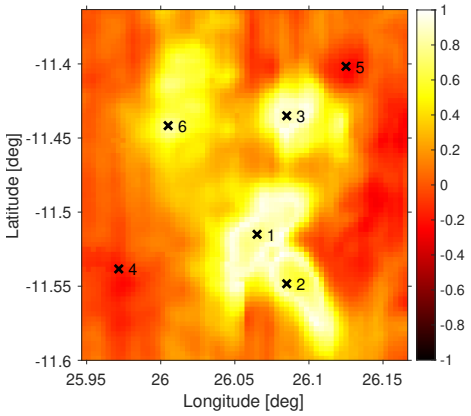

(a) Position on NLBD map.

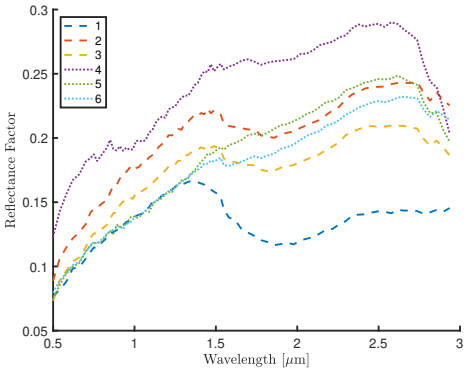

(b) Spectra

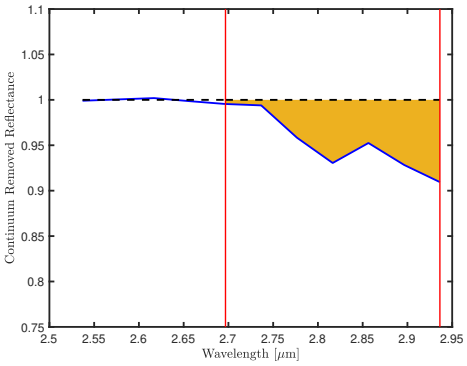

(c) Spectrum 2

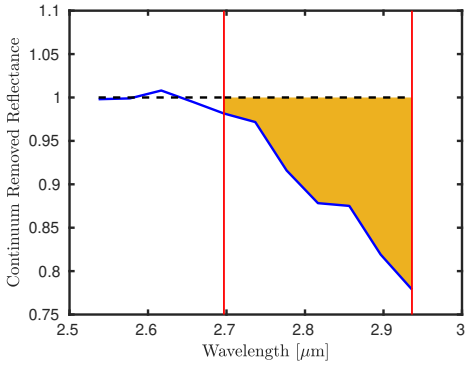

(d) Spectrum 5

Figure 5.32: Selected spectra from the Theophilus region. The spectra in (b) were averaged over 3×3 M^3 pixels. At the spinel-rich locations 1-3 the typical signature of spinel with a deep absorption band around 2 µm is visible. Spectra (c) and (d) illustrate how the OHIBD parameter is calculated at locations 2 and 5, respectively. After the continuum is fitted to the values between 2.537 and 2.657 µm, the integral is determined as shown in (c) and (d).

5.2.4 *Discussion*

Our analysis of M^3 data has demonstrated that the OHIBD values at midday in the mare regions decreases strongly (by a factor of up to about three) with the TiO_2 content

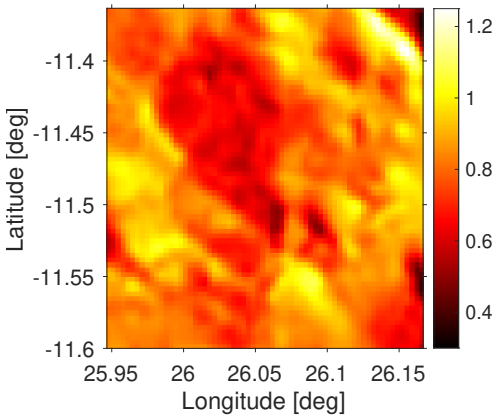

Figure 5.33: Phase-ratio image for the regions of interest at Theophilus crater ($f(44°)/f(31°)$). The phase-ratio image are correlated with the macroscopic and microscopic surface roughness (Shkuratov et al., 2011). In the Theophilus crater the correlation with the OHIBD values is $r = 0.126$, near Mare Moscoviense it is $r = 0.042$ and $r = 0.096$ for morning and midday, respectively.

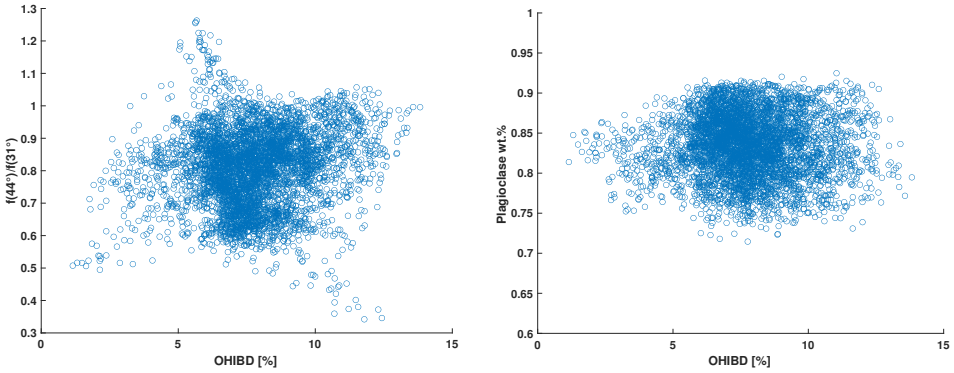

(a) Theophilus ($r = 0.126$)

(b) Theophilus ($r = 0.022$)

Figure 5.34: Correlations of plagioclase abundance and phase ratio values with the OHIBD values at Theophilus crater (Figures 5.35 and 5.33), for the entire region of interest respectively.

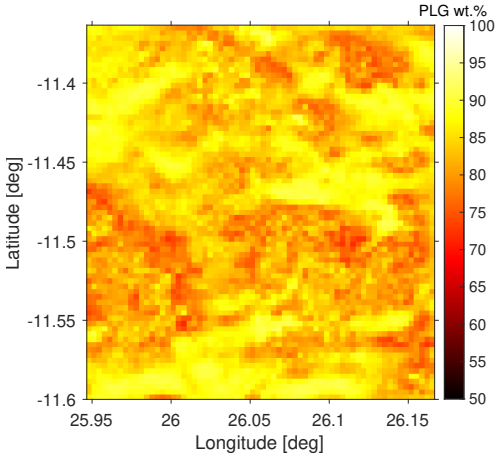

Figure 5.35: Plagioclase abundance data of Lemelin et al. (2019) for the region of interest in the Theophilus crater. The plagioclase abundance is uncorrelated with the OHIBD parameter maps in Figures 5.28c for the Theophilus crater ($r = 0.023$).

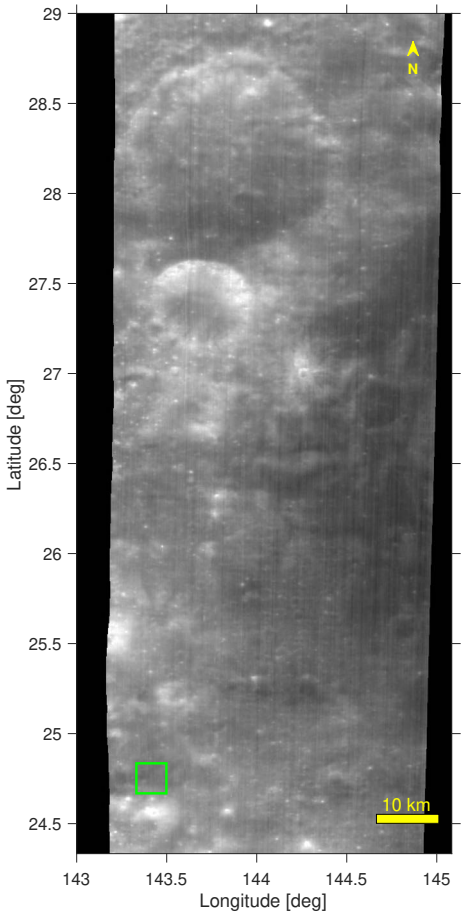

Figure 5.36: Location of the selected region of interest near the western basin ring of Mare Moscoviense. M^3 spectral radiance image M3G20081229T101650 at 1.579 µm wavelength.

of the mare material increasing from near-zero to its maximum value of about 8 wt% (see Wöhler et al., 2017b, for the OHIBD behavior on global scales). At low latitudes, the OHIBD difference between morning and midday, which we interpret as a measure for the amount of weakly bound OH/H_2O in the lunar surface material, is near zero in the highlands and about 20–30 percent of the morning value in low-Ti maria, but increases with increasing TiO_2 content in the mare areas. This suggests that the TiO_2-bearing minerals contained in the lunar surface material bind small amounts of OH/H_2O strongly and large amounts of OH/H_2O weakly to their crystal structure.

The strength of the OHIBD parameter is influenced by a wide range of factors apart from composition, like latitude, time of day and roughness, among others. Additionally, it should be considered, that which part of the composition influences the hydration signatures the most is not always clear. E.g., TiO_2 rich regions are depleted in plagioclase because the TiO_2 abundance is highly correlated with the plagioclase abundance (see also Figure 5.20). Therefore, the reduced amount of strongly bound OHIBD in TiO_2 rich regions might be attributed to the absence of plagioclase that has been found to more strongly bind OH/H_2O (Hibbitts et al., 2011). Similarly, Poston et al. (2015) showed that a feldspathic highland sample retained significantly more OH/H_2O compared to a mare sample. However, the spectral effect of the opaque mineral ilmenite is presumably

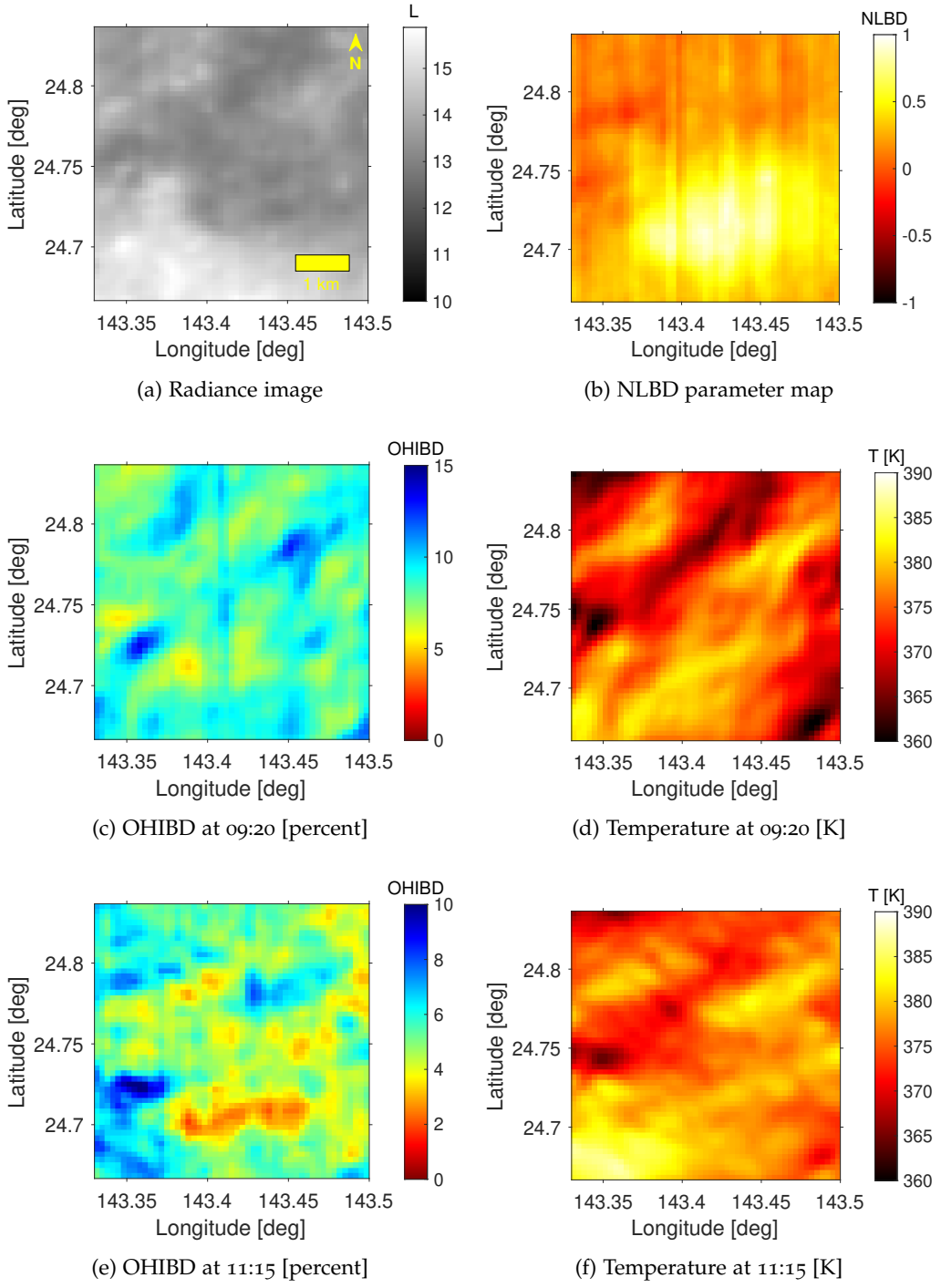

(a) Radiance image

(b) NLBD parameter map

(c) OHIBD at 09:20 [percent]

(d) Temperature at 09:20 [K]

(e) OHIBD at 11:15 [percent]

(f) Temperature at 11:15 [K]

Figure 5.37: Region of interest near the western Mare Moscoviense basin ring. High NLBD values coincide with low OHIBD values at lunar midday, but at lunar morning the high-NLBD areas blend into the surrounding areas.

stronger than to be expected based on its weight fraction. For ilmenite this behavior was shown in laboratory experiments and was attributed to the excessively high extinction coefficient of ilmenite compared to non-opaque minerals (e.g., Grumpe et al., 2018). As a consequence, the OHIBD values might possibly also be strongly influenced already by moderate amounts of opaque minerals. Of course it is not self-evident that this behavior

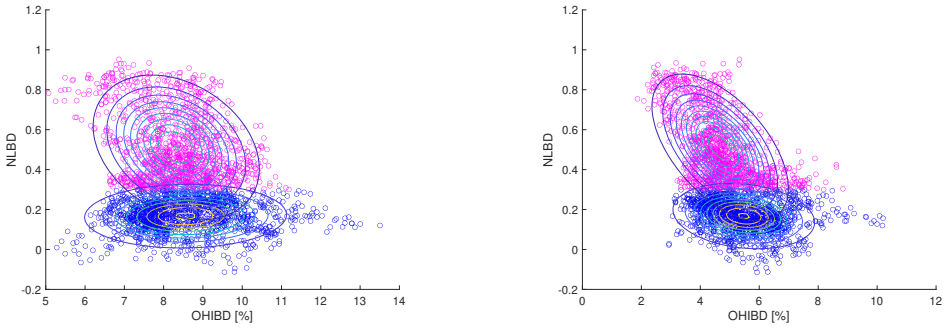

(a) 09:20 local time. $r = -0.295$.

(b) 11:15 local time. $r = -0.563$.

Figure 5.38: Scatter plots of NLBD value vs. OHIBD value for the region of interest in Figure 5.37b. The correlation coefficients listed in the sub-captions are calculated for the cluster assumed to contain spinel, corresponding to all pixels with NLBD values exceeding 0.3 (magenta circles). The correlation coefficients for the regions not containing spinel (blue circles) are $r = 0.043$ and $r = -0.195$ for morning and midday, respectively.

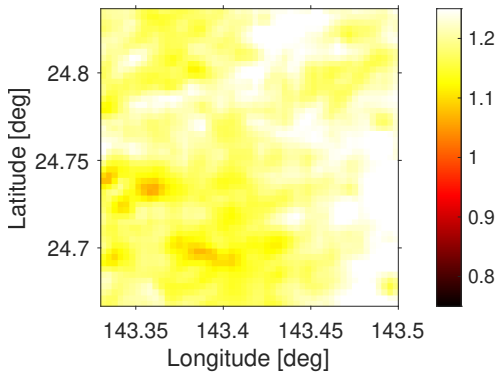

Figure 5.39: Phase-ratio image for the regions of interest at the western basin rim of Mare Moscoviense $f(26°)/f(34°)$. The phase-ratio image are related to the macroscopic and microscopic surface roughness (Shkuratov et al., 2010). In the Theophilus crater the correlation with the OHIBD values is $r = 0.126$, near Mare Moscoviense it is $r = 0.042$ and $r = 0.096$ for morning and midday, respectively.

applies in the same way to the ilmenite-bound OH/H_2O, so that it will be necessary to conduct further studies, e.g., focusing on hydrated ilmenite in the laboratory, to provide a definite explanation.

In addition to that, another solar wind implanted volatile, ^3He, is mainly bound by ilmenite, a behavior which has been attributed to the presence of a large number of defect sites in ilmenite (see e.g., Kim et al., 2019; Shkuratov et al., 1999b). Milliken and Mustard (2007) further suggested that the measured 3-µm band strength is dependent on the albedo. TiO_2 rich regions are generally darker compared to mare areas with low TiO_2 concentration. This effect may have an influence on the overall correlation, but our spectral reflectance data have been carefully photometrically corrected with the model of Hapke (2002) and the albedo is not variable during the day in our data. If the albedo had a strong influence on this correlation we would also expect a stronger correlation in the morning, which is not the case except for plagioclase in the highlands. High-Ti mare basalt might also be influenced by other phases, like olivine (Staid et al., 2011), but we

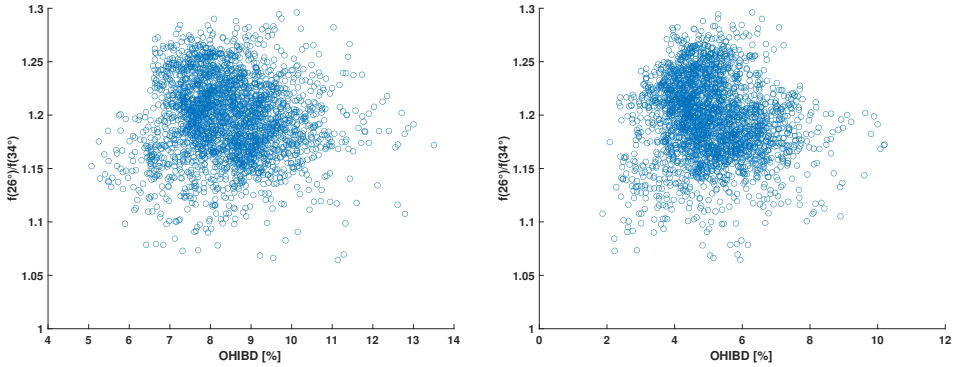

(a) Mare Moscoviense morning (r = 0.043) (b) Mare Moscoviense midday (r = 0.096)

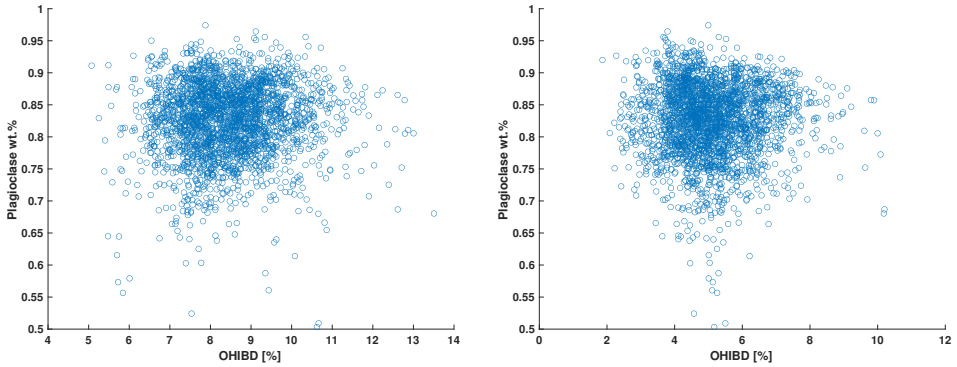

(c) Mare Moscoviense morning (r = 0.055) (d) Mare Moscoviense midday (r = 0.019)

Figure 5.40: Correlations of plagioclase abundance and phase ratio values with the OHIBD values at Mare Moscoviense and Theophilus crater (Figures 5.41 and 5.39), for the entire region of interest respectively.

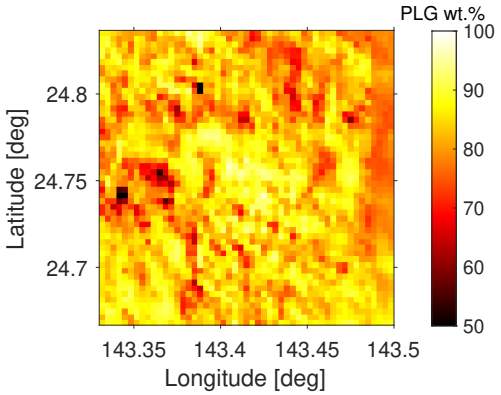

Figure 5.41: Plagioclase abundance data of Lemelin et al. (2019) for the region of interest near Mare Moscoviense. The plagioclase abundance is uncorrelated with the OHIBD parameter maps in Figures 5.37c and 5.37e for Mare Moscoviense in the morning (r = 0.055) and at midday (r = 0.019), respectively.

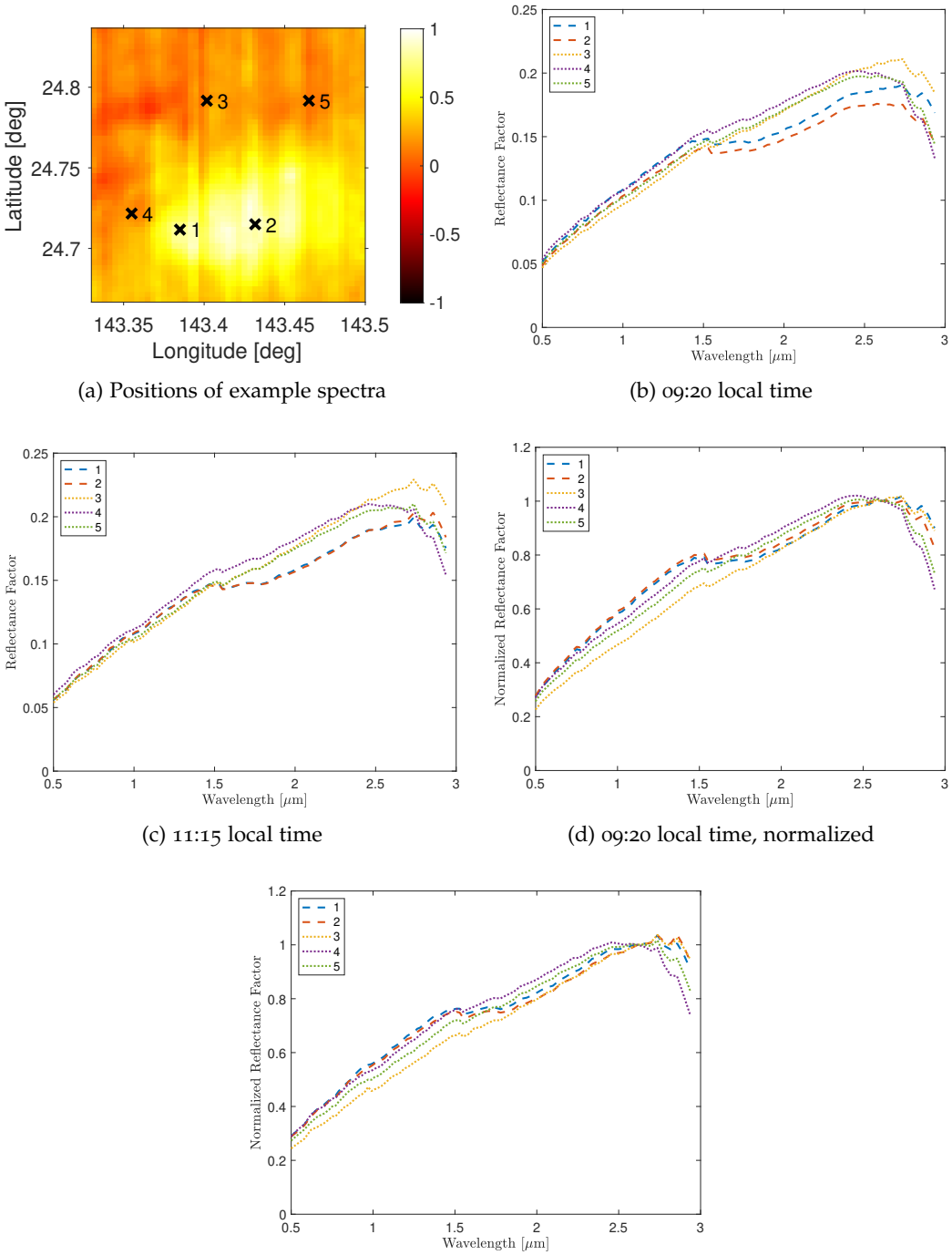

(a) Positions of example spectra

(b) 09:20 local time

(c) 11:15 local time

(d) 09:20 local time, normalized

(e) 11:15 local time, normalized

Figure 5.42: Spectra of the Mare Moscoviense region of interest in the morning and at midday and their corresponding positions in the NLDB map. The second set of spectra is normalized to the reflectance at 2.617 µm (M^3 channel 76).

didn't observe any correlation between olivine abundance and OHIBD in our study (see Figure 5.25).

Plagioclase does not release large amounts of OH/H_2O in the course of the lunar day because the lunar highlands show only weak time-of-day-dependent OHIBD vari-

ations (Wöhler et al., 2017b). Our observations thus suggest that most of the OH/H_2O component in TiO_2-bearing minerals is weakly bound, whereas most of the OH/H_2O component in plagioclase is strongly bound. In this line of thought, the depletion of plagioclase in the TiO_2-rich mare areas explains the low OHIBD values at midday (corresponding to strongly bound OH/H_2O), whereas the presence of large amounts of TiO_2 in the same areas explains the strong time-of-day-dependent OHIBD variations (due to weakly bound OH/H_2O).

Another factor that is, however, difficult to assess is the influence of agglutinitic glasses. As it is difficult to accurately determine the glass content remotely, their effect cannot be estimated directly. It has been found that these glasses contain strongly bound OH/H_2O and possibly internal OH/H_2O (Liu et al., 2012). The correlation of the agglutinitic glass and TiO_2 abundance from Pieters et al. (2002) is $r = -0.408$, therefore, soil with a higher TiO_2 concentration would contain a smaller amount of agglutinates. This could also explain why the plagioclase deprived and TiO_2 rich regions contain only small amounts of strongly bound OH/H_2O. The moderate correlation found by Pieters et al. (2002) in the lunar returned samples is, however, not sufficient to attribute the observed strongly bound component entirely to agglutinates, and the stronger variability during the day compared to other minerals cannot be explained by the strongly bound OH/H_2O component in glasses. For the Mg-spinel rich regions, the difference in agglutinitic glass content with respect to the surrounding areas is expected to be small because there are no measurable maturity differences.

Regarding the midday OHIBD values, we observed a behavior for spinel that is similar to TiO_2. The OHIBD in the spinel-bearing area to the west of Mare Moscoviense is nearly the same as in the surrounding region in the late morning, whereas it shows a strong contrast (by a factor of about two) at midday. In the surrounding highland-like terrain, almost no difference in OHIBD between morning and midday is apparent. For the spinel-bearing area inside Theophilus crater, the contrast of OHIBD values between spinel and no-spinel regions at this intermediate time between morning and midday even amounts to a factor of about three. Even though no comparison between morning and midday is possible for Theophilus crater due to the lack of M^3 data acquired at early lunar morning or late midday, studying this region is important as it is the spatially most extended area with the strongest spectral spinel signature in the lunar highlands. The temperature at Theophilus crater also shows a moderate correlation to OHIBD (see Figure 5.29). An at first sight unintuitive (and not very pronounced) positive correlation between surface temperature and OHIBD is apparent in Figure 5.29 for temperature values between 340 and 380 K. A possible explanation is that if a surface part is first shadowed by another surface part and still contains a large abundance of OH/H_2O from the previous lunar day, but then the sun suddenly falls relatively steeply on the same surface part so that it heats up, it takes a while for the OH/H_2O to evaporate and photo-dissociate. In such a configuration, which often occurs in uneven terrain, it may, therefore, well be the case that relatively large amounts of OH/H_2O occur on warm parts of the surface. Such unexpected correlations should be further examined, e.g., by applying the OH model of Grumpe et al. (2019) to realistic lunar surface topography, which, however, goes beyond the scope of this thesis.

The content of pyroxene and olivine is estimated to be as low as 5 wt.% in the regions rich in Mg-spinel in Theophilus crater and Mare Moscoviense (Dhingra et al., 2011;

Pieters et al., 2011). For this reason, the influence of other mafic minerals on the OHIBD values in these regions should be negligible. As shown in Figure 5.35 and 5.41, the OHIBD values are also not correlated with the plagioclase abundance in these regions of interest. For the spinel-bearing regions, no reliable evaluation of the weakly bound OH/H_2O component can be performed due to the limited amount of data available acquired at different times of day. The strongly bound component, however, is lower in the high-spinel regions when compared to the surrounding low-spinel surface. The general observations at Mare Moscoviense are similar to those at Theophilus in that both show lower OHIBD values for the high-NLBD regions. At Theophilus this correlation is apparent at an earlier time of day than at Mare Moscoviense. Because Mare Moscoviense is located at a higher latitude than the equatorial crater Theophilus, this observation is consistent with the interpretation that the strongly bound OH/H_2O component is less abundant in Mg-spinel-rich areas (Grumpe et al., 2019).

Our observations suggest that lunar minerals containing TiO_2, including ilmenite, and spinel-rich materials have similar tendencies to release (in the late morning to midday) and build up (in the early morning and in the afternoon) large amounts of weakly bound OH/H_2O. In contrast, the amount of strongly bound OH/H_2O that is insensitive to loss processes such as thermal evaporation and photolysis (Grumpe et al., 2019) is small for both types of materials, but large for plagioclase. This behavior differs from low-spinel highland areas and low-ilmenite maria, which consist nearly completely of silicate minerals. They show much smaller time-of-day-dependent OHIBD variations than areas rich in TiO_2 or spinel and thus appear to be dominated by strongly bound OH/H_2O.

5.3 CONTRIBUTION: UNCERTAINTY BASED UNMIXING

This section and subsections herein are adapted or adopted from Hess et al. (2021b).

In this study, we develop a Bayesian approach to hyperspectral unmixing. In Bayesian inference (e.g., Gelman et al., 2013) all parameters of the model are considered as probabilistic variables. In this framework, in addition to the point estimates of the best fit we also estimate the uncertainties of the parameters. Due to the darkening agents, which darken the spectra and dampen the absorption bands, the uncertainties of the mineral abundances are likely to be higher on the Moon than on other planetary bodies with an atmosphere (e.g., Lapotre et al., 2017). Additional prior information can be conveniently incorporated in the Bayesian framework. To reduce uncertainties of the mineral abundances, estimates of elemental abundances can be included such that the algorithm will prefer solutions that use endmember combinations with similar elemental compositions.

5.3.1 *Endmember Catalogs*

In order to generate spectra similar to lunar conditions we need to select endmembers representative of the general mineralogy of the Moon. We are using only mineral endmembers and are not trying to model the influence of agglutinate glasses. This glassy fraction usually has a similar composition to the mineral fraction (Baker et al., 2020), as it is created endogenously. The 1-µm absorption band depth is also not affected by glasses, but by a large amount of $smFe^0$ in the agglutinates (Denevi et al., 2021). However, the absorption bands are broadened by agglutinates and the 2-µm absorption band is flattened (Tompkins and Pieters, 2010). Agglutinates here are only relevant for the unmixing of the LSCC catalog, but this should be kept in mind when evaluating the results.

The highlands are dominated by plagioclase (around 90 wt.%) with the remaining fraction mainly consisting of pyroxenes and minor phases of olivine and spinels (Papike et al., 1991). The composition of the maria is more diverse. About 30–40 wt.% are pyroxenes and plagioclase still forms a major part of the composition with up to 60 wt.% of the mineral composition. Olivine contributes up to 10 wt.% and the opaque mineral ilmenite is abundant in some mare areas with up to 20 wt.% at maximum (Papike et al., 1991).

Among these groups of minerals are also variations depending on the elemental composition. E.g., Sun and Lucey (2021) showed that by generating albedo spectra based on the magnesium number and grain size the abundance estimation of olivine and pyroxenes can be improved. We will use fixed albedo spectra as endmembers that are chosen to be a good representation of a wide variety of possible true endmembers while retaining the most distinct endmembers.

In general, we want to have one representative of each of the major minerals on the Moon. Pyroxenes can be subdivided into low calcium pyroxenes (LCP), mainly orthopyroxenes (OPX), and high calcium pyroxenes (HCP), usually clinopyroxenes (CPX). The LCP pyroxenes exhibit an absorption 0.9-µm and 1.9-µm (Burns and Burns, 1993; Cloutis, 2002). The HCP pyroxenes can be further subdivided into two spectrally distinct groups. Type A, with an absorption at 0.9-µm and at 1.15-µm, but no absorption around 2-µm (Cloutis, 2002) similar to olivine. Type B, exhibits absorption bands at 1.05-µm and 2.35-

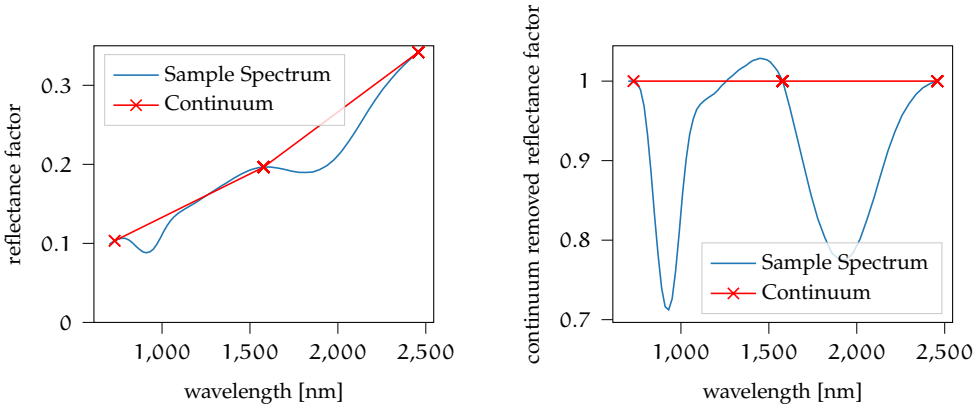

(a) (b)

Figure 5.43: Exemplary calculation of the continuum removed spectrum for endmember AG-TJM-009 from the RELAB database space weathered with 1.5 wt.% $npFe^0$ and 0.8 wt.% mpFe. The continuum is calculated as the linear interpolation between the reflectance factor at 730.48 nm, 1578.86 nm and 2497.11 nm. These channels usually lie outside the absorption bands.

µm (Cloutis, 2002). The absorption band positions, however, are not fixed, but vary with Mg^{2+}, Fe^{2+}, and Ca^{2+} content (Klima et al., 2011, 2007). For the unmixing, the distinction between these three types of pyroxenes (HCP, LCP-A, and LCP-B) is, however, beneficial because we want to minimize the linear dependencies between the endmember spectra.

5.3.2 *Likelihood*

The unmixing problem is that the abundances of the endmembers ($\vec{\theta}_{em}$) and the space weathering components $npFe^0$ and $mpFe^0$ ($\vec{\theta}_{smFe}$) with known albedo spectra, extinction efficiencies and phase functions must be determined. They are the parameters we estimate with the help of MCMC. The known data that is used to calculate the reflectance spectra is denoted $\mathbf{X}$. The likelihood/goodness of fit of the current parameter estimates is evaluated with both the reflectance spectrum (r_{mix}) and the continuum removed spectrum (r_{cr}) to emphasize the absorption band depths over the absolute fit. The reflectance spectrum of the mixture is calculated using Equation 42 to calculate the albedo of the mineral endmembers, Equation 43 for the albedo of the mixture with the iron particles, and Equation 45 for the corresponding phase function of the mixture with the space weathering particles. These albedo and phase function values are then converted to reflectances according to Equation 1 using the AMSA model for the multiple scattering approximation. The continuum removed spectrum is calculated in a straightforward way such that certain fixed wavelengths are chosen as the points of the continuum (see, Figure 5.43). Usually, the continuum is defined by the convex hull of the spectrum (e.g., Fu et al., 2007). Calculating the continuum in this way is very time consuming considering that the function and its derivative must be evaluated thousands of times. The convex hull is not a linear function such that it is inefficient to implement it in Theano because the derivatives cannot be determined easily. The indices of the local maxima would be

dependent on the current spectrum. Because for each of the current parameters of the Markov Chain the continuum is different and depends on the slope, it cannot be computed prior to the sampling. Both the method using the convex hull and the method using fixed wavelengths used in this work are able to characterize the absorption bands usually found on the Moon.

Therefore, the concatenation of the spectrum and the continuum removed spectrum represents the data S. The output of the model is, therefore, a function of the parameters $\vec{\theta}_{em}$ and $\vec{\theta}_{smFe}$ such that

$$\vec{S}_{mix}(\vec{\theta}_{em}, \vec{\theta}_{smFe}) = [\vec{r}_{mix}, \vec{r}_{cr}] \tag{53}$$

The likelihood is then evaluated by building the sum over all log likelihoods or the product of all probability density function values at the measured data ($\vec{S}$) given a normal distribution around the modeled data and some variance σ^2 that is also considered as a parameter of the model and, therefore, also sampled.

$$p(\vec{S} \mid \vec{\theta}_{em}, \vec{\theta}_{smFe}, \mathbf{X}) \sim \prod_{j=1}^{2K} \mathcal{N}(S_j \mid \mu = S_{mix,j}, \sigma^2 \zeta_j) \tag{54}$$

K denotes the number of channels. If we know that the models accuracy is wavelength dependent it is reasonable to include this information in the likelihood function. Therefore, we introduce a wavelength dependent scaling factor ($\vec{\zeta}$) that can be used to emphasize, or de-emphasize certain wavelength channels.

5.3.3 *Prior*

Bayesian inference offers a convenient way to include a-priori knowledge into the sampling process. The posterior is proportional to the likelihood and the prior $p(\Theta)$. For multiple priors the joint probability is given by the product of the individual probabilities. Because our parameters are usually limited to the interval of [0, 1] a good choice for the priors on our parameters is the Beta distribution (see Section A.1.3). Choosing α and β controls the shape of the Beta distribution. For values outside the interval [0,1] the probability is zero.

The prior distribution on the endmember abundances can be set as follows, with the shape parameters being chosen depending on the application.

$$p(\vec{\theta}_{em}) \sim \prod_{i=1}^{N} \text{Beta}(\theta_{em,i} \mid \alpha = \alpha_{em,i}, \beta = \beta_{em,i}) \tag{55}$$

The space weathering components, namely, $npFe^0$ and $mpFe^0$, form only a small fraction of the composition. Therefore, we can choose the prior similar to $\alpha = 1$ and $\beta = 3$ in Figure A.1 for each the abundance of $npFe^0$ and $mpFe^0$ ($\vec{\theta}_{smFe}$)

$$p(\vec{\theta}_{smFe}) \sim \prod_{i=1}^{2} \text{Beta}(\theta_{smFe,i} \mid \alpha = \alpha_{smFe,i}, \beta = \beta_{smFe,i}) \tag{56}$$

The shape parameters will be chosen such that small values are preferred by the sampler.

We do not enforce the sum to one constraint to account for differences in the laboratory setups of the endmembers as well as porosity and other influences. Nonetheless, it is sensible to set a prior on the sum of the endmember weights $\vec{\theta}_{em}$:

$$p(\sum \vec{\theta}_{em}) \sim \mathcal{N}(\sum \vec{\theta}_{em} \mid \mu = 1.0, \sigma^2_{sum}). \tag{57}$$

This prior is centered around one such that solutions where the sum of the endmembers is close to one are favored. The variance σ^2_{sum} is chosen depending on the differences among the endmembers and the investigated samples.

The elemental abundances can be relatively well characterized remotely with, for example, gamma ray spectroscopy (e.g., Lawrence et al., 1998). Spectral parameters in the UV (e.g., Lucey et al., 2000a; Sato et al., 2017) or in the NIR (e.g., Bhatt et al., 2019) can also be used to estimate the elemental abundances, but should be used with care. E.g. according to the TiO_2 maps of Sato et al. (2017) the swirl Reiner Gamma is deprived of TiO_2 compared to its surroundings, which is physically implausible, as the optical differences are likely due to a difference in maturity and/or compaction (Hess et al., 2020a). Setting a prior, however, does not rule out solutions that do not confirm with prior knowledge, as long as the probability of the prior does not become zero. If, for example, the spectrum fits better for a high ilmenite concentration, this solution will be found to be more likely.

The RELAB database provides elemental abundances for many of the samples (e.g., Cloutis, 2002) and the elemental composition of the endmembers from Rommel et al. (2017) were determined by electron microprobe analysis. We here use endmembers with well-defined elemental abundances ($\mathbf{E}_{em}$, $M \times N$ matrix, for M elemental abundances and N endmembers) and use the estimated elemental abundances of the samples ($\vec{e}_{sample}$, $M \times 1$) as prior information. If the samples are mixed directly from the endmembers with weights $\vec{c}$ ($N \times 1$) the actual elemental abundances can be calculated as

$$\vec{e}_{sample} = \mathbf{E}_{em}\vec{c} \tag{58}$$

For realistic mixtures this relationship produces highly nonunique solutions for the mineral weights because, e.g., the MgO abundance could be attributed to a pyroxene or an olivine. For each sample the elemental abundances are calculated based on the proposed parameters of the mineral abundances $\vec{\theta}_{em}$ according to

$$\vec{\theta}_{elem} = \mathbf{E}_{em} \frac{\vec{\theta}_{em}}{\sum_{i=1}^{n} \theta_{em,i}}. \tag{59}$$

As the beta distribution should be centered around the estimated elemental abundance we want to enforce the mode of that distribution to be equal to the estimated elemental abundance. The mode of the Beta distribution for $\alpha > 1$ and $\beta > 1$ is given by

$$\text{mode}(x) = \frac{\alpha - 1}{\alpha + \beta - 2} \widehat{=} \vec{e}_{sample} \tag{60}$$

By increasing α ($\alpha \geqslant 1$) the variance of the distribution decreases. Therefore, we choose a $\vec{\alpha}_{elem}$ approximately according to the desired variance of that particular element and calculate $\vec{\beta}_{elem}$ according to Equation 60 such that

$$\vec{\beta}_{elem} = \frac{\vec{\alpha}_{elem} - 1}{\vec{e}_{sample}} + 2 - \vec{\alpha}_{elem}. \tag{61}$$

Consequently, we define the prior for the elemental abundances to be

$$p(\vec{\theta}_{em}) \sim \prod_{i=1}^{M} \text{Beta}(\theta_{elem,i} \mid \alpha = \alpha_{elem,i}, \beta = \beta_{elem,i}) \tag{62}$$

This distribution then effectively acts as a prior on the weights of the mineral endmembers, but there are multiple combinations that fit equally well.

5.3.4 *Unmixing Experiments*

The measured spectrum of a mixture is influenced by several factors, namely (1) composition (2), space weathering, (3) grain size, and (4) porosity. To disentangle the effects, we designed several experiments. The grain size is constant for all experiments and is expected to be known. Firstly, we calculate mature synthetic spectra to remove effects not described by the mixing model itself, except for noise. This can also be interpreted as a general validation of the sampling approach. Secondly, to remove the influence of space weathering and to test the general viability of the mixing model we used laboratory mixtures of known endmember spectra. And thirdly, we apply the full framework to unmix the LSCC spectra with endmember spectra from the RELAB catalog and include space weathering particles. These LSCC spectra can be seen as a good representation of different maturity levels and the general mineralogy of the lunar maria.

5.3.4.1 *Synthetic Mixtures*

This experiment is designed to estimate the uncertainties of the mixtures when all influences not covered by the model are removed. Spectra are generated with the mixing model including additional Gaussian noise with a standard deviation of $\sigma_n = 0.0008$. This corresponds to a signal-to-noise ratio (SNR) between approximately 170 and 400 (with SNR$= \frac{\mu_{r,ch}}{\sigma_n}$) depending on the channel.

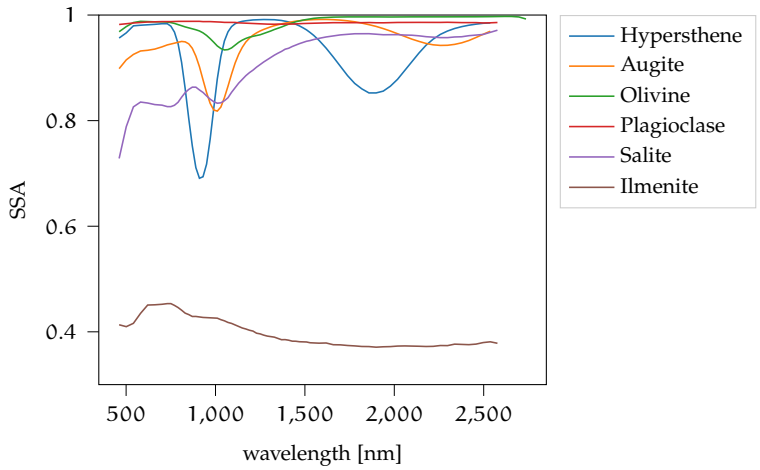

Figure 5.44: The endmembers for the experiments in sections 5.3.4.1 and 5.3.4.3. All the endmembers have a grain size of 0-45µm. The RELAB IDs are: OPX is the hypersthene AG-TJM-009; CPX Type B is the augite AG-TJM-010; OLV is the olivine PO-EAC-056; PLG is the plagioclase PL-EAC-029; CPX Type A is the pyroxene diopside PP-ALS-105; ILM is the ilmenite SC-EAC-034.

We selected the endmembers according to the categorizations above (see Section 5.3.1). A representative of each of the classes LCP, HCP Type A, HCP Type B, Olivine, Plagioclase, and Ilmenite is selected from the RELAB catalog (`http://www.planetary.brown.edu/relab/`) and the SSA values are obtained by inverting the Hapke model (see Equation 1) and displayed in Figure 5.44. All endmembers are samples of the 0-45 µm size fraction. The elemental abundances of the endmembers are listed in Table 5.7.

Table 5.6: Prior setups for the elemental abundances used during this work. The shape parameter β is then calculated according to Equation 61. If $\alpha_{elem} > 1$ and the theoretical elemental abundance is below 1 wt.%, the shape parameters will be set to $\alpha_{elem} = 1$ and $\beta_{elem} = 10$.

	SiO_2	TiO_2	Al_2O_3	Cr_2O_3	MgO	CaO	MnO	FeO	Na_2O	K_2O	P_2O_5	SO_3
None α_{elem}	1	1	1	1	1	1	1	1	1	1	1	1
TiO_2 α_{elem}	1	40	1	1	1	1	1	1	1	1	1	1
Ti/Al α_{elem}	1	40	40	1	1	1	1	1	1	1	1	1
All α_{elem}	30	30	30	1	30	30	1	30	1	1	1	1

Table 5.7: Elemental abundances of endmember catalog for experiments in sections 5.3.4.1 and 5.3.4.3. The sample spectra and elemental abundances are taken from the RELAB library (`http://www.planetary.brown.edu/relab`).

	SiO_2	TiO_2	Al_2O_3	Cr_2O_3	MgO	CaO	MnO	FeO	Na_2O	K_2O	P_2O_5	Fe_2O_3
AG-TJM-009	54.09	0.16	1.23	0.75	26.79	1.52	0.49	15.22	0.05	0.05	0.0	0.00
AG-TJM-010	50.73	0.74	8.73	0.00	16.65	15.82	0.13	5.37	1.27	0.00	0.0	1.08
PO-EAC-056	40.42	0.00	0.03	0.13	48.25	0.19	0.15	11.11	0.00	0.00	0.0	0.00
PL-EAC-029	54.85	0.06	27.71	0.02	0.00	10.97	0.01	0.00	5.15	0.40	0.0	0.46
PP-ALS-105	48.41	1.05	5.29	0.03	12.37	22.15	0.26	6.15	0.36	0.00	0.0	3.79
SC-EAC-034	0.20	47.61	0.01	0.02	0.01	0.00	0.02	45.43	0.00	0.00	0.0	0.00

The generated mixtures are based on a mare composition of the endmembers of 10 wt.% hypersthene, 40 wt.% augite, 5 wt.% olivine, 30 wt.% plagioclase, and 15 wt.% diopside. The ilmenite abundance is varied between 0 wt.% and 16 wt.% and the remaining fraction is normalized, such that the endmember weights again sum up to unity. The abundances of $npFe^0$ and $mpFe^0$ is varied between 0 wt.% and 2.2 wt.%, and 0 wt.% and 1.2 wt.%, respectively. Ultimately, 48 synthetic mixtures (mix_0- mix_{47}) are created. The detailed results for all mixtures are listed in tables B.2 following and B.6 and following.

Generally, all endmembers are measured under similar conditions. According to these conditions the priors have to be chosen. In our case, we do not want to directly employ knowledge about mineral abundances ($\vec{\theta}_{em}$). Therefore, we choose an uninformative prior, that is:

$$p(\vec{\theta}_{em}) \sim \prod_{i=1}^{N} Beta(\theta_{em,i} \mid \alpha = 1, \beta = 1). \tag{63}$$

Both shape parameters of the Beta distribution are set to one for the prior distribution, such that the prior is a uniform distribution between zero and one. Because negative weights are physically implausible, these samples are always rejected. The mixtures are synthetically generated, such that we set $\sigma_{sum} = 0.02$ to prefer solutions where the sum of the fractional abundances is close to one. The experiment is carried out once with no prior on the elemental abundances and once with an elemental prior on the abundances of TiO_2 and Al_2O_3 (see also Table 5.6). For theoretical abundances below 1 wt.% the

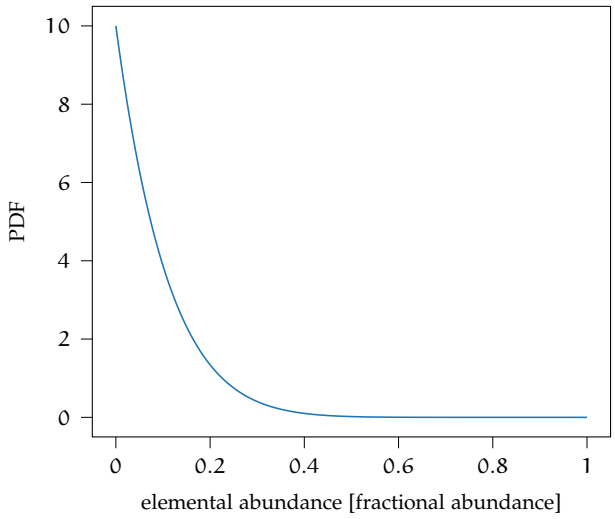

Figure 5.45: The probability distribution function of the prior on the elemental abundances for a theoretical abundance below 1 wt.%.

variance becomes very low when using the method mentioned above. Therefore, we set $\alpha_{elem} = 1$ and $\beta_{elem} = 10$ for the shape of the prior, making the mode zero and the PDF is given in Figure 5.45.

In general, we set the shape parameters for npFe^0 and mpFe^0 to $\alpha_{smFe} = 1$ and $\beta_{smFe} = 30$. These parameters were tuned by hand such that 80 % of the probability density is distributed in the interval [0 wt.%,5 wt.%]. Higher values than 5 % are physically implausible. Trang and Lucey (2019) found about 2 wt.% of smFe at the maximum for the Moon, excluding the polar regions. The model of Trang and Lucey (2019), first versions of which were introduced in Trang et al. (2017) and Lucey and Riner (2011), differs from the model of Wohlfarth et al. (2019), e.g., Trang et al. (2017) do not consider the influence of the phase function. Therefore, the predicted concentration of npFe^0 and mpFe^0 is not necessarily the same, leading us to set a relatively uninformative prior on each of the smFe abundances. The prior on the abundance of smFe particles is consistent throughout this work and is not changed between experiments.

Generally, the mean predicted solution does not necessarily correspond to the actual mixture coefficients used, but the theoretical values are always part of the solution. Classical unmixing approaches are limited to just one solution and small changes may lead to different optimal solutions, which are also not necessarily equal to the ground truth values.

Ilmenite shows, compared to the mafic minerals, an almost featureless spectrum in the NIR wavelength range. Because of its low albedo, the abundance of ilmenite also dampens the absorption bands and darkens the overall spectrum. This is, to some extent, similar to the spectral influence of mpFe^0 particles. If the absolute reflectance is poorly defined, so is the ilmenite abundance. Consequently, depending on the prior setup and the sum constraint the uncertainties of ilmenite are different. If no prior on the elemental or mineral abundances is set, the abundance of ilmenite is relatively poorly defined. For the mixtures that, in theory, do not contain ilmenite, a majority of the accepted mixtures contain significant amounts of ilmenite (see Figure 5.46). A combination of ilmenite and other endmembers can, therefore, equally explain the measured spectrum. For the fresh

mixture (mix_0, without any smFe particles, the uncertainty of the spectrum is small (see Figure 5.48). The mineral uncertainties are small, but for the other mixtures the uncertainties significantly increase. The majority of posterior density of plagioclase (PLG) is generally lower than the actual abundance, and for olivine (OLV) and/or diopside (CPXA) the majority of posterior density is below the actual value. This suggests that a mixture of olivine/diopside and ilmenite produces very similar results to plagioclase. Olivine and diopside have similar absorptions at about 1-µm, making them interchangeable to some extent when the maturity increases. For example, for mix_{15} there are two distinct modes with either high concentration of diopside or olivine or plagioclase. According to the KDE the mode of the multivariate distribution is at OLV 34.60 wt.%, PLG 13.31 wt.%, and CPXA 0.63 wt.%. Even though the modes are very different to the estimated mean (OLV: 11.31 wt.%; PLG: 18.96 wt.%; CPXA: 21.99 wt.%), the mean predicted and mode predicted spectrum are visually identical. Additionally, the mineral uncertainties of mix_5 are large (see Figure 5.46c), but the confidence interval for the predicted spectrum is narrow (see Figure 5.48c). This highlights that there are several solutions that produce nearly identical spectra.

Ilmenite is the only endmember that contains significant amounts of TiO_2. Including prior knowledge about the abundance of TiO_2 can, therefore, favor solutions that are close to the true ilmenite value. In Figure 5.47 the violin plots of the acceptable solutions considering the TiO_2 and Al_2O_3 prior are displayed. The abundance of ilmenite is then much more clearly defined. Also the uncertainties of the other minerals mostly decrease, while the uncertainties of the spectra remain similar.

The results for the most mature spectrum with the highest abundance of ilmenite are shown in Figure 5.49. With the prior, the uncertainties of all endmembers can be reduced. The confidence plots remain very similar. Figure 5.50 shows the distribution of the differences between theoretical values and mean predicted abundance. By including the prior the differences can be reduced. The mean of olivine is usually above the true value, while the mean of plagioclase and clinopyroxene is usually below the theoretical value. The theoretical abundance of olivine is relatively small compared to the other minerals, consequently, the mean is usually higher. The uncertainties of olivine and clinopyroxenes are high for both with and without the prior. This can be seen in Figure 5.51. Including prior knowledge about the elements Al_2O_3 and TiO_2 the uncertainties of all mineral abundances are mitigated. This is despite the fact that these elements are almost depleted in the pyroxenes and olivine.

The abundance of $npFe^0$ and $mpFe^0$ is usually well defined, as changes to the abundance of $npFe^0$ and $mpFe^0$ can have a strong influence on the modeled spectrum. In Figures 5.46, 5.47 and 5.49 it can be seen that the predicted $npFe^0$ and $mpFe^0$ do not change significantly with the introduction of a prior. In Table 5.8 the correlation coefficients between true smFe abundance and the standard deviation of the minerals is listed. For all minerals it can be seen that the correlation coefficients are positive. Therefore, the higher the abundance of smFe is, the larger the uncertainties become. The uncertainty of ilmenite is, however, uncorrelated to the smFe abundance, even if no prior knowledge is used. Because ilmenite does not show a prominent absorption band such a feature cannot be obscured by the smFe particles. This is visible in Figure 5.52. While the overall uncertainties decrease with a prior on the elemental abundances, the trend that the

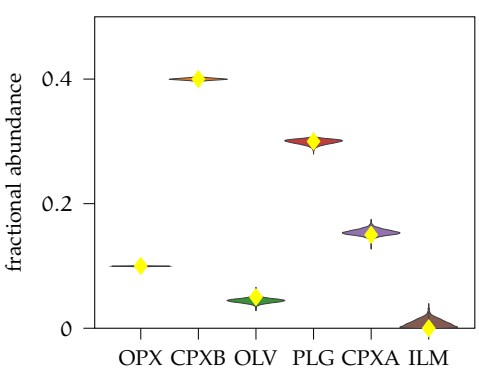

(a) Without elemental prior (mix_0)

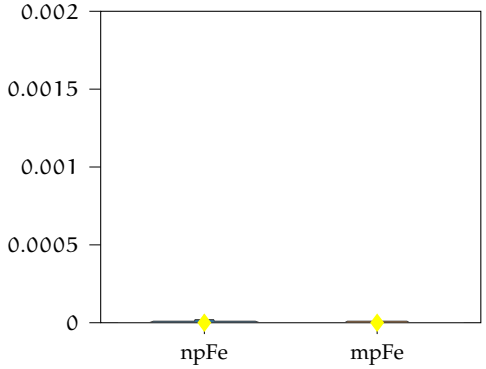

(b) Without elemental prior (mix_0)

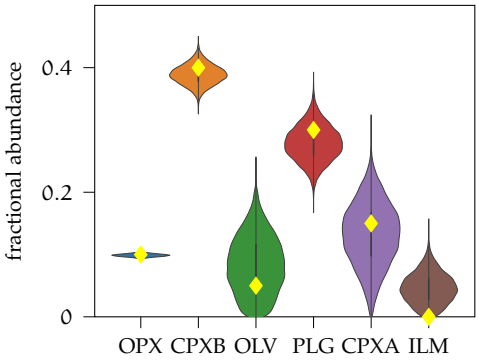

(c) Without elemental prior (mix_5)

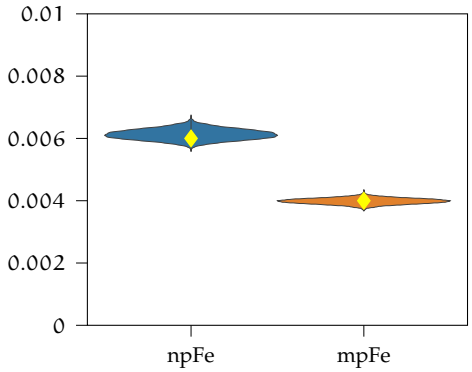

(d) Without elemental prior (mix_5)

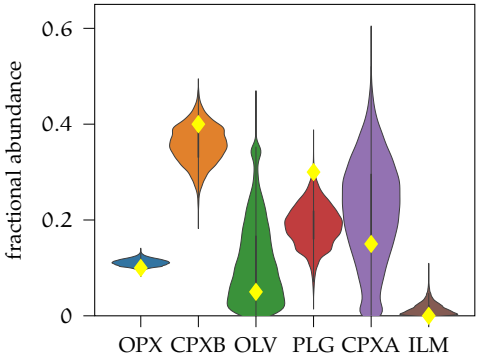

(e) Without elemental prior (mix_{15})

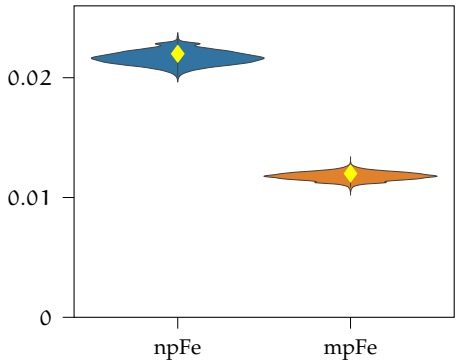

(f) Without elemental prior (mix_{15})

Figure 5.46: Violin plots for synthetic mixtures 0, 5, and 15 for the MCMC sampling without a prior on the elemental abundances. These mixtures do not contain ilmenite, but the posterior distribution contains many solutions with significant amounts of ilmenite. Yellow diamonds mark the true abundances that were used for mixing the endmembers.

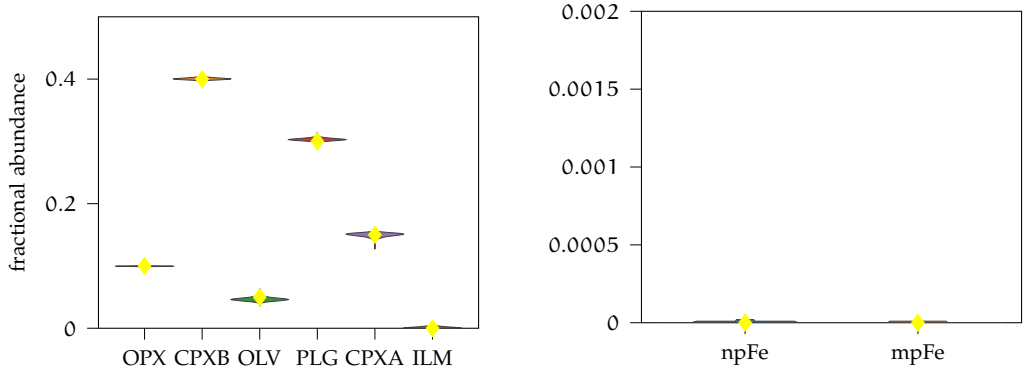

(a) With TiO_2 and Al_2O_3 prior (mix_0)

(b) With TiO_2 and Al_2O_3 prior (mix_0)

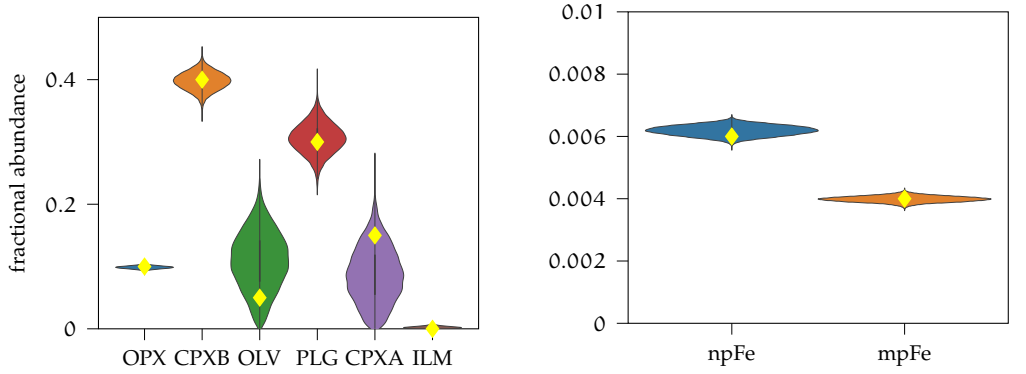

(c) With TiO_2 and Al_2O_3 prior (mix_5)

(d) With TiO_2 and Al_2O_3 prior (mix_5)

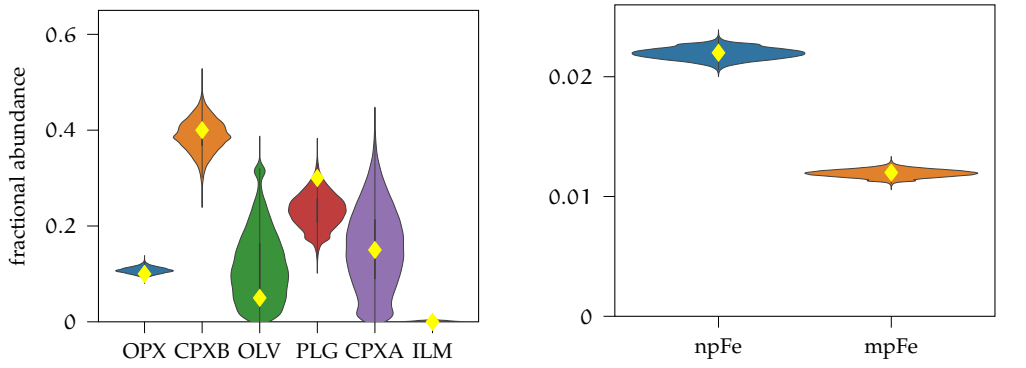

(e) With TiO_2 and Al_2O_3 prior (mix_{15})

(f) With TiO_2 and Al_2O_3 prior (mix_{15})

Figure 5.47: Violin plots for synthetic mixtures 0, 5, and 15 for the MCMC sampling including a prior on the elemental abundances. Compared to the version without a prior the ilmenite abundance could effectively be constrained. This also slightly reduced the uncertainties associated with the other minerals. Yellow diamonds mark the true abundances that were used for mixing the endmembers.

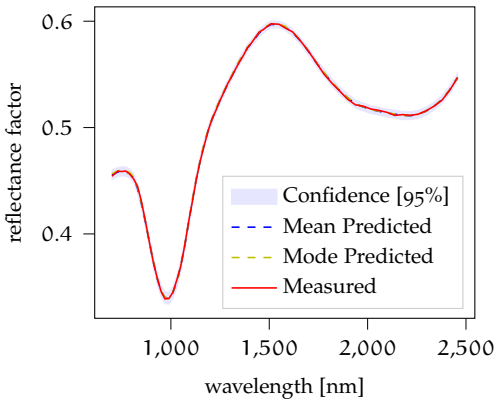

(a) Without elemental prior (mix_0)

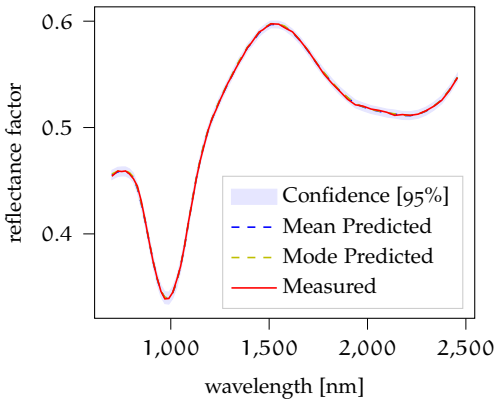

(b) With TiO_2 and Al_2O_3 prior (mix_0)

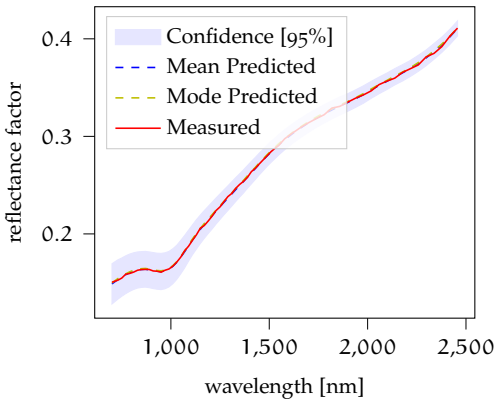

(c) Without elemental prior (mix_5)

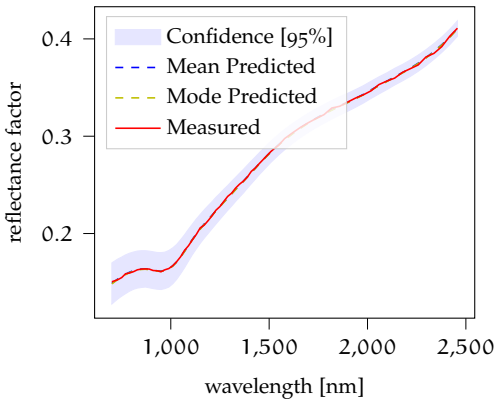

(d) With TiO_2 and Al_2O_3 prior (mix_5)

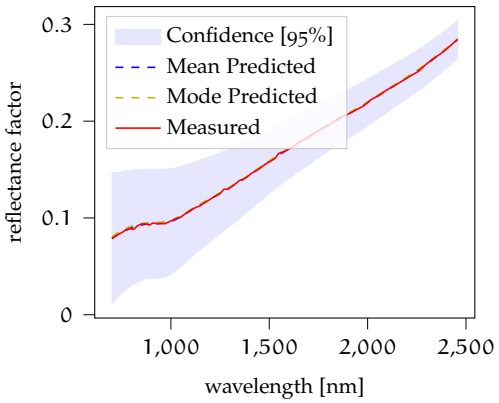

(e) Without elemental prior (mix_{15})

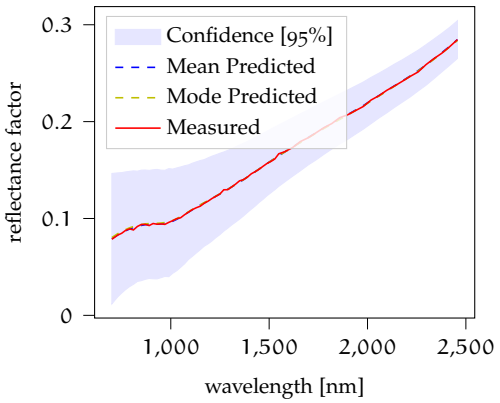

(f) With TiO_2 and Al_2O_3 prior (mix_{15})

Figure 5.48: Confidence plots for synthetic mixtures 0, 5, and 15. In the left column, the plots of the sampling without an elemental prior are displayed. For the confidence plots in the right column, prior information about the elements TiO_2 and Al_2O_3 was included.

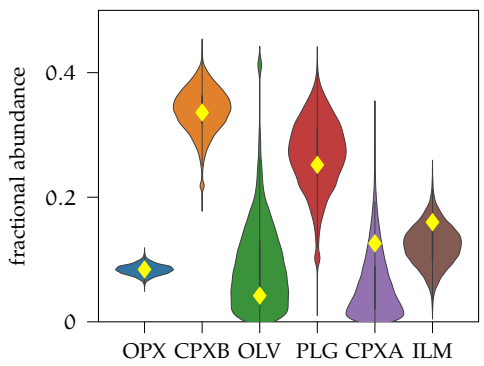

(a) Without elemental prior (mix_{47})

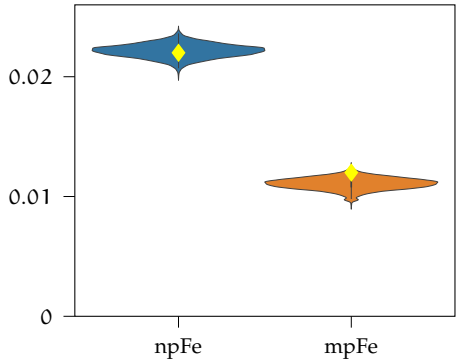

(b) Without elemental prior (mix_{47})

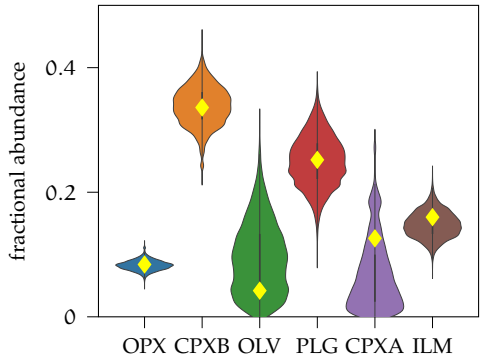

(c) With TiO_2 and Al_2O_3 prior (mix_{47})

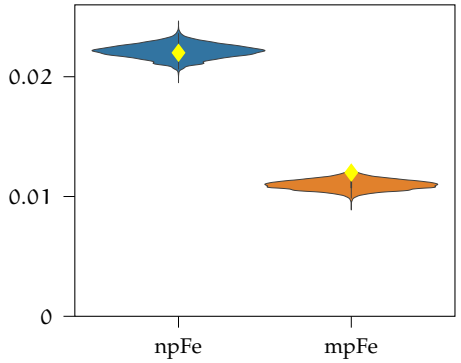

(d) With TiO_2 and Al_2O_3 prior (mix_{47})

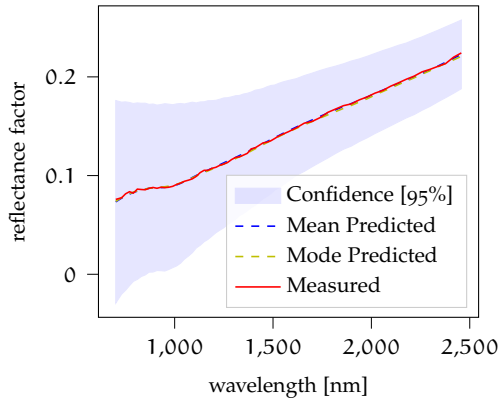

(e) Without elemental prior (mix_{47})

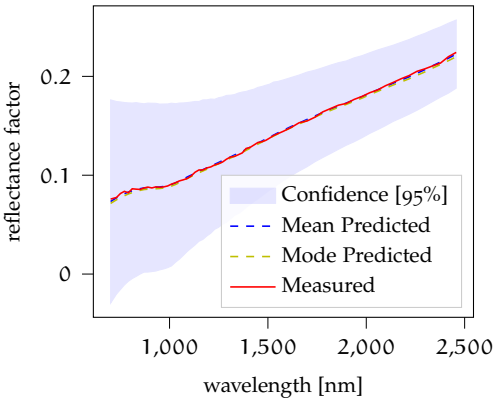

(f) With TiO_2 and Al_2O_3 prior (mix_{47})

Figure 5.49: Results for the most mature spectrum, which also has the highest ilmenite concentration. The spectrum becomes very dark. The abundance of $npFe^0$ and $mpFe^0$ is well defined either with or without the prior information. The uncertainties of the mineral abundances decrease when including the prior. The yellow diamonds in the violin plots mark the true abundances that were used for mixing the endmembers.

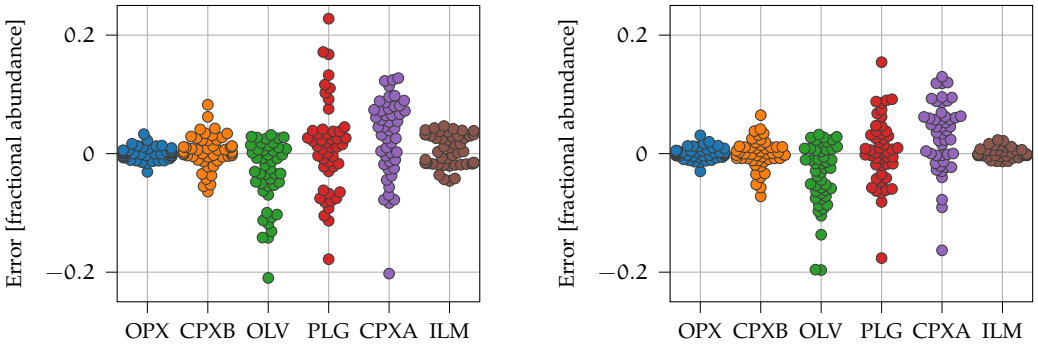

(a) Without prior

(b) TiO_2 and Al_2O_3 prior

Figure 5.50: Differences between mean predicted solution and true abundance. The differences in ilmenite and plagioclase abundance can be reduced with a prior on the TiO_2 and Al_2O_3 abundance. Each circle represents one mixture.

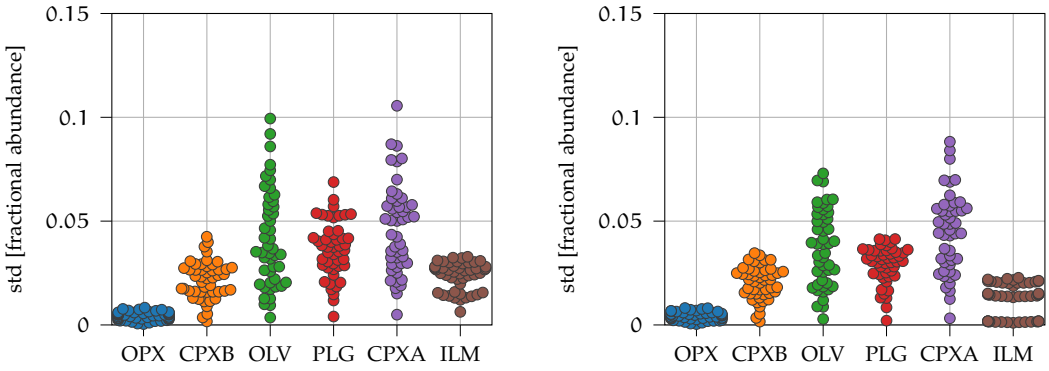

(a) Without prior

(b) TiO_2 and Al_2O_3 prior

Figure 5.51: Uncertainties associated with each of the mineral abundances. With a prior all uncertainties, except for the orthopyroxene, which is already quite low, can be reduced. Each circle represents one mixture.

Table 5.8: Pearson r coefficients for the relationship between theoretical smFe abundance and standard deviation of the respective endmembers. Except for ilmenite with an elemental prior all correlation coefficients are positive. Therefore, with increasing smFe abundance the uncertainties of the mineral abundances increase.

	OPX	CPXB	OLV	PLG	CPXA	ILM
r_{None}	0.93	0.71	0.47	0.54	0.48	0.13
$r_{Ti/Al}$	0.94	0.81	0.56	0.70	0.58	0.02

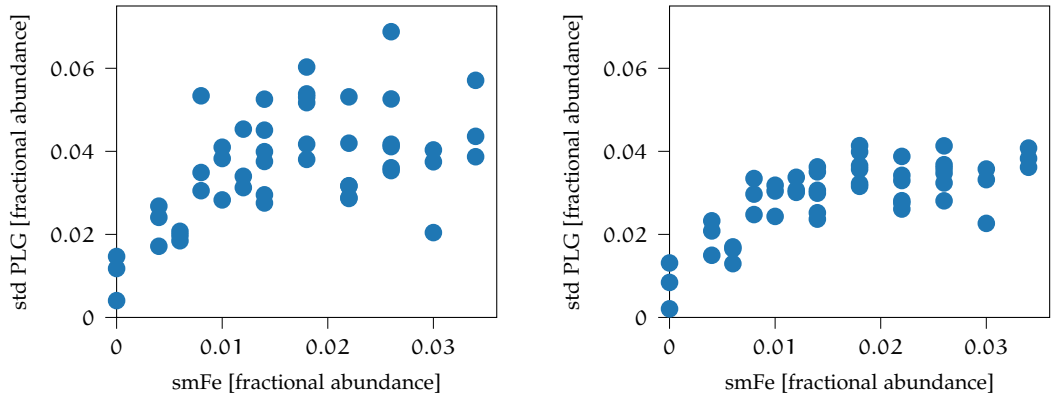

(a) Without prior

(b) TiO_2 and Al_2O_3 prior

Figure 5.52: Correlation between true smFe abundance and the uncertainties (standard deviations) of the plagioclase abundance. It can be seen that the uncertainties generally decrease with the elemental prior.

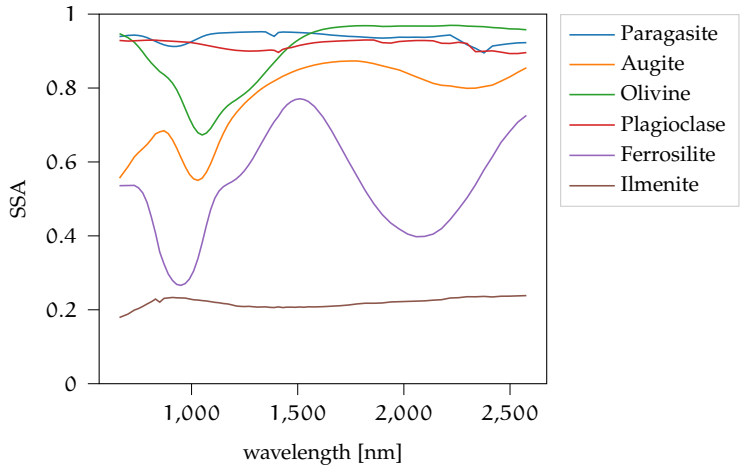

Figure 5.53: The endmembers for the experiment in Section 5.3.4.2 taken from Rommel et al. (2017). PRG: pargasite, AUG: augite, OLV: olivine, PLG: plagioclase (labradorite B), FS: ferrosilite, ILM: hemo-ilmenite.

uncertainties increase with increasing maturity is visible for both with and without a prior.

Generally, it can be seen that the ilmenite abundance is difficult to determine reliably without prior information, for both immature and mature spectra. For mature spectra the uncertainties of all mineral abundances become very large, even for an almost perfect case, where influences which are not modeled, are removed. This illustrates that unmixing on the Moon is an ill-posed problem, and additional knowledge about the composition is necessary. The addition of a prior to indirectly include information about the plagioclase and ilmenite abundance is effective in reducing some of the uncertainties.

5.3.4.2 *Fresh Laboratory Mixtures*

This experiment is set up to unmix real laboratory mixtures (see also Rommel et al. (2017)) from laboratory endmembers. Thus, we select the same endmembers as in Rom-

Table 5.9: Elemental abundances of endmember catalog for section 5.3.4.2 taken from Rommel et al. (2017).

	SiO_2	TiO_2	Al_2O_3	Cr_2O_3	MgO	CaO	MnO	FeO	Na_2O	K_2O	P_2O_5	Fe_2O_3
Pargasite	43.80	1.06	15.63	0.03	18.85	12.39	0.05	0.25	2.84	1.72	0.00	0.28
Augite	50.10	1.26	4.81	0.60	15.22	22.70	0.08	2.41	0.49	0.02	0.00	2.35
Olivine	37.70	0.07	0.04	0.03	35.40	0.16	0.39	26.49	0.03	0.02	0.00	0.23
Plagioclase	54.70	0.00	28.80	0.00	0.00	11.22	0.00	0.28	4.78	0.60	0.00	0.00
Ferrosilite	47.90	0.05	0.32	0.03	5.18	0.88	1.92	44.70	0.03	0.03	0.00	0.20
Ilmenite	0.02	50.40	0.02	0.12	6.15	0.00	0.26	34.10	0.00	0.00	0.00	7.90

mel et al. (2017) but omit one of the two labradorites (plagioclases) as the two are very similar, and we want to select endmembers that are spectrally distinct. We also omit the diallagite endmember, to reduce the catalog to the same size as for the other experiments and this endmember is only present in one mixture, which is, consequently, also omitted here. The amphibole endmember pargasite (PRG) was selected in Rommel et al. (2017) to test whether uncommon minerals can also be detected by the algorithm. We keep this endmember for our analysis even though it is not present on the Moon.

For the inversion of the Hapke model, the parameters are chosen in the same way as in Rommel et al. (2017) for comparability. Therefore, the term for the shadow hiding opposition effect is not set to zero, but B_{SH_0}=3.1 and h_{SH}=0.11 are adopted from Rommel et al. (2017). The resulting SSA spectra are shown in Figure 5.53.

The elemental abundances of the endmembers were determined in Rommel et al. (2017) based on electron microprobe analysis in the laboratory (see Table 5.9) and the modes and shape parameters are determined according to Section 5.3.3. The results were obtained by using no elemental priors on the one hand and using a prior for the TiO_2 abundance on the other hand (see first two rows of Table 5.6).

The true values of the abundance of submicroscopic iron particles in this experiment is zero. In order to test whether fresh and mature spectra can be reliably distinguished from each other, we still employ the same prior for smFe as for the other experiments.

All endmembers and mixtures were measured in the same laboratory and the mixtures are directly mixed from the endmembers, therefore, the weights of the endmembers should sum up to a value close to one. We set a prior on the sum according to Equation 57 with a standard deviation of $\sigma_{sum} = 0.02$.

The detailed results of the unmixing without a prior on the elemental abundances and with a prior on the TiO_2 abundance are listed in tables B.11 following and B.13 and following, respectively. Generally, the mean predicted results are very similar to those of Rommel et al. (2017) considering that the endmembers labradorite A and diallagite, were omitted. Even though we did not use a strong prior on the abundance of iron particles, the predicted abundances are almost exclusively below 0.02 wt.% or a fraction smaller than 2×10^{-4}.

For the version without a prior on the TiO_2 abundance, ilmenite is erroneously predicted in the mixtures of pargasite and plagioclase. For example, Figure 5.54 shows the violin plots of all similarly well-fitting solutions. It can be seen that ilmenite is predicted to be present, and a solution without ilmenite is not part of the uncertainty. Therefore,

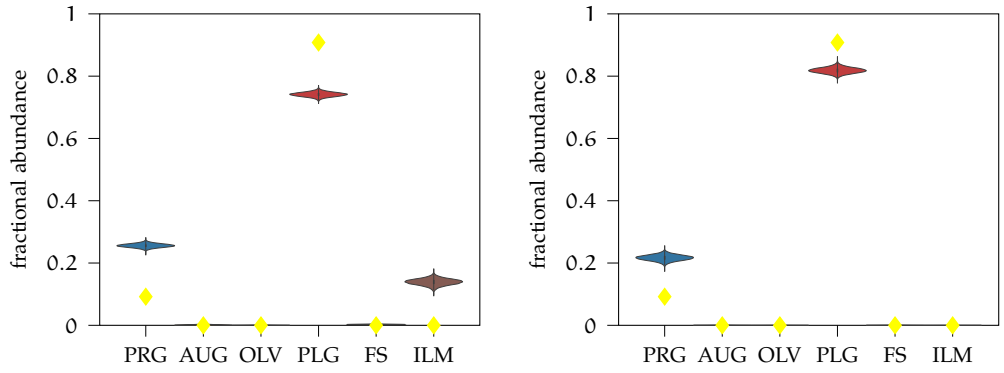

(a) Without prior

(b) TiO_2 prior

Figure 5.54: Violin plots for mix_0 of the fresh laboratory mixtures. Yellow diamonds mark the theoretical abundances that were used for mixing the endmembers.

a solution with ilmenite fits better than one without ilmenite. If we, however, prefer solutions where the contribution of ilmenite is close to zero, we obtain a better result and the errors in pargasite and plagioclase abundance are reduced. In Figure 5.55 the confidence plots are plotted. Here it can be seen that the mean and mode predicted spectra fit quite well for both prior setups. By introducing the prior for the TiO_2 abundance, the uncertainties of the fit increase (σ=0.006 compared to σ=0.003 for no prior). Therefore, slightly less well fitting solutions are accepted if the ilmenite abundance confirms better with the prior knowledge.

In the mixtures containing plagioclase and ferrosilite, plagioclase is confused with pargasite if no prior knowledge is included. The two endmembers are spectrally very similar and are both bright (see Figure 5.53). In Figure 5.56 an example violin plot is shown, where the confusion of plagioclase and pargasite can be seen in Figure 5.56a. Small contributions of ilmenite can already dampen the absorption band of the pargasite endmember, such that the similarity to plagioclase increases. The mean predicted abundance of ilmenite is quite low with 0.48 wt.% for the version without a prior, but still leads to a significantly different solution. The confidence plots in Figure 5.57 look nearly identical, except that for the TiO_2 prior the uncertainty of the 0.9µm absorption band slightly increases. This suggests that both solutions, with and without ilmenite, represent regions of high posterior density. It is, however, very difficult for the sampler to traverse from one region to the other, as the two are far apart and due to the prior on the sum it is unlikely for a limited number of samples that both regions are sampled. But with a relatively uninformative prior as in Figure 5.45 this ambiguity can be removed, such that the solutions with no ilmenite are preferred.

This trend illustrated by the two examples above, can also be seen in Figure 5.58. The differences between mean predicted solution and true abundance for the endmembers augite, olivine, and ferrosilite are not improved by including prior knowledge about the TiO_2 abundance. This is likely because of inaccuracies of the data and the simple mixing model and was also a problem in Rommel et al. (2017). The inherent simplifications of the Hapke model makes it such that the fractional abundances are not necessarily equal to their actual weight fraction (e.g., Grumpe et al., 2018). Similar to a regularization term in classical optimizations, we can use the prior to favor certain solutions,

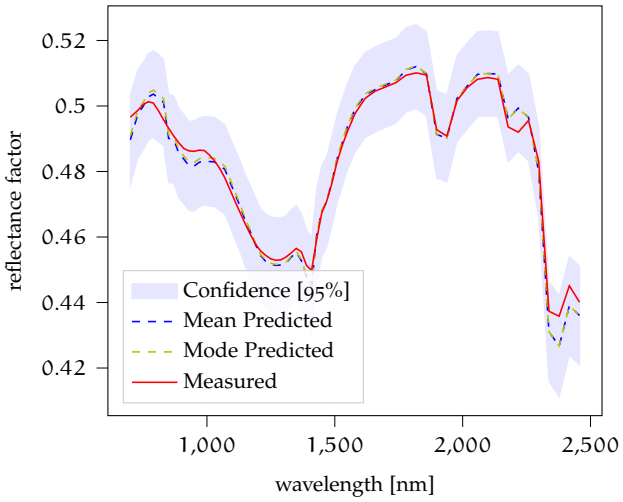

(a) Without prior

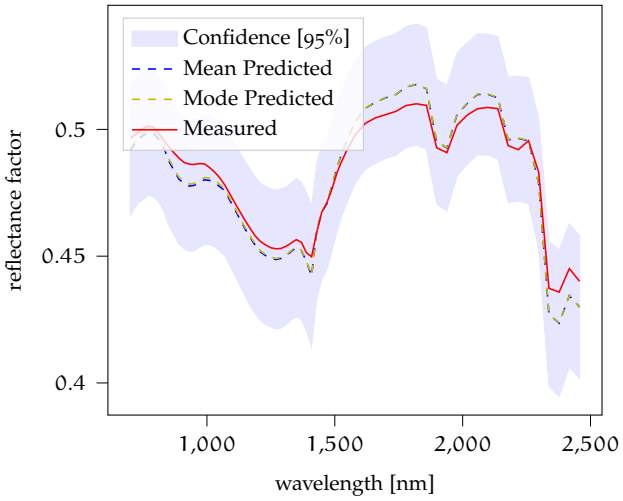

(b) TiO_2 prior

Figure 5.55: Confidence for mix_0 of the fresh laboratory mixtures. Uncertainty of the spectrum slightly increases with the introduction of a prior on the TiO_2 abundance.

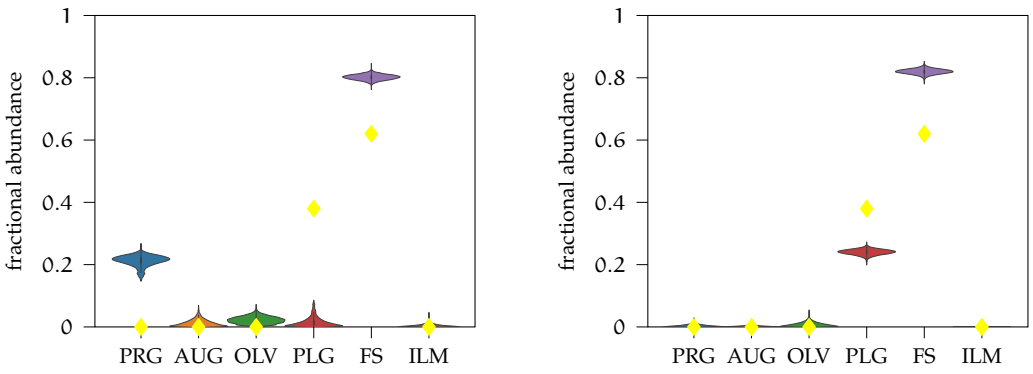

(a) Without prior

(b) TiO_2 prior

Figure 5.56: Violin plots for mix_{10} of the fresh laboratory mixtures. Yellow diamonds mark the theoretical abundances that were used for mixing the endmembers.

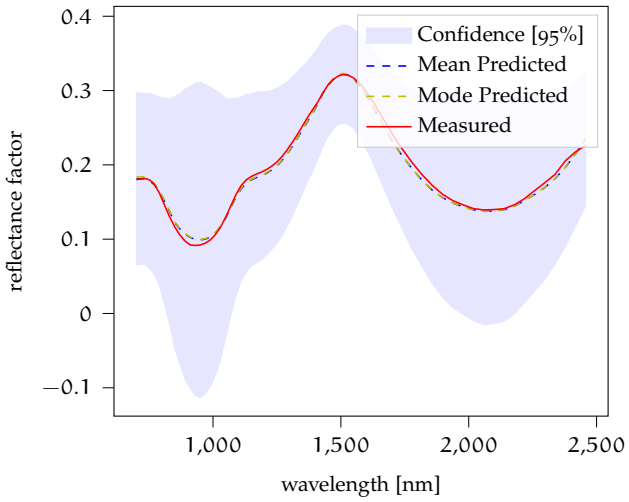

(a) Without prior

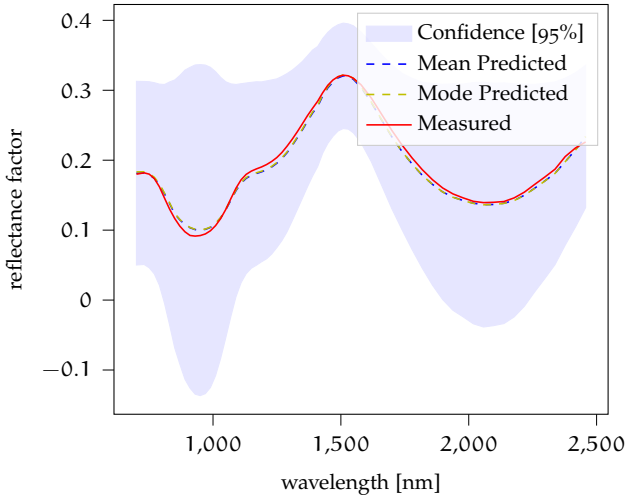

(b) TiO_2 prior

Figure 5.57: Confidence for mix_{10} of the fresh laboratory mixtures. The prediction of the 0.9 µm absorption is slightly less certain for the version with a prior on TiO_2 abundance. Mean predicted spectra are almost identical, even though the weights are quite different. For the version without an elemental prior the sampled σ is 0.011 and 0.012 for the version with a TiO_2 prior.

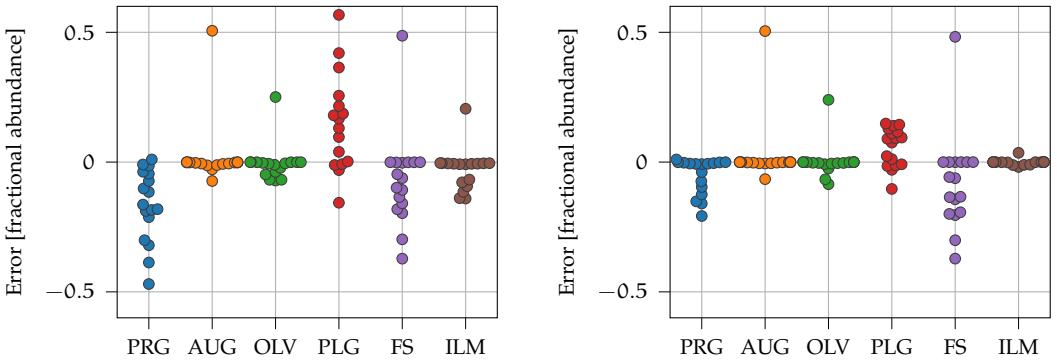

(a) Without prior

(b) TiO_2 prior

Figure 5.58: Prior on the element TiO_2 mainly present in ilmenite, significantly reduces the differences in predicted plagioclase and also pargasite abundance and theoretical abundances. These spectra of the three endmembers are relatively flat and do not show significant absorption bands.

without imposing hard constraints. Generally, without prior knowledge the abundance of plagioclase is usually underestimated, while the abundance of ilmenite and pargasite is overestimated. The uncertainties are mostly small, both with and without TiO_2 prior (see Figure 5.59).

5.3.4.3 *LSCC Samples*

In the final experiment, we unmix spectra from the LSCC catalog with laboratory mineral endmembers and the $npFe^0$ and $mpFe^0$ particles. The LSCC catalog contains mature samples that were returned from the lunar surface by the Apollo missions and is, therefore, a good representation of lunar mineralogy. We use the $< 45\,\mu m$ size fraction spectra for the unmixing, and because there is no data on the mineral abundances of this size fraction we use the mineral abundances from the 20-45 µm size fraction, which correspond to a large portion of the weight, as a reference for evaluating the results. The endmembers are the same samples from the RELAB library listed in Section 5.3.4.1. These endmembers do not correspond to the actual constituent minerals and there are additional minerals that are not covered by the endmember catalog, e.g., spinel. Additionally, the endmember catalog does not contain agglutinates in comparison to the LSCC samples with large fractions of agglutinates. The ground truth abundances are obtained from the tables of Taylor et al. (2001, 2010). The abundances of the minerals were grouped into clinopyroxene, orthopyroxene, olivine, plagioclase, and ilmenite. The abundances were then normalized to the mineral fraction because we are not considering glasses. We have seen that without a prior on the elemental abundances, the uncertainties become very large for mature spectra. Therefore, we will use the same prior on TiO_2 and Al_2O_3 abundance, which in the previous experiments reduced the uncertainties effectively for plagioclase and ilmenite, but also for many of the other minerals. Additionally, we will employ a prior on all elements with a relevant abundance on the Moon, which might contribute to distinguishing between minerals (see also Table 5.6). The elemental abundances of the LSCC samples are listed in Table B.15.

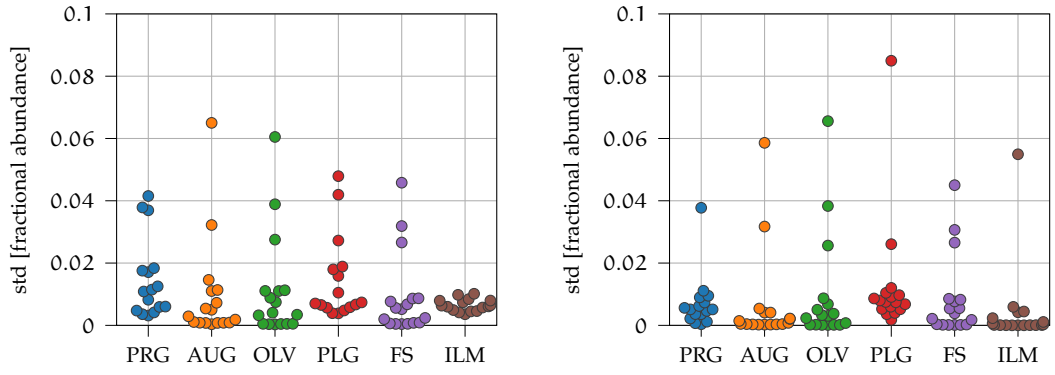

(a) Without prior

(b) TiO_2 prior

Figure 5.59: The uncertainties of the respective endmembers from Rommel et al. (2017) are in general relatively low. Only the mixture containing ilmenite and ferrosilite is highly uncertain. For that particular sample, no good solution has been found considering the prior on the sum of the endmember weights.

The spectra were measured under laboratory conditions, but the mixtures are much more complex compared to the laboratory mixtures from Section 5.3.4.2. We are, therefore, not enforcing the sum-to-one constraint as strongly, as we set $\sigma_{sum} = 0.1$. Because plagioclase and ilmenite have both almost featureless flat spectra, the uncertainties between these two increase significantly the more relaxed the prior on the sum is. Therefore, the prior knowledge about TiO_2 and Al_2O_3 abundance becomes even more essential.

Detailed results for the unmixing of all LSCC spectra is listed in Table B.16-B.17 and B.18-B.19 for the two experiments with different priors. Generally, the uncertainties are similar between both versions, but for some samples the priors on the other elements help in reducing the uncertainties. This can be seen in Figure 5.60. Therefore, we will focus on the Ti/Al prior version.

In some cases the plagioclase abundance is underestimated, such an example can be seen in Figure 5.61. For the violin plots, the two clinopyroxenes are grouped together. The spectrum fits quite well and the true plagioclase abundance is not part of the uncertainty. Therefore, a prior cannot mitigate the differences between mean predicted and theoretical abundance. Instead, olivine and orthopyroxene abundances are overestimated. A similar problem can be seen for 12001 and 15041. These samples are the ones with the highest fraction of agglutinic glasses (12001: 56.2 wt%, and 15041: 51.3 wt%, and 10084: 53.9 wt%) among the mare samples. For all other samples, the predicted abundances are close to the true values.

Figure 5.62 shows typical results for a mature mare spectrum. Most of the abundances are relatively well defined with the prior on the TiO_2 and Al_2O_3 abundance. Compared to sample 10084 in Figure 5.61 there are significantly fewer $npFe^0$ and $mpFe^0$ particles predicted to be present. As sample 14260 contains less FeO (9.65 wt.% compared to 14.8 wt.% in 10084) it is likely that the smFe abundance saturates more quickly, such that additional smFe cannot easily be created as quickly anymore. The ilmenite abundance is comparatively small which might also be a contributing factor that the uncertainties are relatively small. Similarly, for the mature highland spectrum in Figure 5.63 the iron

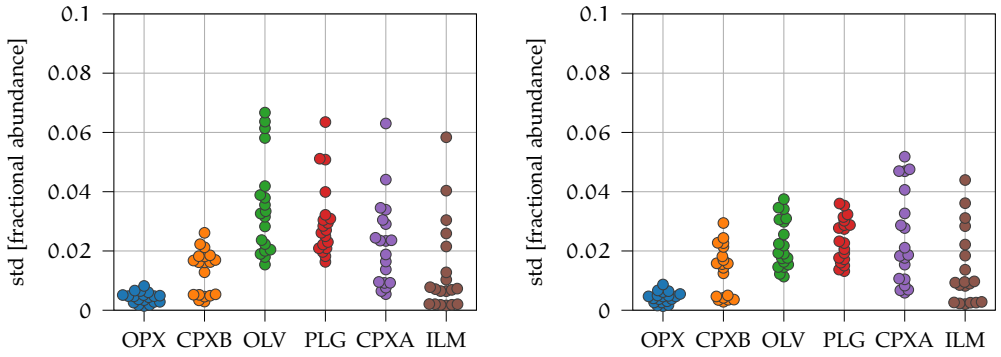

(a) TiO_2 and Al_2O_3 prior

(b) All prior

Figure 5.60: Uncertainties associated with each of the mineral abundances for the unmixing of the LSCC spectra.

abundance in the highlands is generally much smaller so that less smFe can be created. According to the I_s/FeO parameter, this is also a very mature spectrum and the absorption bands are weakly pronounced. But the smFe abundance is small compared to the mare samples. In Figure 5.64 the results for sample 79221 for both with the Ti/Al prior and also with the prior on all major elemental abundances is shown. This sample is rich in ilmenite and also relatively mature, therefore, the uncertainties are quite high. In such cases the results can be improved, when additional elemental abundance information is available. For most other LSCC samples the Ti/Al prior is, however, sufficient to constrain the procedure. The $npFe^0$ and $mpFe^0$ abundance is not much effected by the change in prior knowledge.

In Figure 5.65 the correlations between I_s/FeO or I_s and mean predicted $npFe^0$ or $mpFe^0$ abundance are displayed. The abundances are only weakly correlated with the I_s/FeO maturity index. In contrast the correlation between the ferromagnetic resonance I_s and the abundance is very strong. Even for the small dataset this correlation is significant. Because the I_s is a measure on the amount of iron particles in the size fraction between 4nm and 33nm (Housley et al., 1976), this suggests that the abundance of $npFe^0$ can be obtained relatively reliably even with a limited endmember catalog. This difference between I_s/FeO and I_s also supports the findings of Trang and Lucey (2019) that the saturation limit of $npFe^0$ particles is dependent on the FeO abundance. The saturation limit increases with increasing FeO abundance. Figure 5.66 shows the relationship between $npFe^0$ and $mpFe^0$ abundance in the LSCC samples. Usually the factor between the abundance of $npFe^0$ and $mpFe^0$ abundance is approximately constant, where the amount of $npFe^0$ is typically twice as high as the amount of $mpFe^0$.

5.3.5 *Discussion*

Generally, the three experiments show that a probabilistic perspective gives important insights into the unmixing process overall. When trying to unmix lunar spectra many factors have to be considered to obtain reliable results. A non-probabilistic approach needs to make many assumptions about the composition and the maturity of the surface to obtain plausible results. Even if these assumptions are accurate only a single best

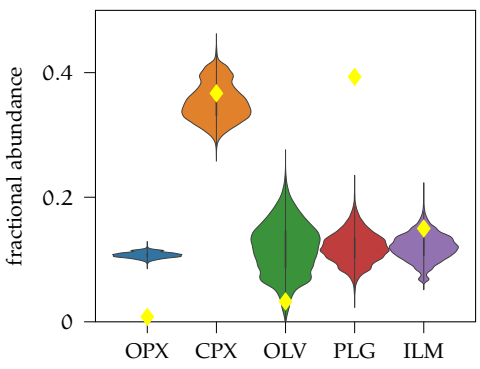

(a) Endmember abundances (10084)

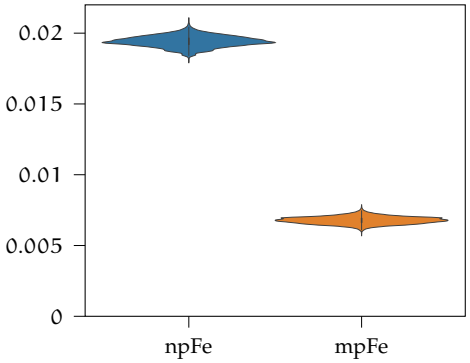

(b) smFe abundances (10084)

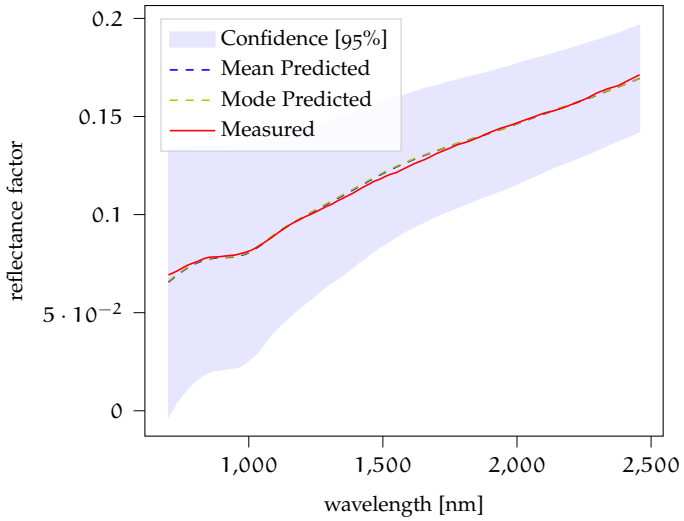

(c) Confidence plot (10084)

Figure 5.61: Results for LSCC sample 10084 with Ti/Al prior. Yellow diamonds mark the estimated theoretical mineral fractional abundances. Plagioclase is underestimated, while olivine is generally overestimated. This is a mature spectrum with an I_s/FeO value of 88, therefore, also the estimated $npFe^0$ and $mpFe^0$ abundance is high. The spectrum is generally very dark.

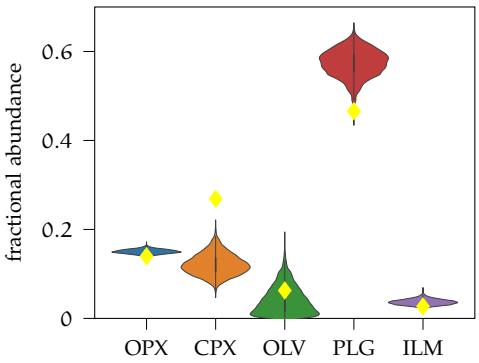

(a) Endmember abundances (14260)

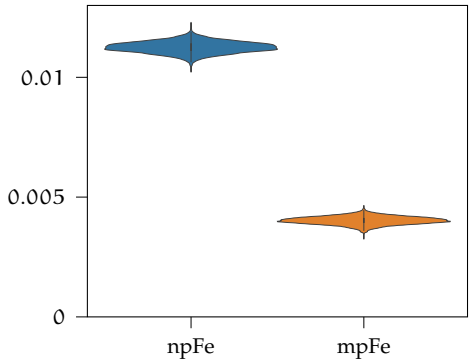

(b) smFe abundances (14260)

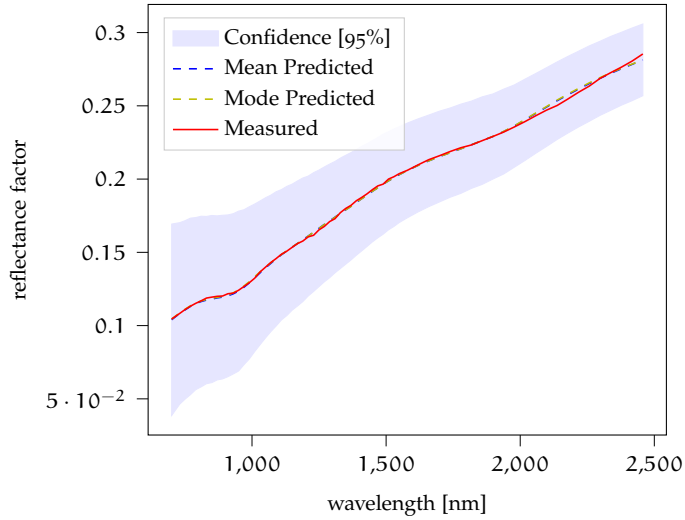

(c) Confidence plot (14260)

Figure 5.62: Results for LSCC sample 14260 with Ti/Al prior. This mature mare spectrum (I_s/FeO=93.3) can be well characterized. Yellow diamonds mark the estimated theoretical mineral fractional abundances. Except for a small difference in theoretical and predicted clinopyroxene abundance, the fit is good.

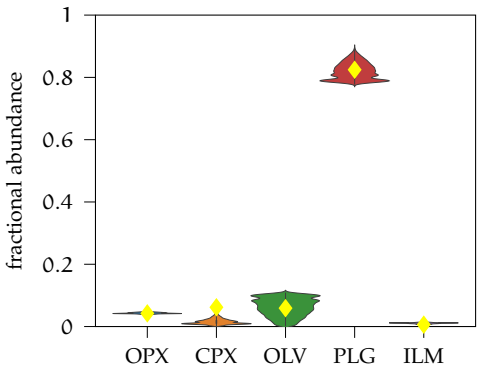

(a) Endmember abundances (62231)

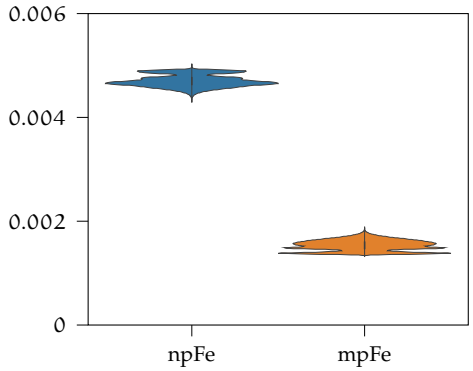

(b) smFe abundances (62231)

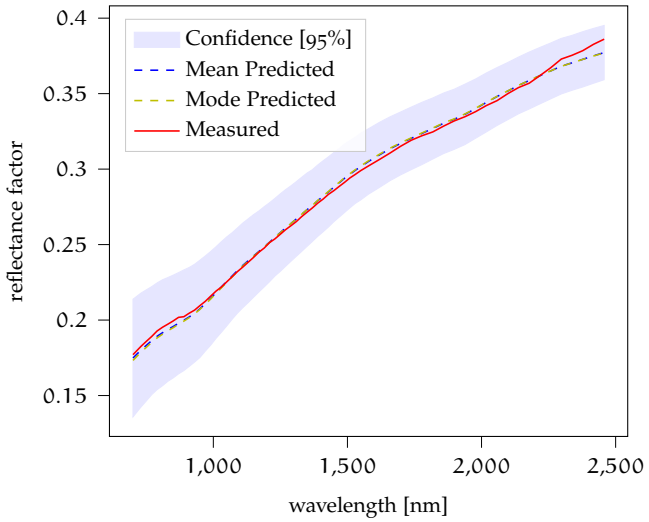

(c) smFe abundances (62231)

Figure 5.63: Results for LSCC sample 62231 with Ti/Al prior. This LSCC sample is a mature (I_s/FeO=116.7) highland spectrum. There are almost no absorption bands visible. Yellow diamonds mark the true mineral fractional abundances. The mean predicted values are close to the theoretical mineral abundances.

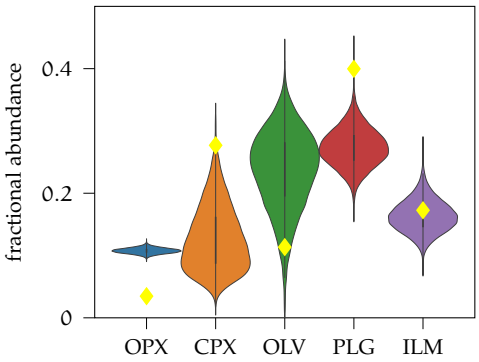

(a) With Ti/Al prior; Sample 79221; Minerals

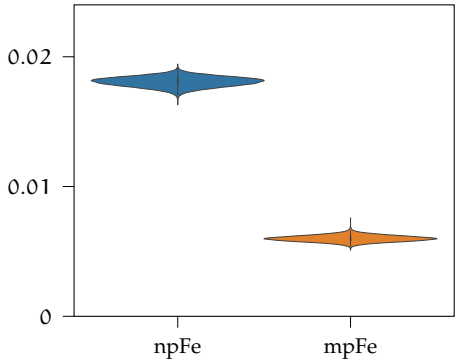

(b) With Ti/Al prior; Sample 79221; smFe

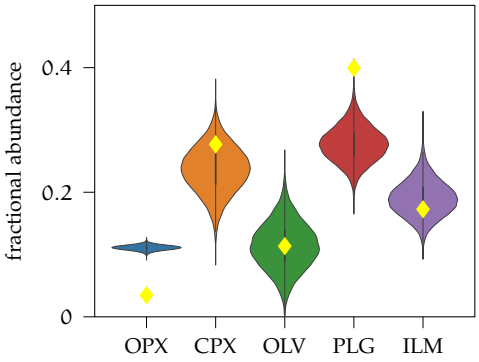

(c) With 'all' prior; Sample 79221; Minerals

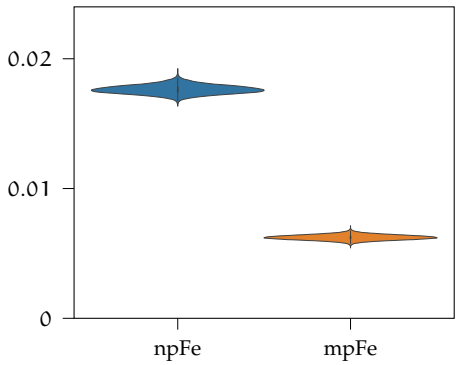

(d) With 'all' prior; Sample 79221; smFe

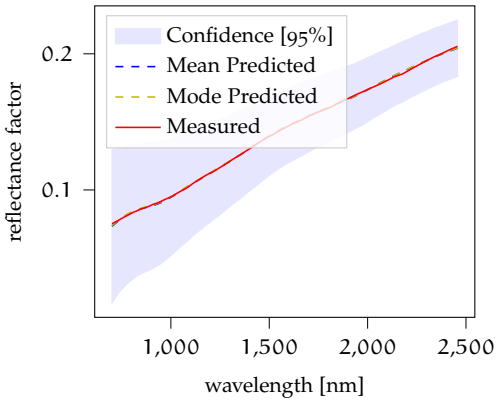

(e) Confidence Ti/Al prior (79221)

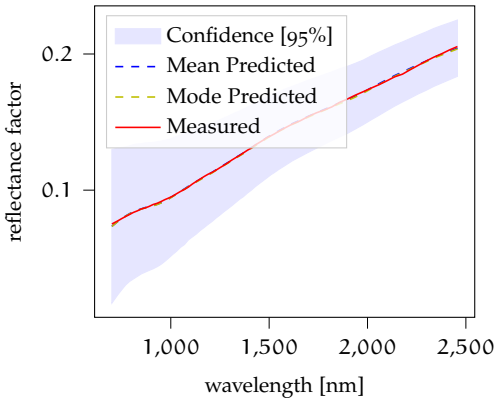

(f) Confidence all elements prior (79221)

Figure 5.64: Results for LSCC sample 79221 both with the prior on TiO_2 and Al_2O_3 abundance and a prior on all relevant elements. Including prior information about the other elements as well can help in mitigating uncertainties between clinopyroxene and olivine. This is also a mature mare spectrum with an I_s/FeO value of 91.0. Yellow diamonds mark the theoretical mineral fractional abundances.

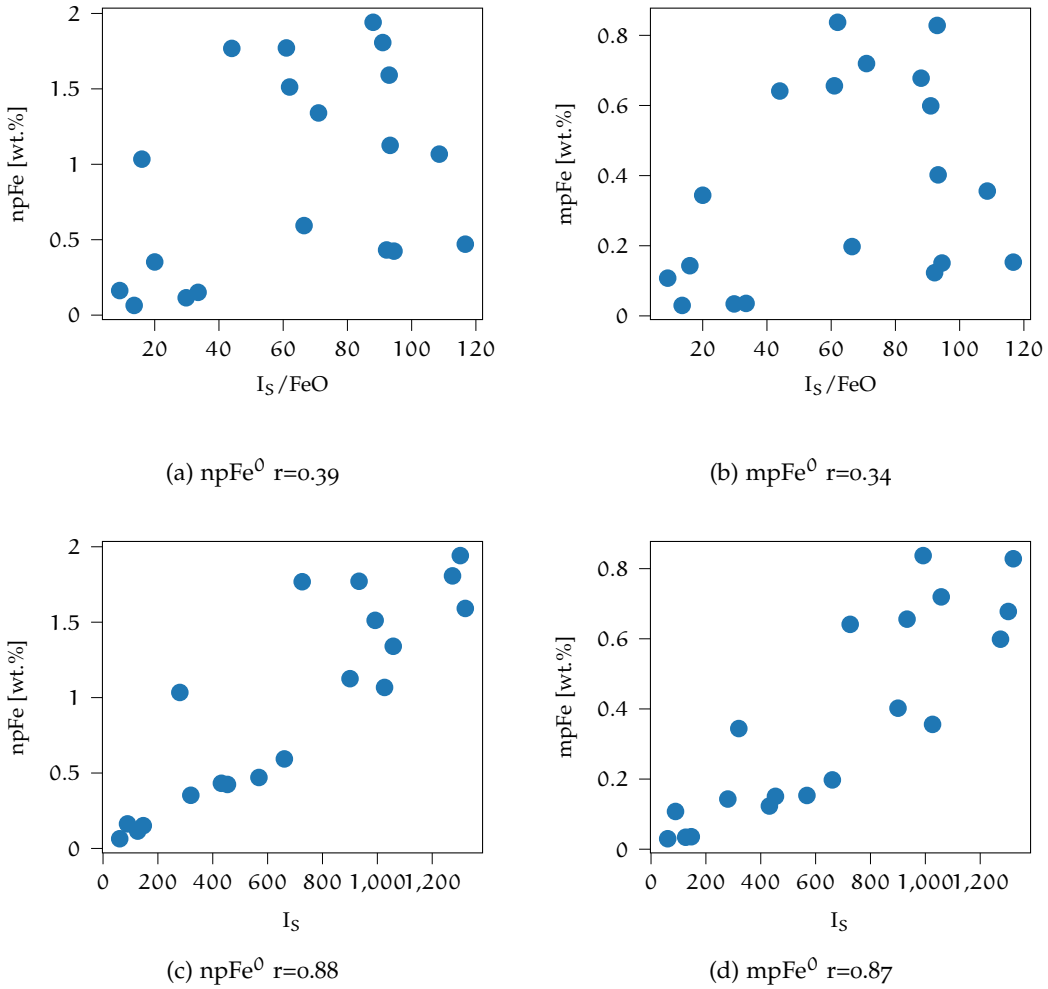

(a) $npFe^0$ r=0.39

(b) $mpFe^0$ r=0.34

(c) $npFe^0$ r=0.88

(d) $mpFe^0$ r=0.87

Figure 5.65: Relationship of $npFe^0$ and $mpFe^0$ abundance to the I_s/FeO maturity parameter and the ferromagnetic resonance (FMR) I_s. The FMR parameter is sensitive to small iron particles in the size range between about 4nm and 33nm (Housley et al., 1976). The correlation between $npFe^0$ and I_s is clearly visible as well as for the larger $mpFe^0$ particles.

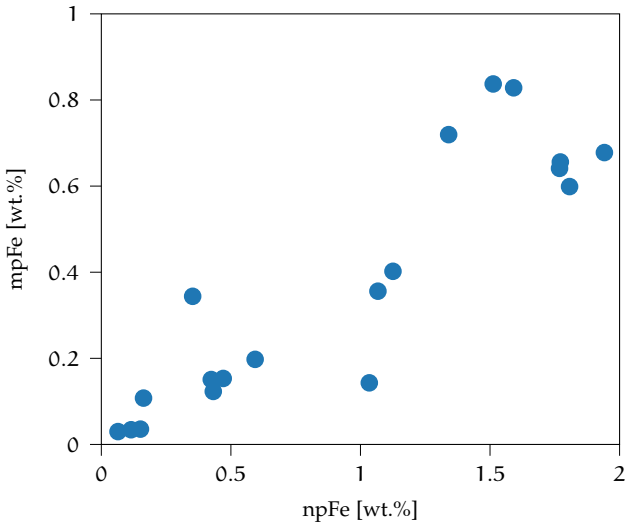

Figure 5.66: The correlation between the mean predicted $npFe^0$ and $mpFe^0$ abundance is r=0.90. Therefore, with increasing $npFe^0$ abundance typically also the $mpFe^0$ abundance increases. The factor $\frac{npFe}{mpFe}$ approximately amounts to 2.

fit solution is obtained. All experiments shown in this work illustrate that there is no unique solution and that a variety of combinations can produce similar results, and, thus a number of different interpretations are possible.

The synthetic mixtures in Section 5.3.4.1 were used to estimate the influence of the darkening agents on the overall uncertainties of the mineral abundances. The results showed that with increasing smFe abundance the uncertainties increased. Ilmenite or TiO_2 also contributed to uncertainties in the data, but there appears to be no direct relationship between true ilmenite abundance and uncertainties. However, introducing prior knowledge about the TiO_2 and Al_2O_3 abundance can significantly reduce the uncertainties of all mineral abundances as well as the errors between mean predicted and true mineral abundances and is, therefore, suitable for the application of the approach to real lunar spectra. For very mature spectra the uncertainties become very large. This illustrates the need for a probabilistic approach to the problem of unmixing spectra for mineral and smFe particle abundances. The abundance of the smFe particles could, however, still be reliably detected for any maturity level. The uncertainties of the minerals all increased with increasing smFe concentration, except for ilmenite. This might be explained by the fact that ilmenite with its featureless spectrum is already difficult to determine accurately if the absolute brightness of the sample is not well defined. Ilmenite, therefore, is not easily distinguished by any absorption bands, which become more difficult to quantify with increasing maturity.

Ambiguities between spectrally similar endmembers like plagioclase, pargasite, and ilmenite in Section 5.3.4.2 can lead to larger errors (up to 57 wt.%) in the best fit solution of the Hapke model and the measured spectra. When these ambiguities are mitigated with using prior information, the errors are usually well below 15 wt.%. All models have to include some simplifications such that they cannot perfectly represent reality. These problems inherent to the mixing model itself usually cannot be predicted by the MCMC sampler. Ambiguities and uncertainties due to the choice of model parameters

on the other hand can be quantified and may indicate problems with the choice of endmembers and/or assumptions made about the data. In some cases where plagioclase and pargasite were confused, two local minima far apart from each other in parameter space were not found by the sampler, even though the mean σ of the confidence plots is very similar. Generally, the fresh laboratory spectra could easily be distinguished as such. The abundance of smFe is predicted to be small or absent.

The final experiment of unmixing the LSCC spectra with RELAB mineral endmembers demonstrated that this approach can be applied to the lunar surface. When the abundance of agglutinitic glasses is high, olivine and plagioclase abundances tend to be poorly defined. The reconstruction is very accurate, but the uncertainties of the mineral abundances are high for mature spectra. This shows that classical optimization techniques are prone to fail on the task of unmixing the spectra with accurate abundances. The abundances of the smFe particles are, however, well defined. The results align with the findings of Trang and Lucey (2019) that the npFe and mpFe abundance for mature spectra depends on the FeO abundance. Furthermore, the predicted abundance of npFe and mpFe particles correlates well with the I_s parameter of the LSCC samples. For npFe, this can be interpreted to be a sign that the algorithm predicts plausible results. The npFe and mpFe abundances are also strongly correlated, such that the correlation of mpFe might be attributed to this nearly constant factor. According to Lucey and Riner (2011) mpFe sized particles are not present in the samples investigated, but the larger particle size is necessary to model the effects of space weathering. Wohlfarth et al. (2019) further suggested that clusters or layers of npFe particles that effectively act as a larger mpFe particle are responsible for the darkening. This effect can also be simulated with light scattering theory as in Arnaut et al. (2021).This would suggest that npFe and mpFe (or clusters of npFe) are both created by the same processes. The cluster/layer theory is consistent with the results of the LSCC unmixing.

5.4 UNMIXING FROM REFRACTIVE INDICES

Including the grain size as a parameter in addition to the space weathering particles was first tested by Julia Slatosch in her Master's thesis (Slatosch, 2023), which was supervised by the author. The implementation of the calculation of albedo from grain size and refractive indices (Lucey, 2002) from Slatosch (2023) is used in this section.

The samples used in Section 5.3 all represent very similar grain size distributions. Instead, the focus was mineral darkening agents and space weathering. However, the grain size (D) strongly influences the brightness and depth of the absorption bands (see Section 3.1.6). To account for this factor, we need to adjust the model. Firstly, we need to obtain the complex indices of refraction of the endmember samples. This process is explained in Section 5.4.1. Secondly, the probabilistic model needs to be adapted to include the grain size (see Section 5.4.2). Thirdly, the adapted model is applied to the same synthetic mixtures as in Section 5.3.4.1 to estimate how much the uncertainties increase if the grain size is added as a parameter (see Section 5.4.3). Finally, the implications for the application of the unmixing to remote sensing data of the lunar surface are reviewed (see Section 5.4.4).

5.4.1 *Refractive Indices Calculation*

To obtain refractive indices, we use the model of Lucey (1998) based on the (Hapke, 1981) model to obtain n and k for a reflectance spectrum with a given grain size. The reflectance is converted to albedo using the definitions of the Hapke model (Hapke, 2012b) and standard parameters as in the previous sections. The real part of the refractive index (n) for typical lunar minerals is almost constant within the VIS-NIR wavelength range (Hapke and Wells, 1981). Lucey (1998) defined the real indices of refraction for ortho-, clinopyroxenes, and olivine depending on the Mg# of the sample as follows:

$$\begin{aligned} n_{opx} &= 1.768 - 0.118(\text{Mg\#}) \\ n_{cpx} &= 1.762 - 0.082(\text{Mg\#}) \\ n_{olv} &= 1.827 - 0.192(\text{Mg\#}) \end{aligned} \tag{64}$$

The real refractive index of plagioclase is significantly smaller than that of pyroxenes and olivine. It varies between 1.526 for albite and 1.59 for anorthite (e.g., Lyne et al., 2013). We set $n_{plg} \approx 1.53$ because of our samples relatively high sodium content (PP-EAC-029: Na_2O 5.15 wt.%).

No perfectly fitting data for the visible and NIR could be found for ilmenite. The National Gem Lab from India lists the refractive index of ilmenite as $n_{ilm} \approx 2.4$ (`https://nationalgemlab.in/ilmenite/`, accessed on: March 1, 2023). This is in agreement with data from Zhang et al. (2015), where in the visible wavelength range (approx. 2.5 eV photon energy), n is approximately 2.4, according to Figure 7 therein. Roush et al. (2021) find an average value of approx. 2.35 across the VIS-NIR wavelength range and different results from the literature for magnetite, which is opaque, similar to ilmenite. Thus, we use $n_{ilm} \approx 2.4$ as the average real refractive index of refraction for ilmenite throughout this work.

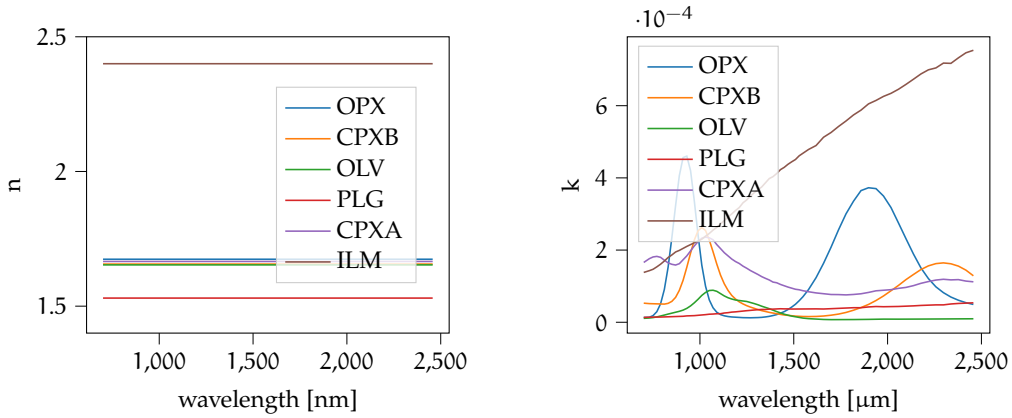

(a) n (b) k

Figure 5.67: Real refractive indices (a) for the endmembers and their respective Mg# numbers calculated based on the elemental abundances listed in Table 5.7. Ilmenite and plagioclase endmembers are set to fixed values from the literature. The imaginary coefficients (b) of the index of refraction for the endmembers. The indices are calculated according to the model from Lucey (1998).

The values for all endmembers used in the previous sections are displayed in Figure 5.67a. These are set to constants over the entire wavelength range because we cannot reliably determine the wavelength-dependent n and k from a single albedo spectrum with a given grain size. Subsequently, we vary k to find the ideal combination of n and k to fit the albedo according to Equation 35 and the albedo spectrum of the endmembers. The resulting imaginary indices of refraction k are displayed in Figure 5.67b.

5.4.2 *Model modifications*

A few changes were made to the models in order to implement the unmixing considering grain sizes. The inputs of the physical model are now the n and k of the endmembers instead of the albedo, and the grain size is added as a parameter.

Instead of the pymc3 (Salvatier et al., 2016) framework used in the previous experiments, the functions are now updated to pymc5 (Oriol et al., 2023), which uses PyTensor instead of Theano for tensor operations and automatic differentiation. PyTensor is a fork of Aesara, which is also based on Theano.

Generally, the probabilistic model described in Sections 5.3.2 and 5.3.3 remains almost unchanged. The likelihood is still evaluated for both the spectrum and the continuum removed spectrum. The priors are defined for the elemental abundances, the sum of the endmember weights, the mineral and iron endmember weights, and the likelihood variance. Additionally, we define a prior on the grain size as follows:

$$p(D) \sim \text{LogNormal}\,(D \mid \mu = \log(25), \sigma = 0.3) \tag{65}$$

The resulting PDF is shown in Figure 5.68. The mode is at $e^{\log(25)-0.3^2} \approx 22.85$ µm, and the effective standard deviation is approximately 7.95. The size fraction of the original endmembers used in these experiments is 0-45 µm, so the mode lies in the middle of that range. While this is an appropriate prior for the spectra investigated here, it should

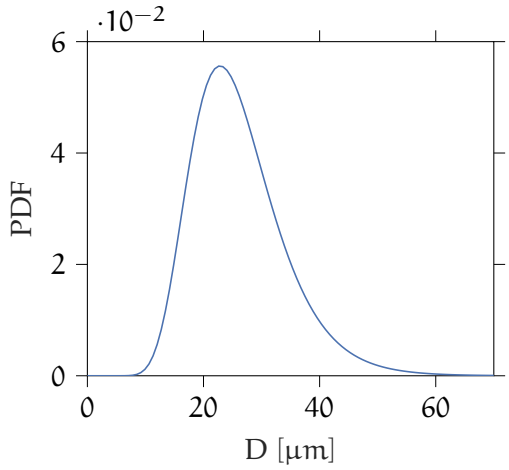

Figure 5.68: Prior distribution for the average grain size according to Equation 65.

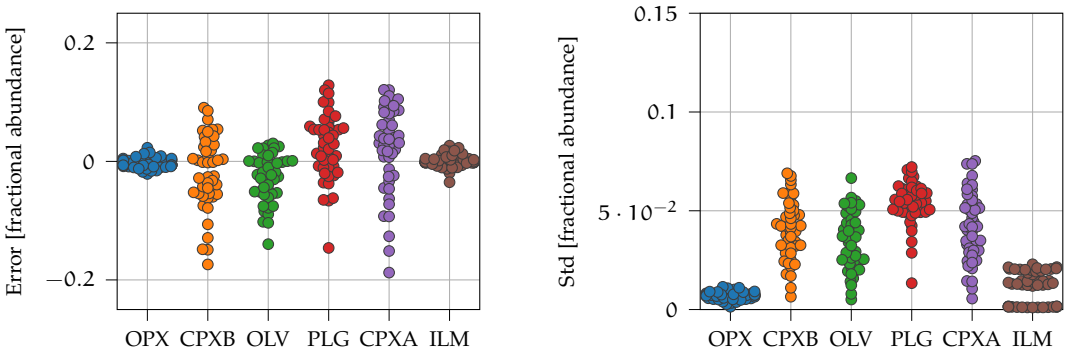

(a) Errors

(b) Uncertainties

Figure 5.69: Errors ((a), the difference between mean predicted and theoretical fractional abundance) and uncertainties ((b), in standard deviation) from the unmixing, including the grain size as a parameter. We used a prior on the TiO_2 and Al_2O_3 abundance in the unmixing. Compare Figure 5.50b and Figure 5.51b.

be noted that the prior needs to be adapted in order to be suitable for remotely sensed lunar spectra. The mean grain size of most lunar soils is in the range between 45-100 µm (McKay et al., 1991). Therefore, the prior should represent the highest density in that interval in the future.

5.4.3 *Results and Discussion*

To be able to separate the influence of the grain size on the overall uncertainties, we used a similar setup as in Section 5.3.4.1. Using the same mineral and iron abundances and a common grain size of 32 µm, we generated the spectra according to the forward mixing model starting from the refractive indices (see Section 5.4.1). The grain size is chosen to be different from the mode of the prior. As a prior, the elemental abundances of TiO_2 and Al_2O_3 are used according to the definitions in Table 5.6 for Ti/Al.

Table 5.10: Comparison of the average uncertainties in standard deviation and the average errors for the model without the grain size (D) as a parameter and the model with the grain size as a parameter. The theoretical npFe values vary between 0 wt.% and 2.2 wt.% and for mpFe particles between 0 wt.% and 1.2 wt.%.

	Average Uncertainty [wt.%]		Average Error [wt.%]	
Mineral	Without D	With D	Without D	With D
OPX	0.43	0.70	0.70	0.74
CPXB	2.05	4.01	1.75	4.91
OLV	3.75	3.48	4.64	3.54
PLG	2.92	5.41	4.05	4.72
CPXA	4.44	4.18	5.31	6.41
ILM	1.22	1.17	0.59	0.70
npFe	0.024	0.130	0.028	0.166
mpFe	0.016	0.084	0.032	0.069

The detailed results of the unmixing are listed in the Appendix (see Tables B.20 -B.25). Figure 5.69 shows the errors and uncertainties in the standard deviation of the mineral abundances. Generally, the trends are very similar to the results without grain size (compare Figure 5.50b and Figure 5.51b). The errors are all, except one, below 10 wt.% and mostly below 5 wt.%. The higher the maturity and the higher the ilmenite abundance, the higher the uncertainties and errors. The uncertainties of CPXB and PLG have visibly increased. Table 5.10 directly compares the average uncertainties and errors between the unmixing without grain size and with grain size. Again, the table illustrates that the PLG and CPXB uncertainties and errors have increased significantly, while most of the other mineral endmembers show comparable values. Table 5.10 also lists the uncertainties and errors for npFe and mpFe abundance. While the uncertainties remain low compared to the absolute wt.% of npFe and mpFe, the uncertainties have increased fivefold when including the grain size as a parameter.

Figure 5.70 shows the correlation matrix of the samples in the chain for all material parameters for the mixture with the highest maturity and ilmenite abundance. This correlation matrix highlights the likely reason for the significantly increased uncertainty of the submicroscopic iron particle abundances. The solutions considered acceptable by the sampler show extremely correlated npFe and mpFe abundance with the grain size. The higher the grain size, the smaller the npFe and mpFe abundance. The spectral effects of grain size and iron are very similar, such that the parameters become interchangeable.

5.4.4 *Conclusion*

The uncertainties remain manageable for the well-constrained setting displayed in this section, but the increased uncertainty is still not negligible. Consequently, for the practical application of the unmixing to the lunar surface, good prior knowledge about the

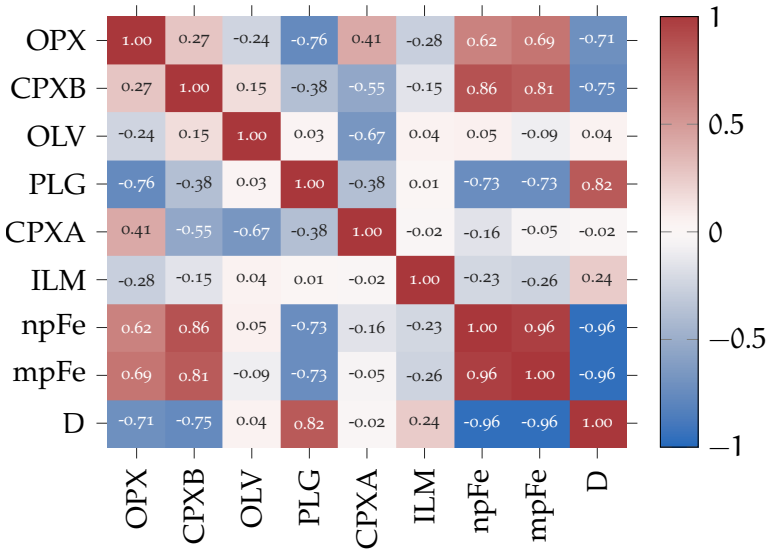

Figure 5.70: Correlation matrix of the samples in the chain for mix_{47} with the highest abundance of smFe and ilmenite. The grain size D and the npFe and mpFe abundance are extremely correlated.

spectra is necessary to effectively constrain the problem and still obtain informative results. However, the results also illustrated the importance of grain size on the spectra. The small size fraction endmembers used throughout this work need to be adapted to the realistic lunar spectra by increasing the grain size.

5.5 APPLICATION SCENARIO: UNMIXING OF M^3 DATA

The unmixing of the LSCC spectra produced promising results. The next logical step is to apply the procedure to remote sensing data. The publicly available data set with the highest spectral and spatial resolution in the VIS-NIR in the M^3 data. The following global maps of the major minerals and space weathering components are produced based on the photometrically and thermally normalized global mosaic at 20 pixels/degree (Wöhler et al., 2017b). The same normalization framework (Wöhler et al., 2017b) is used to create a reflectance map of the Reiner Gamma swirl, and subsequently, the unmixing framework is applied. However, a few modifications are needed to tailor the Bayesian unmixing approach to M^3 data.

In the M^3 data, the reflectance factor is significantly lower in comparison to other data sets. Wu and Hapke (2018) found that the reflectance factor is approximately half compared to the LSCC spectra or about 2/3 compared to the Spectral Profiler onboard the SELENE spacecraft or the LRO WAC in the VIS range. To account for this systematic difference, we assume that the sum of all endmember weights is close to 0.6 instead of 1.0. Such that the prior (compare Equation 57) becomes:

$$p(\sum \vec{\theta}_{em}) \sim \mathcal{N}(\sum \vec{\theta}_{em} \mid \mu = 0.6, \sigma_{sum}). \tag{66}$$

To reduce coupling with other parameters, we set the standard deviation to a comparatively small value of $\sigma_{sum} = 0.01$.

We use the same endmembers as in Sections 5.3.4.1, 5.3.4.3 and 5.4, namely an orthopyroxene, the two types of clinopyroxene A and B, olivine, plagioclase, and ilmenite. Glasses and spinels, for example, are not included to keep the number of endmembers to a minimum. We use the new framework introduced in Section 5.4 such that the unmixing utilizes the refractive indices of the endmembers instead of the albedo and is based on the pymc5 framework. As established in Section 5.4, the grain size and the space weathering components are strongly correlated. Consequently, we set the grain size to a fixed value. After several experiments with different grain sizes the most promising results were obtained for an average grain size of 100 µm, which is the maximum of the most common average grain sizes described by McKay et al. (1991).

The 20 pixels/degree global map contains almost 26 million spectra, and the M^3 mosaic of the Reiner Gamma region also includes almost 4.5 million spectra. Consequently, applying the MCMC sampler to all individual spectra is close to impossible. Thus, we use Gaussian Mixture Models (GMMs) (e.g., Bishop, 2006) to cluster the data similarly to Arnaut et al. (2020). We set the number of clusters to 64, which is sufficient to capture the variations in the data. The unmixing is then applied to each of the 64 centroids. One advantage of GMMs is that there is no hard assignment to the clusters, but all spectra have a certain probability of belonging to each cluster. Furthermore, by matrix multiplication of the probability matrix (Nx64 for N spectra and 64 clusters; each row sums up to one) and the matrix of the fractional abundances of each cluster centroid (64x6 for the six mineral endmembers or 64x2 for the iron endmembers), we obtain the fractional abundances weighted by the probability of each cluster (Nx6 or Nx2 for minerals and iron particles, respectively).

Based on these centroids of the clusters, we estimate the priors elemental abundances using the polynomial regression of Bhatt et al. (2015). From this, we obtain Fe, Mg, Ti,

and Al abundances, and subsequently, the oxide (FeO, MgO, TiO_2, and Al_2O_3) abundances by applying the appropriate conversion factors. We set the priors for the elemental abundances α_{elem} to 40 for TiO_2 and 20 for FeO, MgO, and Al_2O_3.

5.5.1 *Global Maps*

It is challenging to create mineral maps of the Moon. Consequently, there is no ground truth available that we can use to verify our results. The most commonly used data are the mineral maps published by Lemelin et al. (2016) and Lemelin et al. (2019) based on Kaguya MI data. However, the MI instrument only has nine spectral channels between 415 and 1550 nm, so it cannot capture the 2 µm absorption band. Nonetheless, the maps seem mostly very plausible. For example, the predictions of the model at the 19 LSCC sample sites agree well with the LSCC data, if just the four endmembers (olivine, plagioclase, ortho-, and clinopyroxene) are considered (Lemelin et al., 2019). Therefore, we will use these data as a reference for basic sanity checks. Figure 5.71 shows the M^3 reflectance and the main geological features discussed in this section.

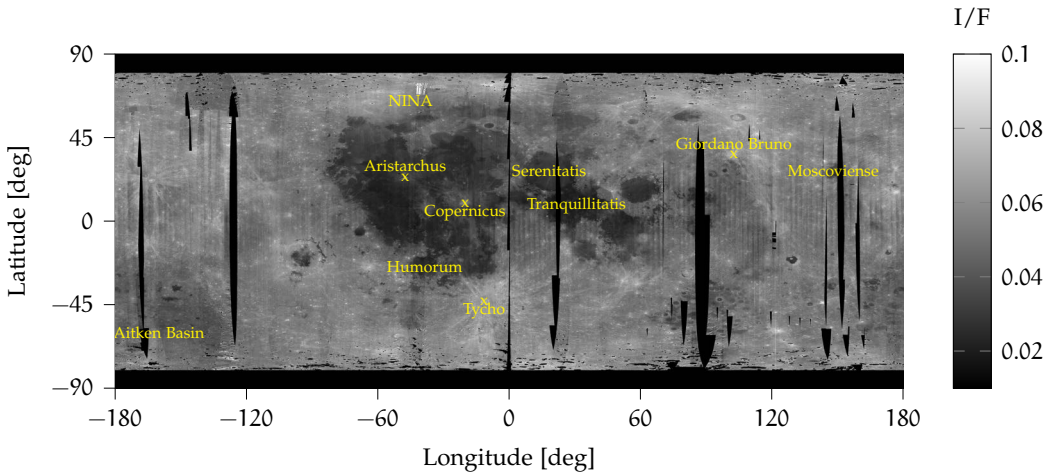

Figure 5.71: M^3 global reflectance at 1578 nm at 20 pixels/degree. Important features are labeled in yellow. NINA refers to the northern imbrium noritic anomaly (Isaacson and Pieters, 2009). Aristarchus, Tycho, Copernicus, and Giordano Bruno are craters and are marked with an x. Serenitatis, Tranquillitatis, and Moscoviense are mare and the name is written in the center.

Figure 5.72a displays the mean predicted plagioclase abundance of the lunar surface. In the highlands, the abundance is approximately 75-85 wt.%, which is about 5-10% lower than would be expected, according to (Lemelin et al., 2016). The remaining fraction is mainly olivine (approx. 8 wt.%) and smaller fractions of ortho- and clinopyroxene (see Figure C.3). Olivine exhibits a secondary absorption feature at approximately 1.25 µm, and CPXA shows an absorption band at 1.15 µm. Plagioclase generally has a very flat spectrum, but there is a broad absorption band centered at 1.3 µm. In the unmixing, we did not include glasses, which lead to a broadening of the absorption bands (e.g., Denevi et al., 2021) and a flattening of the 2-µm absorption band (e.g., Tompkins and Pieters, 2010). Therefore, the unmixing predicts a combination of plagioclase, olivine, and clinopyroxene type A for the highland spectra. Suppose the plagioclase absorp-

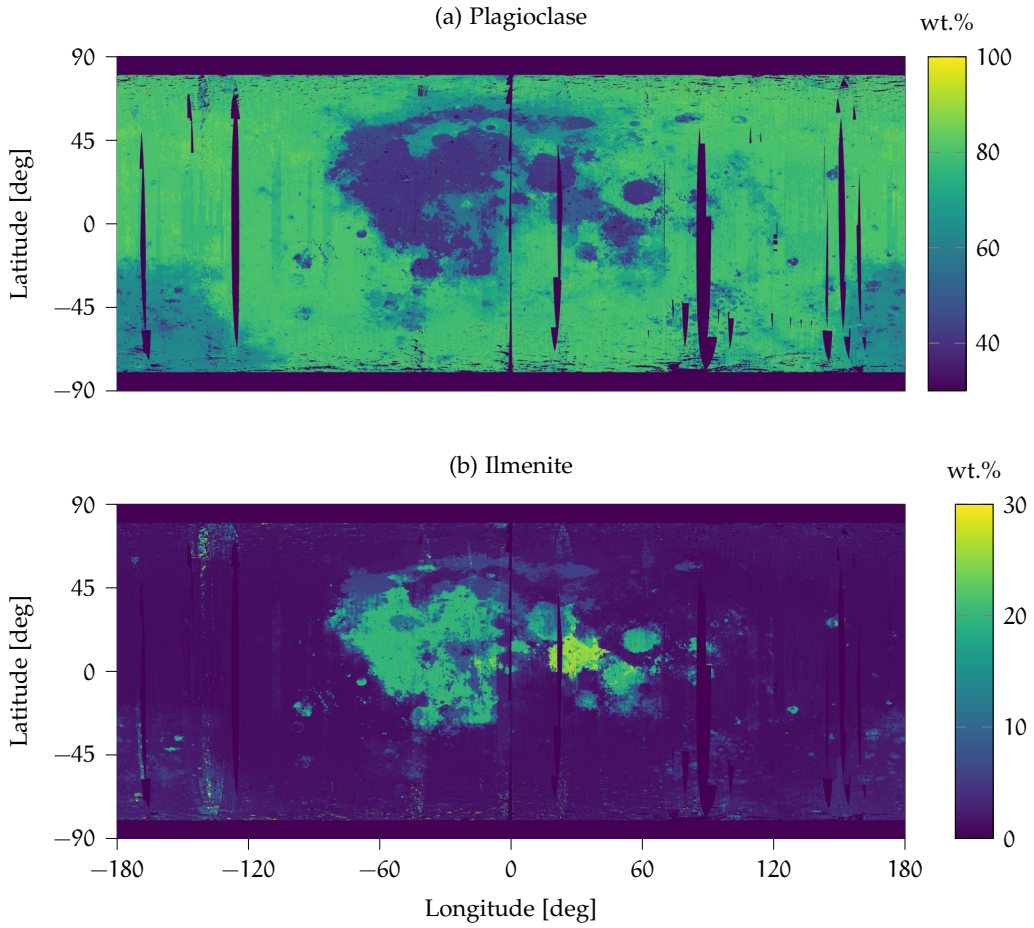

Figure 5.72: Global maps of the mineral (a) plagioclase and (b) ilmenite in wt.%. The resolution is 20 pixels/degree and 64 cluster centroids were used for the unmixing.

tion band becomes even broader through the influence of agglutinates. In that case, it stretches to 1.15 µm, so a certain amount of CPXA and OLV is necessary to match the measured spectrum.

Furthermore, the abundances of plagioclase, olivine, and clinopyroxene type A are strongly correlated for the highland cluster with the largest number of members (cluster 59, refer to Figure C.1 for pixel locations belonging to that cluster, and Figure C.2 for the posterior distribution of the endember abundances). Figure 5.73 shows the correlation matrix for the centroid of that cluster. The abundances of PLG and CPXA are strongly correlated ($r = -0.68$), and the CPXA and OLV abundances are interchangeable to a certain extent ($r = -0.84$). This illustrates that for reproducing the typical highland spectrum, some combination of plagioclase, olivine, and clinopyroxene is necessary.

In the maria, the predicted plagioclase abundance varies between 30 and 60 wt.%. Noticeably, the south pole Aitken basin exhibits an intermediate value between highland and mare composition with about 60-70 wt.%. While in the highlands the olivine abundance is overestimated compared to Lemelin et al. (2016), in the mare, the olivine abundance is likely underestimated (see Figure C.3). In the maria the unmixing predicts abundances of olivine around 2 wt.%, except for the Mare Frigolis, the northern Imbrium noritic anomaly and Mare Serenitatis, where it is around 4-5 wt.%. The northern

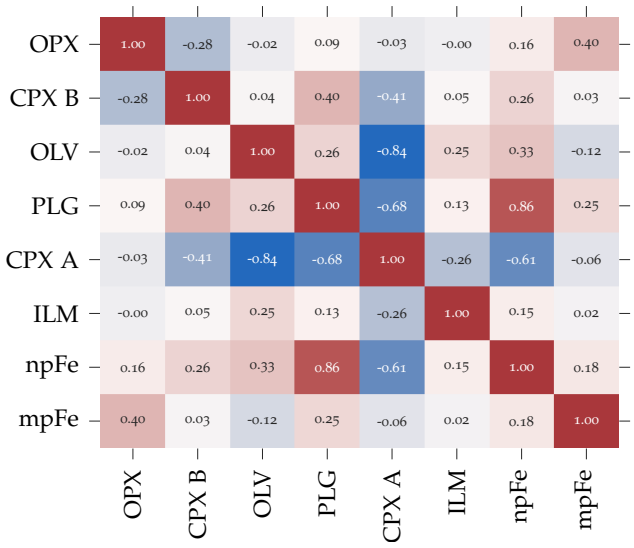

Figure 5.73: Correlation matrix showing the correlations of the samples in the Markov Chain for a typical highland spectrum.

Imbrium noritic anomaly, which was found to be more mafic compared to the other lunar highlands (Isaacson and Pieters, 2009), is also predicted by the unmixing to contain higher orthopyroxene and clinopyroxene abundances.

Figure 5.72b displays the mean predicted fractional abundance of ilmenite. The overall structure closely follows the prior of the TiO_2 abundance, because ilmenite is the major carrier of TiO_2 on the Moon (Papike et al., 1991). Generally, the predicted ilmenite abundance is between 10-20 wt.% in the maria. In Mare Tranquillitatis and the dark mantle deposits in Sinus Aestuum (east of Copernicus crater), the abundance exceeds 20 wt.% and reaches almost 30 wt.%. Previous studies have not predicted values significantly above 20 % (e.g., Sato et al., 2017). In contrast, large parts of the Mare Tranquillitatis seem to contain significantly less clinopyroxene compared to the other maria (see Figure C.3), which is mainly replaced with ilmenite. The ilmenite abundance is near zero in the highlands and in the south pole Aitken basin. The pyroclastic deposit northwest of the Aristarchus crater contains significantly less ilmenite compared to the western Oceanus Procellarum, but not as little as the highlands. This is consistent with previous work that found the Aristarchus Plateau to be deprived of TiO_2 but exhibiting high concentrations of glasses (e.g., Wilcox et al., 2006).

Figure 5.74a shows the npFe abundance predicted by the unmixing. Inside the maria, the Copernicus crater and the Kepler crater west of Copernicus appear to be much less space-weathered, and the rays from the craters are clearly visible. Furthermore, the Aristarchus crater is predicted to be immature as it is very bright. The npFe abundance is correlated with the ilmenite abundance. For example, Mare Tranquillitatis shows the highest ilmenite and npFe abundance. Compared to Trang and Lucey (2019), the contrast between highland and mare is much more pronounced, but the fresh craters and the rays are visible in our results and the results of Trang and Lucey (2019).

The npFe abundance in the highlands is significantly smaller than the mare. Therefore, we adjusted the colormap for Figure 5.74c to cover the npFe range in the highlands. Here, the fresh craters with their respective ray structures are also visible. More detailed views

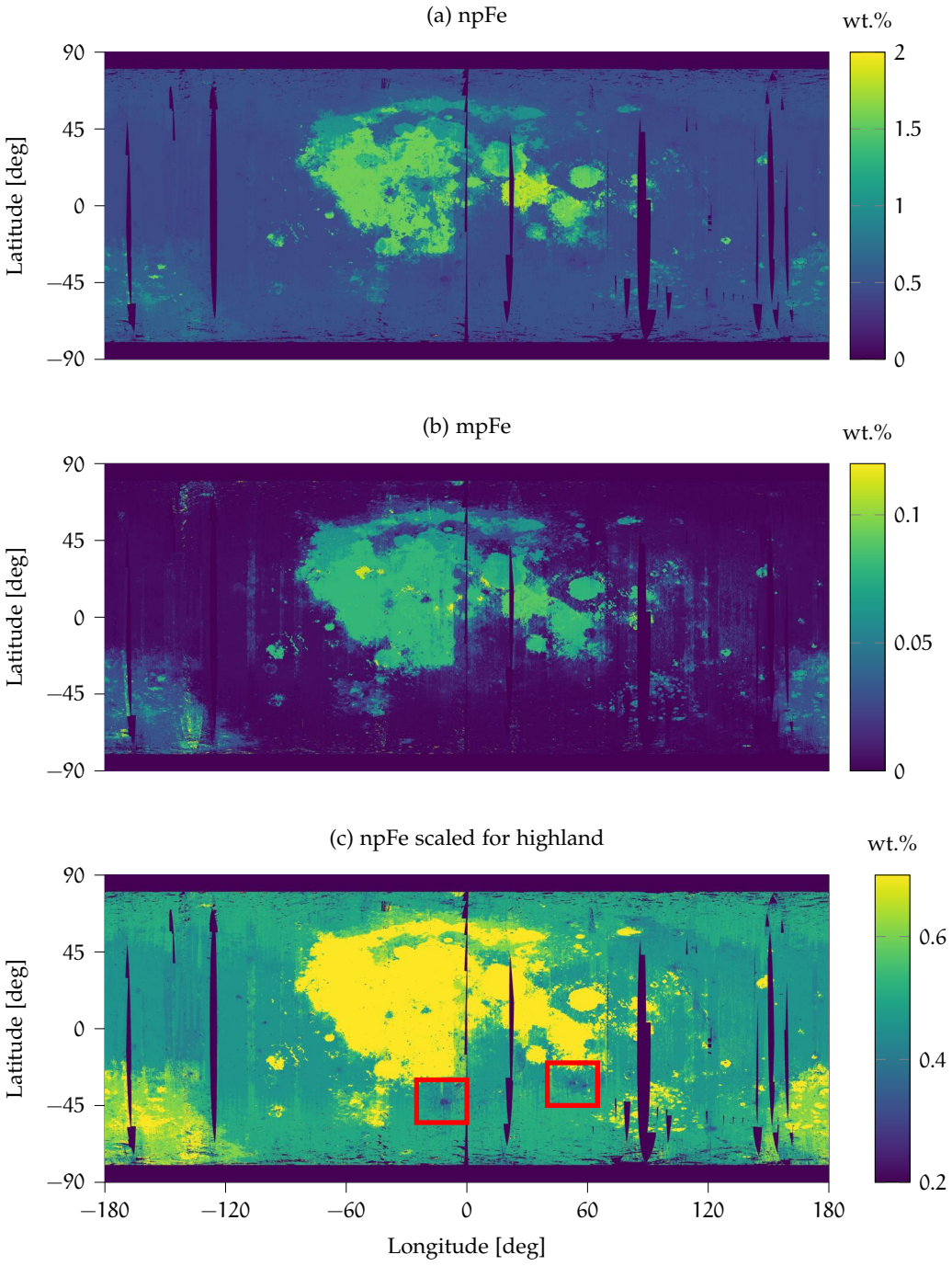

Figure 5.74: Global maps of the iron particles (a) npFe and (b) mpFe in wt.%. To better distinguish the variations in the highlands (c) shows the npFe abundance but scaled to the highland values. The resolution is 20 pixels/degree and 64 cluster centroids were used for the unmixing. The western red square marks Tycho crater and the eastern red square marks the Stevinus crater. A zoomed in version of these two craters are shown in Figure 5.75.

of Tycho and Stevinus craters are shown in Figure 5.75a and 5.75b, respectively. These images illustrate the crater rays that are visible in light blue, where some fresher material is spread across the surrounding highland. Additionally, the crater Giordano Bruno at

35.92 °N and 102.74 °E, one of the freshest craters on the Moon, shows very prominent rays stretching almost to the equator.

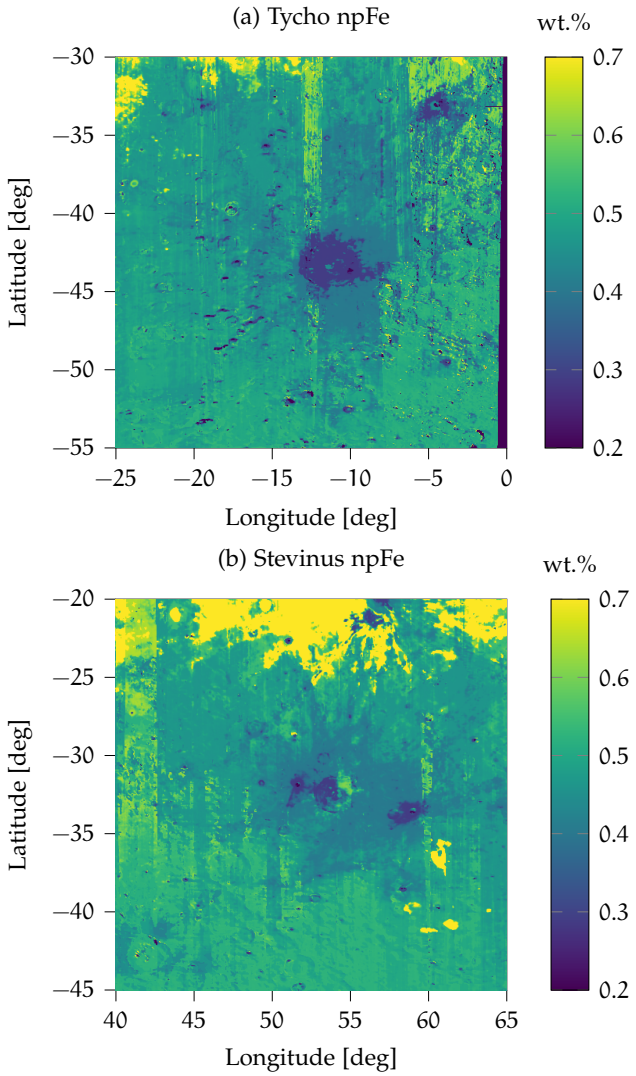

Figure 5.75: Zoomed in versions of the two crater Tycho and Stevinus from Figure 5.74c. The colors indicate the npFe abundance in wt.%.

The mpFe particles (see Figure 5.74b) are more evenly distributed in the mare areas and are predicted to be almost absent in large parts of the highlands. If we choose a smaller grain size for the soil (compared to the 100 µm used in this study), the absolute abundance of mpFe would increase. Furthermore, the pyroclastic deposits in Sinus Aestuum, the Aristarchus Plateau, Mare Serenitatis, and the Mare Humorum show significantly increased mpFe concentrations. In these pyroclastic deposits, various glasses are more abundant (e.g., Wilcox et al., 2006), which are not considered in the unmixing. Large parts of the smFe are found in the agglutinate glasses, so this might not be purely an effect because of the missing endmember but might represent actually more abundant mpFe.

Figure 5.76 shows the ratio between smFe (npFe+mpFe) abundance and the FeO content predicted by the regression from Bhatt et al. (2015) based on the centroid spectra.

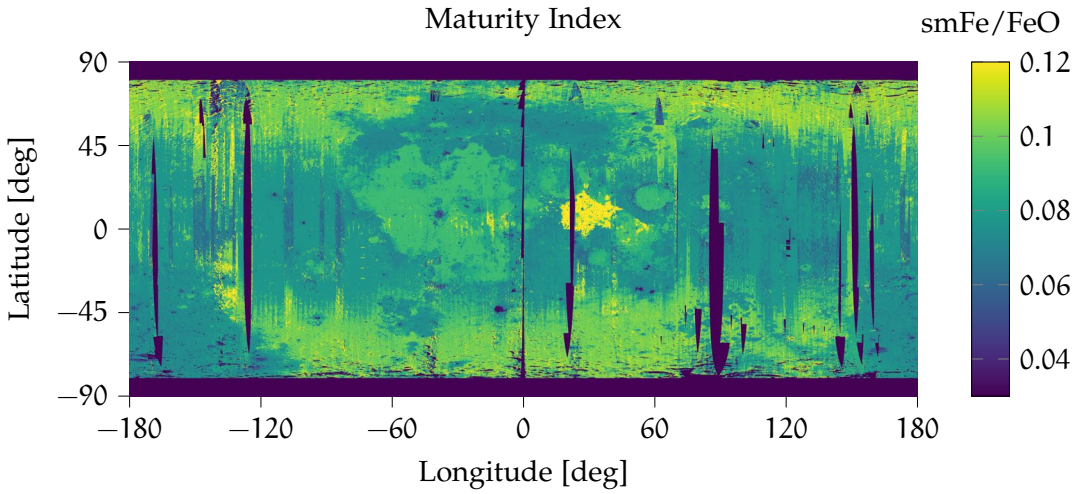

Figure 5.76: Map of the smFe/FeO ratio. The FeO abundance is derived from the centroids of the clusters with the method of Bhatt et al. (2015). The smFe abundance is the mean predicted abundance of npFe + mpFe from the unmixing. As it is physically plausible to assume that the smFe abundance is proportional to the FMR (I_S) the smFe/FeO ratio should be proportional to the maturity index I_S/FeO.

As shown in Section 5.3.4.3, the npFe and mpFe abundances are strongly correlated ($r = 0.88$ and $r = 0.87$, respectively) with the I_S value. Because the amount of smFe that can be created depends on the abundance of FeO, the FMR is usually normalized with FeO. Consequently, I_S/FeO is a reliable index for maturity, and because of the strong correlation of FMR with the smFe abundance, smFe/FeO is also a suitable measure of maturity. The missing difference between highland and mare in the smFe map of Trang and Lucey (2019) would lead to a substantial overestimation of the maturity of the highlands. It is unrealistic that the same amount of smFe is created by space weathering when only approximately 1/5 of Fe is available in the highlands compared to the mare (e.g., Bhatt et al., 2015). Figure 5.76 shows that the fresh craters are much less mature compared to the surrounding terrain. The mare being generally slightly more mature than the highlands might not be realistic and is in contrast to, e.g., Lemelin et al. (2016). The most representative highland cluster (compare Figure C.1) contains too little plagioclase. In the Markov chain the plagioclase abundance and npFe abundance are strongly correlated (see Figure 5.73). Consequently, the mean abundance of smFe with 0.4647 wt.% might be underestimated and assuming a normally distributed posterior distribution and the 2σ ($\approx$ 95 %) confidence interval 0.5241 smFe wt.% would still be a realistic value. Furthermore, the predicted FeO abundance for the centroid is 6.02 wt. %, but according to the global maps from Bhatt et al. (2015) the mean Fe abundance of the pixels belonging to that cluster is 4.14 wt.% so with the conversion to FeO (1.2865) the abundance is approximately 5.33 wt.% with a standard deviation of 2.44 wt.%. Assuming 5.33 wt.% FeO and 0.5241 smFe wt.% the smFe/FeO maturity index is approximately 0.98. This value would then be comparable to the most mature mare areas.

5.5.2 *Reiner Gamma*

We require more research to characterize the relative importance of the different processes contributing to the bright appearance of the Reiner Gamma swirl or swirls in general. Therefore, quantifying the degree of space weathering and the smFe abundance is essential. We apply the unmixing to the photometrically and thermally normalized M^3 data of Reiner Gamma (Grumpe et al., 2015; Hess et al., 2020a; Wöhler et al., 2017a,b; Wohlfarth et al., 2023). The TiO_2 abundance predicted with the method of Bhatt et al. (2015) varies strongly between on-swirl and off-swirl spectra. Similarly, Sato et al. (2017) predict Reiner Gamma to be deprived in TiO_2. Bhatt et al. (2015) trained a regression based on spectral features of M^3 data and Lunar Prospector elemental abundances. The absolute spectral slope of the continuum at 1-µm is highly correlated with the TiO_2 abundance, such that the regression also strongly relies on that measure. However, the absolute spectral slope is also sensitive to the albedo. Figure C.4 illustrates that the effects of grain size, smFe, and ilmenite on the absolute spectral slope are interchangeable. Sato et al. (2017) use the 321/415 nm ratio, which is independent of the albedo. However, in the UV wavelength range, maturity leads to the spectral slope becoming less red (more blue) (Hendrix et al., 2016). Ilmenite also leads to a flatter spectral slope (ratio values closer to one) making the TiO_2 estimate at Reiner Gamma less reliable (Sato et al., 2017). Furthermore, as discussed in Hess et al. (2020a) and previously Kramer et al. (2011), there is no known mechanism that could explain why the swirl should be deprived in ilmenite. A difference in maturity is much more likely. Consequently, we use an average value of 5 wt.% TiO_2 for the priors of the unmixing for all cluster centroids at Reiner Gamma.

Figure 5.77 displays the mean predicted abundances of npFe, mpFe, plagioclase, and ilmenite. The on-swirl locations are significantly deprived in npFe. The values are around 1.3 wt.% at the central oval, 1.5 wt.% at the tail, and above 2.2 wt.% for the majority of the mare background. The contrast between the swirl and the surroundings is larger than for the small bright craters scattered across the area, for which the npFe abundance is predicted to be about 1.7 wt.%. Similar to the results of Trang and Lucey (2019), the difference between mpFe on-swirl and off-swirl is less clear. For mpFe, the abundance difference to the background is more significant for the tail than for the central oval. Hess et al. (2020a) showed that the differences between the normalized spectral slope on-swirl and off-swirl are less pronounced in the tail region of Reiner Gamma. Therefore, the higher difference in mpFe and lower difference in npFe in the tail of Reiner Gamma could also be explained by a higher relative importance of regolith compaction (Hess et al., 2020a).

The unmixing predicts the swirl to be deprived in plagioclase and ilmenite. Intuitively, the reduced ilmenite abundance is an artifact because the bright spectra can be attributed to either the lack of smFe or ilmenite, which both darken the spectrum. In the central oval, the ilmenite abundance is predicted to be 16-17 wt.%, and in the background maria, it is around 19 wt.%. However, the predicted ilmenite abundances are even lower for the small bright craters ($\approx$ 12 wt.%) that is sometimes even below 10 wt.%. At the tail, the contrast between the background and swirl in ilmenite abundance and plagioclase abundance is almost invisible.

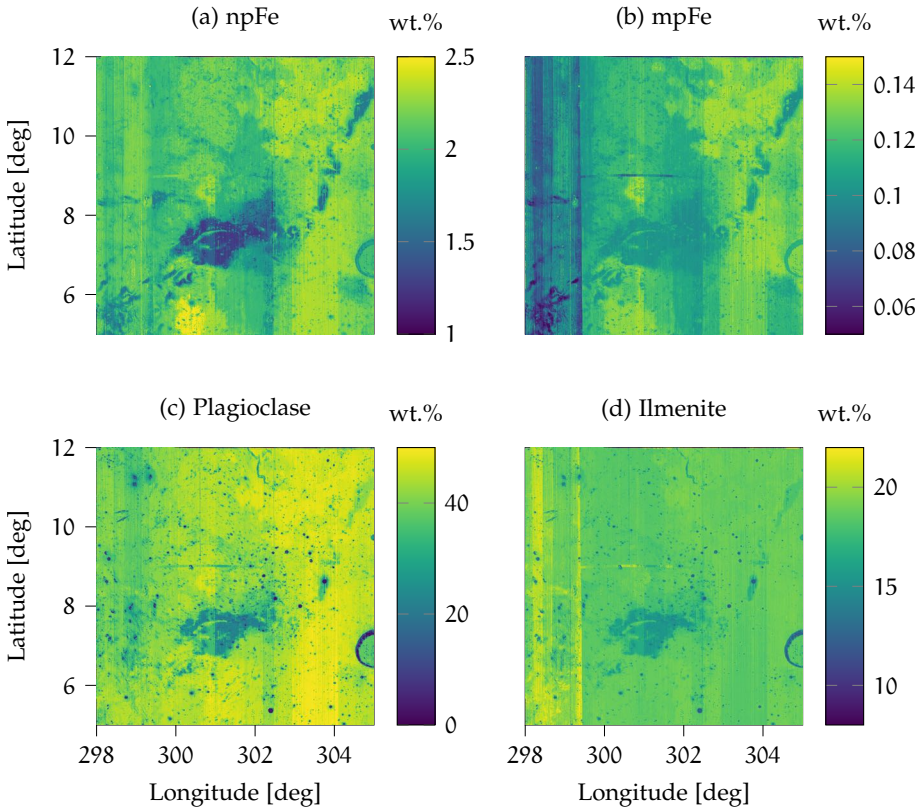

Figure 5.77: Maps of the Reiner Gamma swirl for the mean predicted npFe, mpFe, plagioclase, and ilmenite abundance.

Plagioclase is predicted to be almost only half as abundant at the swirl compared to the surrounding mare. The reason for the underestimation is less intuitive compared to ilmenite. In contrast to plagioclase and ilmenite, Figure C.5 shows that clinopyroxene and olivine are predicted to be more abundant in the central oval. Figure 5.78 displays the correlation matrix for the samples in the chain when unmixing cluster 9 (for pixel locations, refer to Figure C.6). This correlation matrix illustrates that plagioclase, olivine, and clinopyroxene are all to some extent interchangeable. The uncertainties of CPXA, PLG, and OLV are substantial, as illustrated by Figure C.7. For plagioclase, the standard deviation is 5.38 wt.% so that an abundance of 36.46 wt.% is still within the 2σ interval, which would be much closer to the mare background ($\approx$ 42 wt.%). This can likely be attributed to the absorption bands on the swirl being more pronounced. Because the agglutination of plagioclase leads to a broader absorption band, olivine and clinopyroxene may replace parts of the plagioclase abundance.

Consequently, in future work, glasses should be addressed in more detail. However, the spectral properties of glasses are very complex, and not a single glass endmember can represent all elemental compositions. Instead, the composition of the agglutinate glass fraction depends on the bulk composition as well (Denevi et al., 2021). Additionally, a more reliable measure of TiO_2 abundance is necessary that does not depend on the spectral slope. This could, for example, be data derived from better resolved gamma-ray spectroscopy.

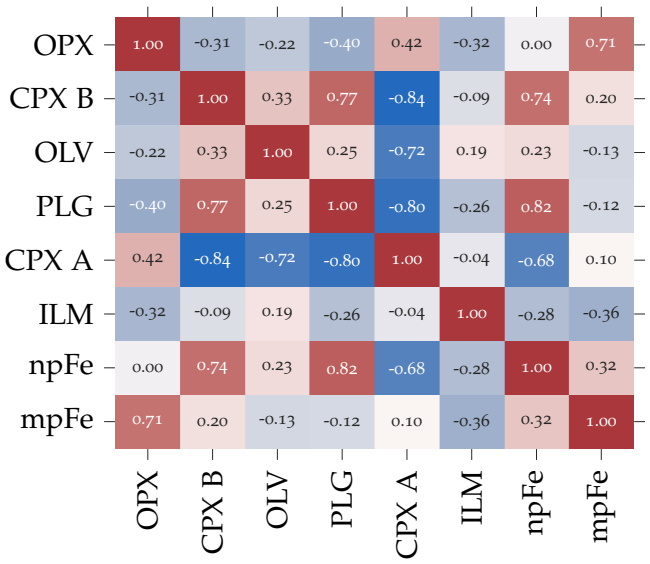

Figure 5.78: Correlation matrix showing the correlations of the samples in the Markov Chain for cluster 9, which represents the central oval of Reiner Gamma (pixel locations shown in Figure C.6).

6

CONTRIBUTION: COMPARATIVE PHOTOMETRIC ANALYSIS OF THE REINER GAMMA SWIRL AND CHANG'E 5 LANDING SITE

This chapter is adapted or adopted from Hess et al. (2023).

In this study, we compare the photometric properties of the Chang'e-5 landing site to those of the Reiner Gamma swirl. Because the physical effects of a landing rocket jet on the lunar regolith are relatively well known, these observations can provide important insights into the physical properties of lunar swirls. We determined the single scattering albedo, opposition effect strength, and surface roughness of the Reiner Gamma swirl and the Chang'e-5 landing site with their respective statistical uncertainties based on the Hapke model and Bayesian inference sampling. The Chang'e-5 landing site and the Reiner Gamma swirl exhibit similar photometric properties, in particular: an increased albedo and a reduced opposition effect strength. Additionally, the landing site is about 20 % less rough compared to the surrounding area. These findings suggest that the swirl surface is less porous compared to the surrounding surface, similarly to a landing site where the top layer of the regolith has been blown away effectively so that the compactness was increased. We conclude that external mechanisms that are able to compress the uppermost regolith layer are involved in lunar swirl formation, such as interactions with the gaseous hull of a passing comet.

6.1 DATA PROCESSING

To be able to use NAC and WAC images for estimating the photometric parameters on the pixel level, the images needed to be co-registered accurately, such that pixels with identical pixel coordinates in all images correspond to the same location on the ground. Furthermore, the images first needed to be radiometrically calibrated to radiances. For this purpose, we used the software ISIS provided by the US Geological Survey (USGS) (Laura et al., 2022).

Due to the push-frame design of the WAC sensor, the images are split into even and odd images that need to be combined in a mosaicking step (the automos routine of ISIS). The images usually do not cover the entire area used for the map projection (Figure 6.1a). The general steps required to process WAC images are displayed in Figure 6.2. All even images were map-projected to the area displayed in Figure 6.1 at a resolution of 400 m/pixel. The even image is then used for the map projection of the odd image. For the pixel grid of latitudes and longitudes, a list was created that was fed into the campt command in ISIS with the usecoordlist option set to True. Since each channel has a slightly different emission angle, the map-projected image cube was split up into the different wavelength channels with the ISIS explode command. The wavelength channel used in this study is the one at 604 nm. Therefore, the cube file for this wavelength channel was used for the campt command. The output for the even and the odd images was parsed to obtain the sub-solar and sub-spacecraft longitude and latitude values, as

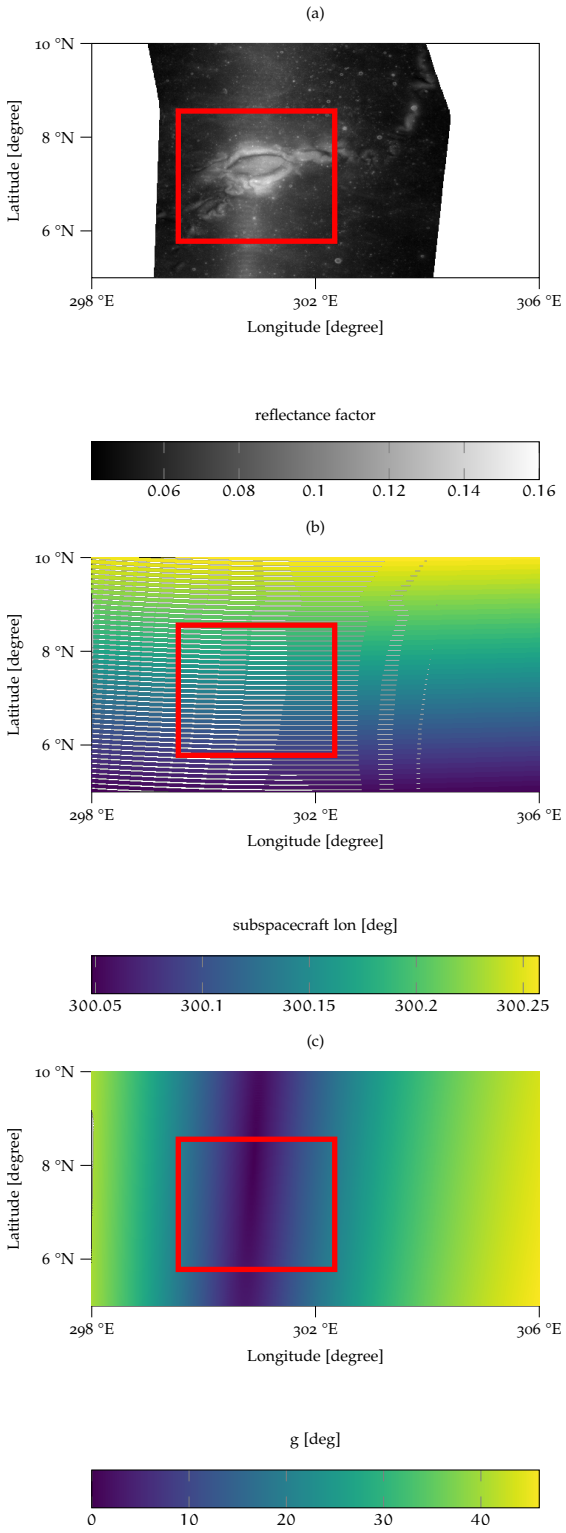

Figure 6.1: Results from different processing steps for image M1147545058CE. The red rectangle marks the region of interest for the oval part of Reiner Gamma. (a) Radiance image after automos step. (b) Sub-spacecraft longitude in degrees for the odd image after the campt step in ISIS reprojected to input longitude and latitude values. The white lines represent missing data where no ground intersection can be calculated by ISIS for the odd image. (c) Phase angle after the step of angle calculation in Figure 6.2.

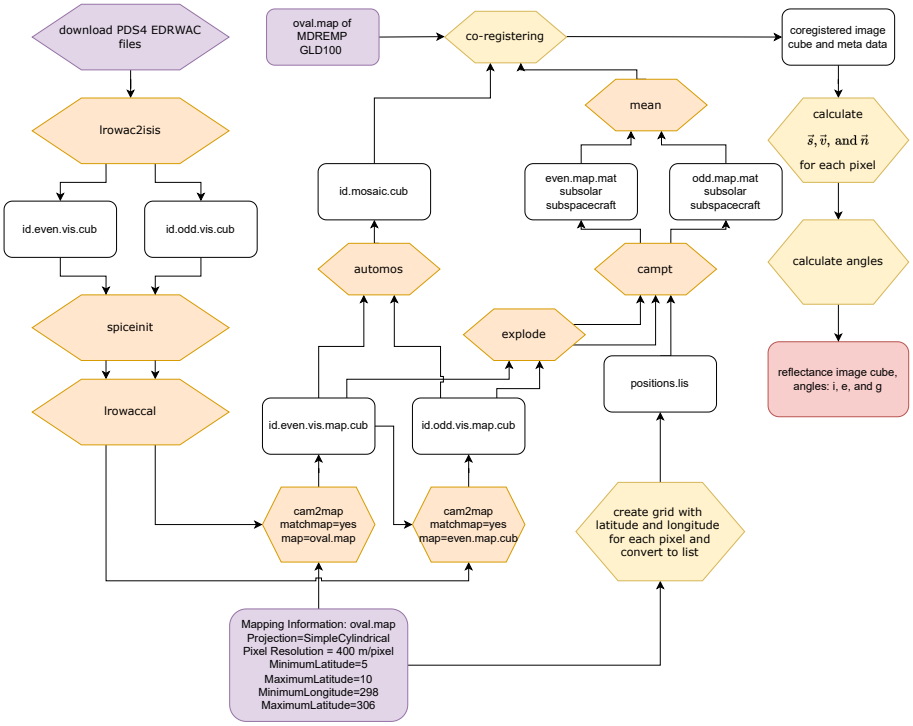

Figure 6.2: Pipeline to radiometrically calibrate and geo-reference WAC images. The output is an image where each pixel location is defined in the coordinate system of the global WAC mosaic and the GLD100 DTM, and the angles i, e, and g are given for each pixel are based on the SPICE kernels. Purple denotes external data input. Orange denotes steps carried out in ISIS. Yellow denotes steps implemented in MATLAB or Python.

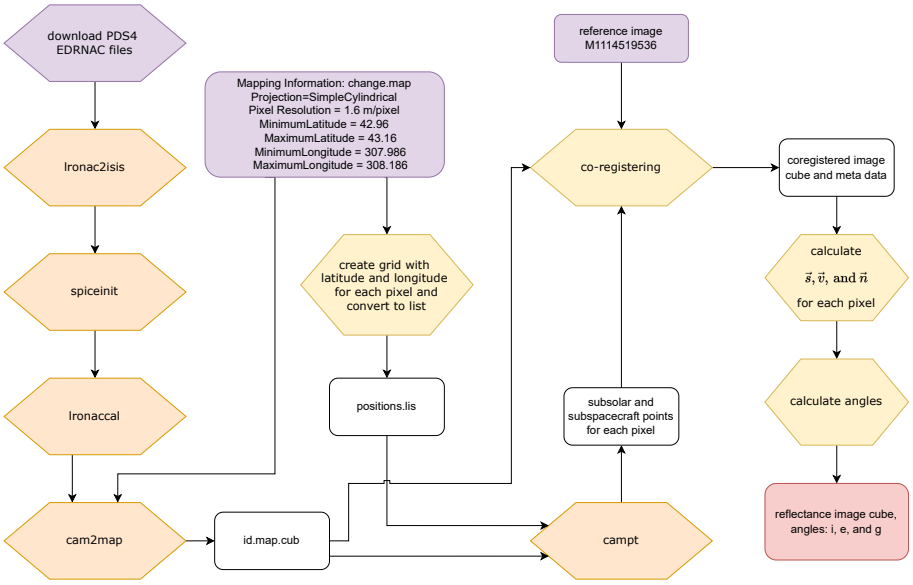

Figure 6.3: Pipeline to radiometrically calibrate and geo-reference NAC images. The output is an image where each pixel corresponds to the pixel in the reference image M1114519536 and the angles i, e, and g for each pixel are based on the SPICE kernels. Purple denotes external input data. Orange denotes steps carried out in ISIS. Steps shown in yellow were implemented in MATLAB or Python.

well as the solar distance and spacecraft altitude, for all the elements on the list. In cases where there was no sample taken for a specific image (even or odd), the values were set to "not a number" (NaN). The values were then reorganized in the grid (Figure 6.1b). The mean over the even and odd images (ignoring NaN values) was calculated such that each location had a value for the parameters listed above. The image and the meta information were then co-registered to the GLD100 and the global WAC mosaic (when necessary). Because of the reduced resolution and the similar map projection (equirectangular or simple cylindrical), the alignment for most WAC images was already almost perfect. Based on the latitude and longitude values of each pixel and the sub-spacecraft and sub-solar latitude and longitudes, as well as the solar distance and spacecraft altitude, which are also given for each pixel, we were able to calculate the vectors pointing to the sun ($\vec{s}$) and to the spacecraft ($\vec{v}$). The DTM is co-registered to the images, such that we could derive the surface normal $\vec{n}$ for each pixel. Subsequently, the vectors $\vec{s}$, $\vec{v}$, and $\vec{n}$ were used to calculate the angles i, e, and g. The resulting phase angle for an image showing a typical opposition surge is displayed in Figure 6.1c.

The processing of NAC images (Figure 6.3) was easier regarding the ISIS calibration. The FOV is much smaller in comparison to WAC images. Therefore, the angles are not as highly variable as for WAC images. Also, no even and odd images needed to be combined. However, because of the higher resolution, much more attention had to be paid to the co-registration process. Consequently, all images were carefully co-registered to the reference image M1114519536, which was also used to create the SfS DTM. The image was much larger compared to the area of interest. Corresponding pixels for co-registration were selected, especially around the landing site, but also across the entire image. Furthermore, the alignment was evaluated and iterated until it was satisfactory. The SfS DTM is inherently co-registered to the reference image because the SfS method is directly based on the image information of that particular image. As with the WAC imagery, the vectors $\vec{s}$ and $\vec{v}$ were calculated based on the output of the campt command. Finally, the angles i, e, and g were obtained, which are required for the subsequent photometric modeling.

6.2 MODEL DEFINITIONS

Some parameters of the Hapke (2012b) model are interdependent (e.g., w and B_{S0}), and some parameters are even mathematically coupled, like the parameters of the phase function b and c (e.g., Helfenstein, 1986; Schmidt and Fernando, 2015). Therefore, there are multiple solutions that can explain measured values equally well. The usage of conventional optimization techniques to invert the Hapke model may return best-fit values but ignores all other solutions that fit equally well. It is important to be aware of these uncertainties to be able to choose parameters that can be determined reliably based on the available image data. A technique that is well suited for these kinds of problems is Bayesian inference because the parameter space is thoroughly explored, and we obtain uncertainties complementary to the best-fit values. Because of the nonlinearities of the model and the not necessarily normally distributed parameters, we use Markov Chain Monte Carlo (MCMC) sampling to numerically estimate the posterior probability density function (PDF) of the parameters instead of solving the problem analytically.

Choosing a suitable likelihood function is inarguably the most important part of the Bayesian modeling approach. The likelihood is evaluated by comparing the model results for a certain set of parameters to the measured data. If the modeled results and the measured data fit well, then it is likely that the data originated from these parameters. To be able to distinguish the effects of the albedo and the other parameters more easily, we additionally used phase ratio information. For M images, we defined the measurements as a vector $\vec{R}$ of length M. The first image is preferentially a medium phase angle image without any shadows. The phase ratios used in this work were the pixel-wise ratios $R_1/\vec{R}_{2\ldots M}$ between the reflectances of the first image divided by the reflectances of the remaining images and calculating the base-10 logarithm. This phase ratio vector has the dimension $M-1$. Subsequently, we combined both by concatenation to obtain the final $(2M-1)\times 1$ data vector:

$$\vec{R}_{meas} = \left[\vec{R}_{M\times 1}, \log_{10}(R_1/\vec{R}_{2\ldots M})_{(M-1)\times 1}\right] \tag{67}$$

Assuming Gaussian noise, it is reasonable to select a normal distribution as the likelihood function. The normal distribution we selected had its mean at the modeled values and was evaluated for the measured values. The standard deviation of the likelihood function is an additional parameter of the model itself. And because the smaller the standard deviation, the higher the probability can become, it has a strong effect. It should be noted that the reflectance values and the phase ratio values were of different orders of magnitude. Therefore, we included two different standard deviations as part of the model. We denoted the standard deviation for the reflectance part as σ_{refl} and for the phase ratio part as σ_{pr}. So we defined the standard deviation vector $\vec{\sigma}_{lh}$ of the likelihood function as:

$$\sigma_{lh} = \left[\sigma_{refl}\vec{1}_{M\times 1}, \sigma_{pr}\vec{1}_{(M-1)\times 1}\right], \tag{68}$$

where $\vec{1}_{M\times 1}$ was a vector of dimension M containing only ones. So the likelihood was evaluated for all observed and modeled values individually and is subsequently marginalized. Using the definitions above, the likelihood became:

$$\begin{aligned} &p(\vec{R}_{meas} \mid w, B_{S0}, \bar{\theta}_b, \sigma_{refl}, \sigma_{pr}) \sim \\ &\prod_{i=1}^{2M-1} \mathcal{N}(R_{meas,i} \mid \mu = R_{model,i}(w, B_{S0}, \bar{\theta}_b), \sigma = \sigma_{lh,i}) \end{aligned} \tag{69}$$

Additionally, we included prior information. The Hapke model has many parameters, and not all of them can be determined reliably simultaneously. The single scattering albedo w, which is the main parameter of the Hapke model, is physically limited to the interval between zero and one. We chose an uninformative prior with a Beta distribution evenly distributed between zero and one as

$$p(w) \sim \text{Beta}(w \mid \alpha = 1, \beta = 1) \tag{70}$$

The opposition effects are collected in a correction term based on the width h_s and the strength B_{S0}. The width is set to a fixed parameter according to Table 6.1. According to Sato et al. (2014), B_{S0} is mainly distributed between 1.5 and 2.1. While in theory the amplitude is limited to the interval $[0, 1]$ because both opposition effect terms are combined in B_S, the amplitude is usually larger than 1. The parameter should not become

negative so that we chose a log-normal distribution as a prior. To avoid penalizing solutions outside of the interval, we we choose a relatively uninformative prior with a mean at $e^{0.4+0.7^2/2} \approx 1.905$ and a large standard deviation of approximately 1.52.

$$p(B_{S0}) \sim \text{LogNormal}\,(B_{S0} \mid \mu = 0.4, \sigma = 0.7) \tag{71}$$

The surface roughness $\bar{\theta}_b$ has a very weak effect for roughness angles below 10 degrees and is rarely larger than 40 degrees. Therefore, we set the prior distribution to be equally distributed between 10 and 50 degrees by using a scaled Beta distribution

$$p(\bar{\theta}_b) \sim \text{Beta}\left(\frac{\bar{\theta}_b - 10}{50 - 10} \mid \alpha = 1, \beta = 1\right). \tag{72}$$

Besides the physical parameters of the model, the standard deviation of the likelihood distribution is also a free parameter. It is common practice to use a half-normal distribution for the prior of the standard deviation such that

$$p(\sigma_{refl}) = \text{HalfNormal}(\sigma_{refl} \mid \sigma_{hn} = 1), \tag{73}$$

$$p(\sigma_{pr}) = \text{HalfNormal}(\sigma_{pr} \mid \sigma_{hn} = 1). \tag{74}$$

The parameters b and c of the phase function influence the shape of the phase curve and determine if the particles are forward or backward scattering and inherently follow the hockey stick relation (e.g., Hapke, 2012a; Schmidt and Fernando, 2015), which is given by Sato et al. (2014) as $c = 3.29e^{-17.4b^2} - 0.908$. The parameter b is limited to the interval $[0, 1]$. Therefore, we again chose an uninformative Beta distribution as a prior for b.

Parameter Name	Symbol	Free	Value
Single scattering albedo	w	✓	Prior Eq. 70
Phase function shape	b	×	0.21
Phase function relative strength	c	×	0.7
Shadow Hiding Opposition Effect (SHOE) strength	B_{S0}	✓	Prior Eq. 71
Shadow Hiding Opposition Effect (SHOE) shape	h_s	×	0.11
Surface roughness angle	$\bar{\theta}_b$	✓	Prior Eq. 72

Table 6.1: Parameters of the Hapke model and their values or estimation methods. The fixed values for b, c, and h_s are global values for the Moon estimated by Warell (2004).

The posterior distribution is then estimated by exploring the parameter space and sampling points until the samples converge to the posterior distribution. The No-U-Turn sampler (NUTS) (Hoffman and Gelman, 2014) was used to sample from the posterior distribution. NUTS is a very efficient algorithm that is widely used in Bayesian applications. We used the implementation of NUTS in pymc3 (Salvatier et al., 2016) and sampled 5,000 tuning steps to set the individual step size, and drew two chains of each 20,000 samples to make sure that the samples converge to the posterior density.

To decide which parameters can ultimately be estimated, we designed an experiment where we estimated the uncertainties of the parameters given data synthetically generated with the Hapke model and a conservative estimate of the noise level (Gaussian noise with $\sigma_n = 0.001$). The observational geometry was selected to represent the data available for the central oval of Reiner Gamma. Given the nine observations, each with the nominal angles i, e, and g, we calculated the reflectance values for $w = 0.3$, $\bar{\theta}_b = 23$ degrees, $B_{S0} = 1.7$, $h_s = 0.11$, $b = 0.21$, and $c = 0.619$. The signal-to-noise ratio is approximately 77.7 compared to > 42 for NAC imagery, for example, not considering the radiometric accuracy. These reflectance values were then used to invert the Hapke model to determine the parameters by employing the Bayesian method outlined in this section. Figure 6.4 shows the results when the b parameter of the phase function is free and c is set according to the hockey stick relation (Hapke, 2002). The results indicate that the phase function parameters cannot be determined reliably. All solutions between strongly backscattering and forward scattering are accepted. Comparing those results to the results when the phase function is fixed (see Figure 6.5) visualizes that the uncertainties of all free parameters can be reduced significantly if the value for b is constant. Additionally, in situations where the mean deviates strongly from the actual value (yellow diamond) in Figure 6.4 it fits well for Figure 6.5. In practice, using b as a free parameter for the actual data often resulted in multimodal posterior distributions for w, b, and c, making the mean an unreliable measure to describe the distribution. As illustrated by the results, the parameter has only a limited influence on the reflectance values. The shape of the phase function simply does not change significantly enough to be able to distinguish variations in b. Figure 6.6 shows some examples of solutions that might possibly be accepted by the Bayesian inference sampling even for the very narrow confidence band. In this example, a strongly backward-scattering but low-albedo material fits the data equally well as a forward-scattering material with higher albedo because there is not enough angular coverage to constrain the model. The other parameters in the example in Figure 6.6 are constant. This is an indication that variations in b and c between, e.g., the swirl and its surroundings, cannot explain the photometric differences we observe in this study. We, therefore, decided to fix the b and c values according to Warell (2004) and infer the values of w, B_{S0}, and $\bar{\theta}_b$ from the data. The parameter choices and corresponding priors are listed in Table 6.1.

6.3 RESULTS

In this study, we want to investigate two regions with respect to their photometric behavior and compare their characteristics. First, we looked at the Chang'e-5 landing site at approximately 43.1 °N and 51.8 °W (see Section 6.3.1) in the northern part of Oceanus Procellarum near Mons Rümker (Zhou et al., 2022). This is an interesting study site because it offers the rare opportunity to investigate the photometric changes caused by a landing rocket jet because high-resolution NAC images from before and after the landing are available. Second, lunar swirls are still not fully understood and the Reiner Gamma swirl (see Section 6.3.2) is a prime research target as it is the most prominent representative of lunar swirls.

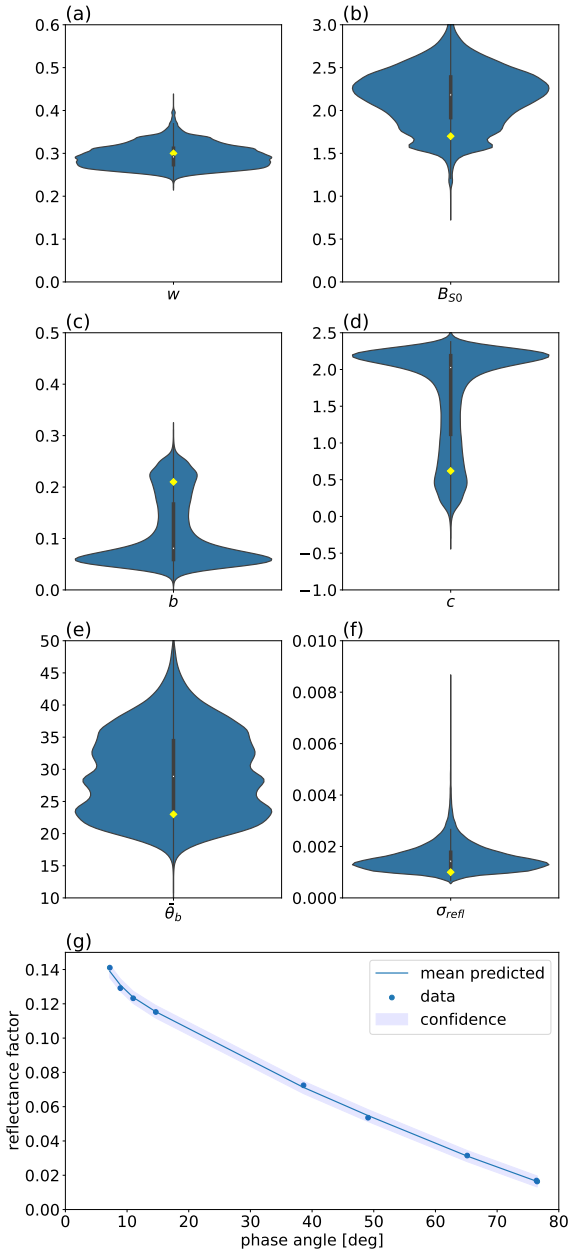

Figure 6.4: Posterior distribution (a-f) of Hapke parameters given the reflectance values for the average angles of the observations at the central oval of Reiner Gamma with additive gaussian noise with a standard deviation of $\sigma_n = 0.001$. Subfigure (g) shows the the posterior predictive values with a mean and confidence interval, which represents the standard deviation of all accepted samples. Yellow diamonds mark the theoretical input values used to generate the phase curve.

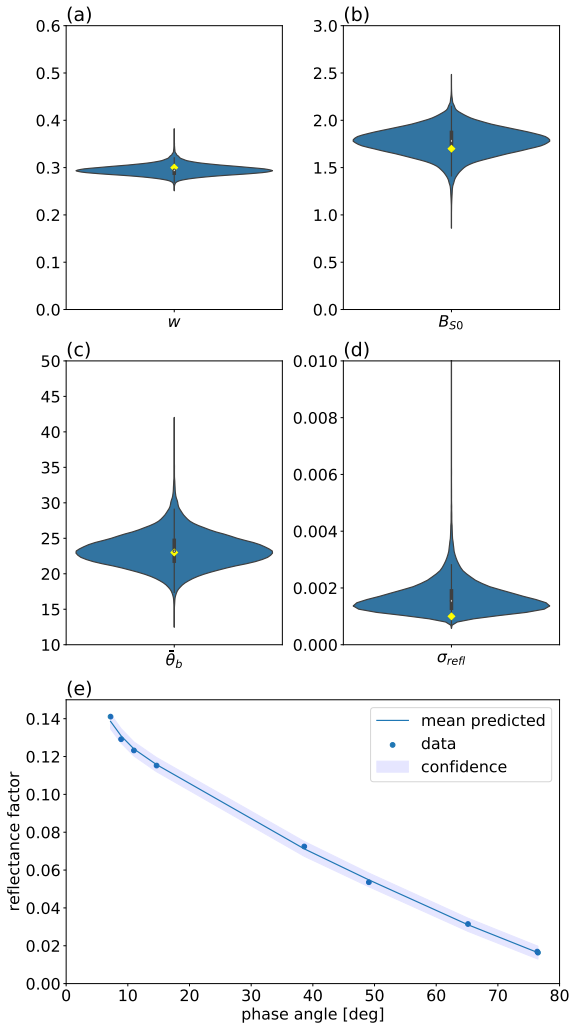

Figure 6.5: Displayed are the posterior distributions (a-d) of the Hapke parameters for the same phase curve as in Figure 6.4, when the parameters b and c of the phase function are set to 0.21 and 0.619, respectively. Subfigure (e) shows the confidence interval of the posterior predictive values.

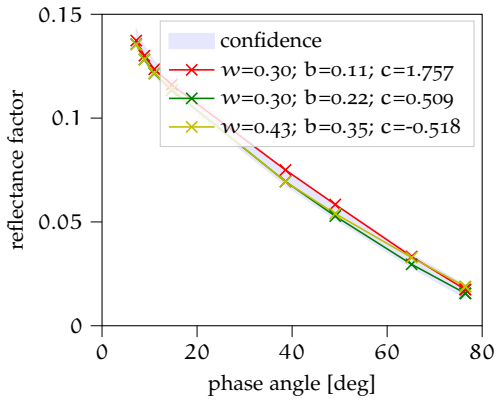

Figure 6.6: The confidence interval from Figure 6.4 with some exemplary reflectance phase curves. Both a strongly backscattering and a forward scattering material can fit into the confidence interval and could be considered acceptable solutions given the noise level. The shape of the phase curve only changes marginally across the accessible range of phase angles.

6.3.1 *Chang'e 5 Landing Site*

The Chinese lunar mission Chang'e-5 landed successfully on December 1st, 2020, at approximately 43.1 °N and 51.8 °W. It collected a number of samples and the ascending stage lifted off two days later and returned to Earth (Zhou et al., 2022). The context of

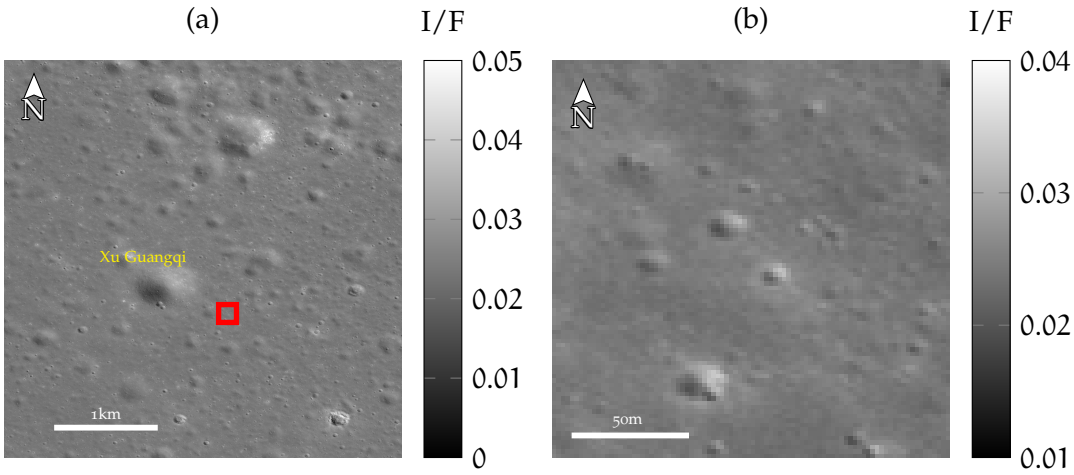

Figure 6.7: Chang'e-5 landing site. Region of interest used in this study marked by the red rectangle in (a) shown in (b). The background image is LROC NAC frame M1114519536 centered at approximately 43.05 °N and 51.95 °W in (a). The larger crater to the northwest of the landing site is the Xu Guangqi crater (below the yellow label).

the landing site is shown in Figure 6.7, where the region of interest evaluated in this study is marked by the red rectangle. The area is characterized by a typical mare terrain with small craters scattered around. The landing site is salient by three small craters in a triangular pattern, where the craters are smaller than 10 m in diameter, as can be seen in Figure 6.7b.

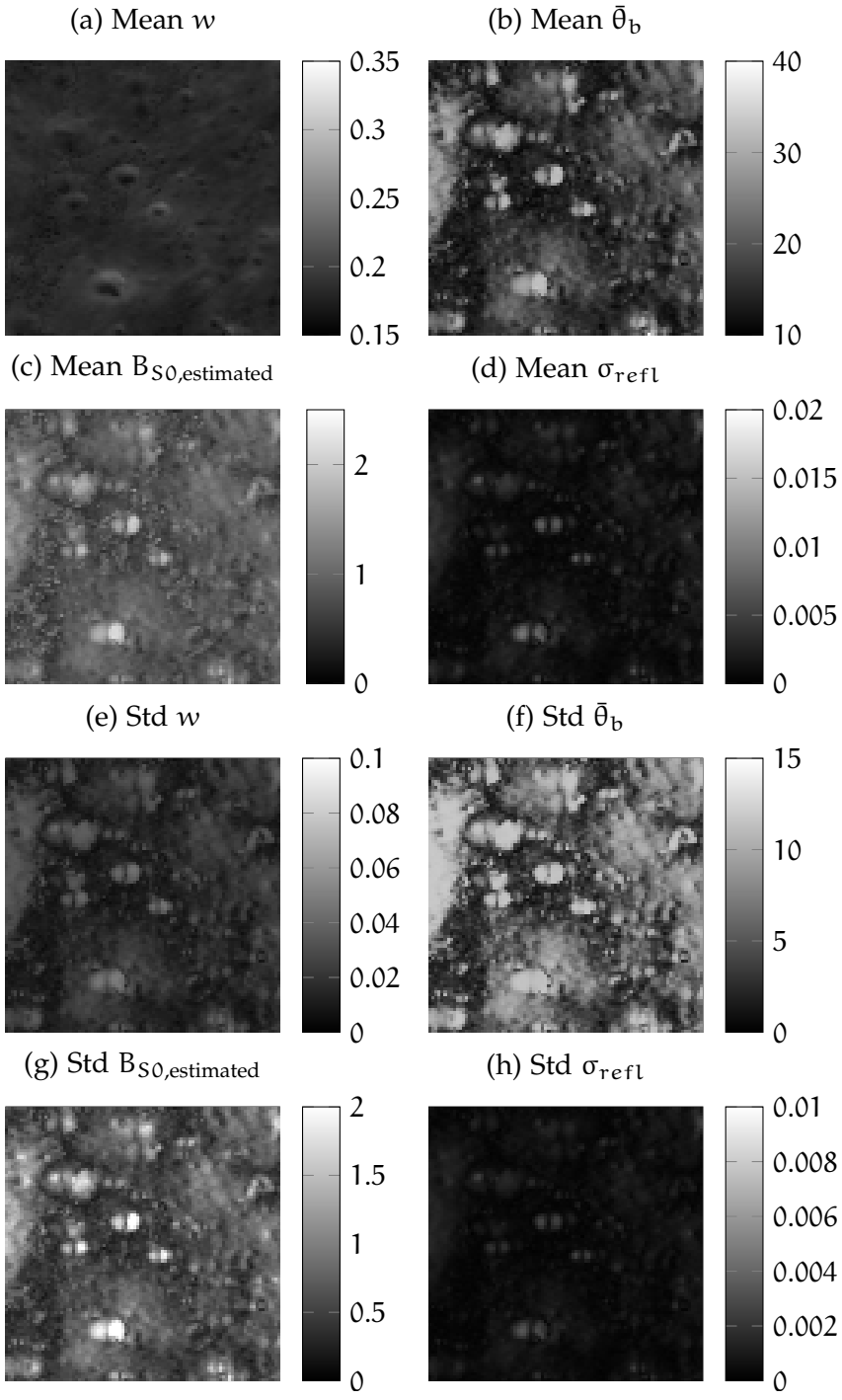

Figure 6.8: Results for the Chang'e-5 landing site before the landing. Means of the posterior distributions (a-d) for the parameters w, $\bar{\theta}_b$, B_{S0} of the Hapke model and the standard deviation, σ_{refl}, of the likelihood function with respect to reflectance. The extents for all maps are 144×144 m. The uncertainties (e-h) of the model parameters correspond to the standard deviations of the posterior distributions.

The modeling results for image data acquired before the landing are shown in Figure 6.8 as the mean predicted values (a-d), and the associated uncertainties are displayed as the standard deviation of the posterior distribution (e-h). The mean albedo of the area is 0.18, with no reliable values above 0.22. The roughness is overall small (mean over the area is 17.5 degrees) compared to the value in Sato et al. (2014), where a global mean value of 23.4 degrees was derived. In the maps of the roughness and the opposition effect amplitude, the craters are associated with higher values but are also associated with worse fits (Figure 6.8d) and higher uncertainties (Figures 6.8f and g). The mean B_{S0} value over the area is 0.90 and, therefore, smaller than the values predicted for the derived low albedo. After the landing, the lander itself is visible in the albedo map as a bright spot between the three craters (Figure 6.9a). The albedo increases significantly around the lander compared to before the landing (Figure 6.8a). The surface roughness and the opposition effect are both reduced immediately around the lander, as can be seen in Figures 6.9b and 6.9c in a similar pattern as the albedo has increased. Because of the Moon's orbit, the images are all illuminated from the east or the west but never from the north or south. Therefore, the shadows of the lander in the image are also cast in these directions. These shadows can be seen in the maps of the mean predicted parameters (Figure 6.9) as increased values in B_{S0} and $\bar{\theta}_b$ and as higher uncertainties for all parameters as a bright line in the center of the image. Higher values of B_{S0} and $\bar{\theta}_b$, in general, are also associated with higher uncertainties, just as craters are (again) not as well constrained. The uncertainties in the craters also stem from shadows at the eastern and western edges of the crater, often leading to the two semi-circles with higher uncertainties and higher values visible in the B_{S0} and $\bar{\theta}_b$ maps (see Figure 6.8 and Figure 6.9).

Using the correlation from Sato et al. (2014), the $B_{S0,corrected}$ values are displayed in Figure 6.10 for before and after the landing. A comparison of the two maps shows that the background has not changed significantly, but a strong negative anomaly can be observed around the lander.

Based on the albedo, which does not exceed 0.22 before the landing, we could segment the region of interest into an area that was affected by the landing ($w > 0.22$) and an area that was not (or at least less so). This segment acts as a background ($w < 0.22$). We also defined pixels for which the standard deviation of the likelihood function σ_{refl} exceeds 0.004 as unreliable and omit them from our analysis. This segmentation is shown in Figure 6.11.

Subsequently, this segmentation can be used to plot the histograms of $B_{S0,estimated}$ and $B_{S0,corrected}$ for the two regions (Figure 6.12). In Figure 6.12a, the $B_{S0,estimated}$ values and in Figure 6.12b the corrected values are displayed, both before the landing. The corrected values are generally below one (roughly normally distributed around approximately 0.53) even though we would not have expected this region to have an abnormally weak opposition effect. The histograms of the study sites show that the B_{S0} values after the landing (Figure 6.12c,d) are generally also small. The segmentation, however, clearly shows that the values of $B_{S0,corrected}$ in the area affected by the lander, are excessively small, corresponding to less than one-third of the typical values of lunar regolith with a comparable albedo. The mean of the background pixels is also smaller, with 0.45 compared to 0.53 before the landing. The segmentation discretely classifies pixels as "landing site" or "background." However, the affected area actually has a diffuse boundary. There-

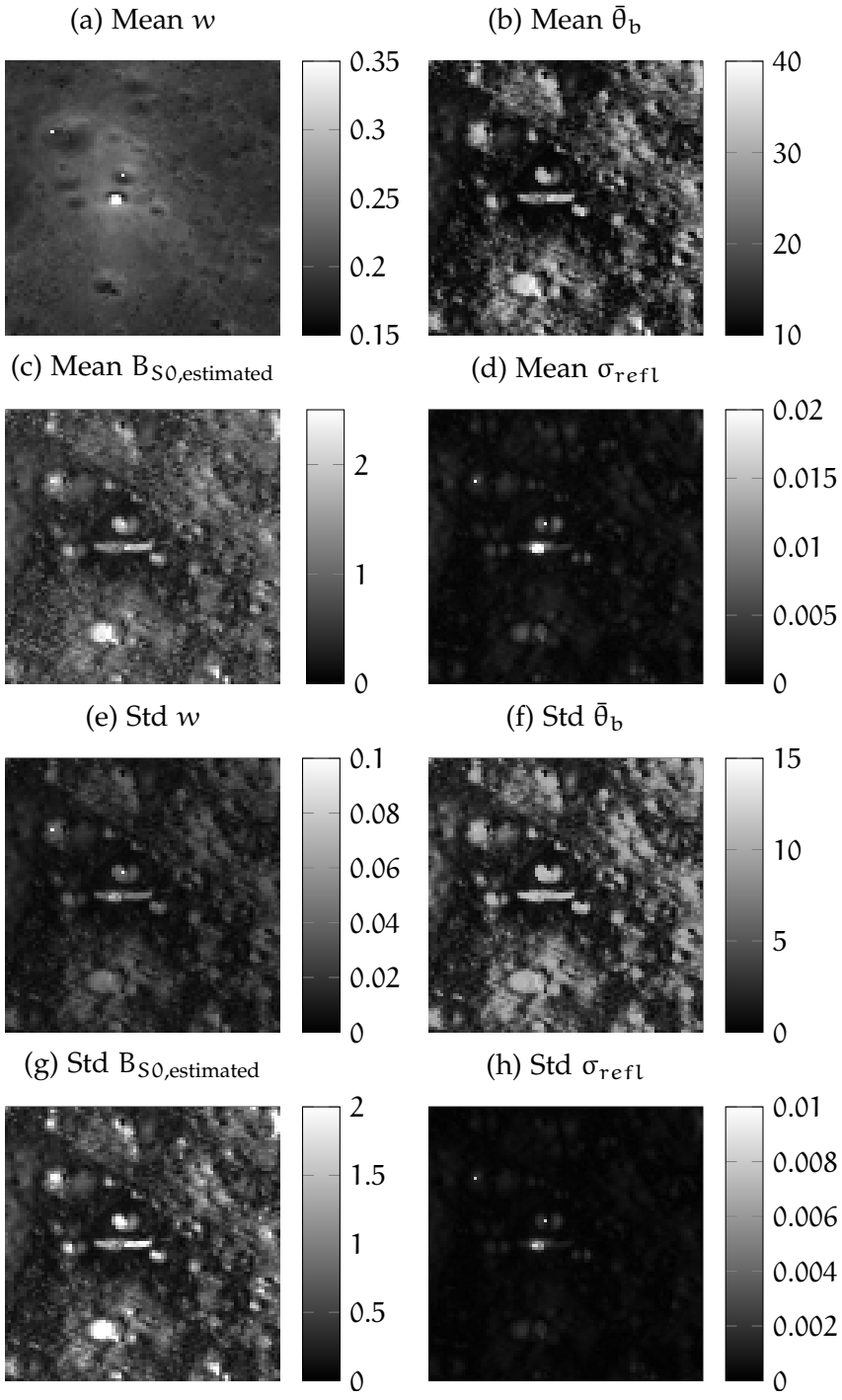

Figure 6.9: Results for the Chang'e-5 landing site after the landing. Means of the posterior distributions (a-d) for the parameters w, $\bar{\theta}_b$, B_{S0} of the Hapke model and the standard deviation of the likelihood function with regards to reflectance σ_{refl}. The extents for all maps are 144×144 m. The uncertainties (e-h) of the model parameters correspond to the standard deviations of the posterior distributions.

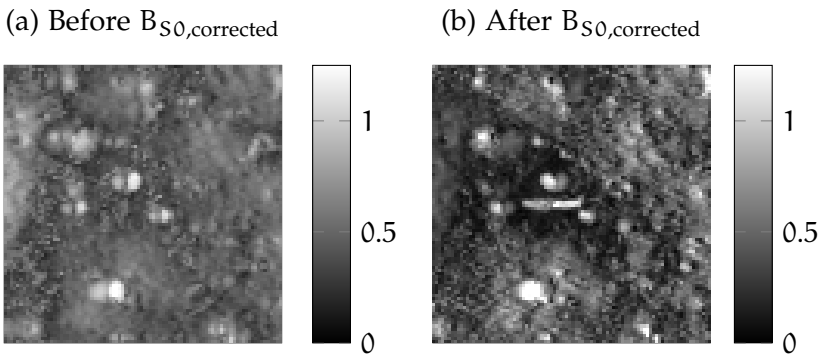

Figure 6.10: Comparison of B_{S0} corrected for the influence of albedo according to Equation 29 between before and after the landing.

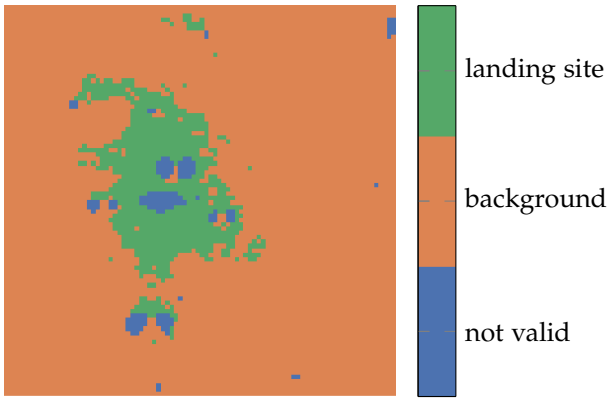

Figure 6.11: Segmentation of the region of interest after the landing into an area strongly influenced by the rocket jet (landing site) and not as clearly influenced by the landing (background). Areas with a mean predicted albedo w above 0.22 are denoted as landing site. Areas with a mean predicted σ above 0.004 are labeled as invalid because the uncertainties are too high. Consequently, these areas are excluded from the analysis of the landing site and background regions.

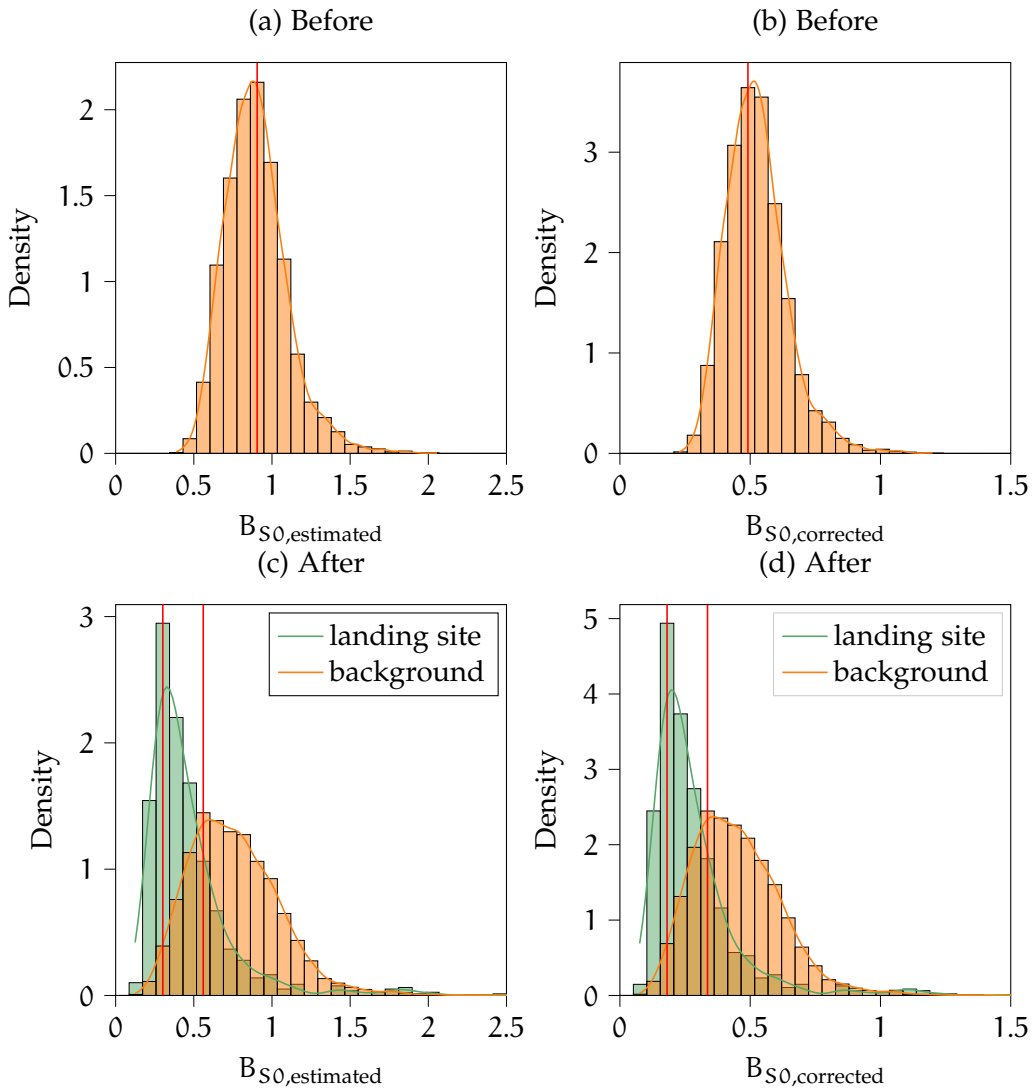

Figure 6.12: Histograms of $B_{S0,estimated}$ and $B_{S0,corrected}$ for before and after the landing. For after the landing, two separate distributions for the landing site and background are shown. The modes of the histograms are indicated by the red vertical lines.

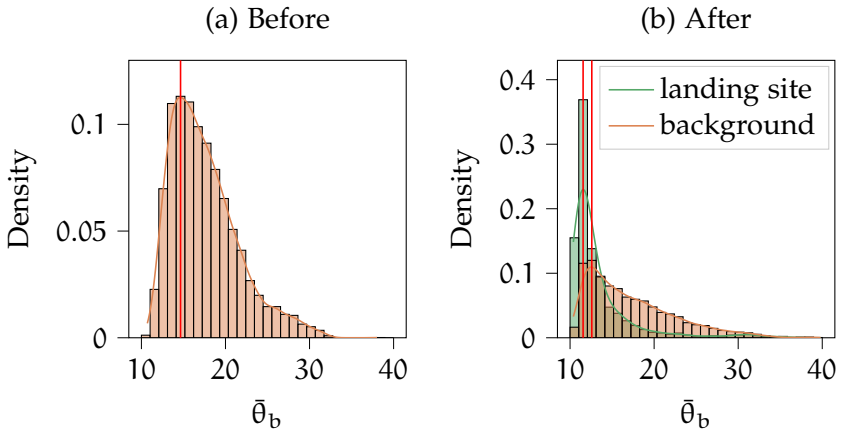

Figure 6.13: Histograms of the roughness angle $\bar{\theta}_b$ in the region of interest (a) before and (b) after the landing. The modes of the histograms are indicated by the red vertical lines. Before the landing, the mode and mean of the background pixels are 14.7 and 17.5 degrees, respectively. Background: mode after the landing: 12.6 degrees; mean after the landing: 17.2 degrees. Landing site: mode after the landing: 11.6 degrees; mean after the landing: 13.4 degrees. The two distributions after the landing for the landing site and background have a KS-test score of $D = 0.436$ with $p = 1.78 \times 10^{-15}$.

fore, it can be stated that background pixels are also affected, even though to a lesser degree compared to the landing site. Consequently, the mean opposition effect strength of the background pixels is also slightly reduced compared to before the landing. The histograms of the two areas, landing site and background, appear to describe systematically different distributions. The mean of the $B_{S0,\text{corrected}}$ values from the landing site is 0.28, compared to the background value of 0.45 after the landing.

The Kolmogorov-Smirnow test (KS-test) statistics for the $B_{S0,\text{estimated}}$ values of the two regions is $D = 0.527$ ($p = 1.8 \times 10^{-15}$) and for the $B_{S0,\text{corrected}}$ values it is $D = 0.511$ ($p = 1.8 \times 10^{-15}$). The critical value for a significance level of 0.01, $m = 885$ landing site pixels, and $n = 2064$ background pixels is 0.065. Because the values of D are significantly above the critical value the null hypothesis can be rejected.

The histograms for the roughness angle $\bar{\theta}_b$ are shown in Figure 6.13 for before and after the landing. Before the landing, the roughness was overall higher with a mean of 17.5 degrees. After the landing, the background pixels appear to be only slightly affected by the landing rocket jet as the mean decreases to 17.2 degrees. The pixels classified as landing site show a reduced average roughness of 13.4 degrees. The modes of the two histograms, background and landing site, are very close to each other (12.5 and 11.6 degrees for background and landing site, respectively) and both are small compared to the mode before the landing, which was 14.7 degrees. The KS-test score is $D = 0.436$ ($p = 1.78 \times 10^{-15}$), suggesting that the effect is not as large as for the opposition effect but still both regions are systematically different.

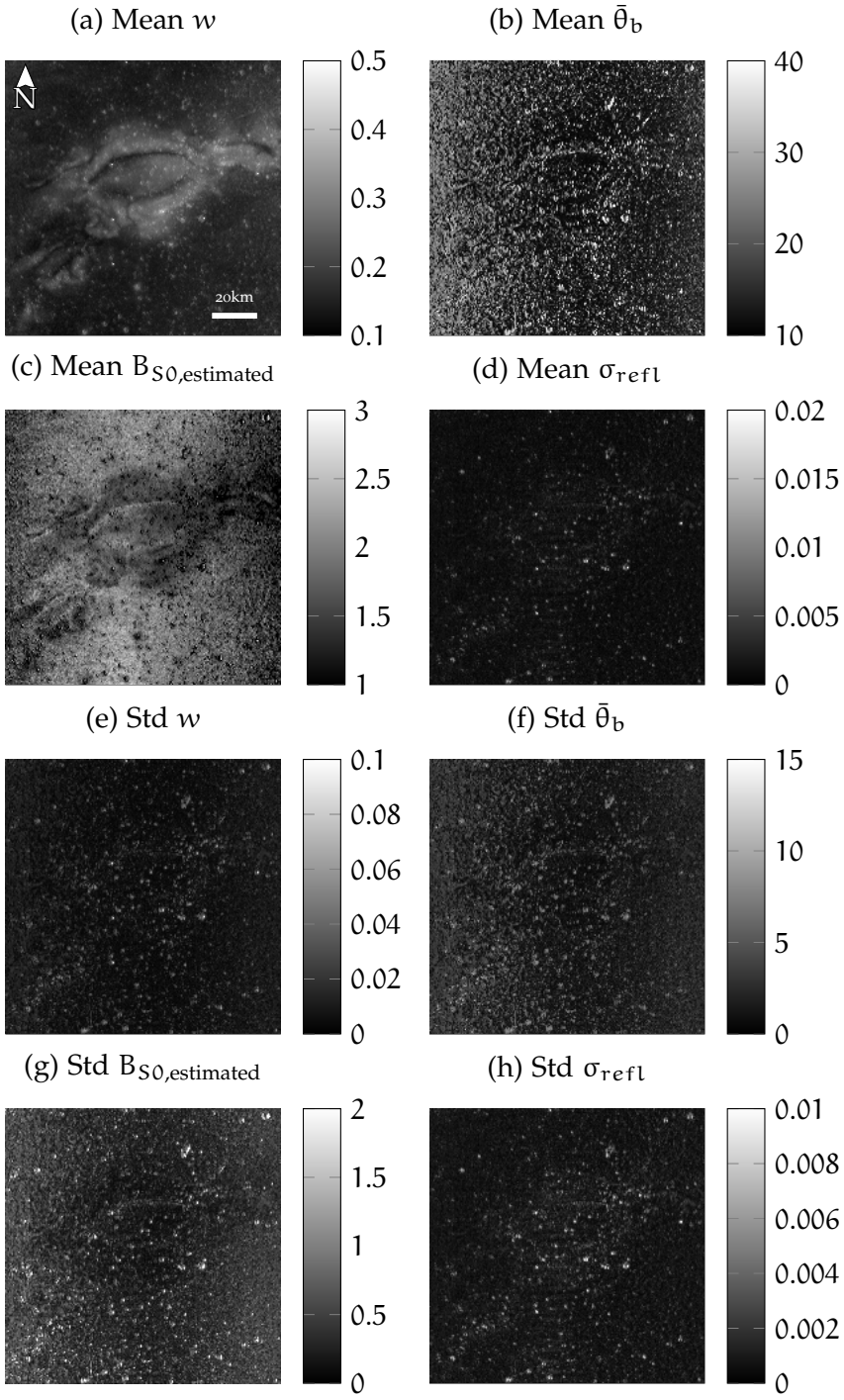

Figure 6.14: Results for the oval region of the Reiner Gamma swirl. Means of the posterior distribution for the Hapke model parameters w, $\bar{\theta}_b$, B_{S0} are shown as well as the mean of the standard deviation parameter σ of the likelihood function.

6.3.2 *Reiner Gamma Swirl*

The Reiner Gamma swirl is centered at 7.5 °N and 59.0 °W in western Oceanus Procellarum, slightly north of the lunar equator. It is the most prominent example of these high-albedo anomalies found on the Moon that are commonly termed lunar swirls.

In the albedo map of the central oval part of the Reiner Gamma swirl, the bright albedo pattern is clearly visible (Figure 6.14a). The roughness map (Figure 6.14b) shows that the values are relatively noisy, and the uncertainties are high with several degrees and even exceed 10 degrees for some craters (Figure 6.14f). A small difference can be observed for the dark lane in the northern oval, which exhibits a higher roughness. In the B_{S0} map, however, the silhouette of the swirl can be distinguished by a weaker opposition effect amplitude. Craters, in turn, often coincide with weak B_{S0} anomalies but are mostly related to higher uncertainties. The standard deviation of the likelihood function is higher for the craters (Figure 6.14), indicating that the fit is worse, just as the uncertainties of all parameters are higher (Figure 6.14). The results for the tail part are very similar to the central oval and are shown in Figure 6.17 and Figure 6.18. The opposition effect strength is clearly smaller for the tail, even after correcting for the general correlation between albedo and B_{S0} (Figure 6.19a). For the roughness in Figure 6.17b a very weak reduction can be observed at some locations, such as in the northernmost and southernmost parts of the tail.

When the dependence on albedo is removed from the opposition effect amplitude, the outlines of the swirl can still be clearly differentiated (Figure 6.15a). The area can be segmented into on-swirl pixels with a higher albedo and off-swirl locations that represent the surrounding background mare. The albedo threshold is set to 0.21 and locations with $\sigma_{refl} > 0.004$ are labeled as invalid. With this segmentation, the histograms of the estimated and corrected values are shown in Figure 6.16. The $B_{S0,estimated}$ values for the

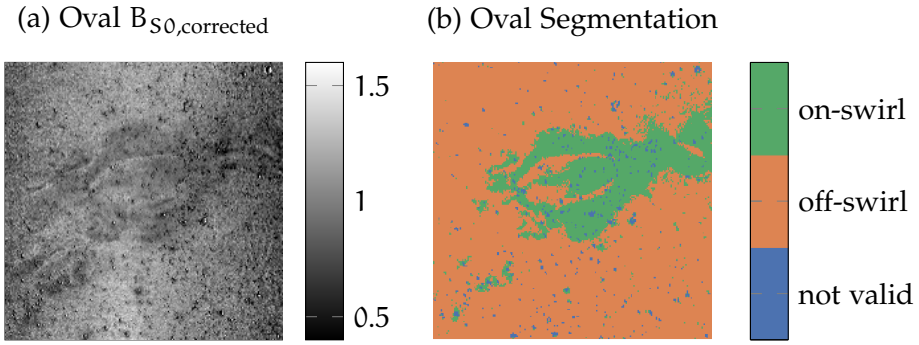

Figure 6.15: Maps of the corrected B_{S0} value to remove the dependence on albedo (a). Segmentation of the region of interest based on the mean albedo (b). Areas with an albedo larger than 0.21 are labeled as on-swirl. Areas with a mean predicted σ above 0.004 are labeled as invalid as the uncertainties are too high.

off-swirl pixels are mostly normally distributed around 1.75, and for the on-swirl locations, the mean is 1.37. On the other hand, the off-swirl $B_{S0,corrected}$ values are almost exactly centered around 1.0, which means that they are on average exactly as predicted by Sato et al. (2014). In contrast, the on-swirl locations have a reduced opposition effect with an average $B_{S0,corrected}$ value of 0.83. Because of the large number of locations in the

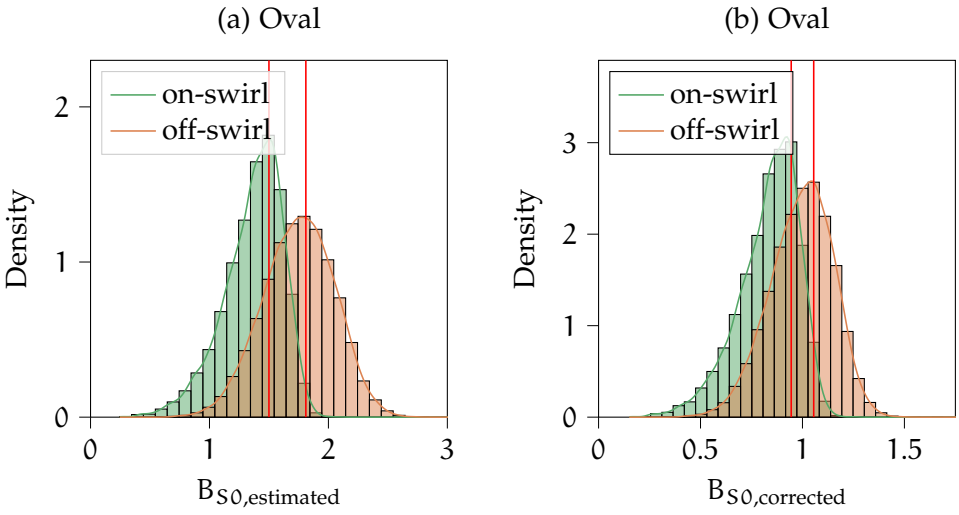

Figure 6.16: Distribution of (a) $B_{S0,estimated}$ and (b) $B_{S0,corrected}$ for on-swirl and off-swirl areas according to Figure 6.15b. The modes of the histograms are indicated by red vertical lines.

distributions, the KS-test is significant with $p = 0.00$ for both corrected and estimated values. For the estimated values, the statistics is $D = 0.539$ and for the corrected values the difference is smaller between the on-swirl and off-swirl distributions. Consequently, $D = 0.422$ is also smaller. This dichotomy between on-swirl and off-swirl locations is even more pronounced for the tail region of Reiner Gamma (see Figures 6.17 and 6.18 for the mean predicted values and uncertainties in standard deviation, respectively). The segmentation for the tail is shown in Figure 6.19b, and the resulting histograms are in Figure 6.20. For that part of the swirl, the KS-test statistics are $D = 0.725$ and $D = 0.607$ for the estimated and corrected values, respectively. The difference between the roughness values on-swirl versus off-swirl is negligible with $D = 0.075$ ($p = 3.98 \times 10^{-33}$) for the central oval and $D = 0.071$ ($p = 6.88 \times 10^{-9}$) for the tail.

6.4 DISCUSSION

The bright regions of the Chang'e-5 landing site and the Reiner Gamma swirl show similar photometric behavior. Compared to the immediate surroundings, the albedo is increased, and the opposition effect is weaker in both cases. Additionally, at the landing site, the roughness is significantly reduced compared to the pre-landing surface, whereas a reduction of swirl roughness is barely discernible. The differences in opposition effect are similar for the landing site and swirl when compared to their respective surroundings, but the absolute values are excessively small at the landing site.

The strongly reduced B_{S0} values at the landing site might be attributed to unsuitable standard parameters considered for the region. For example, the width h_s of the opposition effect could be smaller at higher latitudes, but according to the maps of Sato et al. (2014), the width is almost constant within western Oceanus Procellarum (approx. 0.05 at both locations). Xu et al. (2022) found that the regolith at the landing site is more forward scattering compared to typical lunar regolith, which could also influence the estimated absolute B_{S0} values. Because for the landing site, there are only images at

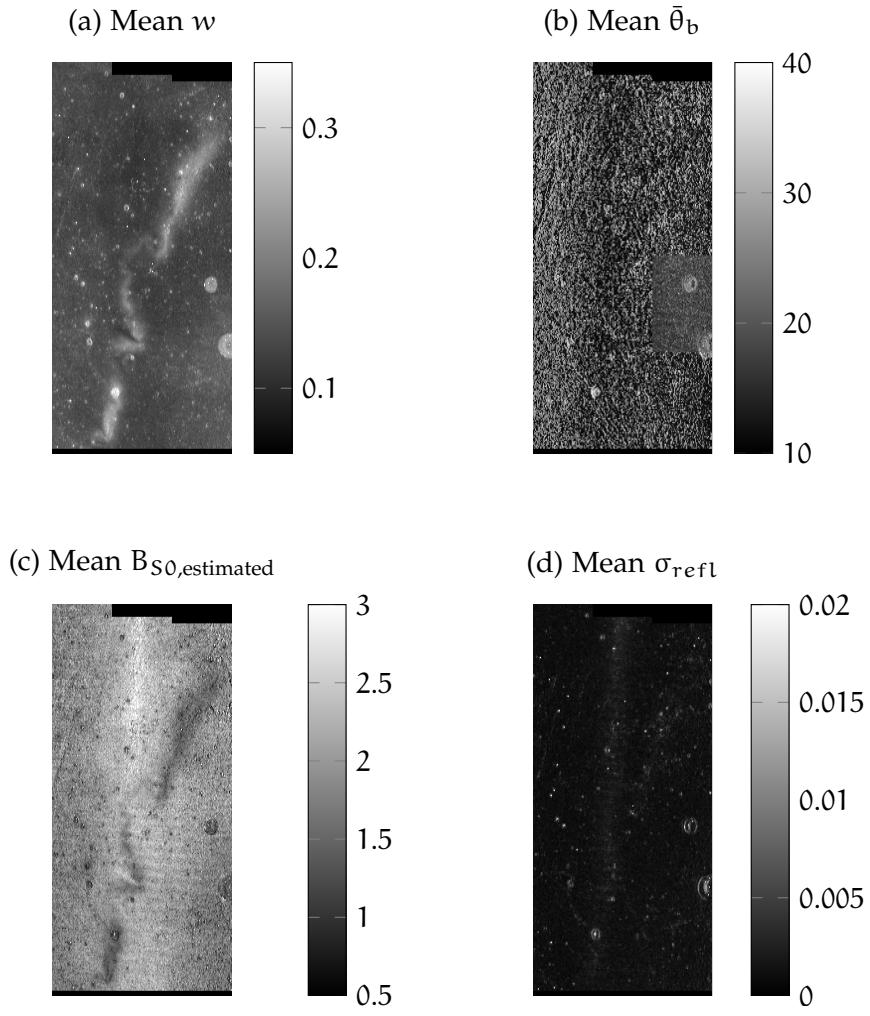

Figure 6.17: Mean predicted values in the tail region of Reiner Gamma of (a) the single scattering albedo w, (b) the surface roughness $\bar{\theta}_b$, (c) the opposition effect amplitude $B_{S0,estimated}$ and (c) the standard deviation of the likelihood function for the reflectance part σ_{refl}.

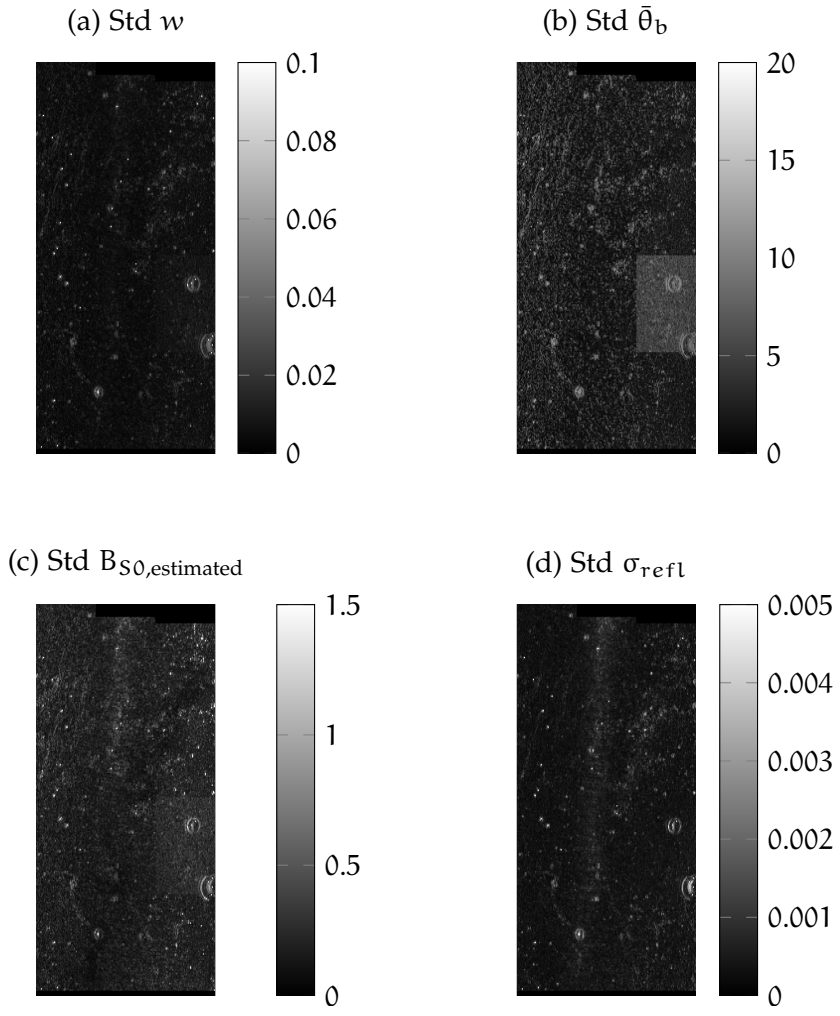

Figure 6.18: Uncertainties in standard deviation in the tail region of Reiner Gamma of (a) the single scattering albedo w, (b) the surface roughness $\bar{\theta}_b$, (c) the opposition effect amplitude $B_{S0,estimated}$ and (c) the standard deviation of the likelihood function for the reflectance part σ_{refl}.

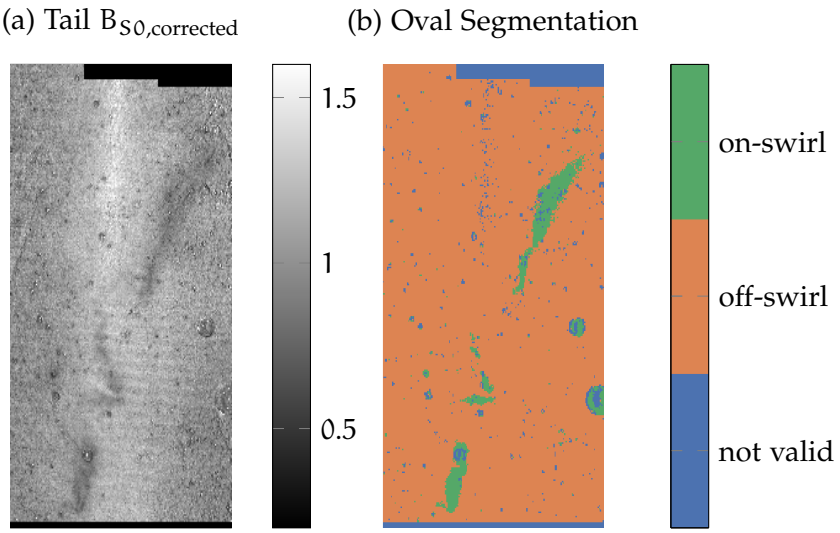

Figure 6.19: (a) Corrected B_{S0} to remove the influence of the albedo. (b) Segmentation of the region of interest based on the mean albedo. Areas with an albedo larger than 0.21 are labeled as on-swirl. Areas with a mean predicted $\sigma > 0.004$ are labeled as invalid because the uncertainties are too high.

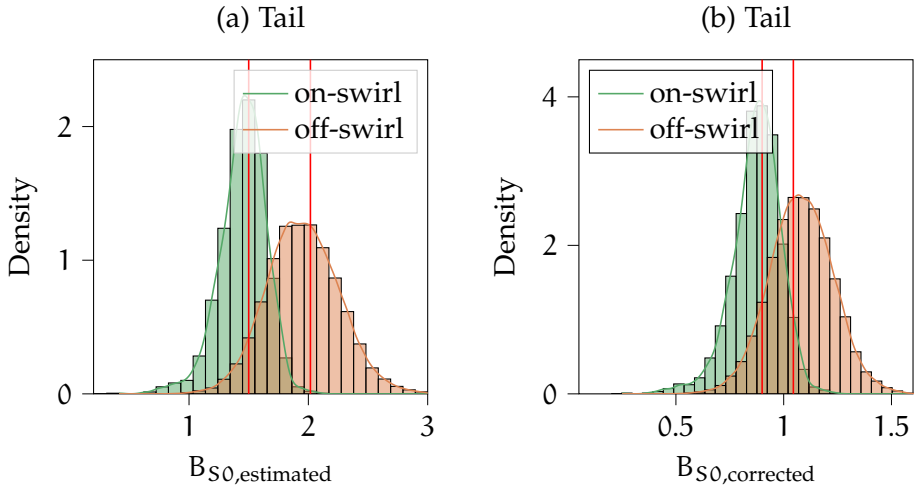

Figure 6.20: Distribution of (a) $B_{S0,estimated}$ and (b) $B_{S0,corrected}$ for on-swirl and off-swirl areas according to Figure 6.19b. The mean of $B_{S0,corrected}$ is 0.87 for the on-swirl pixels and 1.08 for the off-swirl pixels. The KS-Test statistics are $D = 0.725$ ($p = 0.000$) for the estimated values and $D = 0.607$ ($p = 0.000$ for the corrected values between on-swirl and off-swirl. The modes of the histograms are indicated by the red vertical lines.

medium to large phase angles available, the opposition effect is not fully constrained, as can be seen by the mean standard deviation of 0.7 over the landing site area before the landing and 0.51 after the landing, compared to 0.22 for the oval part of Reiner Gamma. The relative differences are, however, still strongly pronounced for the landing site. Importantly, the changes from the before to the after images show that a physical modification of the regolith structure has occurred.

This supports the findings of previous studies that the landing of a rocket on the lunar surface disturbs the microstructure of the regolith and leads to the destruction of the fairy castle structure, effectively making the regolith more compact (Clegg-Watkins et al., 2016; Kreslavsky and Shkuratov, 2003). Xu et al. (2022) investigated a very small area around the Chang'e-5 lander and set the opposition effect and roughness parameters to constant values. Therefore, the results presented in this work are not directly comparable to Xu et al. (2020). Whether the observed behavior is due to a reduced shadow hiding opposition effect or more forward scattering material cannot be reliably determined with NAC imagery. To effectively constrain the b and c parameters of the phase function, images acquired at phase angles well beyond 90 degrees are necessary.

Craters at both the landing site and the swirl coincide with higher uncertainties. The shape of the high uncertainty regions is not round like the crater but often split into two areas, one to the east and one to the west. The source of these uncertainties are shadows in large phase angle images. Considering the topography at each crater location alone, there should be light reflected even at the large phase angles. However, because of the crater topography, these regions are shadowed so that the model cannot adequately explain the large phase angle images, leading to higher uncertainties. In a qualitative analysis using only phase ratio images or in a modeling study with a classical least squares optimization, these areas would have to be carefully removed by hand, but because we are aware of the uncertainties, we can automatically omit them from the subsequent analysis.

The Reiner Gamma swirl consistently shows a reduced opposition effect strength, which is commonly interpreted to correspond to a more compact surface. At the landing site, we observed a similar behavior, and we know that the regolith has become more compact due to the rocket jet that blows away the porous top layer of the regolith. When comparing the Chang'e-5 landing site with the Reiner Gamma swirl, we find that both show a difference in compaction between the bright areas and the background. The difference found in opposition effect strength amounts to more than just the variation associated with albedo differences, suggesting that there must be a physical difference between the surface microstructure of bright and dark areas. The mean predicted roughness at the Reiner Gamma swirl shows only very weak anomalies correlated with the swirl albedo, whereas the landing site shows a more strongly reduced roughness. Shkuratov et al. (2010) theorized that the influence of multiple scattering of immature soils might counteract roughness effects. The gas pressure at the landing site is approximately 170 Pa on average in the exit plane and around 420 Pa at the nozzle wall (Zhang et al., 2022). At the swirls, Starukhina and Shkuratov (2004) calculated that a passing cometary coma creates pressures in the broad range of 40–400 Pa at the surface. Both regions exhibit pressures of a similar order of magnitude. The reduced roughness at the landing site is only visible in a small area around the lander of less than 20 m from the lander, where the pressure from the exhaust was highest. Possibly the pressure of a cometary

coma is closer to the lower end of the range and, therefore, not high enough to completely remove a regolith layer and transport it over much larger distances, but only to compact it without a significant change of the surface roughness. Additionally, the Chang'e-5 mission included an ascending stage that disturbed the surface structure of the regolith for a second time. Despite the presumably slightly higher exhaust pressure, the decrease in roughness is as small as 4 degrees (around 20 %) or less at the landing site compared to before the landing. Furthermore, the macroscopic surface roughness is influenced by the micrometeoroid bombardment, which is not reduced by the local magnetic fields. Therefore, the gardening of the soil could lead to a normalization of the roughness to background levels over time.

Three mechanisms might be considered to play a role in the appearance of lunar swirls. Firstly, reduced or abnormal space weathering due to magnetic shielding (e.g., Blewett et al., 2021; Trang and Lucey, 2019); secondly, the sorting of grains by electric or magnetic fields (e.g., Garrick-Bethell et al., 2011); and finally, the interaction of a cometary coma with the surface (e.g., Hess et al., 2020a; Pinet et al., 2000; Schultz and Srnka, 1980; Starukhina and Shkuratov, 2004; Syal and Schultz, 2015).

The spectral characteristics of swirls can, to a large extent, be explained by abnormal space weathering. This means that swirls lack nanophase iron (npFe) particles but there is no deficiency in larger microphase iron (mpFe) particles (Blewett et al., 2021; Trang and Lucey, 2019). However, this does not explain the photometric differences found between the swirl and its surroundings. Therefore, a difference in compaction or grain size should still be considered a contributing factor. The individual contributions of the various processes might be different depending on the area. The spectral significance of compaction defined by Hess et al. (2020a) is higher in the northeastern tail region of the Reiner Gamma swirl compared to the central oval. This is also consistent with the results presented in this work, where the difference between the opposition effect strength of the swirl and the surrounding terrain is more pronounced for the tail region.

Also, the grain size contributes strongly to the observed spectral and polarimetric properties of the lunar regolith (e.g., Bhatt et al., 2023), but the grain size variation cannot be constrained based on photometric data alone. If the surface at swirls was enriched with finely grained feldspathic dust by electrostatic sorting as proposed by Garrick-Bethell et al. (2011), the spectral effect would be similar to higher compaction and could lead to a reduced roughness as well. However, the forces might not be strong enough to significantly alter the surface structure to have an influence on the surface roughness. While most swirls are co-located with magnetic anomalies, there is a swirl structure in the Mare Moscoviense basin that is not protected by a magnetic field (e.g., Hess et al., 2020a) that would be necessary to create an electric field required for the sorting of dust. A general swirl formation mechanism has to be able to explain these occurrences as well.

The photometric observations favor the interpretation that swirls are created by some interactions between a comet's coma and the lunar surface (Pinet et al., 2000; Shevchenko, 1993; Syal and Schultz, 2015). This could, on the one hand, be attributed to the effects of the coma of an impacting comet. For example, Syal and Schultz (2015) showed that such a coma could cause scouring at scales of lunar swirls and can also explain the complex shapes. On the other hand, the passing of a comet and the interaction of the inner, denser parts of the coma with the surface would cause an effect similar to a landing

rocket jet (Shevchenko, 1993). The parts of a coma dense enough to be able to alter the physical surface properties are less than 1000 km in radius (Syal and Schultz, 2015) and could explain the extent of Reiner Gamma, which has a length of roughly 300 km and a width of 45 km at the central oval. Magnetic shielding can preserve swirls by reducing the solar wind influx so that the surface does not become mature and more porous as quickly as the unshielded surface, which would mean that the Mare Moscoviense swirl not associated with a magnetic field is younger than other swirls (Hess et al., 2019b).

6.5 CONCLUSION

We have introduced a Bayesian framework to estimate the Hapke photometric parameters and their uncertainties. Depending on the available data, a suitable model can be chosen, and it can be inferred directly where the parameters are reliable, which additional data are required to improve the estimation accuracy, or which parameters are difficult to estimate or mutually interrelated. In this way the interpretation of the results can be focused on the areas with higher confidence.

We applied this framework to the Chang'e-5 landing site and the Reiner Gamma swirl. Both regions exhibit excessively weak opposition effects and an increased albedo. The reduction of the opposition effect amplitude goes well beyond the expected value for typical lunar regolith of similar albedo, suggesting that the physical properties of the regolith are also distinct. For the landing site, which in addition exhibits clear characteristics of reduced roughness, this optical change is a direct consequence of the top regolith layer having been blown away by the descent and ascent rocket jets, leaving behind a more compact and smoother surface. At swirls, this difference between the swirl and its surroundings could be attributed to changes caused by a cometary coma acting similarly to a landing rocket jet. There appears to be a minor difference between the roughness of the swirl and the surroundings, but the difference is statistically not significant when compared to the uncertainties. This behavior might be attributed to slight differences in gas pressure between the swirl and the landing site, where the pressure was presumably relatively high so close to the lander. A cometary coma might not generate enough pressure to alter the surface roughness, but it could still destroys the fairy castle structure of the regolith and increase its compaction. The magnetic shielding would then serve as a preservation mechanism resulting in immature surface regolith with a fairy castle structure building up more slowly at the swirls than in the surrounding mare.

7

CONCLUSION

This thesis contributed new analysis and methodology regarding the compositional and photometric properties on the lunar surface. Compositionally, three dimensions were explored in this thesis. Namely, the the volatile species OH/H_2O, the abundance of nanophase and microphase iron particles, and the mineral composition. For the photometric analysis, we introduce a Bayesian framework to compare the Reiner Gamma swirl and the Chang'e 5 landing site.

At lunar swirls, space weathering and volatiles behave abnormally because the local magnetic field partly shields the surface from the solar wind. The data presented in this thesis shows that the OH/H_2O abundance at lunar swirls is reduced throughout the lunar day, and there is less variation between morning and midday. The decreased OH/H_2O abundance is another indicator that the magnetic fields can shield the surface from the solar wind. This shielding, however, does not fully explain the root of these bright albedo patterns. Two alternative factors that lead to a brightening of the surface are smaller grain sizes and higher compaction. This thesis introduces a spectral measure for the influence of compaction compared to reduced space weathering termed the compaction significance spectral index (CSSI). Substantial parts of the swirls exhibit spectral characteristics more consistent with a difference in compaction between on-swirl and off-swirl spectra. Because reduced space weathering cannot explain the creation and shape of lunar swirls, a swirl-forming event changing the porosity of the regolith might be considered.

Photometric effects are an indicator of the physical properties of the surface in general, and the opposition effect strength is a proxy for the porosity of the surface specifically. However, the parameters of a photometric model like the Hapke model are highly interrelated such that multiple solutions are possible. Thus, a Bayesian model was developed to obtain the uncertainties associated with the parameters. Because the effects of a landing rocket jet on the lunar regolith are relatively well understood, we compare the Chang'e 5 landing site to the Reiner Gamma swirl. A landing rocket jet blows away the top layer of the regolith, effectively destroying the very porous structure, and a more compact and smoother surface remains. The Reiner Gamma swirl shows similar photometric properties to the Chang'e 5 landing site. Both show reduced opposition effect strength and the Chang'e 5 landing site exhibits less roughness. Together with the spectral characteristics shown in this thesis, these results strongly indicate that swirls are less porous than the surrounding areas.

Consequently, the results presented in this thesis favor the interpretation that an interaction between a cometary coma and the surface forms swirls. When the comet passes over the surface, the coma acts similarly to the jet of a landing rocket that blows away the porous top layer and effectively compacts the surface. The magnetic shielding then slows the maturation and the build-up of the porosity of the surface so that the swirls are visible for longer timescales.

The OH/H_2O abundance on the lunar surface varies with the time of day but persists even when the temperatures are higher, and thus, loss processes dominate (Grumpe et al., 2019; Honniball et al., 2020; Wöhler et al., 2017b). Therefore, Wöhler et al. (2017b) considered a strongly and weakly bound component. Here, we analyze how the mineralogy might influence these binding states. The results indicate that the strongly bound component is less abundant for TiO_2, mainly ilmenite, but increased for plagioclase. The diurnal variations, however, are more extensive for TiO_2-rich mare areas. Similar to TiO_2, Mg-spinel-rich regions exhibit a reduced OH/H_2O band depth at lunar midday and, therefore, also less strongly bound OH/H_2O.

Similar to the photometric parameters for mature space-weathered lunar spectra, the fractional abundances of the constituent minerals are, to a certain extent, interchangeable. This thesis contributes by introducing a Bayesian inference framework to unmixing that also considers the effects of space weathering by including the nanophase and microphase particles as endmembers. This Bayesian unmixing framework is thoroughly tested and validated using laboratory spectra of varying maturity and synthetic spectra generated with the forward mixing model. We evaluate the relative influences of mineral darkening agents, space weathering components, and grain size on the uncertainties. For mature lunar spectra, we cannot determine the abundance of ilmenite and the space weathering components reliably and simultaneously if no prior information is available. Therefore, this thesis proposes using elemental abundances as priors in the unmixing. The results show that this prior effectively reduces the uncertainties of all endmember abundances. The mature lunar returned samples from the LSCC catalog are well reconstructed, and the high correlation between npFe and mpFe abundance and ferromagnetic resonance shows that the npFe and mpFe abundances can be determined reliably.

Finally, global mineral and space weathering maps are created using this framework. Additionally, we calculated local maps for the Reiner Gamma swirl. The global maps show a more substantial difference between the highland and mare for the npFe and mpFe abundance compared to Trang and Lucey (2019). This would be consistent with the LSCC samples where the amount of npFe and mpFe that can be created strongly depends on the FeO abundance. However, the space weathering maps of Reiner Gamma are consistent with Trang and Lucey (2019) and show no significant difference between mpFe on the swirl and the background but strongly varying npFe abundance.

7.1 FUTURE WORK

In the pursuit of unraveling the compositional and photometric properties of the Moon through reflectance spectroscopy, this thesis has made some contributions listed above. However, with these conclusions, a few possible research paths seem promising to further deepen our understanding of the Moon's surface and its evolution.

This thesis has quantified the effects of space weathering and compaction at lunar swirls. However, the discourse about which formation mechanism is the most likely still needs to be resolved. Larger phase angle images are necessary to obtain the parameters of the phase function, which might give more insight into the space weathering component. For example, telescopic images (Bhatt et al., 2023) could be integrated into the Bayesian Hapke inversion framework to achieve this. Another missing piece is a map of

the grain size at the swirls. For this, polarimetric data for different wavelengths can be used (Bhatt et al., 2023; Wöhler et al., 2023), or possibly thermal inertia.

The diurnal changes of OH/H_2O are by now qualitatively rather well understood. However, to quantify the abundance and to distinguish between OH and H_2O, data beyond 3-µm is necessary to fully capture the absorption feature. The Chandrayaan 2 spacecraft is carrying the imaging infrared spectrometer, which covers the wavelength range between 800 nm and 5000 nm and can give new insights into the diurnal variations of OH/H_2O (Chowdhury et al., 2020). The upcoming Lunar Trailblazer mission is supposed to carry the High-resolution Volatiles and Minerals Moon Mapper to characterize the mineral absorption bands at 1-µm and 2-µm and the OH/H_2O absorption at 3-µm (Ehlmann et al., 2021). Additionally, global maps for all times of the day would significantly improve our understanding. One component that is difficult to assess remotely is lunar glasses. The next step to evaluate the composition dependency of the volatiles is to model the influence based on different binding energies and compare it to the global maps, similar to (Grumpe et al., 2019) but considering the local composition.

Including the space weathering components in the unmixing adresses one of the major challenges in determening the mineral abundances of the lunar surface. Using a Bayesian approach yielded new insights into the uncertainties of the unmixing process. However, the global maps were created with a limited set of endmembers that cannot fully capture the versatile mineralogy. The influence of glasses needs to be included in the model to improve the fit in, e.g., pyroclastic deposits. For glasses in particular, however, a good characterization of the refractive indices is still missing (Varatharajan et al., 2023). The prior on the TiO_2 abundance is essential to constrain the unmixing. Therefore, better maps of TiO_2, e.g., from the Korean Pathfinder Lunar Orbiter Gamma Ray Spectrometer, would help to reduce uncertainties. Especially in areas where the regression approach (Bhatt et al., 2015, 2019), or the spectral ratio (Sato et al., 2017) are unreliable because the features are highly correlated with the maturity (e.g., at lunar swirls).

A

METHODS

A.1 PROBABILITY DISTRIBUTIONS

The descriptions of the Beta, Log-Normal, and Half-Normal distributions are adopted or adapted from the Appendix in Hess et al. (2023).

The probability density of a distribution is commonly parameterized using location and shape parameters, like the mean and the variance for a Normal distribution. In the following sections the probability distributions used in this work are briefly defined.

A.1.1 *Normal Distribution*

The Normal distribution also commonly referred to as the Gaussian distribution (Gauss, 1809) is the most widely used probability distribution. Its broad applicability can be attributed to the central limit theorem, which states that the mean of independent random variables approaches a normal distribution for a large number of samples even if the individual distributions are not normally distributed. It can be parameterized as follows (Bishop, 2006):

$$\mathcal{N}(x \mid \mu, \sigma) = \frac{1}{\sqrt{2\pi\sigma^2}} e^{-\frac{1}{2\sigma^2}(x-\mu)^2} \tag{75}$$

with the mean at μ and a standard deviation of σ and a variance of σ^2. The standard normal variable (S) with $\mathcal{N}(S \mid \mu = 0, \sigma = 1)$ can be converted to any other normally distributed variable (X) by applying $X = \mu + \sigma S$. Therefore, we commonly use the standard deviation instead of the variance in this work. Furthermore, the standard deviation has the same unit as the mean and is easier to interpret.

The Normal distribution can be extended to the multivariate case. For K variables the mean vector $\vec{\mu}$ has K components and the covariance matrix $\mathbf{\Sigma}$ is of dimensions $K \times K$ and must be symmetric and positive definite (Bishop, 2006). The probability density then becomes:

$$\mathcal{N}(\vec{x} \mid \vec{\mu}, \mathbf{\Sigma}) = \frac{1}{\sqrt{2\pi}^K} \frac{1}{|\mathbf{\Sigma}|^{1/2}} e^{-\frac{1}{2}(\vec{x}-\vec{\mu})^T \mathbf{\Sigma}^{-1} (\vec{x}-\vec{\mu})} \tag{76}$$

with $|\mathbf{\Sigma}|$ being the determinant of the covariance matrix $\mathbf{\Sigma}$, which is also termed generalized variance.

In this work, when evaluating the likelihood function for example, we often use the probability for each of the K data points individually and calculate the marginalized likelihood as:

$$p(\vec{x} \mid \vec{\mu}, \vec{\sigma}) = \prod_{i=1}^{K} \mathcal{N}(x_i \mid \mu_i, \sigma_i). \tag{77}$$

This is not be confused with the multivariate expression of the Normal distribution.

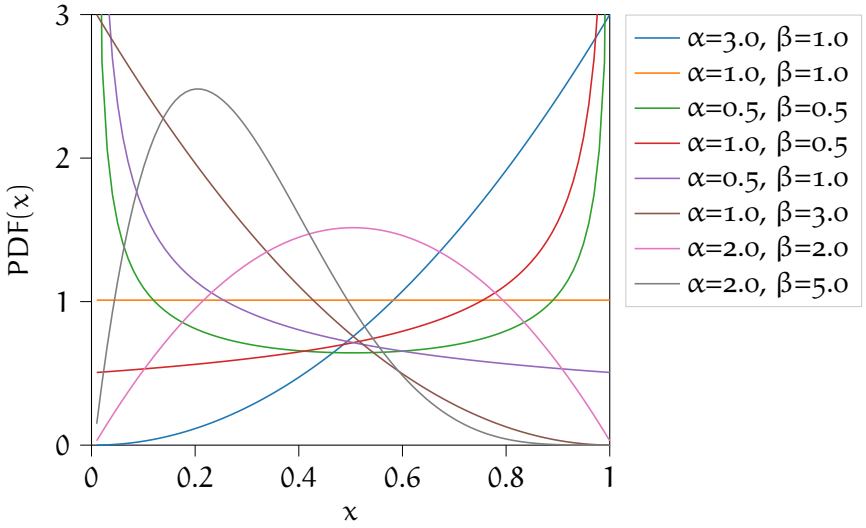

Figure A.1: Examples of a Beta distribution.

A.1.2 *Student t-distribution*

An infinite mixture of Normal distributions having the same mean (here zero) but different variances can be expressed with the Student-t distribution (Bishop, 2006). It was introduced in Student (1908) and is often used for hypothesis testing in so called t-Tests. Instead of a variance σ^2 the Student-t distribution is parameterized with the degrees of freedom variable m, which represents the number of variables that can be freely varied. The probability density is defined as (Bronstein et al., 2012):

$$\mathrm{St}(x \mid \mu = 0, m) = \frac{1}{\sqrt{m\pi}} \frac{\Gamma(\frac{m+1}{2})}{\Gamma(\frac{m}{2})} \left(1 + \frac{x^2}{m}\right)^{-\frac{m+1}{2}}, \tag{78}$$

with the Gamma function

$$\Gamma(z) = \int_0^\infty t^{z-1} e^{-t} dt. \tag{79}$$

A.1.3 *Beta Distribution*

The Beta distribution is a continous probability distribution limited to the interval [0,1] and is defined as

$$\mathrm{Beta}(x \mid \alpha, \beta) = \frac{\Gamma(\alpha + \beta)}{\Gamma(\alpha)\Gamma(\beta)} x^{\alpha-1}(1-x)^{\beta-1}, \tag{80}$$

with the Gamma function as defined in Equation 79. Some example distributions are shown in Figure A.1. For $\alpha = 1$ and $\beta = 1$ the PDF is equally distributed between zero and one. If α and β are larger than one the distribution has a single mode at $\frac{\alpha-1}{\alpha+\beta-2}$. It is bimodal if α and β are both below one. If $\alpha = 1$ and $\beta > 1$ the mode is zero and if $\alpha > 1$ and $\beta = 1$ the mode is at one.

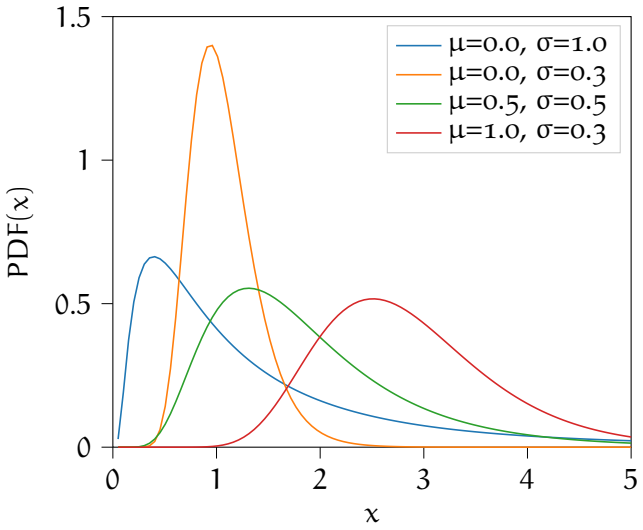

Figure A.2: Examples of Log-Normal distributions for varying mean and standard deviation.

A.1.4 *Log-Normal Distribution*

The Log-Normal distribution is given by

$$\text{LogNormal}(x \mid \mu, \tau) = \frac{1}{x}\sqrt{\frac{1}{2\pi\sigma^2}}e^{-\frac{1}{2\sigma^2}(\log(x)-\mu)^2} \tag{81}$$

and is only valid for positive values of x. The mean of the distribution is at $e^{\mu+\frac{\sigma^2}{2}}$. For example, for $\mu = 0$ and $\sigma = 0.1$ the mean is approximately 1.005. Some examples are shown in Figure A.2. The variance is given by $Var(X) = (e^{\sigma^2} - 1)e^{2\mu+\sigma^2}$.

A.1.5 *Half-Normal Distribution*

The Half-Normal distribution is a normal distribution with a mode at zero and all values below zero having zero probability. It is defined as

$$\text{HalfNormal}(x \mid \sigma) = \begin{cases} \sqrt{\frac{2}{\pi\sigma^2}}e^{\frac{-x^2}{2\sigma^2}} & \text{, for } x \geqslant 0 \\ 0 & \text{, for } x < 0 \end{cases} . \tag{82}$$

An example distribution with a variance of $\sigma^2 = 1$ is shown in Figure A.3.

A.1.6 *Dirichlet Distribution*

The Dirichlet distribution is the multivariate extension of the Beta distribution. It is defined over K variables, where the sum over all values is limited to one effectively also limiting each of the variables to the interval $[0, 1]$ resulting in a K-1 simplex. For each variable a shape parameter α is specified. The probability density is defined as:

$$\text{Dir}(\vec{x} \mid \vec{\alpha}) = \frac{1}{B(\vec{\alpha})}\prod_{i=1}^{K} x_i^{\alpha_i - 1}, \tag{83}$$

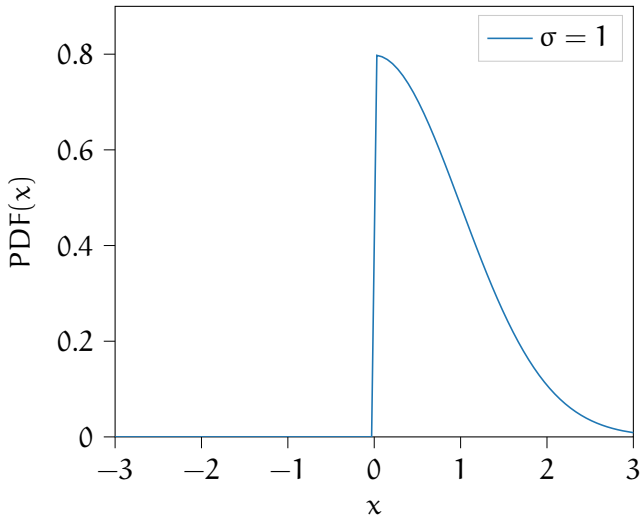

Figure A.3: Example Half-Normal distribution. The mode is always zero but the variance is variable.

where $B(\vec{\alpha})$ is the Beta function:

$$B(\vec{\alpha}) = \frac{\prod_{i=1}^{K} \Gamma(\alpha_i)}{\Gamma(\prod_{i=1}^{K} \alpha_i)}. \tag{84}$$

Figure A.4 shows two examplary dirichlet distributions for three variables. The 2-simplex is a triangle with the corners corresponding to a value of 1 for one of the variables and 0 for the others. Similarly to the Beta distribution if one $\alpha > 1$ for all variables the mode shifts towards higher values for the variable with the highest α (see Figure A.4a). If $\alpha_1 = 1$ the mode is $x_1 = 0$ (see Figure A.4b).

A.2 STATISTICAL METHODS

Throughout this work interrelationships between parameters are observed and interpreted. The most common measure for a linear relationships between two parameters is the correlation coefficient (see Section A.2.1). On the other hand, the case sometimes arises where we want to test whether two sets of samples stem from the same distribution or if they are systematically different. In these cases the Kolmogorov-Smirnow test (KS-Test) can be used (see Section A.2.2). Finally, we want to determine the probability density distribution of a set of a data set without assuming a parametric probability distribution. For this kernel density estimation (KDE) is briefly described in Section A.2.3.

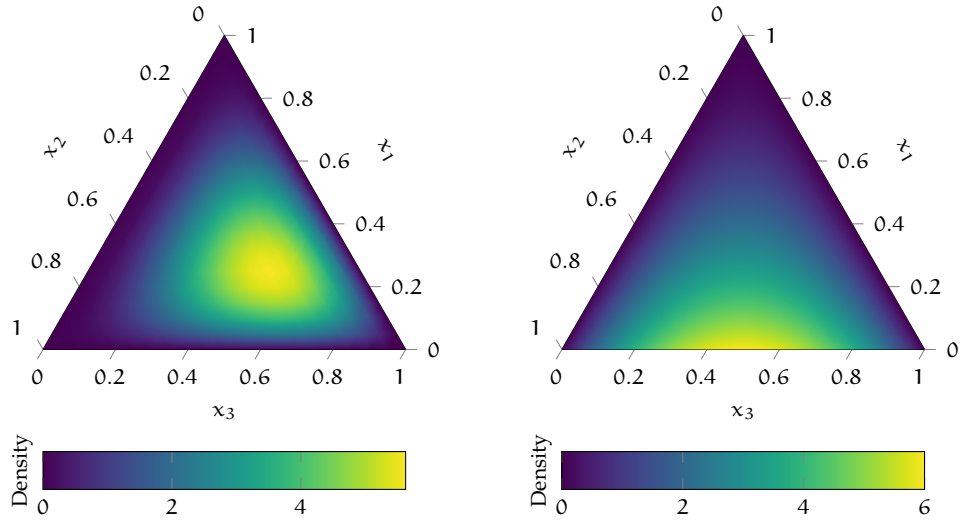

(a) $\alpha = [2, 2, 3]$ (b) $\alpha = [1, 2, 2]$

Figure A.4: Examples for the Dirichlet distribution for three variables. The shape parameters are listed in the captions of Figures (a) and (b).

A.2.1 *Correlation Coefficient*

Pearson's r is defined by the covariance of two variables that are observed normalized by the product of the standard deviations (e.g., Bronstein et al., 2012):

$$r = \frac{\sum_{i=1}^{N}(X_i - \mu_X)(Y_i - \mu_Y)}{\sqrt{\sum_{i=1}^{N}(X_i - \mu_X)^2 \sum_{j=1}^{N}(Y_j - \mu_Y)^2}}, \tag{85}$$

with $\mu_X = \sum_{i=1}^{N} \frac{X_i}{N}$ and $\mu_Y = \sum_{i=1}^{N} \frac{Y_i}{N}$ denoting the mean values of X and Y, respectively and N is the number of data points. Positive values of r describes a correlation where for increasing X also Y increases and for a value of 1 all of the data lies on a line. Similarly, for an $r = -1$ all values lie on a line for which X increases and Y decreases or vice versa.

The null hypothesis is that the data are drawn from normal distributions with a correlation of zero and the correlation is observed by chance. To test this hypothesis a t-test is performed. The test statistic is defined as (Bronstein et al., 2012):

$$t = \frac{r\sqrt{N-2}}{\sqrt{1-r^2}}. \tag{86}$$

The p-value then corresponds to the remaining probability density outside of the interval $[-t, t]$ of the Student-t distribution. If, for example, the significance level is set to $\alpha = 0.01$ for N=102 data points the degree of freedom is m=N-2=100 then the critical value of t is $t_{crit} = 2.626$. Consequently, p can be defined as:

$$p = 1 - \int_{-t}^{t} St(x \mid \mu = 0, m)dx. \tag{87}$$

Common significance levels (α) are 0.05 and 0.01 but the choice depends on the field of application. In research fields where the data sets have limited sizes, like psychology, these significance levels might be appropriate but for planetary science applications the critical value is commonly well below the 0.01 significance threshold. Here it should be noted that correlation does not necessarily imply a causality. In this work we use the categorization of strong ($|r| \geqslant 0.5$), moderate ($0.3 \geqslant |r| < 0.5$), and weak ($|r| < 0.3$) correlations.

A.2.2 *Kolmogorov-Smirnow Test*

Given are two sets of samples drawn from unknown distributions. In this situation the two sample KS-test can be used to test the null-hypotheses that both sets of samples are drawn from the same distribution. The two sample KS-test calculates a statistic:

$$D_{n,m} = \sup_x |F_{1,n}(x) - F_{2,m}(x)| \tag{88}$$

with the cumulative distribution functions $F_{1,n}(x)$ derived from n samples, and $F_{2,m}(x)$ from m samples. Therefore, the test statistic D is a measure of the maximum difference between the two empirical cumulative probability distributions.

The result is considered significant if the value of D is above a certain threshold, which can be calculated based on a chosen significance level α and the number of samples m and n as follows:

$$D_{n,m} > \sqrt{-\ln(\frac{\alpha}{2})\frac{1 + m/n}{2m}}. \tag{89}$$

For example, for $\alpha = 0.01$ and $n = 3000$ and $m = 1000$ the kolmogorov-smirnov score $D_{n,m}$ must be above 0.0594 such that the observation that the two distributions are different is considered significant. Inversely the significance level can be calculated from the KS-Test statistic D and the sizes of the data sets:

$$p = exp(\frac{-2D^2mn + \ln(2)n + \ln(2)m}{n + m}). \tag{90}$$

The test statistic can be considered a value for the degree of difference between the two distributions or the effect size. The test is sensitive to shape and location of the distributions. In contrast to, for example, the effect size measure Cohen-d, where only the means or locations of the distributions are compared and the variance is assumed to be equal. Therefore, the KS-test is also well suited for non-normally distributed variables.

A.2.3 *Kernel Density Estimation*

In Bayesian inference the case often arises that common parametric description of probability distributions (e.g. Normal-distribution) cannot accurately describe the posterior distribution. Consequently, a non-parameteric way to estimate the probability density is required. This way a reliable mode of the distribution can be calculated even if the distribution is multimodal. The simplest approach is to accumulate the values in bins of a histogram and normalize the bins to the number of samples overall. But in that case

the mode(s) and the shape of the PDF depend on the size of the bins. While for small bins noise influences the shape more strongly it is overfitted. However, for large bins the distribution becomes too smooth and details are lost. Additionally, the complexity of the histogram for multivariate posterior distributions increases exponentially with the number of parameters.

The Kernel Density Estimation (KDE) method (e.g., Bishop, 2006) follows a similar way of thinking as the histogram approach as that the probability mass for large number of N is the number of points in a specific area. If we try to estimate the probability density for a certain sample in the d dimensional parameter space we can for example count all the points in the local neighbourhood (e.g., a d-dimensional cube) and divide that number by the volume of the cube and the total number of samples from that distribution. This assumption is, however, only true if the probability density in that region is almost constant, therefore, requiring the region to be sufficiently small. But the region also has to be large enough and the local probability high enough that the samples from that region are representative of the distribution.

Generalizing this idea we can define a kernel function, which in the previous example was a hypercube of dimension d, but that can be chosen freely. We sum up the points in that volume according to the kernel function so that the number of points K is (Bishop, 2006):

$$K = \sum_{n=1}^{N} k\left(\frac{x - x_n}{h}\right), \tag{91}$$

for a sample x from all the samples $\vec{x}$ and a distance measure h. In the case of a hypercube h would be side length of the cube. By normalizing K with the number of samples and volume, we obtain the probability density for each sample x from $\vec{x}$ (Bishop, 2006):

$$p(\vec{x}) = \frac{1}{N} \sum_{n=1}^{N} \frac{1}{h^d} k\left(\frac{x - x_n}{h}\right). \tag{92}$$

In this work, we will exclusively use a Gaussian kernel function (see Equation 75) so that the estimated probability density for all samples in $\vec{x}$ becomes (Bishop, 2006):

$$p(\vec{x}) = \frac{1}{N} \sum_{n=1}^{N} \frac{1}{\sqrt{2\pi h^2}^d} e^{\frac{\|x - x_n\|^2}{2h^2}}. \tag{93}$$

In the case of a Gaussian kernel function h is equal to the standard deviation of the Normal distributions. Similarly to the bin width, poor choice of the h parameter can lead to an over smoothing so that the multimodal distribution cannot be characterized, or too small so that noise strongly influences the density estimates.

B

UNMIXING RESULTS

B.1 SYNTHETIC

Table B.1: Origin of endmember samples 5.3.4.1 and 5.3.4.3. All samples except for the AG-TJM-009 Hypersthene endmember, which is of meteoritic origin, originate from Earth.

Sample ID	Mineral	Origin	Abbreviation
AG-TJM-009	Hypersthene	Johnstown Meteorite	OPX
AG-TJM-010	Augite	Kakanui, New Zealand	CPXB
PO-EAC-056	Olivine	Green sand beach near S Point, HI	OLV
PL-EAC-029	Plagioclase	Ylijarvi, Ylamaaa, Kimi, Finland	PLG
PP-ALS-105	Diopside	Trail Creek, Grand Co., CO	CPXA
SC-EAC-034	Ilmenite	Telemark, Norway	ILM

Table B.2: Detailed results for the unmixing of the synthetically generated spectra by using the forward mixing model. Only a uniform prior on the elemental and mineral abundances was set.

	mix0				mix1				mix2			
	mode	mean	std	theo	mode	mean	std	theo	mode	mean	std	theo
OPX	9.96	9.96	0.04	10.00	9.90	9.82	0.14	10.00	10.72	10.66	0.27	10.00
CPXB	39.95	40.00	0.17	40.00	40.20	40.33	0.89	40.00	35.72	37.75	1.58	40.00
OLV	4.45	4.44	0.36	5.00	7.70	8.35	1.84	5.00	17.93	19.20	3.19	5.00
PLG	30.03	29.93	0.41	30.00	29.29	28.45	1.71	30.00	14.05	16.75	3.05	30.00
CPXA	15.43	15.38	0.50	15.00	12.56	12.43	2.13	15.00	18.91	13.99	3.56	15.00
ILM	0.52	0.83	0.63	0.00	0.79	1.50	1.21	0.00	6.20	3.60	2.21	0.00
npFe	0.00	0.00	0.00	0.00	0.00	0.00	0.00	0.00	0.00	0.01	0.01	0.00
mpFe	0.00	0.00	0.00	0.00	0.40	0.40	0.00	0.40	0.78	0.79	0.01	0.80
SUM	100.35	100.54	-	100.00	100.45	100.87	-	100.00	103.53	101.96	-	100.00

	mix3				mix4				mix5			
	mode	mean	std	theo	mode	mean	std	theo	mode	mean	std	theo
OPX	9.38	9.91	0.34	10.00	10.38	10.46	0.19	10.00	9.75	9.87	0.24	10.00
CPXB	42.00	39.32	1.69	40.00	38.45	39.69	1.30	40.00	39.46	38.86	1.60	40.00
OLV	28.84	32.95	5.25	5.00	6.76	2.48	2.05	5.00	19.90	8.40	4.56	5.00
PLG	16.21	12.86	4.53	30.00	25.94	28.15	1.97	30.00	23.96	27.86	2.83	30.00
CPXA	1.75	2.73	2.17	15.00	18.38	18.76	2.92	15.00	4.59	13.21	5.03	15.00
ILM	3.43	4.19	2.49	0.00	0.23	1.62	1.40	0.00	5.16	4.61	2.42	0.00
npFe	0.05	0.05	0.01	0.00	0.58	0.57	0.01	0.60	0.65	0.61	0.02	0.60
mpFe	1.18	1.16	0.02	1.20	0.01	0.01	0.00	0.00	0.38	0.40	0.01	0.40
SUM	101.61	101.95	-	100.00	100.14	101.15	-	100.00	102.83	102.81	-	100.00

	mix6				mix7				mix8			
	mode	mean	std	theo	mode	mean	std	theo	mode	mean	std	theo
OPX	8.52	8.63	0.33	10.00	11.80	10.68	0.58	10.00	11.45	11.64	0.39	10.00
CPXB	45.91	45.51	1.59	40.00	32.82	39.95	2.91	40.00	34.97	31.75	2.44	40.00
OLV	15.93	14.98	5.36	5.00	10.50	11.96	7.17	5.00	10.93	2.41	2.63	5.00
PLG	26.78	26.74	4.51	30.00	21.09	29.30	5.31	30.00	19.60	18.35	2.76	30.00
CPXA	1.07	2.26	2.07	15.00	23.37	7.81	5.97	15.00	22.59	35.25	5.78	15.00
ILM	4.07	4.32	2.50	0.00	1.60	1.90	1.55	0.00	0.66	1.64	1.38	0.00
npFe	0.69	0.69	0.02	0.60	0.55	0.57	0.03	0.60	1.35	1.32	0.02	1.40
mpFe	0.76	0.76	0.02	0.80	1.24	1.29	0.03	1.20	0.01	0.01	0.00	0.00
SUM	102.27	102.45	-	100.00	101.18	101.60	-	100.00	100.21	101.04	-	100.00

	mix9				mix10				mix11			
	mode	mean	std	theo	mode	mean	std	theo	mode	mean	std	theo
OPX	9.49	10.46	0.49	10.00	9.73	9.44	0.37	10.00	9.85	8.86	0.54	10.00
CPXB	39.81	36.92	2.93	40.00	43.53	44.30	1.60	40.00	39.66	46.41	2.76	40.00
OLV	24.36	9.75	6.68	5.00	1.38	5.74	3.67	5.00	8.56	9.25	5.80	5.00
PLG	20.17	22.45	3.81	30.00	34.41	36.19	2.89	30.00	21.03	27.35	4.11	30.00
CPXA	4.62	19.44	8.02	15.00	10.23	3.59	2.98	15.00	20.08	7.79	5.47	15.00
ILM	2.39	1.74	1.46	0.00	2.53	2.07	1.59	0.00	1.70	1.54	1.31	0.00
npFe	1.49	1.40	0.04	1.40	1.44	1.46	0.02	1.40	1.38	1.44	0.03	1.40
mpFe	0.33	0.37	0.02	0.40	0.81	0.79	0.02	0.80	1.18	1.22	0.03	1.20
SUM	100.83	100.77	-	100.00	101.81	101.33	-	100.00	100.88	101.19	-	100.00

Table B.3: Continuation of Table B.2...

	mix12				mix13				mix14			
	mode	mean	std	theo	mode	mean	std	theo	mode	mean	std	theo
OPX	10.12	10.09	0.50	10.00	11.32	11.44	0.48	10.00	6.82	6.71	0.60	10.00
CPXB	38.98	38.96	2.82	40.00	37.77	36.57	2.24	40.00	38.30	39.38	1.64	40.00
OLV	9.98	9.79	5.69	5.00	24.28	35.29	6.59	5.00	2.19	2.24	1.72	5.00
PLG	20.40	19.74	3.17	30.00	10.95	7.23	3.54	30.00	46.35	47.81	2.04	30.00
CPXA	19.90	20.65	7.95	15.00	13.71	7.60	5.67	15.00	5.40	2.57	1.89	15.00
ILM	1.39	1.81	1.49	0.00	3.21	1.93	1.56	0.00	0.56	1.77	1.43	0.00
npFe	2.16	2.15	0.04	2.20	2.21	2.23	0.03	2.20	2.23	2.29	0.04	2.20
mpFe	0.01	0.01	0.01	0.00	0.34	0.32	0.02	0.40	0.76	0.74	0.02	0.80
SUM	100.77	101.04	-	100.00	101.24	100.06	-	100.00	99.62	100.48	-	100.00

	mix15				mix16				mix17			
	mode	mean	std	theo	mode	mean	std	theo	mode	mean	std	theo
OPX	10.26	11.09	0.74	10.00	9.18	9.16	0.07	9.20	9.15	9.07	0.18	9.20
CPXB	39.32	35.75	3.99	40.00	36.61	36.79	0.36	36.80	38.39	38.89	1.13	36.80
OLV	34.60	11.31	8.60	5.00	5.37	5.39	0.99	4.60	3.70	5.90	2.80	4.60
PLG	13.31	18.96	4.36	30.00	26.24	26.32	1.18	27.60	28.17	28.03	2.41	27.60
CPXA	0.63	21.99	10.56	15.00	13.98	13.66	1.51	13.80	11.91	9.52	3.24	13.80
ILM	2.64	1.53	1.31	0.00	9.72	9.87	1.98	8.00	10.12	9.71	2.56	8.00
npFe	2.29	2.17	0.06	2.20	0.00	0.00	0.00	0.00	0.00	0.01	0.01	0.00
mpFe	1.12	1.18	0.03	1.20	0.00	0.00	0.00	0.00	0.41	0.41	0.01	0.40
SUM	100.75	100.63	-	100.00	101.10	101.20	-	100.00	101.42	101.12	-	100.00

	mix18				mix19				mix20			
	mode	mean	std	theo	mode	mean	std	theo	mode	mean	std	theo
OPX	9.00	9.10	0.30	9.20	10.51	10.39	0.33	9.20	8.70	8.68	0.20	9.20
CPXB	37.53	40.48	1.75	36.80	36.97	37.34	1.64	36.80	35.94	35.97	1.24	36.80
OLV	7.98	8.05	3.45	4.60	12.19	14.88	3.52	4.60	1.62	2.77	1.96	4.60
PLG	21.63	26.48	3.49	27.60	21.72	25.06	3.40	27.60	29.46	29.81	1.85	27.60
CPXA	16.51	9.28	3.77	13.80	10.24	4.85	2.97	13.80	16.07	14.84	3.51	13.80
ILM	5.78	4.08	2.38	8.00	8.48	6.38	2.67	8.00	8.49	7.69	2.65	8.00
npFe	0.00	0.01	0.01	0.00	0.00	0.01	0.01	0.00	0.59	0.60	0.01	0.60
mpFe	0.78	0.79	0.01	0.80	1.19	1.21	0.02	1.20	0.00	0.00	0.00	0.00
SUM	98.43	97.46	-	100.00	100.11	98.89	-	100.00	100.29	99.77	-	100.00

	mix21				mix22				mix23			
	mode	mean	std	theo	mode	mean	std	theo	mode	mean	std	theo
OPX	9.76	9.52	0.30	9.20	10.59	10.38	0.41	9.20	8.79	8.92	0.51	9.20
CPXB	33.89	36.21	1.75	36.80	31.31	33.40	2.69	36.80	34.73	40.23	2.33	36.80
OLV	7.94	15.35	6.16	4.60	13.24	3.79	3.24	4.60	25.13	9.92	5.96	4.60
PLG	24.23	23.85	4.10	27.60	19.22	23.85	3.99	27.60	17.94	28.95	5.17	27.60
CPXA	16.15	7.67	5.11	13.80	17.75	21.58	6.11	13.80	4.11	4.22	3.59	13.80
ILM	7.91	5.71	2.72	8.00	6.63	5.00	2.67	8.00	9.32	7.87	3.06	8.00
npFe	0.59	0.61	0.02	0.60	0.58	0.57	0.02	0.60	0.64	0.65	0.02	0.60
mpFe	0.40	0.39	0.01	0.40	0.77	0.79	0.02	0.80	1.15	1.22	0.03	1.20
SUM	99.88	98.31	-	100.00	98.76	97.99	-	100.00	100.02	100.11	-	100.00

Table B.4: Continuation of Table B.3...

	mix24				mix25				mix26			
	mode	mean	std	theo	mode	mean	std	theo	mode	mean	std	theo
OPX	9.07	8.84	0.34	9.20	8.74	7.87	0.45	9.20	8.40	8.31	0.57	9.20
CPXB	32.63	36.47	1.91	36.80	28.60	33.90	2.65	36.80	35.43	38.13	2.52	36.80
OLV	6.87	10.07	4.20	4.60	1.43	7.63	5.54	4.60	16.20	6.57	5.01	4.60
PLG	23.48	28.49	2.95	27.60	22.84	27.96	4.17	27.60	33.20	34.10	4.20	27.60
CPXA	19.23	8.47	5.43	13.80	31.59	15.13	7.00	13.80	0.58	6.23	5.01	13.80
ILM	9.69	6.86	2.81	8.00	2.72	4.79	2.65	8.00	3.24	5.38	2.75	8.00
npFe	1.38	1.41	0.02	1.40	1.34	1.41	0.03	1.40	1.44	1.43	0.03	1.40
mpFe	0.00	0.01	0.01	0.00	0.32	0.33	0.02	0.40	0.82	0.85	0.02	0.80
SUM	100.97	99.20	-	100.00	95.91	97.28	-	100.00	97.06	98.72	-	100.00

	mix27				mix28				mix29			
	mode	mean	std	theo	mode	mean	std	theo	mode	mean	std	theo
OPX	10.34	10.40	0.73	9.20	9.83	9.22	0.51	9.20	8.96	7.92	0.64	9.20
CPXB	35.38	35.52	3.77	36.80	33.60	36.95	2.28	36.80	31.58	37.27	2.93	36.80
OLV	22.17	18.77	9.94	4.60	7.57	1.88	1.80	4.60	8.91	4.14	3.35	4.60
PLG	17.95	18.42	6.88	27.60	33.05	38.10	3.16	27.60	29.98	35.60	4.17	27.60
CPXA	7.58	10.64	7.87	13.80	7.74	7.37	4.35	13.80	13.88	8.37	5.73	13.80
ILM	5.51	4.75	2.76	8.00	7.25	3.35	2.26	8.00	4.02	5.15	2.80	8.00
npFe	1.35	1.34	0.04	1.40	2.17	2.19	0.03	2.20	2.12	2.21	0.04	2.20
mpFe	1.31	1.32	0.05	1.20	0.01	0.01	0.00	0.00	0.46	0.44	0.02	0.40
SUM	98.92	98.50	-	100.00	99.03	96.88	-	100.00	97.33	98.43	-	100.00

	mix30				mix31				mix32			
	mode	mean	std	theo	mode	mean	std	theo	mode	mean	std	theo
OPX	7.83	7.53	0.62	9.20	8.28	8.67	0.77	9.20	8.44	8.42	0.11	8.40
CPXB	35.17	39.00	2.65	36.80	32.99	37.86	2.66	36.80	34.50	34.78	0.53	33.60
OLV	1.69	3.31	2.81	4.60	5.19	4.45	3.48	4.60	2.93	3.53	1.27	4.20
PLG	28.91	35.79	4.03	27.60	29.75	35.14	3.87	27.60	27.17	27.42	1.47	25.20
CPXA	18.48	7.14	5.08	13.80	15.75	5.79	4.24	13.80	10.99	10.02	1.77	12.60
ILM	5.87	4.99	2.62	8.00	4.00	5.02	2.72	8.00	16.06	15.64	2.28	16.00
npFe	2.22	2.25	0.04	2.20	2.22	2.27	0.05	2.20	0.00	0.00	0.00	0.00
mpFe	0.70	0.76	0.03	0.80	1.01	1.03	0.04	1.20	0.00	0.00	0.00	0.00
SUM	97.95	97.76	-	100.00	95.96	96.94	-	100.00	100.08	99.81	-	100.00

	mix33				mix34				mix35			
	mode	mean	std	theo	mode	mean	std	theo	mode	mean	std	theo
OPX	8.84	8.81	0.20	8.40	8.70	8.31	0.41	8.40	8.95	8.35	0.54	8.40
CPXB	30.77	30.99	1.14	33.60	28.80	33.86	3.05	33.60	29.79	34.01	3.11	33.60
OLV	7.95	7.58	2.04	4.20	10.34	5.00	3.82	4.20	1.83	2.41	1.87	4.20
PLG	21.05	20.71	2.68	25.20	13.78	22.96	5.34	25.20	30.05	31.94	3.13	25.20
CPXA	15.07	15.24	2.63	12.60	23.43	15.10	6.09	12.60	14.84	8.71	5.22	12.60
ILM	16.60	17.59	2.72	16.00	11.47	12.02	2.84	16.00	11.47	11.80	2.47	16.00
npFe	0.00	0.00	0.00	0.00	0.01	0.02	0.01	0.00	0.00	0.02	0.01	0.00
mpFe	0.39	0.39	0.01	0.40	0.71	0.75	0.02	0.80	1.17	1.18	0.01	1.20
SUM	100.29	100.92	-	100.00	96.53	97.25	-	100.00	96.93	97.23	-	100.00

Table B.5: Continuation of B.4...

	mix36				mix37				mix38			
	mode	mean	std	theo	mode	mean	std	theo	mode	mean	std	theo
OPX	8.50	8.83	0.23	8.40	8.07	8.18	0.33	8.40	8.88	8.70	0.35	8.40
CPXB	34.34	32.56	1.26	33.60	32.76	32.42	2.06	33.60	29.24	32.76	1.83	33.60
OLV	5.05	1.05	0.95	4.20	5.44	6.78	4.66	4.20	15.53	17.31	6.27	4.20
PLG	27.43	28.19	2.07	25.20	24.61	24.11	3.83	25.20	14.18	21.09	5.26	25.20
CPXA	8.46	14.40	2.78	12.60	12.57	12.18	5.67	12.60	13.77	3.74	3.29	12.60
ILM	16.38	13.48	2.74	16.00	16.89	16.27	2.95	16.00	22.09	16.69	3.10	16.00
npFe	0.61	0.59	0.01	0.60	0.62	0.62	0.02	0.60	0.60	0.61	0.02	0.60
mpFe	0.00	0.00	0.00	0.00	0.37	0.37	0.01	0.40	0.80	0.82	0.02	0.80
SUM	100.17	98.51	-	100.00	100.35	99.94	-	100.00	103.69	100.30	-	100.00

	mix39				mix40				mix41			
	mode	mean	std	theo	mode	mean	std	theo	mode	mean	std	theo
OPX	7.84	8.03	0.49	8.40	9.47	9.68	0.45	8.40	12.33	11.47	0.60	8.40
CPXB	33.49	31.33	2.62	33.60	28.82	29.51	2.66	33.60	21.59	27.39	3.07	33.60
OLV	16.91	15.45	7.72	4.20	8.65	3.16	2.58	4.20	21.82	25.18	9.20	4.20
PLG	23.60	21.88	6.03	25.20	20.77	22.75	3.76	25.20	3.80	8.45	5.38	25.20
CPXA	1.98	6.93	5.59	12.60	17.43	20.38	6.31	12.60	24.76	12.35	8.62	12.60
ILM	16.63	17.02	3.22	16.00	12.47	12.15	3.03	16.00	14.23	12.78	3.08	16.00
npFe	0.64	0.63	0.03	0.60	1.35	1.35	0.03	1.40	1.32	1.35	0.04	1.40
mpFe	1.23	1.22	0.03	1.20	0.00	0.01	0.01	0.00	0.40	0.40	0.03	0.40
SUM	100.44	100.64	-	100.00	97.61	97.63	-	100.00	98.53	97.63	-	100.00

	mix42				mix43				mix44			
	mode	mean	std	theo	mode	mean	std	theo	mode	mean	std	theo
OPX	7.77	7.45	0.50	8.40	6.92	6.17	0.69	8.40	9.65	9.22	0.60	8.40
CPXB	37.35	38.83	1.61	33.60	28.02	32.31	2.35	33.60	27.34	31.30	4.25	33.60
OLV	8.60	2.77	2.21	4.20	2.42	4.39	3.39	4.20	0.93	1.32	1.27	4.20
PLG	29.65	32.75	2.86	25.20	34.79	36.52	3.60	25.20	19.21	22.58	5.31	25.20
CPXA	0.53	2.84	2.50	12.60	11.86	3.98	3.25	12.60	27.80	20.93	8.71	12.60
ILM	15.59	14.32	3.01	16.00	13.06	14.96	3.00	16.00	12.29	11.68	2.40	16.00
npFe	1.45	1.46	0.03	1.40	1.45	1.52	0.04	1.40	2.05	2.10	0.06	2.20
mpFe	0.78	0.78	0.02	0.80	1.07	1.04	0.03	1.20	0.01	0.01	0.01	0.00
SUM	99.49	98.95	-	100.00	97.07	98.33	-	100.00	97.22	97.04	-	100.00

	mix45				mix46				mix47			
	mode	mean	std	theo	mode	mean	std	theo	mode	mean	std	theo
OPX	8.70	8.68	0.56	8.40	8.72	7.77	0.68	8.40	8.95	8.37	0.83	8.40
CPXB	31.09	30.84	2.74	33.60	29.76	34.15	2.39	33.60	21.72	33.91	3.53	33.60
OLV	21.08	16.03	7.45	4.20	15.91	4.38	4.14	4.20	41.39	9.24	6.99	4.20
PLG	21.24	21.32	5.26	25.20	29.26	34.42	3.75	25.20	10.19	26.87	5.71	25.20
CPXA	3.13	8.10	6.44	12.60	0.49	4.51	3.90	12.60	0.11	6.11	5.19	12.60
ILM	12.32	13.42	3.24	16.00	13.75	12.24	3.05	16.00	14.12	12.32	3.28	16.00
npFe	2.21	2.19	0.04	2.20	2.18	2.23	0.05	2.20	2.24	2.22	0.06	2.20
mpFe	0.42	0.43	0.03	0.40	0.80	0.79	0.03	0.80	0.97	1.11	0.05	1.20
SUM	97.56	98.39	-	100.00	97.89	97.47	-	100.00	96.48	96.83	-	100.00

Table B.6: Detailed results for the unmixing of the synthetically generated spectra by using the forward mixing model. A prior on the TiO_2 and the Al_2O_3 was set with $\alpha_{elem} = 40$. All results are displayed in wt.%.

	mix0				mix1				mix2			
	mode	mean	std	theo	mode	mean	std	theo	mode	mean	std	theo
OPX	9.98	9.96	0.04	10.00	9.82	9.82	0.14	10.00	10.81	10.59	0.26	10.00
CPXB	39.93	40.04	0.16	40.00	40.43	40.51	0.88	40.00	37.38	39.10	1.50	40.00
OLV	4.65	4.65	0.28	5.00	8.04	8.81	1.78	5.00	16.38	18.69	2.89	5.00
PLG	30.23	30.31	0.21	30.00	29.53	29.28	1.50	30.00	18.97	20.83	2.48	30.00
CPXA	15.20	14.98	0.32	15.00	12.07	11.43	1.99	15.00	16.25	10.46	3.19	15.00
ILM	0.07	0.17	0.13	0.00	0.07	0.19	0.14	0.00	0.04	0.23	0.16	0.00
npFe	0.00	0.00	0.00	0.00	0.00	0.00	0.00	0.00	0.00	0.01	0.01	0.00
mpFe	0.00	0.00	0.00	0.00	0.40	0.40	0.00	0.40	0.79	0.80	0.01	0.80
SUM	100.06	100.12	-	100.00	99.98	100.04	-	100.00	99.83	99.90	-	100.00

	mix3				mix4				mix5			
	mode	mean	std	theo	mode	mean	std	theo	mode	mean	std	theo
OPX	9.71	9.81	0.34	10.00	10.22	10.45	0.20	10.00	10.27	9.87	0.23	10.00
CPXB	40.04	40.80	1.53	40.00	41.91	40.26	1.31	40.00	36.38	39.75	1.46	40.00
OLV	20.00	24.58	4.53	5.00	5.24	2.24	1.60	5.00	9.73	10.86	4.62	5.00
PLG	20.60	21.22	3.38	30.00	30.74	29.87	1.65	30.00	26.09	30.55	2.43	30.00
CPXA	9.34	3.12	2.34	15.00	12.00	17.28	3.12	15.00	17.32	8.75	4.43	15.00
ILM	0.27	0.31	0.18	0.00	0.02	0.15	0.13	0.00	0.01	0.25	0.17	0.00
npFe	0.02	0.03	0.01	0.00	0.59	0.58	0.01	0.60	0.60	0.62	0.02	0.60
mpFe	1.19	1.19	0.02	1.20	0.02	0.02	0.00	0.00	0.39	0.40	0.01	0.40
SUM	99.96	99.84	-	100.00	100.13	100.24	-	100.00	99.79	100.03	-	100.00

	mix6				mix7				mix8			
	mode	mean	std	theo	mode	mean	std	theo	mode	mean	std	theo
OPX	8.66	8.71	0.32	10.00	10.93	10.60	0.52	10.00	11.26	11.44	0.39	10.00
CPXB	45.95	45.72	1.51	40.00	38.38	40.78	2.39	40.00	33.64	33.52	2.29	40.00
OLV	15.09	12.66	4.60	5.00	0.54	11.20	5.91	5.00	6.16	2.28	1.85	5.00
PLG	29.39	30.60	3.51	30.00	33.17	31.71	4.14	30.00	20.38	21.46	2.52	30.00
CPXA	0.55	2.03	1.80	15.00	17.61	6.07	4.41	15.00	28.52	31.32	4.86	15.00
ILM	0.37	0.28	0.18	0.00	0.01	0.26	0.18	0.00	0.09	0.11	0.10	0.00
npFe	0.69	0.68	0.01	0.60	0.52	0.57	0.02	0.60	1.35	1.33	0.02	1.40
mpFe	0.76	0.77	0.02	0.80	1.30	1.30	0.03	1.20	0.00	0.01	0.01	0.00
SUM	100.00	99.99	-	100.00	100.63	100.63	-	100.00	100.04	100.14	-	100.00

	mix9				mix10				mix11			
	mode	mean	std	theo	mode	mean	std	theo	mode	mean	std	theo
OPX	9.90	10.30	0.45	10.00	9.95	9.51	0.36	10.00	8.78	8.77	0.47	10.00
CPXB	40.11	38.58	2.54	40.00	42.65	43.97	1.56	40.00	46.96	47.21	2.19	40.00
OLV	20.28	10.13	6.04	5.00	0.46	6.67	3.90	5.00	18.30	9.47	5.32	5.00
PLG	23.43	25.36	3.16	30.00	34.71	36.59	2.81	30.00	25.38	29.05	3.24	30.00
CPXA	5.48	15.29	6.99	15.00	12.23	3.14	2.56	15.00	0.62	5.72	4.58	15.00
ILM	0.71	0.20	0.17	0.00	0.44	0.27	0.17	0.00	0.04	0.19	0.15	0.00
npFe	1.46	1.41	0.03	1.40	1.47	1.45	0.02	1.40	1.44	1.44	0.03	1.40
mpFe	0.35	0.37	0.02	0.40	0.77	0.79	0.02	0.80	1.23	1.22	0.02	1.20
SUM	99.91	99.85	-	100.00	100.44	100.15	-	100.00	100.09	100.40	-	100.00

Table B.7: Continuation of Table B.6...

	mix12				mix13				mix14			
	mode	mean	std	theo	mode	mean	std	theo	mode	mean	std	theo
OPX	9.69	9.86	0.47	10.00	11.67	11.36	0.48	10.00	7.78	6.91	0.67	10.00
CPXB	40.97	40.94	2.49	40.00	36.11	38.91	2.19	40.00	36.06	38.95	1.80	40.00
OLV	13.27	11.35	5.42	5.00	21.55	24.65	5.87	5.00	1.58	2.73	2.15	5.00
PLG	21.95	22.60	2.75	30.00	13.10	14.57	2.81	30.00	43.90	47.63	2.27	30.00
CPXA	13.91	15.13	6.96	15.00	16.85	9.78	5.80	15.00	9.63	3.00	2.45	15.00
ILM	0.06	0.17	0.14	0.00	0.22	0.24	0.16	0.00	0.32	0.31	0.18	0.00
npFe	2.17	2.17	0.03	2.20	2.20	2.23	0.03	2.20	2.24	2.28	0.04	2.20
mpFe	0.01	0.01	0.01	0.00	0.34	0.34	0.02	0.40	0.71	0.73	0.03	0.80
SUM	99.84	100.04	-	100.00	99.50	99.50	-	100.00	99.27	99.54	-	100.00

	mix15				mix16				mix17			
	mode	mean	std	theo	mode	mean	std	theo	mode	mean	std	theo
OPX	10.65	10.71	0.68	10.00	9.17	9.16	0.07	9.20	9.17	9.07	0.18	9.20
CPXB	38.27	38.87	3.35	40.00	36.58	36.82	0.34	36.80	38.30	38.93	1.14	36.80
OLV	31.86	11.69	7.30	5.00	5.02	5.55	0.89	4.60	5.63	6.02	2.66	4.60
PLG	17.13	23.21	3.62	30.00	26.62	26.63	0.84	27.60	28.07	28.34	2.08	27.60
CPXA	1.09	15.30	8.40	15.00	14.22	13.38	1.25	13.80	10.43	9.24	3.01	13.80
ILM	0.31	0.18	0.14	0.00	9.10	9.32	1.37	8.00	9.18	9.18	1.51	8.00
npFe	2.27	2.19	0.05	2.20	0.00	0.00	0.00	0.00	0.01	0.01	0.01	0.00
mpFe	1.13	1.19	0.03	1.20	0.00	0.00	0.00	0.00	0.41	0.41	0.01	0.40
SUM	99.32	99.96	-	100.00	100.72	100.85	-	100.00	100.78	100.79	-	100.00

	mix18				mix19				mix20			
	mode	mean	std	theo	mode	mean	std	theo	mode	mean	std	theo
OPX	9.06	9.07	0.30	9.20	10.42	10.31	0.34	9.20	8.59	8.68	0.20	9.20
CPXB	39.78	40.16	1.71	36.80	37.90	37.60	1.71	36.80	37.84	35.96	1.22	36.80
OLV	6.37	7.04	3.25	4.60	8.88	13.89	3.35	4.60	6.50	2.64	1.86	4.60
PLG	24.81	24.46	2.97	27.60	25.63	24.97	3.01	27.60	30.40	29.36	1.29	27.60
CPXA	12.17	11.42	3.67	13.80	9.26	5.16	2.91	13.80	8.87	15.16	3.34	13.80
ILM	7.30	7.44	1.33	8.00	7.84	8.09	1.41	8.00	7.29	8.47	1.45	8.00
npFe	0.00	0.01	0.01	0.00	0.00	0.01	0.01	0.00	0.62	0.60	0.01	0.60
mpFe	0.79	0.79	0.01	0.80	1.21	1.22	0.02	1.20	0.00	0.00	0.00	0.00
SUM	99.49	99.59	-	100.00	99.93	100.02	-	100.00	99.50	100.27	-	100.00

	mix21				mix22				mix23			
	mode	mean	std	theo	mode	mean	std	theo	mode	mean	std	theo
OPX	9.59	9.46	0.31	9.20	10.29	10.32	0.40	9.20	8.81	8.91	0.49	9.20
CPXB	34.15	36.45	1.82	36.80	32.00	33.40	2.44	36.80	40.92	40.28	2.16	36.80
OLV	7.35	13.25	5.71	4.60	7.35	2.62	2.02	4.60	12.34	9.98	5.34	4.60
PLG	22.40	23.82	3.18	27.60	22.22	22.89	2.99	27.60	28.19	28.40	3.99	27.60
CPXA	17.44	8.89	5.46	13.80	20.39	22.87	5.16	13.80	1.66	4.34	3.58	13.80
ILM	10.75	7.87	1.39	8.00	6.49	7.48	1.37	8.00	8.48	8.75	1.52	8.00
npFe	0.59	0.61	0.02	0.60	0.56	0.56	0.02	0.60	0.65	0.65	0.02	0.60
mpFe	0.40	0.40	0.01	0.40	0.79	0.79	0.01	0.80	1.21	1.22	0.03	1.20
SUM	101.68	99.74	-	100.00	98.73	99.58	-	100.00	100.40	100.66	-	100.00

Table B.8: Continuation of Table B.7...

	mix24				mix25				mix26			
	mode	mean	std	theo	mode	mean	std	theo	mode	mean	std	theo
OPX	8.95	8.78	0.33	9.20	8.19	7.85	0.44	9.20	8.11	8.31	0.57	9.20
CPXB	35.29	36.75	1.77	36.80	30.64	33.65	2.57	36.80	39.11	37.55	2.75	36.80
OLV	7.76	10.36	3.89	4.60	17.57	7.06	5.10	4.60	6.45	7.52	4.99	4.60
PLG	24.72	27.79	2.37	27.60	20.13	26.11	3.22	27.60	33.96	31.06	3.88	27.60
CPXA	14.48	8.10	4.91	13.80	14.85	16.77	6.89	13.80	4.77	7.74	5.60	13.80
ILM	10.06	8.38	1.47	8.00	6.93	7.63	1.40	8.00	7.90	8.24	1.48	8.00
npFe	1.40	1.41	0.02	1.40	1.42	1.41	0.03	1.40	1.42	1.42	0.03	1.40
mpFe	0.00	0.01	0.01	0.00	0.31	0.33	0.01	0.40	0.85	0.84	0.02	0.80
SUM	101.26	100.15	-	100.00	98.30	99.07	-	100.00	100.30	100.42	-	100.00

	mix27				mix28				mix29			
	mode	mean	std	theo	mode	mean	std	theo	mode	mean	std	theo
OPX	9.91	10.16	0.73	9.20	10.09	9.36	0.55	9.20	7.60	7.94	0.65	9.20
CPXB	33.72	37.10	3.46	36.80	32.74	35.56	2.70	36.80	34.07	36.30	3.07	36.80
OLV	1.76	12.13	6.96	4.60	0.02	1.76	1.66	4.60	14.62	5.14	3.96	4.60
PLG	20.94	21.37	4.13	27.60	30.17	33.73	3.30	27.60	29.16	32.25	3.68	27.60
CPXA	26.43	12.28	8.00	13.80	19.06	11.52	5.49	13.80	6.11	10.43	6.24	13.80
ILM	8.68	7.47	1.38	8.00	6.77	7.43	1.39	8.00	8.00	8.13	1.47	8.00
npFe	1.26	1.33	0.04	1.40	2.12	2.17	0.04	2.20	2.23	2.21	0.04	2.20
mpFe	1.36	1.34	0.04	1.20	0.00	0.00	0.00	0.00	0.39	0.43	0.02	0.40
SUM	101.44	100.50	-	100.00	98.85	99.37	-	100.00	99.56	100.19	-	100.00

	mix30				mix31				mix32			
	mode	mean	std	theo	mode	mean	std	theo	mode	mean	std	theo
OPX	8.16	7.50	0.64	9.20	8.99	8.73	0.81	9.20	8.45	8.42	0.11	8.40
CPXB	34.83	38.72	2.63	36.80	31.42	36.89	3.15	36.80	34.50	34.75	0.53	33.60
OLV	1.96	3.93	3.03	4.60	7.41	5.65	4.13	4.60	2.96	3.34	1.19	4.20
PLG	26.88	33.34	3.32	27.60	23.59	31.73	3.83	27.60	26.89	27.07	1.31	25.20
CPXA	18.91	8.03	4.96	13.80	18.19	7.61	5.31	13.80	11.18	10.36	1.63	12.60
ILM	10.10	8.18	1.47	8.00	9.66	8.08	1.46	8.00	16.15	16.29	1.87	16.00
npFe	2.22	2.25	0.04	2.20	2.19	2.26	0.05	2.20	0.00	0.00	0.00	0.00
mpFe	0.74	0.75	0.03	0.80	1.01	1.02	0.04	1.20	0.00	0.00	0.00	0.00
SUM	100.83	99.70	-	100.00	99.27	98.68	-	100.00	100.14	100.23	-	100.00

	mix33				mix34				mix35			
	mode	mean	std	theo	mode	mean	std	theo	mode	mean	std	theo
OPX	8.85	8.78	0.20	8.40	8.76	8.24	0.39	8.40	8.21	8.13	0.39	8.40
CPXB	30.86	31.25	1.08	33.60	31.77	34.37	2.40	33.60	31.66	34.73	2.09	33.60
OLV	7.60	7.33	1.93	4.20	3.69	3.65	2.87	4.20	7.42	3.33	2.64	4.20
PLG	20.99	21.42	2.33	25.20	18.86	22.73	3.35	25.20	24.99	29.44	3.07	25.20
CPXA	15.24	14.69	2.30	12.60	20.67	15.34	5.50	12.60	13.09	8.71	4.40	12.60
ILM	16.98	17.27	2.10	16.00	16.21	14.59	2.01	16.00	10.73	14.55	2.23	16.00
npFe	0.00	0.00	0.00	0.00	0.02	0.02	0.01	0.00	0.03	0.03	0.01	0.00
mpFe	0.39	0.39	0.01	0.40	0.75	0.76	0.01	0.80	1.12	1.17	0.02	1.20
SUM	100.52	100.73	-	100.00	99.96	98.93	-	100.00	96.09	98.89	-	100.00

Table B.9: Continuation of Table B.8...

	mix36				mix37				mix38			
	mode	mean	std	theo	mode	mean	std	theo	mode	mean	std	theo
OPX	8.91	8.82	0.22	8.40	8.01	8.17	0.32	8.40	8.57	8.64	0.35	8.40
CPXB	31.94	32.55	1.21	33.60	35.57	32.49	2.02	33.60	34.43	33.40	1.60	33.60
OLV	0.66	0.98	0.87	4.20	14.73	5.94	4.03	4.20	15.51	14.69	4.96	4.20
PLG	26.81	27.14	1.70	25.20	24.30	24.35	3.04	25.20	24.20	23.26	3.63	25.20
CPXA	16.34	14.89	2.59	12.60	0.78	12.60	5.48	12.60	1.18	3.77	3.19	12.60
ILM	14.45	15.23	2.02	16.00	17.02	16.68	2.11	16.00	16.31	16.57	2.16	16.00
npFe	0.59	0.59	0.01	0.60	0.68	0.62	0.02	0.60	0.61	0.60	0.02	0.60
mpFe	0.00	0.00	0.00	0.00	0.37	0.37	0.01	0.40	0.83	0.83	0.02	0.80
SUM	99.10	99.62	-	100.00	100.41	100.23	-	100.00	100.19	100.34	-	100.00

	mix39				mix40				mix41			
	mode	mean	std	theo	mode	mean	std	theo	mode	mean	std	theo
OPX	8.98	8.13	0.59	8.40	9.63	9.61	0.44	8.40	11.77	11.40	0.60	8.40
CPXB	28.47	31.69	2.45	33.60	28.72	29.79	2.50	33.60	27.72	29.47	3.14	33.60
OLV	18.43	12.95	5.56	4.20	1.08	3.03	2.55	4.20	6.01	11.39	6.90	4.20
PLG	22.90	24.61	3.57	25.20	20.93	21.88	3.06	25.20	16.22	16.22	3.66	25.20
CPXA	5.74	6.64	4.33	12.60	24.32	20.38	5.89	12.60	23.43	16.61	8.82	12.60
ILM	13.94	16.28	2.27	16.00	14.43	14.33	2.07	16.00	13.68	13.70	2.03	16.00
npFe	0.61	0.62	0.02	0.60	1.35	1.36	0.03	1.40	1.30	1.34	0.04	1.40
mpFe	1.21	1.23	0.03	1.20	0.01	0.01	0.01	0.00	0.45	0.45	0.02	0.40
SUM	98.46	100.30	-	100.00	99.11	99.02	-	100.00	98.83	98.78	-	100.00

	mix42				mix43				mix44			
	mode	mean	std	theo	mode	mean	std	theo	mode	mean	std	theo
OPX	6.64	7.42	0.52	8.40	7.13	6.40	0.77	8.40	8.62	8.72	0.50	8.40
CPXB	37.45	38.80	1.70	33.60	27.30	31.09	3.00	33.60	34.90	34.99	2.71	33.60
OLV	10.87	3.42	2.58	4.20	3.90	5.29	3.46	4.20	0.79	1.85	1.71	4.20
PLG	25.74	31.16	2.61	25.20	30.38	33.35	3.48	25.20	25.44	24.89	3.42	25.20
CPXA	2.70	3.05	2.40	12.60	13.53	6.28	4.87	12.60	15.22	14.23	5.74	12.60
ILM	16.52	16.30	2.19	16.00	17.99	17.29	2.03	16.00	13.16	13.84	2.03	16.00
npFe	1.47	1.47	0.03	1.40	1.48	1.51	0.04	1.40	2.16	2.16	0.04	2.20
mpFe	0.75	0.77	0.02	0.80	1.06	1.04	0.03	1.20	0.00	0.01	0.01	0.00
SUM	99.91	100.15	-	100.00	100.24	99.71	-	100.00	98.13	98.53	-	100.00

	mix45				mix46				mix47			
	mode	mean	std	theo	mode	mean	std	theo	mode	mean	std	theo
OPX	9.17	8.59	0.54	8.40	8.13	7.72	0.69	8.40	8.38	8.26	0.81	8.40
CPXB	30.06	31.74	2.36	33.60	29.33	33.81	2.60	33.60	30.68	33.86	3.12	33.60
OLV	1.84	13.91	6.05	4.20	14.94	5.23	3.93	4.20	4.50	9.46	5.67	4.20
PLG	21.92	22.24	3.59	25.20	23.72	31.50	3.57	25.20	21.01	25.01	4.08	25.20
CPXA	21.04	8.08	5.92	12.60	7.06	5.68	4.30	12.60	19.10	6.88	5.62	12.60
ILM	16.85	14.87	2.08	16.00	15.49	15.36	2.13	16.00	12.93	14.82	2.11	16.00
npFe	2.13	2.20	0.04	2.20	2.21	2.23	0.05	2.20	2.11	2.21	0.06	2.20
mpFe	0.47	0.44	0.02	0.40	0.71	0.78	0.03	0.80	1.05	1.10	0.04	1.20
SUM	100.89	99.42	-	100.00	98.68	99.31	-	100.00	96.59	98.28	-	100.00

B.2 LABORATORY SAMPLES

Table B.10: Origins of endmember catalog for section 5.3.4.2 taken from Rommel et al. (2017). All samples were provided by the University of Göttingen and originate from Earth.

Mineral	Origin	Abbreviation
Pargasite	Merelani Hill, Tanzania	PRG
Augite	Paškopole, Czech Republic	AUG
Olivine	China	OLV
Plagioclase	Nordingrå, Sweden	PLG
Ferrosilite	Mansjöberg, Sweden	FS
Ilmenite	Rogaland, Norway	ILM

Table B.11: Detailed results for the unmixing of fresh laboratory spectra from Rommel et al. (2017). The results were obtained without the use of an elemental prior.

	mix0				mix1				mix2			
	mode	mean	std	theo	mode	mean	std	theo	mode	mean	std	theo
PRG	25.64	25.58	0.60	9.20	36.76	36.95	0.59	18.50	46.07	46.24	0.47	28.10
AUG	0.11	0.14	0.11	0.00	0.05	0.11	0.09	0.00	0.05	0.10	0.08	0.00
OLV	0.02	0.05	0.05	0.00	0.02	0.05	0.04	0.00	0.02	0.04	0.04	0.00
PLG	74.08	74.13	0.70	90.80	63.10	62.83	0.67	81.50	54.16	53.88	0.57	71.90
FS	0.30	0.28	0.09	0.00	0.16	0.14	0.08	0.00	0.11	0.10	0.06	0.00
ILM	14.05	13.91	1.01	0.00	13.87	14.04	0.98	0.00	11.24	11.47	0.84	0.00
npFe	0.00	0.00	0.00	-	0.00	0.00	0.00	-	0.00	0.00	0.00	-
mpFe	0.00	0.00	0.00	-	0.00	0.00	0.00	-	0.00	0.00	0.00	-
SUM	114.20	114.09	-	100.00	113.98	114.12	-	100.00	111.65	111.83	-	100.00

	mix3				mix4				mix5			
	mode	mean	std	theo	mode	mean	std	theo	mode	mean	std	theo
PRG	78.24	78.19	0.32	68.00	83.10	82.98	0.42	78.50	90.02	90.04	0.36	89.10
AUG	0.16	0.14	0.08	0.00	0.20	0.13	0.08	0.00	0.02	0.04	0.04	0.00
OLV	0.04	0.06	0.05	0.00	0.02	0.05	0.05	0.00	0.01	0.03	0.03	0.00
PLG	22.32	22.36	0.39	32.00	17.40	17.55	0.48	21.50	10.73	10.67	0.38	10.90
FS	0.05	0.06	0.04	0.00	0.04	0.07	0.05	0.00	0.06	0.07	0.05	0.00
ILM	6.69	6.74	0.60	0.00	9.39	9.32	0.74	0.00	7.77	7.80	0.64	0.00
npFe	0.00	0.00	0.00	-	0.00	0.00	0.00	-	0.00	0.00	0.00	-
mpFe	0.00	0.00	0.00	-	0.00	0.00	0.00	-	0.00	0.00	0.00	-
SUM	107.50	107.55	-	100.00	110.14	110.10	-	100.00	108.61	108.65	-	100.00

	mix6				mix7				mix8			
	mode	mean	std	theo	mode	mean	std	theo	mode	mean	std	theo
PRG	18.40	18.85	1.71	0.00	29.32	30.11	3.69	0.00	42.99	46.99	4.15	0.00
AUG	0.03	0.08	0.08	0.00	0.10	0.19	0.19	0.00	0.22	0.30	0.29	0.00
OLV	0.56	0.62	0.34	0.00	3.66	3.80	0.89	0.00	5.39	6.82	1.10	0.00
PLG	71.75	71.21	1.89	92.80	44.17	43.11	4.19	85.10	19.52	14.11	4.79	76.90
FS	11.97	11.88	0.24	7.20	25.71	25.64	0.56	14.90	33.38	32.96	0.68	23.10
ILM	0.33	0.61	0.57	0.00	0.23	0.68	0.63	0.00	0.13	0.82	0.79	0.00
npFe	0.00	0.00	0.00	-	0.00	0.00	0.00	-	0.00	0.00	0.00	-
mpFe	0.00	0.00	0.00	-	0.00	0.00	0.00	-	0.00	0.00	0.00	-
SUM	103.05	103.25	-	100.00	103.19	103.52	-	100.00	101.63	101.99	-	100.00

	mix9				mix10				mix11			
	mode	mean	std	theo	mode	mean	std	theo	mode	mean	std	theo
PRG	33.45	38.70	1.84	0.00	22.57	21.22	1.76	0.00	12.33	11.52	0.82	0.00
AUG	0.26	0.72	0.72	0.00	0.58	1.27	1.10	0.00	0.41	0.57	0.50	0.00
OLV	5.65	4.77	1.11	0.00	2.22	2.21	1.13	0.00	0.20	0.50	0.40	0.00
PLG	7.00	2.09	1.80	58.80	0.95	1.58	1.59	38.00	0.31	0.72	0.65	26.30
FS	57.00	57.11	0.76	41.20	79.98	80.17	0.87	62.00	93.44	93.39	0.52	73.70
ILM	0.62	0.64	0.61	0.00	0.20	0.48	0.46	0.00	0.20	0.43	0.41	0.00
npFe	0.00	0.00	0.00	-	0.00	0.01	0.01	-	0.00	0.01	0.01	-
mpFe	0.00	0.00	0.00	-	0.00	0.00	0.00	-	0.00	0.00	0.00	-
SUM	103.97	104.03	-	100.00	106.49	106.93	-	100.00	106.89	107.12	-	100.00

Table B.12: Continuation of Table B.11...

	mix12				mix13				mix14			
	mode	mean	std	theo	mode	mean	std	theo	mode	mean	std	theo
PRG	4.23	3.73	1.15	0.00	8.59	7.30	3.79	0.00	56.13	55.49	1.09	56.50
AUG	3.36	2.81	1.46	0.00	1.54	3.51	3.22	54.10	0.29	0.56	0.54	0.00
OLV	0.38	1.05	0.75	0.00	8.99	6.81	3.89	0.00	0.12	0.34	0.32	0.00
PLG	0.24	0.61	0.58	13.70	1.08	3.10	2.72	0.00	0.44	0.80	0.74	0.00
FS	99.88	99.79	0.20	86.30	83.70	83.11	3.19	45.90	49.77	49.68	0.86	43.50
ILM	0.14	0.36	0.36	0.00	0.30	0.85	0.80	0.00	0.26	0.51	0.49	0.00
npFe	0.00	0.00	0.00	-	0.02	0.03	0.03	-	0.01	0.01	0.01	-
mpFe	0.00	0.00	0.00	-	0.01	0.01	0.01	-	0.00	0.00	0.00	-
SUM	108.23	108.35	-	100.00	104.20	104.68	-	100.00	107.01	107.38	-	100.00

	mix15				mix16			
	mode	mean	std	theo	mode	mean	std	theo
PRG	0.66	1.40	1.25	0.00	44.63	32.04	16.29	0.00
AUG	0.17	1.16	1.14	0.00	3.87	7.30	6.50	0.00
OLV	30.77	28.54	2.75	53.60	4.56	7.10	6.05	0.00
PLG	0.60	1.13	1.05	0.00	3.81	15.67	13.11	0.00
FS	75.76	76.17	2.66	46.40	4.95	5.92	4.58	54.60
ILM	0.18	0.46	0.45	0.00	31.72	24.85	11.52	45.40
npFe	0.00	0.01	0.01	-	6.43	6.82	1.85	-
mpFe	0.00	0.01	0.01	-	0.02	0.06	0.06	-
SUM	108.13	108.85	-	100.00	93.54	92.88	-	100.00

Table B.13: Detailed results for the unmixing of laboratory spectra from Rommel et al. (2017).

	mix0				mix1				mix2			
	mode	mean	std	theo	mode	mean	std	theo	mode	mean	std	theo
PRG	21.88	21.67	0.90	9.20	33.77	33.63	0.95	18.50	43.93	44.07	0.73	28.10
AUG	0.02	0.04	0.04	0.00	0.02	0.04	0.04	0.00	0.01	0.03	0.03	0.00
OLV	0.01	0.02	0.02	0.00	0.02	0.02	0.02	0.00	0.00	0.02	0.02	0.00
PLG	81.64	81.82	0.91	90.80	69.74	69.84	0.97	81.50	59.24	59.06	0.75	71.90
FS	0.02	0.04	0.04	0.00	0.01	0.03	0.03	0.00	0.01	0.02	0.02	0.00
ILM	0.01	0.01	0.01	0.00	0.01	0.03	0.03	0.00	0.03	0.07	0.06	0.00
npFe	0.01	0.01	0.00	-	0.01	0.01	0.00	-	0.01	0.01	0.00	-
mpFe	0.00	0.00	0.00	-	0.00	0.00	0.00	-	0.00	0.00	0.00	-
SUM	103.58	103.60	-	100.00	103.57	103.60	-	100.00	103.23	103.26	-	100.00

	mix3				mix4				mix5			
	mode	mean	std	theo	mode	mean	std	theo	mode	mean	std	theo
PRG	77.58	77.62	0.36	68.00	82.40	82.36	0.56	78.50	90.02	89.82	0.46	89.10
AUG	0.01	0.02	0.02	0.00	0.02	0.03	0.03	0.00	0.01	0.02	0.02	0.00
OLV	0.01	0.01	0.01	0.00	0.01	0.02	0.02	0.00	0.01	0.01	0.01	0.00
PLG	24.60	24.50	0.40	32.00	20.35	20.37	0.60	21.50	12.25	12.40	0.52	10.90
FS	0.01	0.01	0.01	0.00	0.01	0.02	0.01	0.00	0.01	0.01	0.01	0.00
ILM	1.04	1.13	0.42	0.00	1.10	1.07	0.44	0.00	1.77	1.88	0.59	0.00
npFe	0.00	0.00	0.00	-	0.00	0.00	0.00	-	0.00	0.00	0.00	-
mpFe	0.00	0.00	0.00	-	0.00	0.00	0.00	-	0.00	0.00	0.00	-
SUM	103.24	103.31	-	100.00	103.89	103.86	-	100.00	104.06	104.15	-	100.00

	mix6				mix7				mix8			
	mode	mean	std	theo	mode	mean	std	theo	mode	mean	std	theo
PRG	0.02	0.04	0.04	0.00	0.03	0.07	0.07	0.00	0.07	0.13	0.12	0.00
AUG	0.01	0.02	0.02	0.00	0.02	0.05	0.05	0.00	0.02	0.08	0.08	0.00
OLV	0.03	0.07	0.07	0.00	0.10	0.26	0.23	0.00	0.15	0.42	0.37	0.00
PLG	90.55	90.52	0.18	92.80	76.18	75.95	0.36	85.10	66.02	65.87	0.53	76.90
FS	12.95	12.97	0.21	7.20	28.22	28.27	0.39	14.90	37.72	37.46	0.55	23.10
ILM	0.00	0.00	0.00	0.00	0.00	0.00	0.00	0.00	0.00	0.00	0.00	0.00
npFe	0.00	0.00	0.00	-	0.00	0.00	0.00	-	0.00	0.00	0.00	-
mpFe	0.00	0.00	0.00	-	0.00	0.00	0.00	-	0.00	0.00	0.00	-
SUM	103.56	103.63	-	100.00	104.54	104.60	-	100.00	103.98	103.96	-	100.00

	mix9				mix10				mix11			
	mode	mean	std	theo	mode	mean	std	theo	mode	mean	std	theo
PRG	0.19	0.24	0.22	0.00	0.17	0.41	0.36	0.00	0.33	0.65	0.51	0.00
AUG	0.05	0.15	0.14	0.00	0.12	0.24	0.22	0.00	0.09	0.22	0.21	0.00
OLV	0.25	0.57	0.50	0.00	0.36	0.81	0.68	0.00	0.15	0.33	0.30	0.00
PLG	44.15	43.97	0.74	58.80	24.72	24.01	0.86	38.00	12.33	11.87	0.68	26.30
FS	60.72	60.54	0.77	41.20	81.94	81.98	0.82	62.00	94.25	94.14	0.54	73.70
ILM	0.00	0.00	0.00	0.00	0.00	0.01	0.01	0.00	0.00	0.01	0.01	0.00
npFe	0.00	0.01	0.01	-	0.00	0.01	0.01	-	0.00	0.01	0.01	-
mpFe	0.00	0.00	0.00	-	0.00	0.00	0.00	-	0.00	0.00	0.00	-
SUM	105.36	105.47	-	100.00	107.31	107.45	-	100.00	107.15	107.22	-	100.00

Table B.14: Continuation of Table B.13...

	mix12				mix13				mix14			
	mode	mean	std	theo	mode	mean	std	theo	mode	mean	std	theo
PRG	0.49	0.79	0.62	0.00	11.04	7.41	3.77	0.00	56.58	55.50	1.11	56.50
AUG	0.34	0.48	0.41	0.00	1.44	3.63	3.17	54.10	0.20	0.55	0.54	0.00
OLV	2.63	2.48	0.87	0.00	7.03	6.65	3.83	0.00	0.17	0.34	0.33	0.00
PLG	4.47	4.26	1.04	13.70	1.55	2.99	2.61	0.00	0.29	0.86	0.80	0.00
FS	99.90	99.82	0.18	86.30	82.24	83.10	3.07	45.90	49.54	49.72	0.85	43.50
ILM	0.00	0.01	0.01	0.00	0.91	1.00	0.23	0.00	0.06	0.13	0.11	0.00
npFe	0.00	0.01	0.00	-	0.02	0.03	0.03	-	0.00	0.01	0.01	-
mpFe	0.00	0.00	0.00	-	0.00	0.01	0.01	-	0.00	0.00	0.00	-
SUM	107.83	107.82	-	100.00	104.22	104.78	-	100.00	106.84	107.10	-	100.00

	mix15				mix16			
	mode	mean	std	theo	mode	mean	std	theo
PRG	0.34	0.57	0.51	0.00	34.53	20.78	11.02	0.00
AUG	0.28	0.45	0.41	0.00	2.53	6.57	5.86	0.00
OLV	31.91	29.63	2.56	53.60	4.78	8.53	6.56	0.00
PLG	0.54	1.34	1.20	0.00	5.23	10.36	8.50	0.00
FS	74.88	76.51	2.66	46.40	4.84	6.34	4.50	54.60
ILM	0.01	0.02	0.01	0.00	40.90	41.83	5.49	45.40
npFe	0.00	0.01	0.01	-	5.99	5.65	1.63	-
mpFe	0.01	0.01	0.01	-	0.01	0.04	0.05	-
SUM	107.95	108.51	-	100.00	92.81	94.42	-	100.00

B.3 LSCC

Table B.15: Elemental abundances used for the LSCC samples taken from Taylor et al. (2001) and Taylor et al. (2010). The elemental and mineral abundances of the 20-45 μm size fraction were used for the priors, but the 0-45 μm size fraction spectra were used for the unmixing. The 0-45μm size fraction mineral abundances were not available.

	SiO_2	TiO_2	Al_2O_3	Cr_2O_3	MgO	CaO	MnO	FeO	Na_2O	K_2O	P_2O_5	Fe_2O_3
10084	41.3	8.30	12.00	0.30	8.46	11.60	0.21	15.50	0.39	0.12	0.12	0.17
12001	45.3	3.20	11.00	0.41	10.60	9.83	0.21	16.90	0.39	0.21	0.23	0.11
12030	46.1	3.74	10.50	0.40	9.94	9.09	0.23	17.60	0.41	0.26	0.19	0.12
14141	47.2	1.96	15.00	0.26	11.00	10.10	0.15	11.60	0.59	0.47	0.26	0.07
14163	47.1	2.00	15.40	0.23	11.00	10.20	0.15	11.50	0.57	0.41	0.21	0.08
14259	47.1	1.99	15.80	0.24	10.70	10.50	0.15	11.00	0.60	0.43	0.26	0.09
14260	47.4	1.86	16.30	0.22	10.40	10.70	0.14	10.70	0.60	0.44	0.22	0.10
15041	46.1	2.03	12.50	0.39	11.20	9.91	0.20	15.20	0.36	0.16	0.19	0.11
15071	45.8	2.33	12.40	0.43	11.40	9.81	0.21	15.60	0.36	0.14	0.15	0.10
61141	44.5	0.58	26.10	0.11	6.56	15.20	0.08	5.15	0.46	0.10	0.06	0.05
61221	44.5	0.56	27.20	0.09	5.45	15.90	0.06	4.62	0.46	0.07	0.05	0.04
62231	44.5	0.58	25.70	0.11	6.59	15.30	0.09	5.31	0.42	0.09	0.07	0.08
64801	44.6	0.63	26.50	0.10	6.09	15.60	0.08	4.82	0.44	0.12	0.06	0.10
67461	44.4	0.44	27.30	0.09	5.11	16.10	0.07	4.93	0.41	0.05	0.03	0.07
67481	44.7	0.49	26.70	0.09	5.98	15.60	0.08	5.19	0.45	0.06	0.05	0.04
70181	40.7	8.11	11.50	0.43	10.10	10.30	0.22	16.00	0.35	0.08	0.06	0.16
71061	39.2	9.48	9.33	0.48	10.80	9.58	0.23	18.50	0.34	0.07	0.04	0.17
71501	38.4	10.70	9.94	0.46	9.97	9.94	0.24	17.80	0.35	0.07	0.07	0.17
79221	40.5	7.38	11.60	0.40	10.90	10.30	0.22	15.80	0.38	0.09	0.06	0.17

Table B.16: Detailed results for the unmixing of LSCC spectra with the catalog of RELAB end-members. A prior on the TiO_2 and the Al_2O_3 was set with $\alpha_{elem} = 40$.

	10084				12001				12030			
	mode	mean	std	theo	mode	mean	std	theo	mode	mean	std	theo
OPX	11.57	10.73	0.47	0.80	23.23	22.92	0.61	1.99	22.52	22.88	0.82	6.48
CPX	39.69	35.27	1.85	36.69	50.91	45.63	1.70	43.75	42.37	37.70	2.23	50.40
OLV	7.10	11.70	4.19	3.28	1.22	2.31	1.90	8.24	7.79	4.59	3.55	7.24
PLG	13.26	11.94	2.50	39.34	7.05	11.68	2.09	32.46	13.57	21.34	3.99	25.77
OTH	-	-	-	4.92	-	-	-	7.27	-	-	-	5.73
ILM	6.72	12.01	2.15	14.98	5.95	5.50	1.03	6.30	7.94	7.88	1.28	4.38
npFe	1.88	1.94	0.04	-	1.54	1.51	0.03	-	0.34	0.35	0.02	-
mpFe	0.70	0.68	0.03	-	0.79	0.84	0.02	-	0.32	0.34	0.02	-
SUM	78.34	81.66	-	100.00	88.35	88.03	-	100.00	94.19	94.39	-	100.00

	14141				14163				14259			
	mode	mean	std	theo	mode	mean	std	theo	mode	mean	std	theo
OPX	17.05	16.99	0.51	13.93	11.90	11.86	0.48	16.34	12.95	12.67	0.49	20.03
CPX	6.23	7.71	1.63	22.53	13.60	6.36	1.68	24.33	5.49	9.77	1.62	29.09
OLV	16.61	14.45	5.81	7.36	16.11	21.99	6.14	6.03	14.44	5.12	3.79	6.22
PLG	53.25	54.11	5.08	48.96	46.85	48.62	5.11	47.51	54.98	60.57	3.22	38.16
OTH	-	-	-	3.72	-	-	-	3.77	-	-	-	2.98
ILM	4.51	4.29	0.73	3.50	5.32	4.19	0.71	2.01	4.11	4.09	0.69	3.52
npFe	0.17	0.16	0.01	-	0.57	0.59	0.02	-	1.10	1.07	0.02	-
mpFe	0.11	0.11	0.01	-	0.19	0.20	0.02	-	0.32	0.36	0.02	-
SUM	97.65	97.56	-	100.00	93.78	93.03	-	100.00	91.97	92.21	-	100.00

	14260				15041				15071			
	mode	mean	std	theo	mode	mean	std	theo	mode	mean	std	theo
OPX	14.92	15.01	0.51	13.98	23.92	23.26	0.66	8.13	23.40	23.12	0.65	6.66
CPX	8.85	12.13	1.82	26.88	44.86	40.74	2.61	40.35	43.31	39.39	2.12	38.97
OLV	10.43	4.16	3.15	6.27	6.11	4.73	3.34	7.11	1.22	4.42	3.26	8.06
PLG	54.45	57.35	3.04	46.59	10.84	16.89	2.84	33.41	19.76	20.43	2.70	37.42
OTH	-	-	-	3.58	-	-	-	8.41	-	-	-	4.96
ILM	2.94	3.65	0.65	2.69	3.23	3.19	0.64	2.59	3.36	4.05	0.78	3.93
npFe	1.12	1.13	0.02	-	1.60	1.59	0.04	-	1.28	1.34	0.03	-
mpFe	0.40	0.40	0.02	-	0.80	0.83	0.03	-	0.75	0.72	0.02	-
SUM	91.59	92.30	-	100.00	88.95	88.81	-	100.00	91.05	91.42	-	100.00

	61141				61221				62231			
	mode	mean	std	theo	mode	mean	std	theo	mode	mean	std	theo
OPX	4.44	4.54	0.28	3.39	4.48	4.46	0.17	4.18	4.21	4.30	0.28	4.23
CPX	0.69	1.81	0.54	5.39	0.54	1.18	0.33	6.22	0.84	1.59	0.46	6.19
OLV	6.51	4.21	2.37	4.24	18.43	17.15	2.00	5.50	10.19	6.20	2.83	5.90
PLG	83.24	84.45	2.30	85.77	74.14	74.80	1.82	82.83	78.69	81.98	2.61	82.45
OTH	-	-	-	0.61	-	-	-	0.42	-	-	-	0.61
ILM	1.20	1.11	0.20	0.61	1.04	1.14	0.20	0.85	1.19	1.10	0.18	0.61
npFe	0.43	0.42	0.01	-	0.07	0.06	0.00	-	0.49	0.47	0.01	-
mpFe	0.15	0.15	0.01	-	0.03	0.03	0.00	-	0.14	0.15	0.01	-
SUM	96.07	96.11	-	100.00	98.64	98.73	-	100.00	95.13	95.17	-	100.00

Table B.17: Continuation of Table B.16...

	64801				67461				67481			
	mode	mean	std	theo	mode	mean	std	theo	mode	mean	std	theo
OPX	4.28	4.20	0.26	4.40	5.65	5.90	0.18	3.97	5.11	5.06	0.14	4.09
CPX	1.78	1.83	0.52	5.40	6.58	4.41	0.52	5.80	0.63	0.97	0.29	5.06
OLV	7.56	3.14	2.04	3.90	5.81	7.89	2.23	3.36	13.83	12.80	1.80	5.55
PLG	80.50	85.12	2.09	85.21	81.34	81.08	1.97	86.33	78.49	79.24	1.63	84.88
OTH	-	-	-	0.43	-	-	-	0.13	-	-	-	0.28
ILM	1.19	1.20	0.21	0.65	0.63	0.81	0.16	0.40	0.93	0.99	0.18	0.14
npFe	0.44	0.43	0.01	-	0.11	0.11	0.00	-	0.15	0.15	0.00	-
mpFe	0.11	0.12	0.01	-	0.03	0.03	0.00	-	0.03	0.04	0.00	-
SUM	95.31	95.49	-	100.00	100.02	100.10	-	100.00	98.99	99.05	-	100.00

	70181				71061				71501			
	mode	mean	std	theo	mode	mean	std	theo	mode	mean	std	theo
OPX	13.62	13.64	0.37	3.25	0.34	0.38	0.34	2.33	12.71	12.80	0.48	2.62
CPX	29.16	25.51	1.61	30.63	0.93	2.16	0.49	39.16	31.64	31.59	1.28	35.99
OLV	4.59	7.64	3.89	7.75	19.87	11.64	6.67	7.90	0.45	1.87	1.54	6.56
PLG	25.47	24.47	2.94	36.40	53.20	61.00	6.35	28.14	20.19	18.95	2.22	30.05
OTH	-	-	-	2.80	-	-	-	1.42	-	-	-	2.37
ILM	15.23	19.81	3.04	19.17	38.50	37.29	5.84	21.06	27.85	27.04	4.04	22.40
npFe	1.70	1.77	0.03	-	1.03	1.03	0.04	-	1.77	1.77	0.03	-
mpFe	0.66	0.66	0.02	-	0.12	0.14	0.03	-	0.64	0.64	0.02	-
SUM	88.07	91.08	-	100.00	112.85	112.47	-	100.00	92.84	92.24	-	100.00

	79221			
	mode	mean	std	theo
OPX	10.52	10.76	0.44	3.48
CPX	10.00	12.80	1.82	27.70
OLV	26.35	23.59	6.37	11.35
PLG	27.15	27.31	3.09	39.97
OTH	-	-	-	0.24
ILM	17.34	16.34	2.59	17.27
npFe	1.83	1.81	0.04	-
mpFe	0.59	0.60	0.02	-
SUM	91.36	90.80	-	100.00

Table B.18: Detailed results for the unmixing of LSCC spectra with the catalog of RELAB end-members. For all relevant elemental abundances a prior was introduced.

	10084				12001				12030			
	mode	mean	std	theo	mode	mean	std	theo	mode	mean	std	theo
OPX	10.87	10.90	0.47	0.80	22.99	22.88	0.61	1.99	22.97	22.88	0.87	6.48
CPX	44.72	42.22	2.44	36.69	47.20	45.81	1.58	43.75	37.94	37.88	2.14	50.40
OLV	1.97	2.55	1.93	3.28	2.03	1.33	1.13	8.24	0.85	1.80	1.46	7.24
PLG	11.48	13.44	2.74	39.34	10.66	12.03	1.61	32.46	24.17	23.19	2.27	25.77
OTH	-	-	-	4.92	-	-	-	7.27	-	-	-	5.73
ILM	14.91	14.58	2.22	14.98	5.21	6.96	1.37	6.30	9.76	10.18	1.84	4.38
npFe	1.95	1.93	0.05	-	1.51	1.51	0.03	-	0.35	0.35	0.02	-
mpFe	0.68	0.71	0.02	-	0.86	0.84	0.02	-	0.36	0.35	0.02	-
SUM	83.95	83.69	-	100.00	88.09	89.02	-	100.00	95.69	95.95	-	100.00

	14141				14163				14259			
	mode	mean	std	theo	mode	mean	std	theo	mode	mean	std	theo
OPX	16.99	16.94	0.48	13.93	12.07	11.76	0.46	16.34	12.13	12.75	0.50	20.03
CPX	13.98	8.50	1.43	22.53	15.44	8.42	1.58	24.33	19.43	9.38	1.69	29.09
OLV	7.67	12.81	3.41	7.36	11.94	16.65	3.46	6.03	4.09	9.80	3.10	6.22
PLG	54.57	54.75	3.15	48.96	49.49	51.88	3.23	47.51	51.51	55.64	2.87	38.16
OTH	-	-	-	3.72	-	-	-	3.77	-	-	-	2.98
ILM	4.76	5.14	0.95	3.50	4.22	5.02	0.93	2.01	5.16	4.99	0.90	3.52
npFe	0.14	0.16	0.01	-	0.56	0.59	0.02	-	1.02	1.07	0.02	-
mpFe	0.11	0.11	0.01	-	0.20	0.21	0.01	-	0.32	0.34	0.02	-
SUM	97.96	98.13	-	100.00	93.17	93.72	-	100.00	92.31	92.56	-	100.00

	14260				15041				15071			
	mode	mean	std	theo	mode	mean	std	theo	mode	mean	std	theo
OPX	15.88	15.14	0.55	13.98	24.02	23.36	0.67	8.13	23.46	23.19	0.64	6.66
CPX	20.04	12.82	2.27	26.88	47.09	42.50	2.94	40.35	46.24	40.36	2.28	38.97
OLV	5.97	7.51	2.98	6.27	2.38	2.85	2.24	7.11	0.20	2.95	2.18	8.06
PLG	46.01	52.69	3.60	46.59	11.21	16.75	3.02	33.41	17.48	20.63	2.33	37.42
OTH	-	-	-	3.58	-	-	-	8.41	-	-	-	4.96
ILM	4.44	4.38	0.85	2.69	4.60	3.76	0.82	2.59	4.61	4.92	0.97	3.93
npFe	1.04	1.12	0.04	-	1.50	1.58	0.04	-	1.34	1.34	0.03	-
mpFe	0.39	0.39	0.02	-	0.82	0.83	0.03	-	0.71	0.72	0.02	-
SUM	92.35	92.54	-	100.00	89.31	89.21	-	100.00	91.98	92.05	-	100.00

	61141				61221				62231			
	mode	mean	std	theo	mode	mean	std	theo	mode	mean	std	theo
OPX	4.28	4.74	0.26	3.39	4.48	4.33	0.17	4.18	4.66	4.50	0.30	4.23
CPX	2.92	1.18	0.35	5.39	3.15	2.11	0.42	6.22	0.59	1.35	0.35	6.19
OLV	8.99	10.48	1.76	4.24	13.91	14.02	1.75	5.50	11.87	11.42	1.90	5.90
PLG	78.32	78.33	1.77	85.77	76.10	77.15	1.51	82.83	76.74	76.57	1.93	82.45
OTH	-	-	-	0.61	-	-	-	0.42	-	-	-	0.61
ILM	1.72	1.32	0.26	0.61	1.22	1.26	0.26	0.85	1.24	1.28	0.25	0.61
npFe	0.42	0.44	0.01	-	0.06	0.06	0.00	-	0.48	0.48	0.01	-
mpFe	0.13	0.13	0.01	-	0.03	0.03	0.00	-	0.14	0.14	0.01	-
SUM	96.23	96.05	-	100.00	98.85	98.88	-	100.00	95.10	95.12	-	100.00

Table B.19: Continuation of Table B.16...

	64801				67461				67481			
	mode	mean	std	theo	mode	mean	std	theo	mode	mean	std	theo
OPX	4.62	4.42	0.26	4.40	5.92	5.93	0.16	3.97	5.06	5.05	0.14	4.09
CPX	3.22	1.42	0.36	5.40	6.01	4.39	0.47	5.80	0.67	1.09	0.29	5.06
OLV	8.58	9.09	1.63	3.90	5.97	8.29	1.54	3.36	13.14	12.59	1.46	5.55
PLG	77.69	79.08	1.72	85.21	81.33	80.61	1.37	86.33	79.14	79.28	1.32	84.88
OTH	-	-	-	0.43	-	-	-	0.13	-	-	-	0.28
ILM	1.09	1.42	0.28	0.65	1.14	0.95	0.21	0.40	1.12	1.13	0.23	0.14
npFe	0.44	0.44	0.01	-	0.11	0.12	0.00	-	0.15	0.15	0.00	-
mpFe	0.10	0.11	0.01	-	0.04	0.03	0.00	-	0.04	0.04	0.00	-
SUM	95.20	95.45	-	100.00	100.37	100.17	-	100.00	99.13	99.15	-	100.00

	70181				71061				71501			
	mode	mean	std	theo	mode	mean	std	theo	mode	mean	std	theo
OPX	14.08	13.71	0.38	3.25	0.12	0.40	0.37	2.33	13.41	12.77	0.47	2.62
CPX	33.49	28.56	1.82	30.63	1.15	2.63	0.50	39.16	33.15	32.03	1.25	35.99
OLV	1.52	4.28	2.56	7.75	19.56	18.69	3.06	7.90	0.36	1.46	1.22	6.56
PLG	22.59	24.09	2.78	36.40	55.12	54.66	3.53	28.14	17.06	18.64	2.06	30.05
OTH	-	-	-	2.80	-	-	-	1.42	-	-	-	2.37
ILM	18.49	21.83	3.11	19.17	34.03	32.99	4.39	21.06	30.79	27.94	3.61	22.40
npFe	1.71	1.76	0.03	-	1.02	1.03	0.04	-	1.75	1.77	0.03	-
mpFe	0.65	0.66	0.02	-	0.12	0.11	0.02	-	0.66	0.64	0.02	-
SUM	90.17	92.47	-	100.00	109.98	109.37	-	100.00	94.77	92.84	-	100.00

	79221			
	mode	mean	std	theo
OPX	11.33	11.10	0.40	3.48
CPX	26.20	23.64	1.56	27.70
OLV	9.30	11.37	3.75	11.35
PLG	27.35	27.74	2.88	39.97
OTH	-	-	-	0.24
ILM	18.27	19.00	2.84	17.27
npFe	1.74	1.76	0.03	-
mpFe	0.63	0.62	0.02	-
SUM	92.45	92.85	-	100.00

B.4 GRAIN SIZE

Table B.20: Detailed results for the unmixing of the synthetically generated spectra by using the forward mixing model including the grain size as a parameter. A prior on the TiO_2 and the Al_2O_3 was set with $\alpha_{elem} = 40$. All results are displayed in wt.%.

	mix0				mix1				mix2			
	mode	mean	std	theo	mode	mean	std	theo	mode	mean	std	theo
OPX	9.93	9.95	0.14	10.00	9.45	9.53	0.34	10.00	10.22	10.30	0.56	10.00
CPXB	39.48	39.81	0.65	40.00	40.12	40.12	1.80	40.00	44.69	45.98	3.34	40.00
OLV	4.94	5.12	0.51	5.00	10.63	10.31	2.50	5.00	12.56	13.41	3.98	5.00
PLG	31.12	30.82	1.34	30.00	31.24	30.77	3.43	30.00	25.07	24.09	5.07	30.00
CPXA	14.51	14.22	0.56	15.00	8.42	9.09	2.45	15.00	7.11	5.84	3.46	15.00
ILM	0.07	0.16	0.12	0.00	0.17	0.20	0.14	0.00	0.20	0.19	0.14	0.00
npFe	0.00	0.00	0.00	0.00	0.02	0.02	0.01	0.00	0.03	0.04	0.01	0.00
mpFe	0.00	0.00	0.00	0.00	0.38	0.38	0.02	0.40	0.85	0.87	0.07	0.80
D	30.40	30.24	0.64	32.00	31.46	31.29	1.62	32.00	28.35	27.93	2.19	32.00
SUM	100.06	100.09	-	100.00	100.02	100.03	-	100.00	99.84	99.81	-	100.00

	mix3				mix4				mix5			
	mode	mean	std	theo	mode	mean	std	theo	mode	mean	std	theo
OPX	10.15	9.87	0.69	10.00	10.26	10.49	0.47	10.00	11.00	10.88	0.69	10.00
CPXB	42.87	42.49	4.00	40.00	47.20	47.46	2.51	40.00	43.12	44.49	3.78	40.00
OLV	13.62	15.19	4.05	5.00	6.34	4.96	2.43	5.00	0.63	3.11	2.48	5.00
PLG	24.84	29.07	5.80	30.00	26.32	24.78	4.24	30.00	27.68	27.10	5.27	30.00
CPXA	8.20	2.97	2.48	15.00	9.54	11.92	3.27	15.00	17.54	14.28	4.03	15.00
ILM	0.02	0.27	0.16	0.00	0.06	0.13	0.11	0.00	0.07	0.13	0.11	0.00
npFe	0.04	0.05	0.02	0.00	0.71	0.72	0.05	0.60	0.64	0.66	0.06	0.60
mpFe	1.25	1.20	0.13	1.20	0.00	0.00	0.00	0.00	0.45	0.45	0.04	0.40
D	28.45	30.18	3.14	32.00	26.22	25.74	1.58	32.00	27.51	27.46	2.44	32.00
SUM	99.70	99.86	-	100.00	99.72	99.75	-	100.00	100.04	100.00	-	100.00

	mix6				mix7				mix8			
	mode	mean	std	theo	mode	mean	std	theo	mode	mean	std	theo
OPX	10.53	10.62	0.69	10.00	10.14	10.51	0.82	10.00	10.70	9.85	0.68	10.00
CPXB	43.70	45.53	4.22	40.00	41.99	43.16	4.69	40.00	37.87	36.18	3.17	40.00
OLV	7.89	10.15	5.23	5.00	9.01	9.83	4.85	5.00	11.37	5.68	3.40	5.00
PLG	24.54	23.37	5.47	30.00	32.65	30.15	6.24	30.00	27.14	36.63	5.54	30.00
CPXA	12.91	9.82	5.32	15.00	6.33	6.37	4.43	15.00	12.69	12.08	4.64	15.00
ILM	0.08	0.16	0.12	0.00	0.19	0.22	0.15	0.00	0.24	0.21	0.14	0.00
npFe	0.69	0.71	0.07	0.60	0.59	0.61	0.07	0.60	1.34	1.21	0.12	1.40
mpFe	0.88	0.91	0.09	0.80	1.16	1.21	0.15	1.20	0.00	0.01	0.01	0.00
D	26.88	26.48	2.41	32.00	31.67	30.64	3.54	32.00	31.09	35.14	3.51	32.00
SUM	99.65	99.64	-	100.00	100.32	100.23	-	100.00	100.01	100.63	-	100.00

Table B.21: Continuation of Table B.20...

	mix9				mix10				mix11			
	mode	mean	std	theo	mode	mean	std	theo	mode	mean	std	theo
OPX	10.20	10.83	0.65	10.00	10.10	9.82	0.57	10.00	9.87	10.05	0.95	10.00
CPXB	37.77	37.58	3.43	40.00	36.06	39.06	3.89	40.00	32.39	37.33	5.71	40.00
OLV	21.21	10.11	5.50	5.00	10.96	13.92	3.82	5.00	11.44	7.58	4.88	5.00
PLG	20.05	20.05	4.88	30.00	29.26	28.66	4.42	30.00	33.69	32.39	6.73	30.00
CPXA	10.31	21.29	6.39	15.00	13.18	8.02	5.34	15.00	12.61	12.99	6.07	15.00
ILM	0.10	0.12	0.10	0.00	0.37	0.33	0.13	0.00	0.13	0.18	0.15	0.00
npFe	1.31	1.32	0.11	1.40	1.39	1.45	0.12	1.40	1.20	1.30	0.18	1.40
mpFe	0.34	0.40	0.04	0.40	0.76	0.78	0.07	0.80	1.00	1.22	0.19	1.20
D	32.41	30.77	2.49	32.00	30.66	30.16	2.34	32.00	35.28	32.00	4.49	32.00
SUM	99.64	99.98	-	100.00	99.94	99.82	-	100.00	100.14	100.52	-	100.00

	mix12				mix13				mix14			
	mode	mean	std	theo	mode	mean	std	theo	mode	mean	std	theo
OPX	11.10	10.63	0.81	10.00	8.80	9.11	0.80	10.00	11.21	10.66	0.83	10.00
CPXB	49.14	57.39	5.30	40.00	51.81	54.91	5.87	40.00	24.67	32.93	4.34	40.00
OLV	0.11	2.30	1.94	5.00	10.22	7.24	4.38	5.00	9.21	18.97	6.65	5.00
PLG	25.74	24.65	6.12	30.00	24.75	22.62	6.08	30.00	25.55	24.25	5.50	30.00
CPXA	13.55	4.68	3.29	15.00	3.42	5.20	3.98	15.00	28.71	12.31	7.52	15.00
ILM	0.18	0.13	0.11	0.00	0.08	0.14	0.11	0.00	0.31	0.23	0.16	0.00
npFe	2.65	2.92	0.28	2.20	2.75	2.89	0.29	2.20	1.62	1.88	0.20	2.20
mpFe	0.01	0.02	0.01	0.00	0.41	0.45	0.06	0.40	0.54	0.61	0.08	0.80
D	24.92	23.25	2.31	32.00	24.85	23.78	2.47	32.00	38.86	35.41	3.69	32.00
SUM	99.83	99.78	-	100.00	99.09	99.22	-	100.00	99.67	99.35	-	100.00

	mix15				mix16				mix17			
	mode	mean	std	theo	mode	mean	std	theo	mode	mean	std	theo
OPX	8.78	9.24	0.92	10.00	9.18	9.13	0.27	9.20	9.70	9.81	0.53	9.20
CPXB	37.88	46.18	5.90	40.00	36.11	36.43	1.10	36.80	41.40	42.20	2.86	36.80
OLV	12.50	7.44	4.55	5.00	5.28	5.08	0.79	4.60	7.19	7.73	1.94	4.60
PLG	30.43	31.08	6.65	30.00	28.41	28.66	2.87	27.60	23.18	22.21	5.02	27.60
CPXA	9.87	6.00	4.20	15.00	12.90	12.45	1.06	13.80	10.45	9.82	2.08	13.80
ILM	0.21	0.20	0.14	0.00	8.36	8.64	1.20	8.00	7.70	7.85	1.25	8.00
npFe	2.37	2.60	0.31	2.20	0.00	0.00	0.00	0.00	0.00	0.00	0.00	0.00
mpFe	1.21	1.42	0.19	1.20	0.00	0.00	0.00	0.00	0.44	0.45	0.04	0.40
D	28.85	26.45	3.33	32.00	30.49	30.55	1.29	32.00	27.86	27.53	2.13	32.00
SUM	99.68	100.14	-	100.00	100.25	100.40	-	100.00	99.63	99.63	-	100.00

Table B.22: Continuation of Table B.21...

	mix18				mix19				mix20			
	mode	mean	std	theo	mode	mean	std	theo	mode	mean	std	theo
OPX	7.12	6.90	0.40	9.20	9.52	8.99	0.66	9.20	9.50	9.61	0.51	9.20
CPXB	31.65	31.38	2.17	36.80	34.63	39.43	4.17	36.80	45.00	42.66	2.44	36.80
OLV	10.61	10.14	2.83	4.60	17.36	14.97	4.29	4.60	5.80	2.09	1.58	4.60
PLG	40.77	42.20	4.93	27.60	18.32	22.71	5.40	27.60	22.45	21.98	4.76	27.60
CPXA	1.90	1.73	1.45	13.80	11.41	5.35	3.37	13.80	9.29	15.10	3.00	13.80
ILM	10.20	9.95	1.46	8.00	8.01	8.03	1.30	8.00	6.75	8.08	1.26	8.00
npFe	0.03	0.03	0.01	0.00	0.04	0.03	0.02	0.00	0.75	0.71	0.05	0.60
mpFe	0.60	0.58	0.06	0.80	1.21	1.28	0.15	1.20	0.00	0.00	0.00	0.00
D	40.51	42.10	3.96	32.00	28.49	28.31	2.99	32.00	24.97	25.54	1.82	32.00
SUM	102.26	102.31	-	100.00	99.24	99.48	-	100.00	98.79	99.52	-	100.00

	mix21				mix22				mix23			
	mode	mean	std	theo	mode	mean	std	theo	mode	mean	std	theo
OPX	8.77	8.79	0.53	9.20	9.90	8.97	0.68	9.20	12.19	11.32	0.73	9.20
CPXB	27.13	27.74	2.34	36.80	36.97	37.00	3.96	36.80	35.74	31.43	4.24	36.80
OLV	0.58	1.57	1.42	4.60	6.62	12.44	5.67	4.60	8.71	2.37	2.14	4.60
PLG	31.64	31.19	4.92	27.60	20.74	23.30	5.35	27.60	4.77	14.75	5.00	27.60
CPXA	24.20	23.04	3.48	13.80	17.57	9.51	5.75	13.80	30.94	32.57	5.04	13.80
ILM	9.45	9.25	1.44	8.00	7.31	8.48	1.37	8.00	6.16	6.87	1.24	8.00
npFe	0.43	0.44	0.04	0.60	0.66	0.66	0.07	0.60	0.57	0.48	0.05	0.60
mpFe	0.32	0.33	0.03	0.40	0.88	0.80	0.10	0.80	1.41	1.23	0.13	1.20
D	37.43	37.31	3.48	32.00	26.96	29.31	3.13	32.00	25.79	29.57	2.78	32.00
SUM	101.77	101.58	-	100.00	99.10	99.70	-	100.00	98.52	99.29	-	100.00

	mix24				mix25				mix26			
	mode	mean	std	theo	mode	mean	std	theo	mode	mean	std	theo
OPX	9.49	9.76	0.73	9.20	8.41	8.60	0.68	9.20	8.47	8.73	0.81	9.20
CPXB	33.06	34.95	3.22	36.80	36.46	36.34	3.50	36.80	33.98	33.99	4.23	36.80
OLV	1.13	2.39	2.02	4.60	12.48	10.70	3.55	4.60	13.73	12.15	4.96	4.60
PLG	28.69	26.79	5.81	27.60	33.44	33.80	5.97	27.60	31.93	31.35	6.49	27.60
CPXA	19.97	18.29	4.20	13.80	0.97	2.77	2.20	13.80	3.74	5.75	4.33	13.80
ILM	7.86	7.91	1.29	8.00	9.83	9.04	1.40	8.00	9.13	9.01	1.43	8.00
npFe	1.31	1.39	0.14	1.40	1.24	1.24	0.14	1.40	1.27	1.28	0.17	1.40
mpFe	0.01	0.01	0.01	0.00	0.36	0.36	0.05	0.40	0.72	0.73	0.11	0.80
D	31.23	30.03	3.08	32.00	35.32	35.43	4.19	32.00	34.24	34.15	4.67	32.00
SUM	100.19	100.08	-	100.00	101.59	101.24	-	100.00	101.00	100.97	-	100.00

Table B.23: Continuation of Table B.22...

	mix27				mix28				mix29			
	mode	mean	std	theo	mode	mean	std	theo	mode	mean	std	theo
OPX	8.81	9.34	1.02	9.20	9.67	10.22	0.74	9.20	9.74	10.22	0.75	9.20
CPXB	40.09	42.22	5.88	36.80	25.40	28.26	3.13	36.80	26.33	31.60	3.26	36.80
OLV	6.88	6.43	4.01	4.60	9.20	3.13	2.55	4.60	13.20	8.06	5.30	4.60
PLG	34.44	30.13	7.07	27.60	26.66	22.27	5.57	27.60	15.27	15.58	4.90	27.60
CPXA	1.78	3.60	3.10	13.80	21.97	28.92	5.14	13.80	27.15	26.44	7.37	13.80
ILM	8.63	8.77	1.44	8.00	7.38	7.57	1.28	8.00	6.75	6.89	1.24	8.00
npFe	1.47	1.59	0.23	1.40	1.70	1.86	0.19	2.20	1.99	2.15	0.18	2.20
mpFe	1.25	1.36	0.22	1.20	0.00	0.02	0.01	0.00	0.30	0.36	0.04	0.40
D	29.90	28.09	4.30	32.00	37.17	33.83	3.37	32.00	31.67	29.70	2.55	32.00
SUM	100.61	100.48	-	100.00	100.27	100.37	-	100.00	98.45	98.79	-	100.00

	mix30				mix31				mix32			
	mode	mean	std	theo	mode	mean	std	theo	mode	mean	std	theo
OPX	10.22	10.75	1.08	9.20	8.48	7.70	1.15	9.20	8.95	9.02	0.38	8.40
CPXB	48.42	47.42	6.33	36.80	46.42	51.63	6.55	36.80	37.18	37.52	1.70	33.60
OLV	5.22	4.59	3.63	4.60	11.48	3.54	2.93	4.60	7.09	7.23	1.24	4.20
PLG	23.21	20.50	6.25	27.60	23.94	25.31	6.97	27.60	20.30	19.89	3.98	25.20
CPXA	3.81	7.61	5.24	13.80	1.13	3.30	2.90	13.80	10.11	9.89	1.42	12.60
ILM	7.88	7.64	1.34	8.00	7.94	8.29	1.44	8.00	15.80	15.87	1.78	16.00
npFe	2.85	2.90	0.35	2.20	3.05	3.18	0.40	2.20	0.00	0.00	0.00	0.00
mpFe	0.91	0.94	0.13	0.80	1.61	1.75	0.24	1.20	0.01	0.01	0.00	0.00
D	23.94	23.58	2.89	32.00	22.67	21.95	2.97	32.00	27.15	26.99	1.58	32.00
SUM	98.76	98.51	-	100.00	99.39	99.76	-	100.00	99.43	99.42	-	100.00

	mix33				mix34				mix35			
	mode	mean	std	theo	mode	mean	std	theo	mode	mean	std	theo
OPX	10.05	10.17	0.63	8.40	8.63	8.93	0.59	8.40	10.07	10.01	0.74	8.40
CPXB	45.51	46.51	4.13	33.60	32.10	33.73	3.26	33.60	36.97	36.85	4.79	33.60
OLV	4.24	4.11	2.32	4.20	8.37	9.82	2.61	4.20	4.47	4.45	2.72	4.20
PLG	14.96	15.17	4.94	25.20	27.69	24.98	5.39	25.20	17.55	16.76	5.06	25.20
CPXA	9.53	8.25	2.99	12.60	7.45	6.51	2.75	12.60	15.46	15.96	4.18	12.60
ILM	13.20	13.35	1.86	16.00	16.39	16.46	2.03	16.00	13.42	14.32	2.00	16.00
npFe	0.00	0.01	0.00	0.00	0.00	0.01	0.00	0.00	0.00	0.01	0.01	0.00
mpFe	0.55	0.56	0.06	0.40	0.76	0.80	0.09	0.80	1.37	1.36	0.16	1.20
D	22.50	22.39	1.95	32.00	32.43	31.14	3.16	32.00	25.73	26.08	2.80	32.00
SUM	97.49	97.55	-	100.00	100.64	100.43	-	100.00	97.94	98.36	-	100.00

Table B.24: Continuation of Table B.23...

	mix36				mix37				mix38			
	mode	mean	std	theo	mode	mean	std	theo	mode	mean	std	theo
OPX	8.52	8.23	0.49	8.40	6.88	7.10	0.52	8.40	8.85	9.03	0.75	8.40
CPXB	34.92	33.42	2.29	33.60	28.58	29.46	2.85	33.60	28.77	29.34	3.69	33.60
OLV	10.17	4.14	2.88	4.20	12.49	11.76	3.67	4.20	2.83	4.34	3.24	4.20
PLG	21.25	27.22	5.20	25.20	35.09	31.69	5.87	25.20	28.65	27.07	5.90	25.20
CPXA	8.68	10.74	3.50	12.60	0.87	3.22	2.38	12.60	15.78	14.99	4.88	12.60
ILM	16.29	17.07	1.92	16.00	18.74	19.52	2.29	16.00	15.64	15.54	2.05	16.00
npFe	0.64	0.58	0.05	0.60	0.49	0.52	0.06	0.60	0.51	0.53	0.07	0.60
mpFe	0.00	0.01	0.01	0.00	0.29	0.31	0.04	0.40	0.76	0.77	0.11	0.80
D	28.83	31.32	2.78	32.00	40.17	37.99	4.54	32.00	32.97	32.52	4.09	32.00
SUM	99.83	100.83	-	100.00	102.65	102.74	-	100.00	100.51	100.30	-	100.00

	mix39				mix40				mix41			
	mode	mean	std	theo	mode	mean	std	theo	mode	mean	std	theo
OPX	8.31	9.05	0.77	8.40	8.25	9.67	0.76	8.40	9.49	9.37	0.89	8.40
CPXB	29.84	37.84	4.77	33.60	32.38	37.23	4.33	33.60	28.65	38.10	5.01	33.60
OLV	21.36	6.03	4.40	4.20	6.34	3.21	2.52	4.20	1.46	5.22	3.71	4.20
PLG	17.37	22.06	5.76	25.20	27.81	17.56	5.56	25.20	24.00	23.13	6.18	25.20
CPXA	4.97	9.48	5.04	12.60	11.01	17.23	5.53	12.60	22.58	8.74	5.14	12.60
ILM	20.35	15.73	2.15	16.00	13.65	14.09	1.96	16.00	13.04	15.63	2.08	16.00
npFe	0.56	0.61	0.07	0.60	1.27	1.52	0.16	1.40	1.25	1.47	0.19	1.40
mpFe	0.99	1.30	0.17	1.20	0.00	0.02	0.01	0.00	0.43	0.49	0.08	0.40
D	34.64	29.45	3.64	32.00	33.20	27.51	2.87	32.00	31.44	28.90	3.74	32.00
SUM	102.20	100.19	-	100.00	99.45	98.99	-	100.00	99.22	100.19	-	100.00

	mix42				mix43				mix44			
	mode	mean	std	theo	mode	mean	std	theo	mode	mean	std	theo
OPX	7.27	7.61	0.74	8.40	8.90	9.08	0.88	8.40	9.51	9.64	0.70	8.40
CPXB	23.16	30.32	6.76	33.60	31.33	31.91	4.62	33.60	38.10	38.82	4.87	33.60
OLV	3.24	7.06	5.23	4.20	9.65	8.15	5.09	4.20	1.38	1.95	1.80	4.20
PLG	29.31	24.33	7.21	25.20	26.44	24.92	6.02	25.20	15.27	13.72	5.07	25.20
CPXA	23.01	15.16	6.78	12.60	8.70	10.92	6.31	12.60	19.90	19.83	5.83	12.60
ILM	12.56	14.73	2.10	16.00	15.26	15.26	2.06	16.00	13.47	13.72	2.02	16.00
npFe	1.12	1.38	0.27	1.40	1.27	1.32	0.17	1.40	2.65	2.70	0.27	2.20
mpFe	0.62	0.80	0.17	0.80	1.17	1.22	0.18	1.20	0.00	0.01	0.01	0.00
D	35.84	30.86	4.99	32.00	32.58	31.73	4.29	32.00	24.11	23.89	2.25	32.00
SUM	98.55	99.20	-	100.00	100.27	100.25	-	100.00	97.64	97.68	-	100.00

Table B.25: Continuation of Table B.24...

	mix45				mix46				mix47			
	mode	mean	std	theo	mode	mean	std	theo	mode	mean	std	theo
OPX	8.54	9.28	0.92	8.40	8.10	9.05	1.10	8.40	9.36	9.25	0.91	8.40
CPXB	31.73	36.41	5.15	33.60	28.55	41.46	6.90	33.60	25.70	28.60	5.39	33.60
OLV	18.03	8.59	5.41	4.20	20.87	6.49	5.37	4.20	1.98	4.50	3.98	4.20
PLG	22.54	20.81	5.47	25.20	23.97	22.26	6.12	25.20	22.22	21.26	5.88	25.20
CPXA	3.09	8.85	6.09	12.60	1.41	4.33	3.71	12.60	26.34	21.89	7.37	12.60
ILM	14.67	14.98	2.04	16.00	16.20	15.72	2.14	16.00	13.85	14.19	2.04	16.00
npFe	2.12	2.37	0.29	2.20	2.06	2.75	0.41	2.20	1.84	1.94	0.26	2.20
mpFe	0.27	0.38	0.07	0.40	0.68	1.05	0.18	0.80	1.10	1.13	0.17	1.20
D	31.99	28.68	3.50	32.00	32.15	24.96	3.80	32.00	33.38	32.99	4.35	32.00
SUM	98.59	98.93	-	100.00	99.11	99.30	-	100.00	99.45	99.68	-	100.00

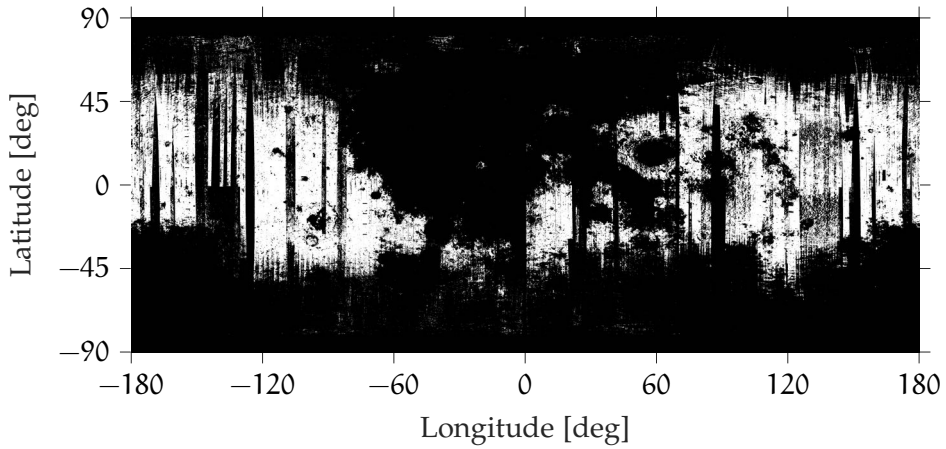

Figure C.1: Pixels belonging to the largest highland cluster (59).

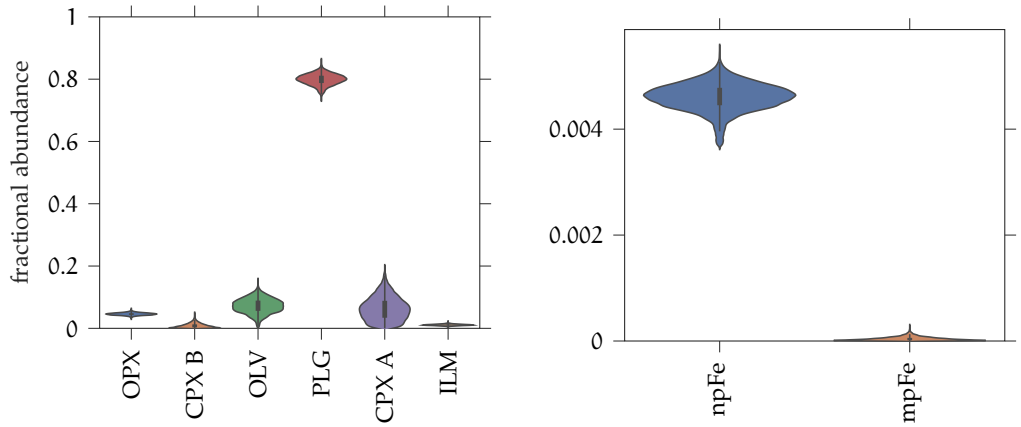

(a) Minerals

(b) smFe

Figure C.2: Violinplots of the endmember weights for cluster 59, which is representative for a typical highland spectrum. The weights of the endmembers in the chain are normalized so that for each sample the endmember weights sum up to one.

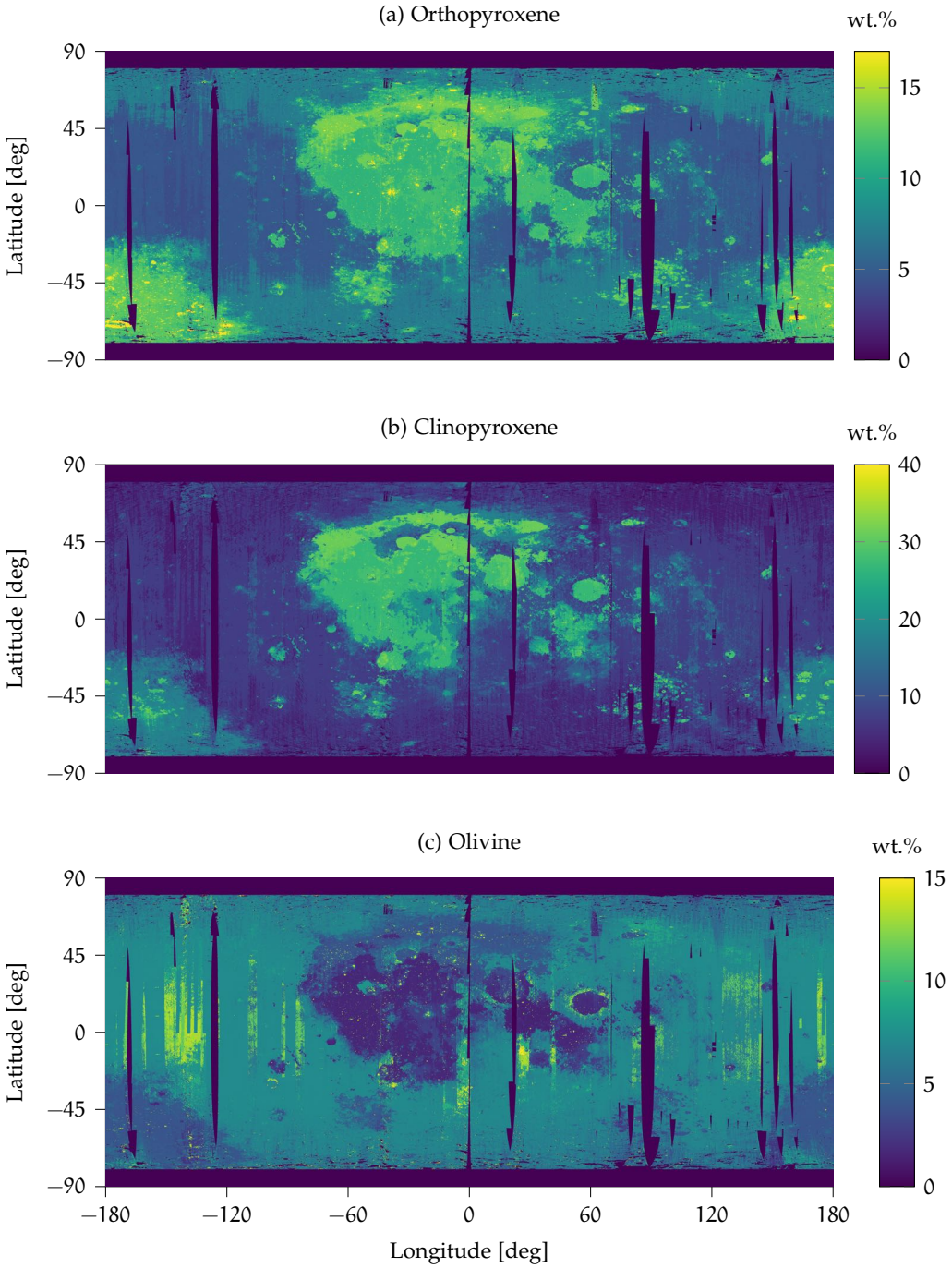

Figure C.3: Global maps at 20 pixels/degree of the minerals orthopyroxene, clinopyroxene (type A+ type B), and olivine. The abundances are displayed in wt.%.

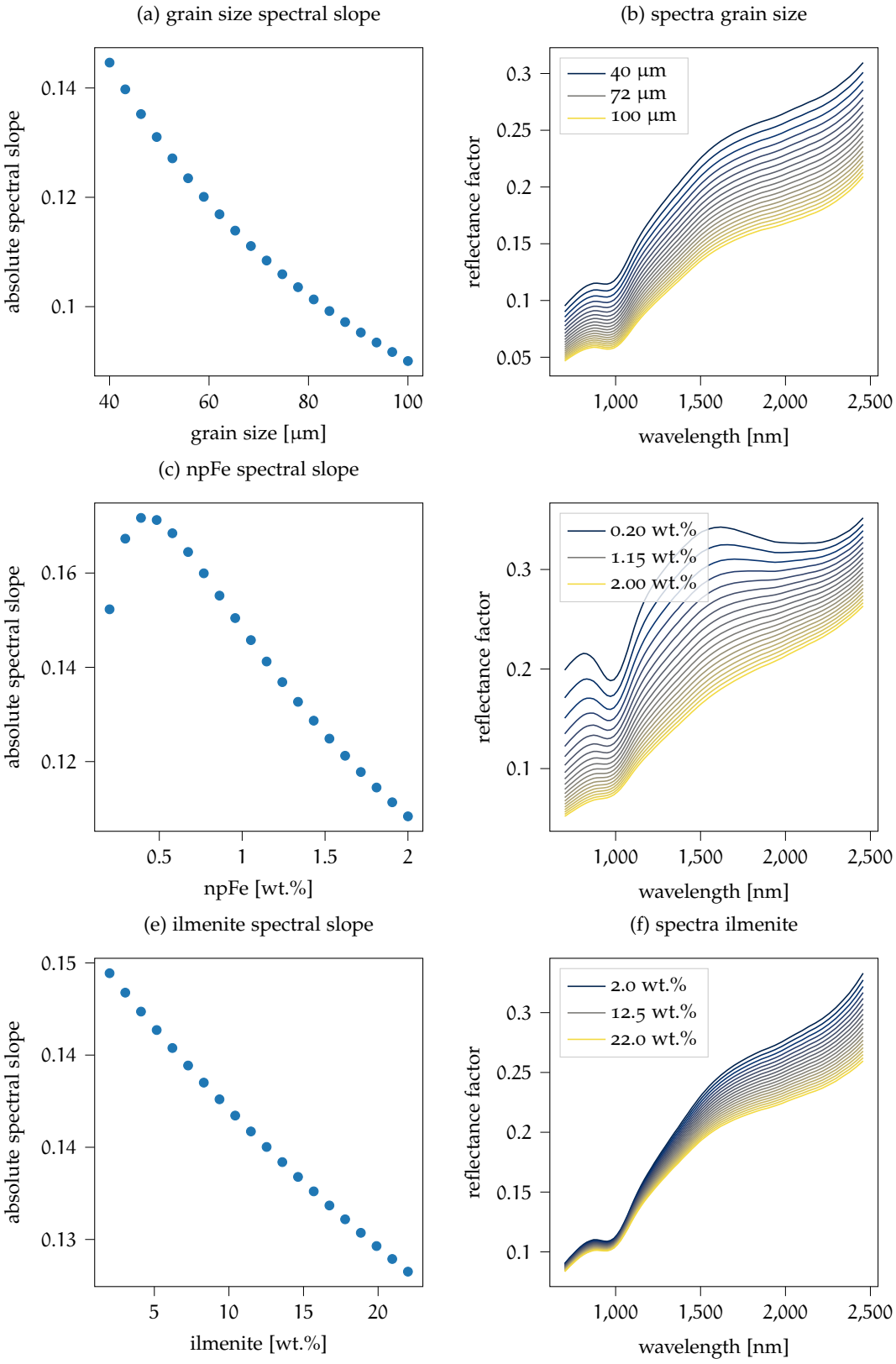

Figure C.4: The absolute spectral slope at a shorter wavelength than the 1000 nm absorption band is indirectly a measure of the ilmenite content in the method of Bhatt et al. (2015). However, the spectral slope, here represented by $(R_{0.810\mu m} - R_{0.701\mu m})/(0.810 - 0.701\mu m)$, is also strongly influenced by the grain size and npFe abundance because it is sensitive to albedo differences.

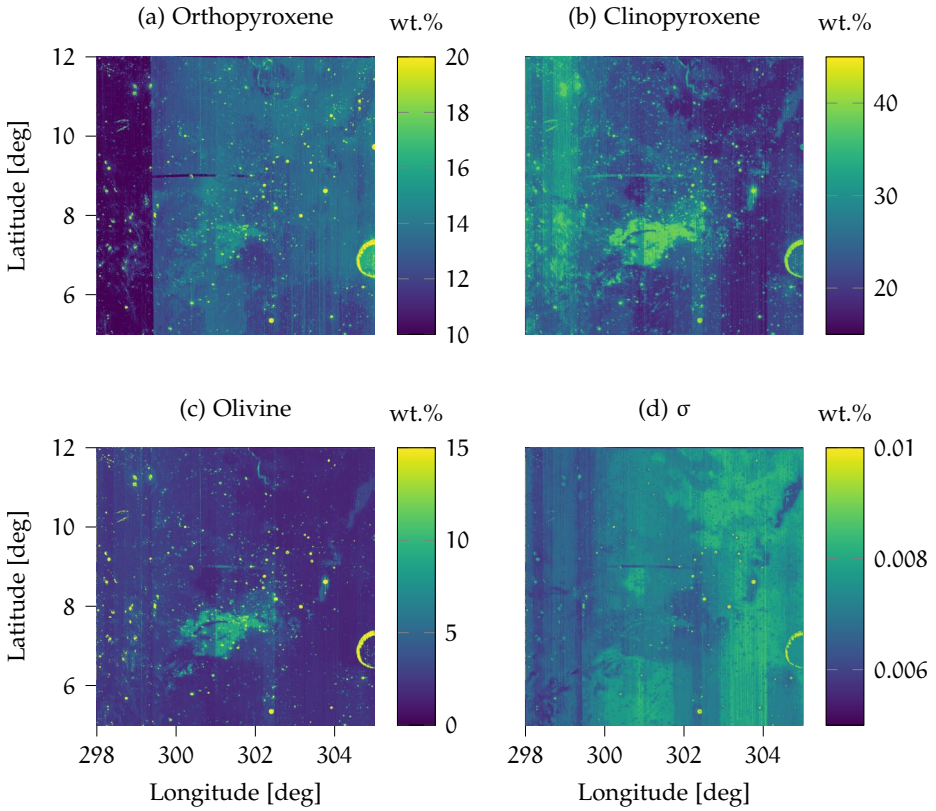

Figure C.5: Maps of the Reiner Gamma swirl for (a) orthopyroxene, (b) clinopyroxene, (c) olivine, and (d) the average standard deviation of the likelihood function.

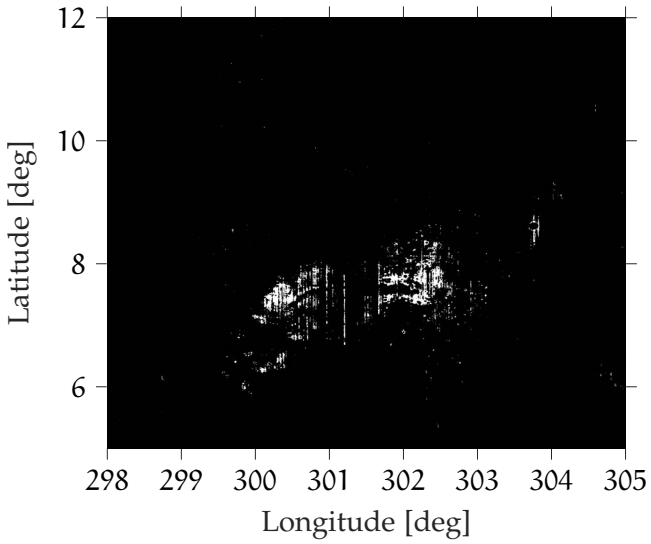

Figure C.6: Pixels belonging to cluster 9 representing the central oval of Reiner Gamma.

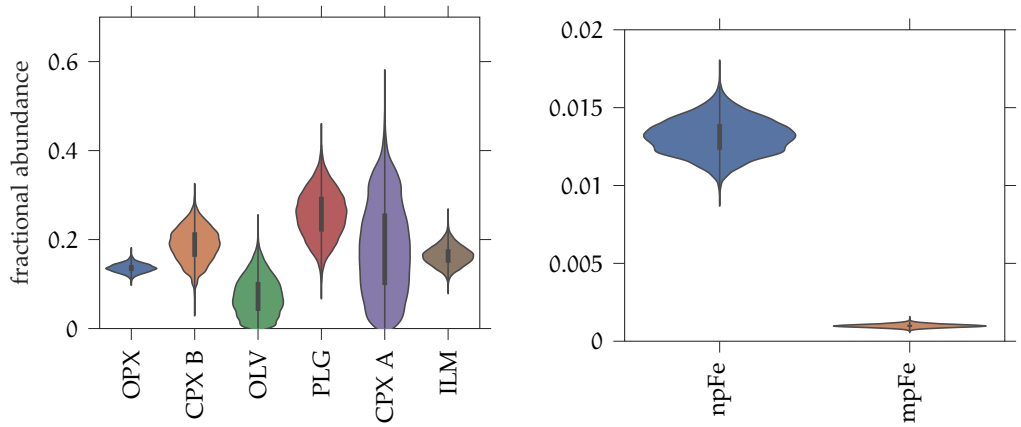

(a) Minerals

(b) smFe

Figure C.7: Violin plots of the endmember weights for cluster 9, which represents parts of the central oval of Reiner Gamma. The weights of the endmembers in the chain are normalized so that for each sample, the endmember weights sum up to one.

BIBLIOGRAPHY

Adams, J. and T. McCord (1970). "Remote sensing of lunar surface mineralogy: Implications from visible and near-infrared reflectivity of Apollo 11 samples." In: *Geochimica et Cosmochimica Acta Supplement, Volume 1. Proceedings of the Apollo 11 Lunar Science Conference held 5-8 January, 1970 in Houston, TX.* Ed. by A. Levinson. Vol. 3. New York: Pergammon Press, p. 1937.

Adams, J. B. and R. L. Jones (1970). "Spectral reflectivity of lunar samples." In: *Science* 167.3918, pp. 737–739.

Adams, J. B. and T. B. McCord (1973). "Vitrification darkening in the lunar highlands and identification of Descartes material at the Apollo 16 site." In: *Lunar and Planetary Science Conference Proceedings*. Vol. 4, p. 163.

Anderl, S. (2017). *Das Universum und ich: die Philosophie der Astrophysik*. Munich, Germany: Carl Hanser Verlag GmbH Co KG.

Arnaut, M., K. Wohlfarth, and C. Wöhler (2021). "The interaction between multiple nanophase iron particles changes the slope of lunar reflectance spectra." In: *European Planetary Science Congress*, EPSC2021–770.

Arnaut, M., K. Wohlfarth, and C. Wöhler (Mar. 2020). "A Study Of Hyperspectral Clustering - How To Speed Up Spectral Unmixing Of Moon Mineralogy Mapper Data." In: *51st Lunar and Planetary Science Conference*, p. 3008.

Baker, A., B. Jolliff, C. Yasanayake, B. Denevi, and S. Lawrence (2020). "Lunar Agglutinate Glass Compositions and Comparison to Soil Grain-Size Fractions." In: *Lunar and Planetary Science Conference*. 2326, p. 1321.

Bandfield, J. L., M. Poston, R. L. Klima, and E. Christopher (Feb. 2018). "Widespread distribution of OH/H_2O on the lunar surface inferred from spectral data." In: *Nature Geoscience* 11.

Bandfield, J., C. Edwards, M. Poston, and R. Klima (2016). "Lunar H2O/OH-distributions: Revised infrared spectra from improved thermal corrections." In: *47th Annual Lunar and Planetary Science Conference*. 1903, p. 1594.

Barker, M., E. Mazarico, G. Neumann, M. Zuber, J. Haruyama, and D. Smith (2016). "A new lunar digital elevation model from the Lunar Orbiter Laser Altimeter and SELENE Terrain Camera." In: *Icarus* 273, pp. 346–355.

Bastien, F., P. Lamblin, R. Pascanu, J. Bergstra, I. Goodfellow, A. Bergeron, N. Bouchard, D. Warde-Farley, and Y. Bengio (2012). "Theano: new features and speed improvements." In: *arXiv preprint arXiv:1211.5590*.

Belgacem, I., F. Schmidt, and G. Jonniaux (2020). "Regional study of Europa's photometry." In: *Icarus* 338, p. 113525.

Belgacem, I., F. Schmidt, and G. Jonniaux (2021). "Regional study of Ganymede's photometry." In: *Icarus* 369, p. 114631.

Bhatt, M., U. Mall, C. Wöhler, A. Grumpe, and R. Bugiolacchi (2015). "A comparative study of iron abundance estimation methods: Application to the western nearside of the Moon." In: *Icarus* 248, pp. 72–88. ISSN: 0019-1035.

Bhatt, M., C. Wöhler, A. Grumpe, N. Hasebe, and M. Naito (June 2019). "Global mapping of lunar refractory elements: Multivariate regression vs. machine learning." In: *Astronomy & Astrophysics* 627.155, A155.

Bhatt, M., C. Wöhler, J. Rogall, K. Aravind, S. Ganesh, and A. Bhardwaj (2023). "Unique regolith characteristics of the lunar swirl Reiner Gamma as revealed by imaging polarimetry at large phase angles." In: *Astronomy & Astrophysics*.

Bhatt, M., C. Wöhler, D. Dhingra, G. Thangjam, D. Rommel, U. Mall, A. Bhardwaj, and A. Grumpe (2018). ""Compositional studies of Mare Moscoviense: New perspectives from Chandrayaan-1 VIS-NIR data"." In: *Icarus* 303, pp. 149–165. ISSN: 0019-1035.

Bishop, C. M. (2006). *Pattern recognition and machine learning*. Vol. 4. 4. New York, USA: Springer.

Bishop, J. L., J. F. Bell III, and J. E. Moersch (2019). *Remote compositional analysis: Techniques for understanding spectroscopy, mineralogy, and geochemistry of planetary surfaces*. Vol. 24. Cambridge, United Kingdom: Cambridge University Press.

Blewett, D. T., E. I. Coman, B. R. Hawke, J. J. Gillis-Davis, M. E. Purucker, and C. G. Hughes (2011). "Lunar swirls: Examining crustal magnetic anomalies and space weathering trends." In: *Journal of Geophysical Research: Planets* 116.E2.

Blewett, D. T., B. W. Denevi, J. T. Cahill, and R. L. Klima (2021). "Near-UV and near-IR reflectance studies of lunar swirls: Implications for nanosize iron content and the nature of anomalous space weathering." In: *Icarus* 364, p. 114472.

Blewett, D. T., P. G. Lucey, B. R. Hawke, and B. L. Jolliff (1997). "Clementine images of the lunar sample-return stations: Refinement of FeO and TiO_2 mapping techniques." In: *Journal of Geophysical Research: Planets* 102.E7, pp. 16319–16325.

Britt, D. and C. Pieters (1994). "Darkening in black and gas-rich ordinary chondrites: The spectral effects of opaque morphology and distribution." In: *Geochimica et Cosmochimica Acta* 58.18, pp. 3905–3919.

Bronstein, I. N., J. Hromkovic, B. Luderer, H.-R. Schwarz, J. Blath, A. Schied, S. Dempe, G. Wanka, and S. Gottwald (2012). *Taschenbuch der Mathematik*. Vol. 1. Frankfurt am Main, Germany: Springer-Verlag.

Burns, R. G. and R. G. Burns (1993). *Mineralogical applications of crystal field theory*. 5. New York, USA: Cambridge university press.

Carrier III, W. D., G. R. Olhoeft, and W. Mendell (1991). "Physical properties of the lunar surface." In: *Lunar sourcebook, a user's guide to the moon*, pp. 475–594.

Chandrasekhar, S. (1960). *Radiative transfer*. New York, USA: Dover Publications Inc.

Cheek, L. and C. Pieters (Oct. 2014). "Reflectance spectroscopy of plagioclase-dominated mineral mixtures: Implications for characterizing lunar anorthosites remotely." In: *American Mineralogist* 99, pp. 1871–1892.

Chowdhury, A. R., A. Banerjee, S. Joshi, M. Dutta, A. Kumar, S. Bhattacharya, S. U. R. Amitabh, S. Bhati, J. Karelia, A. Biswas, et al. (2020). "Imaging infrared spectrometer onboard Chandrayaan-2 orbiter." In: *Curr. Sci* 118.3, pp. 368–375.

Chrbolková, K., T. Kohout, and J. Ďurech (2019). "Reflectance spectra of seven lunar swirls examined by statistical methods: A space weathering study." In: *Icarus* 333, pp. 516–527.

Clark, R. N. et al. (Dec. 2009). "Water, Hydroxyl, and the Search for Alteration and Oxidation on the Moon (Invited)." In: *AGU Fall Meeting Abstracts*, P34A-03, P34A–03.

Clark, R. N., C. M. Pieters, R. O. Green, J. Boardman, and N. E. Petro (2011). "Thermal removal from near-infrared imaging spectroscopy data of the Moon." In: *Journal of Geophysical Research: Planets* 116.E6.

Clegg-Watkins, R., B. Jolliff, A. Boyd, M. Robinson, R. Wagner, J. Stopar, J. Plescia, and E. Speyerer (2016). "Photometric characterization of the Chang'e-3 landing site using LROC NAC images." In: *Icarus* 273, pp. 84–95.

Cloutis, E. A. (2002). "Pyroxene reflectance spectra: Minor absorption bands and effects of elemental substitutions." In: *Journal of Geophysical Research: Planets* 107.E6, pp. 6–1.

Cloutis, E. A., J. Sunshine, and R. Morris (2004). "Spectral reflectance-compositional properties of spinels and chromites: Implications for planetary remote sensing and geothermometry." In: *Meteoritics & Planetary Science* 39.4, pp. 545–565.

Coman, E. O., B. L. Jolliff, and P. Carpenter (2018). "Mineralogy and chemistry of Ti-Bearing lunar soils: Effects on reflectance spectra and remote sensing observations." In: *Icarus* 306, pp. 243–255.

Delbo, M., M. Mueller, J. P. Emery, B. Rozitis, and M. T. Capria (2015). *Asteroid thermophysical modeling*. Arizona, USA: University of Arizona Press Tucson.

Denevi, B. W., M. S. Robinson, A. K. Boyd, D. T. Blewett, and R. L. Klima (2016). "The distribution and extent of lunar swirls." In: *Icarus* 273, pp. 53–67.

Denevi, B., C. Yasanayake, B. Jolliff, S. Lawrence, T. Hiroi, and A. Martin (2021). "The Spectral Properties of Lunar Agglutinates." In: *Lunar and Planetary Science Conference*. 2548, p. 2368.

Dhingra, D., C. M. Pieters, J. W. Boardman, J. W. Head, P. J. Isaacson, and L. A. Taylor (2011). "Compositional diversity at Theophilus Crater: Understanding the geological context of Mg-spinel bearing central peaks." In: *Geophysical Research Letters* 38.11, A11.

Dollfus, A. (1999). "Lunar surface imaging polarimetry: Ii. mare fecunditatis and messier." In: *Icarus* 140.2, pp. 313–327.

Domingue, D., J. Weirich, F. Chuang, A. Sickafoose, and E. Palmer (2022). "Topographic Correlations Within Lunar Swirls in Mare Ingenii." In: *Geophysical Research Letters* 49.6, e2021GL095285.

Ehlmann, B. L., R. L. Klima, C. L. Bennett, D. Blaney, N. Bowles, S. Calcutt, J. Dickson, K. Donaldson Hanna, C. S. Edwards, R. Green, et al. (2021). "Lunar Trailblazer: A pioneering smallsat for lunar water and lunar geology." In: *Proceedings of the 52nd Lunar and Planetary Science Conference*. Vol. 2548.

Farrell, W., D. Hurley, and M. Zimmerman (2015). "Solar wind implantation into lunar regolith: Hydrogen retention in a surface with defects." In: *Icarus* 255, pp. 116–126. ISSN: 0019-1035.

Farrell, W., D. Hurley, V. Esposito, J. McLain, and M. Zimmerman (2017). "The statistical mechanics of solar wind hydroxylation at the Moon, within lunar magnetic anomalies, and at Phobos." In: *Journal of Geophysical Research: Planets* 122.1, pp. 269–289.

Feldman, W. C., S. Maurice, A. Binder, B. Barraclough, R. Elphic, and D. Lawrence (1998). "Fluxes of fast and epithermal neutrons from Lunar Prospector: Evidence for water ice at the lunar poles." In: *Science* 281.5382, pp. 1496–1500.

Fernando, J., F. Schmidt, X. Ceamanos, P. Pinet, S. Douté, and Y. Daydou (2013). "Surface reflectance of Mars observed by CRISM/MRO: 2. Estimation of surface photomet-

ric properties in Gusev Crater and Meridiani Planum." In: *Journal of Geophysical Research: Planets* 118.3, pp. 534–559.

Fernando, J., F. Schmidt, C. Pilorget, P. Pinet, X. Ceamanos, S. Douté, Y. Daydou, and F. Costard (2015). "Characterization and mapping of surface physical properties of Mars from CRISM multi-angular data: application to Gusev Crater and Meridiani Planum." In: *Icarus* 253, pp. 271–295.

Fowler, B. W. (1983). "Expansion of Mie-theory phase functions in series of Legendre polynomials." In: *JOSA* 73.1, pp. 19–22.

Fu, Z., A. Robles-Kelly, T. Caelli, and R. T. Tan (2007). "On automatic absorption detection for imaging spectroscopy: A comparative study." In: *IEEE transactions on geoscience and remote sensing* 45.11, pp. 3827–3844.

Garrick-Bethell, I., J. W. Head III, and C. M. Pieters (2011). "Spectral properties, magnetic fields, and dust transport at lunar swirls." In: *Icarus* 212.2, pp. 480–492.

Gauss, C. F. (1809). *Theoria motus corporum coelestium in sectionibus conicis solem ambientium*. Hamburg, Germany: sumtibus Frid. Perthes et IH Besser.

Gehrig, S. and U. Franke (2016). "Handbook of Driver Assistance Systems." In: Amsterdam, The Netherlands: Springer International Publishing. Chap. Stereovision for ADAS, pp. 495–524.

Gelman, A., J. B. Carlin, H. S. Stern, D. B. Dunson, A. Vehtari, and D. B. Rubin (2013). *Bayesian data analysis*. New York, USA: Chapman and Hall/CRC press.

Glotch, T. D., J. L. Bandfield, P. G. Lucey, P. O. Hayne, B. T. Greenhagen, J. A. Arnold, R. R. Ghent, and D. A. Paige (2015). "Formation of lunar swirls by magnetic field standoff of the solar wind." In: *Nature communications* 6.1, pp. 1–8.

Gold, T. and S. Soter (1976). "Cometary impact and the magnetization of the Moon." In: *Planetary and Space Science* 24.1, pp. 45–54.

Green, R., C. Pieters, P. Mouroulis, M. Eastwood, J. Boardman, T. Glavich, P. Isaacson, M. Annadurai, S. Besse, D. Barr, et al. (2011). "The Moon Mineralogy Mapper (M3) imaging spectrometer for lunar science: Instrument description, calibration, on-orbit measurements, science data calibration and on-orbit validation." In: *Journal of Geophysical Research: Planets* 116.E10.

Grumpe, A., F. Belkhir, and C. Wöhler (2014). "Construction of lunar DEMs based on reflectance modelling." In: *Advances in Space Research* 53.12, pp. 1735–1767.

Grumpe, A., N. Mengewein, D. Rommel, U. Mall, and C. Wöhler (2018). "Interpreting spectral unmixing coefficients: from spectral weights to mass fractions." In: *Icarus* 299, pp. 1–14.

Grumpe, A. and C. Wöhler (2014). "Recovery of elevation from estimated gradient fields constrained by digital elevation maps of lower lateral resolution." In: *ISPRS journal of photogrammetry and remote sensing* 94, pp. 37–54.

Grumpe, A., C. Wöhler, A. A. Berezhnoy, and V. V. Shevchenko (2019). "Time-of-day-dependent behavior of surficial lunar hydroxyl/water: Observations and modeling." In: *Icarus* 321, pp. 486–507.

Grumpe, A., V. Zirin, and C. Wöhler (2015). "A normalisation framework for (hyper-) spectral imagery." In: *Planetary and Space Science* 111, pp. 1–33.

Grynko, Y. and Y. Shkuratov (2007). "Ray tracing simulation of light scattering by spherical clusters consisting of particles with different shapes." In: *Journal of Quantitative Spectroscopy and Radiative Transfer* 106.1-3, pp. 56–62.

Haario, H., M. Laine, A. Mira, and E. Saksman (2006). "DRAM: efficient adaptive MCMC." In: *Statistics and computing* 16.4, pp. 339–354.

Haario, H., E. Saksman, J. Tamminen, et al. (2001). "An adaptive Metropolis algorithm." In: *Bernoulli* 7.2, pp. 223–242.

Hapke, B. (1981). "Bidirectional reflectance spectroscopy: 1. Theory." In: *Journal of Geophysical Research: Solid Earth* 86.B4, pp. 3039–3054.

Hapke, B. (1984). "Bidirectional reflectance spectroscopy: 3. Correction for macroscopic roughness." In: *Icarus* 59.1, pp. 41–59.

Hapke, B. (1986). "Bidirectional reflectance spectroscopy: 4. The extinction coefficient and the opposition effect." In: *Icarus* 67.2, pp. 264–280.

Hapke, B. (2001). "Space weathering from Mercury to the asteroid belt." In: *Journal of Geophysical Research: Planets* 106.E5, pp. 10039–10073.

Hapke, B. (2002). "Bidirectional reflectance spectroscopy: 5. The coherent backscatter opposition effect and anisotropic scattering." In: *Icarus* 157.2, pp. 523–534.

Hapke, B. (2008). "Bidirectional reflectance spectroscopy: 6. Effects of porosity." In: *Icarus* 195.2, pp. 918–926.

Hapke, B. (2012a). "Bidirectional reflectance spectroscopy 7: The single particle phase function hockey stick relation." In: *Icarus* 221.2, pp. 1079–1083.

Hapke, B. (2012b). *Theory of reflectance and emittance spectroscopy*. Cambridge, United Kingdom: Cambridge university press.

Hapke, B. and H. van Horn (1963). "Photometric studies of complex surfaces, with applications to the moon." In: *Journal of Geophysical Research* 68.15, pp. 4545–4570.

Hapke, B. and E. Wells (1981). "Bidirectional reflectance spectroscopy: 2. Experiments and observations." In: *Journal of Geophysical Research: Solid Earth* 86.B4, pp. 3055–3060.

Hastings, W. K. (1970). "Monte Carlo sampling methods using Markov chains and their applications." In.

Heiken, G., D. Vaniman, and B. M. French (1991). *Lunar sourcebook: A user's guide to the Moon*. 1259. Cambridge University Press.

Helfenstein, P. (1986). "Photometrically determined surface physical properties of terrains on Ganymede." In: *Lunar and Planetary Science Conference*. Vol. 17, pp. 333–334.

Hemingway, D. J. and S. M. Tikoo (2018). "Lunar swirl morphology constrains the geometry, magnetization, and origins of lunar magnetic anomalies." In: *Journal of Geophysical Research: Planets* 123.8, pp. 2223–2241.

Hendrix, A. R., D. M. Hurley, W. M. Farrell, B. T. Greenhagen, P. O. Hayne, K. D. Retherford, F. Vilas, J. T. Cahill, M. J. Poston, and Y. Liu (2019). "Diurnally migrating lunar water: evidence from ultraviolet data." In: *Geophysical Research Letters* 46.5, pp. 2417–2424.

Hendrix, A., T. Greathouse, K. Retherford, K. Mandt, G. Gladstone, D. Kaufmann, D. Hurley, P. Feldman, W. Pryor, S. Stern, et al. (2016). "Lunar swirls: far-UV characteristics." In: *Icarus* 273, pp. 68–74.

Henyey, L. G. and J. L. Greenstein (1941). "Diffuse radiation in the galaxy." In: *Astrophysical Journal, vol. 93, p. 70-83 (1941).* 93, pp. 70–83.

Hess, M., T. Wilhelm, M. Arnaut, and C. Wöhler (2021a). "Uncertainty-Based Unmixing of Space Weathered Lunar Spectra." In: *52nd Lunar and Planetary Science Conference*. 2548, p. 1048.

Hess, M., T. Wilhelm, C. Wöhler, and K. Wohlfarth (2021b). "Uncertainty Introduced by Darkening Agents in the Lunar Regolith: An Unmixing Perspective." In: *Remote Sensing* 13.22, p. 4702. DOI: 10.3390/rs13224702.

Hess, M., C. Wöhler, A. A. Berezhnoy, J. L. Bishop, and V. V. Shevchenko (2021c). "Dependence of the Hydration of the Lunar Surface on the Concentrations of TiO2, Plagioclase, and Spinel." In: *Remote Sensing* 14.1, p. 47. DOI: 10.3390/rs14010047.

Hess, M., C. Wöhler, M. Bhatt, A. A. Berezhnoy, A. Grumpe, K. Wohlfarth, A. Bhardwaj, and V. V. Shevchenko (2020a). "Processes governing the VIS/NIR spectral reflectance behavior of lunar swirls." In: *Astronomy & Astrophysics* 639, A12. DOI: 10.1051/0004-6361/201937299.

Hess, M., C. Wöhler, and J. Bishop (2019a). "Low Abundances of Strongly Bound Hydroxyl in Spinel-rich Areas of the Lunar Crater Theophilus." In: *EPSC-DPS Joint Meeting 2019*. Vol. 13, pp. 1608–1.

Hess, M., C. Wöhler, L. Qiao, and M. Bhatt (2023). "Comparative photometric analysis of the Reiner Gamma swirl and the Chang'e 5 landing site." In: *Astronomy & Astrophysics* 674. DOI: 10.1051/0004-6361/202346098.

Hess, M., K. Wohlfarth, and C. Wöhler (2020b). "Quantifying Lunar Spinel-Rich Lithologies with Nonlinear Spectral Unmixing Considering Space-Weathering Effects." In: *51st Annual Lunar and Planetary Science Conference*. 2326, p. 1863.

Hess, M., K. Wohlfarth, C. Wöhler, A. A. Berezhnoy, M. Bhatt, and A. Bhardwaj (2019b). "Space Weathering Trends at the Mare Moscoviense Swirl." In: *Europlanet Science Congress 2020*. Vol. 14, EPSC2020–716. DOI: https://doi.org/10.5194/epsc2020-716.

Hibbitts, C., G. Grieves, M. Poston, M. Dyar, A. Alexandrov, M. Johnson, and T. Orlando (2011). "Thermal stability of water and hydroxyl on the surface of the Moon from temperature-programmed desorption measurements of lunar analog materials." In: *Icarus* 213.1, pp. 64–72.

Hiesinger, H., J. W. Head III, U. Wolf, R. Jaumann, and G. Neukum (2011). "Ages and stratigraphy of lunar mare basalts: A synthesis." In: *Recent advances and current research issues in lunar stratigraphy*. Vol. 477. Boulder, Colorado, USA: Geological Society of America, pp. 1–51.

Hiesinger, H., J. W. Head III, U. Wolf, R. Jaumann, and G. Neukum (2003). "Ages and stratigraphy of mare basalts in oceanus procellarum, mare nubium, mare cognitum, and mare insularum." In: *Journal of Geophysical Research: Planets* 108.E7.

Hiesinger, H., R. Jaumann, G. Neukum, and J. W. Head III (2000). "Ages of mare basalts on the lunar nearside." In: *Journal of Geophysical Research: Planets* 105.E12, pp. 29239–29275.

Hinners, N. and F. El-Baz (1972). "Surface disturbances at the Apollo 15 landing site." In: *Apollo 15: Preliminary Science Report* 289, p. 50.

Hoffman, M. D. and A. Gelman (2014). "The No-U-Turn sampler: adaptively setting path lengths in Hamiltonian Monte Carlo." In: *J. Mach. Learn. Res.* 15.1, pp. 1593–1623.

Honniball, C. I., P. Lucey, C. M. Ferrari-Wong, A. Flom, S. Li, H. M. Kaluna, and D. Takir (2020). "Telescopic Observations of Lunar Hydration: Variations and Abundance." In: *Journal of Geophysical Research: Planets* 125.9, e2020JE006484.

Honniball, C., P. Lucey, S. Li, S. Shenoy, T. Orlando, C. Hibbitts, D. Hurley, and W. Farrell (2021). "Molecular water detected on the sunlit Moon by SOFIA." In: *Nature Astronomy* 5.2, pp. 121–127.

Hood, L. and G. Schubert (1980). "Lunar magnetic anomalies and surface optical properties." In: *Science* 208.4439, pp. 49–51.

Hood, L. and C. Williams (1989). "The lunar swirls-Distribution and possible origins." In: *Lunar and Planetary Science Conference Proceedings*. Vol. 19, pp. 99–113.

Horn, B. K. (1990). "Height and gradient from shading." In: *International journal of computer vision* 5.1, pp. 37–75.

Housley, R. M., R. W. Grant, and N. Paton (1973). "Origin and characteristics of excess Fe metal in lunar glass welded aggregates." In: *Proceedings of the Lunar Science Conference, vol. 4, p. 2737*. Vol. 4, p. 2737.

Housley, R., E. Cirlin, I. Goldberg, and H. Crowe (1976). "Ferromagnetic resonance studies of lunar core stratigraphy." In: *Lunar and Planetary Science Conference Proceedings*. Vol. 7, pp. 13–26.

Isaacson, P., S. Besse, N. Petro, J. Nettles, and the M^3 Team (Nov. 2011). *M^3 Overview and Working with M^3 Data*. Tech. rep. PDS. URL: `https://pds-imaging.jpl.nasa.gov/documentation/Isaacson_M3_Workshop_Final.pdf`.

Isaacson, P. J. and C. M. Pieters (2009). "Northern imbrium noritic anomaly." In: *Journal of Geophysical Research: Planets* 114.E9.

Kallio, E., S. Dyadechkin, P. Wurz, and M. Khodachenko (2019). "Space weathering on the Moon: Farside-nearside solar wind precipitation asymmetry." In: *Planetary and space science* 166, pp. 9–22.

Kaydash, V., M. Kreslavsky, Y. Shkuratov, S. Gerasimenko, P. Pinet, J.-L. Josset, S. Beauvivre, B. Foing, et al. (2009). "Photometric anomalies of the lunar surface studied with SMART-1 AMIE data." In: *Icarus* 202.2, pp. 393–413.

Keller, L. P. and D. S. McKay (1993). "Discovery of vapor deposits in the lunar regolith." In: *Science* 261.5126, pp. 1305–1307.

Keller, L. P. and D. S. McKay (1997). "The nature and origin of rims on lunar soil grains." In: *Geochimica et Cosmochimica Acta* 61.11, pp. 2331–2341.

Keshava, N. and J. F. Mustard (2002). "Spectral unmixing." In: *IEEE signal processing magazine* 19.1, pp. 44–57.

Kim, K. J., C. Wöhler, A. A. Berezhnoy, M. Bhatt, and A. Grumpe (2019). "Prospective 3He-rich landing sites on the Moon." In: *Planetary and Space Science* 177, p. 104686.

Klima, R., J. Cahill, J. Hagerty, and D. Lawrence (2013). "Remote detection of magmatic water in Bullialdus Crater on the Moon." In: *Nature Geoscience* 6.9, pp. 737–741.

Klima, R. L., M. D. Dyar, and C. M. Pieters (2011). "Near-infrared spectra of clinopyroxenes: Effects of calcium content and crystal structure." In: *Meteoritics & Planetary Science* 46.3, pp. 379–395.

Klima, R. L., C. M. Pieters, and M. D. Dyar (2007). "Spectroscopy of synthetic Mg-Fe pyroxenes I: Spin-allowed and spin-forbidden crystal field bands in the visible and near-infrared." In: *Meteoritics & Planetary Science* 42.2, pp. 235–253.

Kramer, G. Y., S. Besse, D. Dhingra, J. Nettles, R. Klima, I. Garrick-Bethell, R. N. Clark, J.-P. Combe, J. W. Head III, L. A. Taylor, et al. (2011). "M3 spectral analysis of lunar swirls and the link between optical maturation and surface hydroxyl formation at magnetic anomalies." In: *Journal of Geophysical Research: Planets* 116.E9.

Kreslavsky, M. and Y. G. Shkuratov (2003). "Photometric anomalies of the lunar surface: Results from Clementine data." In: *Journal of Geophysical Research: Planets* 108.E3.

Kurahashi, E., C. Yamanaka, K. Nakamura, and S. Sasaki (2002). "Laboratory simulation of space weathering: ESR measurements of nanophase metallic iron in laser-irradiated materials." In: *Earth, planets and space* 54, e5–e7.

Lapotre, M. G., B. L. Ehlmann, and S. E. Minson (2017). "A probabilistic approach to remote compositional analysis of planetary surfaces." In: *Journal of Geophysical Research: Planets* 122.5, pp. 983–1009.

Laura, J. et al. (May 2022). *Integrated Software for Imagers and Spectrometers*. Version 7.0.0.

Lawrence, D., W. Feldman, B. Barraclough, A. Binder, R. Elphic, S. Maurice, and D. Thomsen (1998). "Global elemental maps of the Moon: The Lunar Prospector gamma-ray spectrometer." In: *Science* 281.5382, pp. 1484–1489.

Lemelin, M., P. Lucey, L. Gaddis, T. Hare, and M. Ohtake (2016). "Global map products from the Kaguya multiband imager at 512 ppd: Minerals, FeO, and OMAT." In: *Lunar and Planetary Science Conference*. Vol. 47, p. 2994.

Lemelin, M., P. G. Lucey, K. Miljković, L. R. Gaddis, T. Hare, and M. Ohtake (2019). "The compositions of the lunar crust and upper mantle: Spectral analysis of the inner rings of lunar impact basins." In: *Planetary and Space Science* 165, pp. 230–243.

Lemelin, M., P. G. Lucey, E. Song, and G. J. Taylor (2015). "Lunar central peak mineralogy and iron content using the Kaguya Multiband Imager: Reassessment of the compositional structure of the lunar crust." In: *Journal of Geophysical Research: Planets* 120.5, pp. 869–887.

Li, L. (2008). "Quantifying lunar soil composition with partial least squares modeling of reflectance." In: *Advances in Space Research* 42.2, pp. 267–274.

Li, S. and I. Garrick-Bethell (2019). "Surface water at lunar magnetic anomalies." In: *Geophysical Research Letters* 46.24, pp. 14318–14327.

Li, S. and R. E. Milliken (2017). "Water on the surface of the Moon as seen by the Moon Mineralogy Mapper: Distribution, abundance, and origins." In: *Science Advances* 3, e1701471.

Liu, Y., T. D. Glotch, N. A. Scudder, M. L. Kraner, T. Condus, R. E. Arvidson, E. A. Guinness, M. J. Wolff, and M. D. Smith (2016). "End-member identification and spectral mixture analysis of CRISM hyperspectral data: A case study on southwest Melas Chasma, Mars." In: *Journal of Geophysical Research: Planets* 121.10, pp. 2004–2036.

Liu, Y., Y. Guan, Y. Zhang, G. R. Rossman, J. M. Eiler, and L. A. Taylor (2012). "Direct measurement of hydroxyl in the lunar regolith and the origin of lunar surface water." In: *Nature Geoscience* 5.11, pp. 779–782.

Lucey, P. G. (1998). "Model near-infrared optical constants of olivine and pyroxene as a function of iron content." In: *Journal of Geophysical Research: Planets* 103.E1, pp. 1703–1713.

Lucey, P. G. (2004). "Mineral maps of the Moon." In: *Geophysical Research Letters* 31.8.

Lucey, P. G., D. T. Blewett, and B. L. Jolliff (2000a). "Lunar iron and titanium abundance algorithms based on final processing of Clementine ultraviolet-visible images." In: *Journal of Geophysical Research: Planets* 105.E8, pp. 20297–20305.

Lucey, P. G., D. T. Blewett, G. J. Taylor, and B. R. Hawke (2000b). "Imaging of lunar surface maturity." In: *Journal of Geophysical Research: Planets* 105.E8, pp. 20377–20386.

Lucey, P. G. and S. K. Noble (2008). "Experimental test of a radiative transfer model of the optical effects of space weathering." In: *Icarus* 197.1, pp. 348–353.

Lucey, P. G. and M. A. Riner (2011). "The optical effects of small iron particles that darken but do not redden: Evidence of intense space weathering on Mercury." In: *Icarus* 212.2, pp. 451–462.

Lucey, P. G. (2002). "Radiative transfer model constraints on the shock state of remotely sensed lunar anorthosites." In: *Geophysical Research Letters* 29.10, pp. 124-1-124–3.

Lue, C., Y. Futaana, S. Barabash, M. Wieser, M. Holmström, A. Bhardwaj, M. Dhanya, and P. Wurz (2011). "Strong influence of lunar crustal fields on the solar wind flow." In: *Geophysical Research Letters* 38.3.

Lyne, Å. L., P. Redelius, M. Collin, and B. Birgisson (2013). "Characterization of stripping properties of stone material in asphalt." In: *Materials and structures* 46, pp. 47–61.

Markley, M. and G. Kletetschka (2016). "Nanophase iron production through laser irradiation and magnetic detection of space weathering analogs." In: *Icarus* 268, pp. 204–214.

Marsland, S. (2015). *Machine Learning: An Algorithmic Perspective*. 2nd ed. New Jersey, USA: CRC Press.

McCord, T., L. Taylor, J.-P. Combe, G. Kramer, C. Pieters, J. Sunshine, and R. Clark (2011). "Sources and physical processes responsible for OH/H_2O in the lunar soil as revealed by the Moon Mineralogy Mapper (M^3)." In: *Journal of Geophysical Research: Planets* 116.E6.

McCord, T. B. (1969). "Color differences on the lunar surface." In: *Journal of Geophysical Research* 74.12, pp. 3131–3142.

McCord, T. B., R. N. Clark, B. R. Hawke, L. A. McFadden, P. Owensby, C. M. Pieters, and J. B. Adams (1981). "Moon: Near-infrared spectral reflectance, a first good look." In: *Journal of Geophysical Research: Solid Earth* 86.B11, pp. 10883–10892.

McCord, T. B. and T. V. Johnson (1970). "Lunar spectral reflectivity (0.30 to 2.50 microns) and implications for remote mineralogical analysis." In: *Science* 169.3948, pp. 855–858.

McKay, D. S., G. Heiken, A. Basu, G. Blanford, S. Simon, R. Reedy, B. M. French, and J. Papike (1991). "The lunar regolith." In: *Lunar sourcebook* 567, pp. 285–356.

Metropolis, N., A. W. Rosenbluth, M. N. Rosenbluth, A. H. Teller, and E. Teller (1953). "Equation of state calculations by fast computing machines." In: *The journal of chemical physics* 21.6, pp. 1087–1092.

Milliken, R. E. and J. F. Mustard (2007). "Estimating the water content of hydrated minerals using reflectance spectroscopy: I. Effects of darkening agents and low-albedo materials." In: *Icarus* 189.2, pp. 550–573.

Mishchenko, M. I. (2002). "Vector radiative transfer equation for arbitrarily shaped and arbitrarily oriented particles: a microphysical derivation from statistical electromagnetics." In: *Applied optics* 41.33, pp. 7114–7134.

Mishchenko, M. I., L. D. Travis, and A. A. Lacis (2006). *Multiple scattering of light by particles: radiative transfer and coherent backscattering*. Cambridge, United Kingdom: Cambridge University Press.

Morris, R. (1976). "Surface exposure indices of lunar soils-A comparative FMR study." In: *In: Lunar Science Conference, 7th, Houston, Tex., March 15-19, 1976, Proceedings.*

Volume 1.(A77-34651 15-91) New York, Pergamon Press, Inc., 1976, p. 315-335. Vol. 7, pp. 315–335.

Morris, R. (1980). "Origins and size distribution of metallic iron particles in the lunar regolith." In: *Lunar and Planetary Science Conference Proceedings*. Vol. 11, pp. 1697–1712.

Mustard, J. F. et al. (2011). "Compositional diversity and geologic insights of the Aristarchus crater from Moon Mineralogy Mapper data." In: *Journal of Geophysical Research: Planets* 116, E00G12.

Mustard, J. F. and C. M. Pieters (1987). "Quantitative abundance estimates from bidirectional reflectance measurements." In: *Journal of Geophysical Research: Solid Earth* 92.B4, E617–E626.

Nash, D. B. and J. E. Conel (1974). "Spectral reflectance systematics for mixtures of powdered hypersthene, labradorite, and ilmenite." In: *Journal of Geophysical Research (1896-1977)* 79.11, pp. 1615–1621.

Neal, R. M. (1993). *Probabilistic inference using Markov chain Monte Carlo methods*. Toronto, Ontario, Canada: Department of Computer Science, University of Toronto.

Neal, R. M. et al. (2011). "MCMC using Hamiltonian dynamics." In: *Handbook of markov chain monte carlo* 2.11, p. 2.

Neish, C., D. Blewett, D. Bussey, S. Lawrence, M. Mechtley, and B. Thomson (2011). "The surficial nature of lunar swirls as revealed by the Mini-RF instrument." In: *Icarus* 215.1, pp. 186–196. ISSN: 0019-1035.

Nelson, D., S. Koeber, K. Daud, M. Robinson, T. Watters, M. Banks, and N. Williams (2014). "Mapping lunar maria extents and lobate scarps using LROC image products." In: *LPI* 1777, p. 2861.

Neukum, G. and B. Ivanov (1994). "Crater size distributions and impact probabilities on Earth from lunar, terrestrial-planet, and asteroid cratering data." In: *Hazards Due to Comets and Asteroids*. 1. Tucson, USA: University of Arizona Press, pp. 359–416.

Neukum, G., B. A. Ivanov, and W. K. Hartmann (2001). "Cratering records in the inner solar system in relation to the lunar reference system." In: *Chronology and Evolution of Mars: Proceedings of an ISSI Workshop, 10–14 April 2000, Bern, Switzerland*. Springer, pp. 55–86.

Noble, S., T. Hiroi, L. Keller, and C. Pieters (2011). "Experimental space weathering of ordinary chondrites by nanopulse laser: TEM results." In: *42nd Lunar and Planetary Science Conference*. JSC-CN-22818.

Nozette, S., C. L. Lichtenberg, P. Spudis, R. Bonner, W. Ort, E. Malaret, M. Robinson, and E. M. Shoemaker (1996). "The Clementine Bistatic Radar Experiment." In: *Science* 274.5292, pp. 1495–1498.

Nozette, S., P. Rustan, L. Pleasance, J. Kordas, I. Lewis, H. Park, R. Priest, D. Horan, P. Regeon, C. Lichtenberg, et al. (1994). "The Clementine mission to the Moon: Scientific overview." In: *Science* 266.5192, pp. 1835–1839.

Ohtake, M., J. Haruyama, T. Matsunaga, Y. Yokota, T. Morota, C. Honda, and L. team (2008). "Performance and scientific objectives of the SELENE (KAGUYA) Multiband Imager." In: *Earth, planets and space* 60, pp. 257–264.

Oriol, A.-P. et al. (2023). "PyMC: A Modern and Comprehensive Probabilistic Programming Framework in Python." In: *PeerJ Computer Science* 9, e1516.

Papike, J., L. Taylor, and S. Simon (1991). "Lunar minerals." In: *Lunar sourcebook; a user's guide to the Moon*. Ed. by G. Heiken, D. Vaniman, and B. French. Cambridge University Press, pp. 121–182.

Pieters, C. M., K. Donaldson Hanna, L. Cheek, D. Dhingra, T. Prissel, C. Jackson, D. Moriarty, S. Parman, and L. A Taylor (Oct. 2014). "The distribution of Mg-spinel across the Moon and constraints on crustal origin." In: *American Mineralogist* 99.11, pp. 1893–1910.

Pieters, C. M. et al. (Nov. 2009). "The Moon Mineralogy Mapper (M3) on Chandrayaan-1." In: *Curr. Sci.* 96, pp. 500–505.

Pieters, C. M. et al. (2011). "Mg-spinel lithology: A new rock type on the lunar farside." In: *Journal of Geophysical Research: Planets* 116, E6.

Pieters, C. M. and J. F. Mustard (1988). "Exploration of crustal/mantle material for the earth and moon using reflectance spectroscopy." In: *Remote sensing of Environment* 24.1, pp. 151–178.

Pieters, C. M. and S. K. Noble (2016). "Space weathering on airless bodies." In: *Journal of Geophysical Research: Planets* 121.10, pp. 1865–1884.

Pieters, C. M., D. Stankevich, Y. Shkuratov, and L. Taylor (2002). "Statistical Analysis of the Links among Lunar Mare Soil Mineralogy, Chemistry, and Reflectance Spectra." In: *Icarus* 155.2, pp. 285–298. ISSN: 0019-1035.

Pieters, C. M., T. Hiroi, S. F. Pratt, and B. Patterson (2004). "Reflectance Experiment Laboratory (RELAB) Description and User's Manual." In.

Pieters, C. (2018). "What Lunar Swirls Represent (.. Probably)." In: *6th European Lunar Symposium (Toulouse, France)*.

Pieters, C., K. Donaldson Hanna, J. Sunshine, and I. Garrick-Bethell (2021). "New M-Cube Insights on the Character of the Mysterious Reiner Gamma Swirls." In: *52nd Lunar and Planetary Science Conference*. 2548, p. 1686.

Pieters, C. and I. Garrick-Bethell (2015). "Hydration variations at lunar swirls." In: *46th Annual Lunar and Planetary Science Conference*. 1832, p. 2120.

Pinet, P. C., V. V. Shevchenko, S. D. Chevrel, Y. Daydou, and C. Rosemberg (2000). "Local and regional lunar regolith characteristics at Reiner Gamma Formation: Optical and spectroscopic properties from Clementine and Earth-based data." In: *Journal of Geophysical Research: Planets* 105.E4, pp. 9457–9475.

Pinet, P., A. Cord, S. Chevrel, and Y. Daydou (2004). "Optical response and surface physical properties of the lunar regolith at Reiner Gamma Formation from Clementine orbital photometry: Derivation of the Hapke parameters at local scale." In: *Lunar and Planetary Science Conference*, p. 1660.

Poston, M. J., G. A. Grieves, A. B. Aleksandrov, C. A. Hibbitts, M. D. Dyar, and T. M. Orlando (2015). "Temperature programmed desorption studies of water interactions with Apollo lunar samples 12001 and 72501." In: *Icarus* 255, pp. 24–29.

Poulet, F., J. Carter, J. Bishop, D. Loizeau, and S. Murchie (2014). "Mineral abundances at the final four curiosity study sites and implications for their formation." In: *Icarus* 231, pp. 65–76.

Pour, A. B., Y. Park, T.-Y. S. Park, J. K. Hong, M. Hashim, J. Woo, and I. Ayoobi (2018). "Regional geology mapping using satellite-based remote sensing approach in Northern Victoria Land, Antarctica." In: *Polar Science* 16, pp. 23–46.

Prettyman, T. H., J. Hagerty, R. Elphic, W. Feldman, D. Lawrence, G. McKinney, and D. Vaniman (2006). "Elemental composition of the lunar surface: Analysis of gamma ray spectroscopy data from Lunar Prospector." In: *Journal of Geophysical Research: Planets* 111.E12.

Prinz, M., E. Dowty, K. Keil, and T. E. Bunch (1973). "Spinel Troctolite and Anorthosite in Apollo 16 Samples." In: *Science* 179.4068, pp. 74–76.

Qiao, L., J. W. Head, Z. Ling, and L. Wilson (2020). "Lunar irregular mare patches: Classification, characteristics, geologic settings, updated catalog, origin, and outstanding questions." In: *Journal of Geophysical Research: Planets* 125.7, e2019JE006362.

Robinson, M., S. Brylow, M. Tschimmel, D. Humm, S. Lawrence, P. Thomas, B. Denevi, E. Bowman-Cisneros, J. Zerr, M. Ravine, et al. (2010). "Lunar reconnaissance orbiter camera (LROC) instrument overview." In: *Space science reviews* 150.1, pp. 81–124.

Rommel, D., A. Grumpe, M. P. Felder, C. Wöhler, U. Mall, and A. Kronz (2017). "Automatic endmember selection and nonlinear spectral unmixing of Lunar analog minerals." In: *Icarus* 284, pp. 126–149.

Rossman, G. R. and J. R. Smyth (Aug. 1990). "Hydroxyl contents of accessory minerals in mantle eclogites and related rocks." In: *American Mineralogist* 75.7-8, pp. 775–780. ISSN: 0003-004X.

Roush, T. L., L. F. Teodoro, D. T. Blewett, and J. T. Cahill (2021). "Optical constants and diffuse reflectance of opaque minerals: A modeling study using magnetite." In: *Icarus* 361, p. 114331.

Rout, S., L. Moroz, D. Baither, C. van der Bogert, and A. Bischoff (2008). "Laboratory simulations of space weathering and impact heating of planetary surfaces: The TEM studies." In: *3rd European Planetary Science Congress*, EPSC2008–A.

Salvatier, J., T. V. Wiecki, and C. Fonnesbeck (2016). "Probabilistic programming in Python using PyMC3." In: *PeerJ Computer Science* 2, e55.

Sato, H., M. S. Robinson, B. Hapke, B. Denevi, and A. Boyd (2014). "Resolved Hapke parameter maps of the Moon." In: *Journal of Geophysical Research: Planets* 119.8, pp. 1775–1805.

Sato, H., M. S. Robinson, S. J. Lawrence, B. W. Denevi, B. Hapke, B. L. Jolliff, and H. Hiesinger (2017). "Lunar mare TiO2 abundances estimated from UV/Vis reflectance." In: *Icarus* 296, pp. 216–238.

Schmidt, F. and J. Fernando (2015). "Realistic uncertainties on Hapke model parameters from photometric measurement." In: *Icarus* 260, pp. 73–93.

Scholten, F., J. Oberst, K.-D. Matz, T. Roatsch, M. Wählisch, E. Speyerer, and M. Robinson (2012). "GLD100: The near-global lunar 100 m raster DTM from LROC WAC stereo image data." In: *Journal of Geophysical Research: Planets* 117.E12.

Schörghofer, N., M. Benna, A. A. Berezhnoy, B. Greenhagen, B. M. Jones, S. Li, T. M. Orlando, P. Prem, O. J. Tucker, and C. Wöhler (2021). "Water group exospheres and surface interactions on the Moon, Mercury, and Ceres." In: *Space Science Reviews* 217.6, pp. 1–35.

Schultz, P. H. and L. J. Srnka (1980). "Cometary collisions on the Moon and Mercury." In: *Nature* 284.5751, pp. 22–26.

Shevchenko, V. (1993). "Observable evidence for cometary impacts on the Moon and their age." In: *Astronomy Reports* 37, pp. 314–319.

Shevchenko, V., P. Pinet, and S. Chevrel (1994). "Remote-sensing studies of immature lunar soils (Reiner-γ formation)." In: *Solar System Research* 27.4, pp. 310–321.

Shkuratov, Y., V. Kaydash, V. Korokhin, Y. Velikodsky, N. Opanasenko, and G. Videen (2011). "Optical measurements of the Moon as a tool to study its surface." In: *Planetary and Space Science* 59.13. Exploring Phobos, pp. 1326–1371. ISSN: 0032-0633.

Shkuratov, Y., V. Kaydash, S. Gerasimenko, N. Opanasenko, Y. Velikodsky, V. Korokhin, G. Videen, and C. Pieters (2010). "Probable swirls detected as photometric anomalies in Oceanus Procellarum." In: *Icarus* 208.1, pp. 20–30.

Shkuratov, Y. G., M. Kreslavsky, A. Ovcharenko, D. Stankevich, E. Zubko, C. Pieters, and G. Arnold (1999a). "Opposition effect from Clementine data and mechanisms of backscatter." In: *Icarus* 141.1, pp. 132–155.

Shkuratov, Y. G., L. Starukhina, V. Kaidash, and N. Bondarenko (1999b). "3 He Distribution over the Lunar Visible Hemisphere." In: *Solar System Research* 33, p. 409.

Shkuratov, Y. G., L. Starukhina, M. Kreslavsky, N. Opanasenko, D. Stankevich, and V. Shevchenko (1994). "Principle of undulatory invariance in photometry of atmosphereless celestial bodies." In: *Icarus* 109.1, pp. 168–190.

Shkuratov, Y., L. Starukhina, H. Hoffmann, and G. Arnold (1999c). "A model of spectral albedo of particulate surfaces: Implications for optical properties of the Moon." In: *Icarus* 137.2, pp. 235–246.

Shkuratov, Y., N. Opanasenko, E. Zubko, Y. Grynko, V. Korokhin, C. Pieters, G. Videen, U. Mall, and A. Opanasenko (2007). "Multispectral polarimetry as a tool to investigate texture and chemistry of lunar regolith particles." In: *Icarus* 187.2, pp. 406–416.

Slatosch, J. (2023). "Bayesian Inference of Grain Size for Space Weathered Lunar Spectra." Master Thesis. Image Analysis Group, TU Dortmund University.

Speyerer, E., M. Robinson, B. Denevi, et al. (2011). "Lunar Reconnaissance Orbiter Camera global morphological map of the Moon." In: *42nd Annual Lunar and Planetary Science Conference*. 1608, p. 2387.

Staid, M., C. M. Pieters, S. Besse, J. Boardman, D. Dhingra, R. Green, J. Head, P. Isaacson, R. Klima, G. Kramer, et al. (2011). "The mineralogy of late stage lunar volcanism as observed by the Moon Mineralogy Mapper on Chandrayaan-1." In: *Journal of Geophysical Research: Planets* 116.E6.

Staid, M. I. and C. M. Pieters (2000). "Integrated spectral analysis of mare soils and craters: Applications to eastern nearside basalts." In: *Icarus* 145.1, pp. 122–139.

Starukhina, L. (July 2013). "Water on the Moon: What Is Derived from the Observations?" In: *Moon: Prospective Energy and Material Resources*, pp. 57–85.

Starukhina, L. V. and Y. G. Shkuratov (2004). "Swirls on the Moon and Mercury: Meteoroid swarm encounters as a formation mechanism." In: *Icarus* 167.1, pp. 136–147.

Student (1908). "The probable error of a mean." In: *Biometrika* 6.1, pp. 1–25.

Sun, L. and P. G. Lucey (2021). "Unmixing Mineral Abundance and Mg# With Radiative Transfer Theory: Modeling and Applications." In: *Journal of Geophysical Research: Planets* 126.2, e2020JE006691.

Sunshine, J. M. et al. (Mar. 2010). "Hidden in Plain Sight: Spinel-rich Deposits on the Nearside of the Moon as Revealed by Moon Mineralogy Mapper (M^3)." In: *Lunar and Planetary Science Conference*. Vol. 41. Lunar and Planetary Science Conference, p. 1508.

Sunshine, J. M. and C. M. Pieters (1998). "Determining the composition of olivine from reflectance spectroscopy." In: *Journal of Geophysical Research: Planets* 103.E6, pp. 13675–13688.

Surkov, Y., Y. Shkuratov, V. Kaydash, S. Velichko, V. Korokhin, and G. Videen (2021). "Characterizing southern portion of Mare Vaporum with improved Chandrayaan-1 M3 data." In: *Icarus* 355, p. 114123.

Syal, M. B. and P. H. Schultz (2015). "Cometary impact effects at the Moon: Implications for lunar swirl formation." In: *Icarus* 257, pp. 194–206.

Taylor, L., A. Patchen, D. Taylor, J. Chambers, and D. McKay (1996). "X-ray digital imaging and petrography of lunar mare soils: Data input for remote sensing calibrations." In: *Icarus* 124, pp. 500–512.

Taylor, L., C. Pieters, A. Patchen, D. Taylor, R. Morris, L. Keller, and D. McKay (2003). "Mineralogical characterization of lunar highland soils." In: *Lunar Planet. Sci., XXXIV*.

Taylor, L. A., C. Pieters, L. P. Keller, R. V. Morris, D. S. McKAY, A. Patchen, and S. Wentworth (2001). "The effects of space weathering on Apollo 17 mare soils: Petrographie and chemical characterization." In: *Meteoritics & Planetary Science* 36.2, pp. 285–299.

Taylor, L. A., C. Pieters, A. Patchen, D.-H. S. Taylor, R. V. Morris, L. P. Keller, and D. S. McKay (2010). "Mineralogical and chemical characterization of lunar highland soils: Insights into the space weathering of soils on airless bodies." In: *Journal of Geophysical Research: Planets* 115.E2.

Thompson, M. S., T. J. Zega, and J. Y. Howe (2017). "In situ experimental formation and growth of Fe nanoparticles and vesicles in lunar soil." In: *Meteoritics & Planetary Science* 52.3, pp. 413–427.

Tompkins, S. and C. M. Pieters (2010). "Spectral characteristics of lunar impact melts and inferred mineralogy." In: *Meteoritics & Planetary Science* 45.7, pp. 1152–1169.

Trang, D. and P. G. Lucey (2019). "Improved space weathering maps of the lunar surface through radiative transfer modeling of Kaguya multiband imager data." In: *Icarus* 321, pp. 307–323.

Trang, D., P. G. Lucey, and N. R. Izenberg (2017). "Radiative transfer modeling of MESSENGER VIRS spectra: Detection and mapping of submicroscopic iron and carbon." In: *Icarus* 293, pp. 206–217.

Tsunakawa, H., F. Takahashi, H. Shimizu, H. Shibuya, and M. Matsushima (2015). "Surface vector mapping of magnetic anomalies over the Moon using Kaguya and Lunar Prospector observations." In: *Journal of Geophysical Research: Planets* 120.6, pp. 1160–1185.

Tucker, O. J., W. M. Farrell, and A. R. Poppe (2021). "On the effect of magnetospheric shielding on the lunar hydrogen cycle." In: *Journal of Geophysical Research: Planets* 126.2, e2020JE006552.

Varatharajan, I., E. Sklute, T. Glotch, and M. Dyar (2023). "A Genetic Algorithm Approach for Obtaining Wavelength Dependent Mid-Infrared Optical Constants (5-25 μm) of Silicate Glasses." In: *LPI Contributions* 2806, p. 1665.

Vasavada, A. R., D. A. Paige, and S. E. Wood (1999). "Near-surface temperatures on Mercury and the Moon and the stability of polar ice deposits." In: *Icarus* 141.2, pp. 179–193.

Wagner, R., E. Speyerer, M. Robinson, L. Team, et al. (2015). "New mosaicked data products from the LROC team." In: *46th Annual Lunar and Planetary Science Conference*. 1832, p. 1473.

Warell, J. (2004). "Properties of the Hermean regolith: IV. Photometric parameters of Mercury and the Moon contrasted with Hapke modelling." In: *Icarus* 167.2, pp. 271–286.

Weitz, C. M., J. W. Head III, and C. M. Pieters (1998). "Lunar regional dark mantle deposits: Geologic, multispectral, and modeling studies." In: *Journal of Geophysical Research: Planets* 103.E10, pp. 22725–22759.

Weitz, C. M., M. I. Staid, L. R. Gaddis, S. Besse, and J. M. Sunshine (2017). "Investigation of Lunar Spinels at Sinus Aestuum." In: *Journal of Geophysical Research: Planets* 122.10, pp. 2013–2033.

Whitaker, E. A. (1972). "Lunar color boundaries and their relationship to topographic features: A preliminary survey." In: *The Moon* 4, pp. 348–355.

Wieser, M., S. Barabash, Y. Futaana, M. Holmström, A. Bhardwaj, R. Sridharan, M. Dhanya, A. Schaufelberger, P. Wurz, and K. Asamura (2010). "First observation of a mini-magnetosphere above a lunar magnetic anomaly using energetic neutral atoms." In: *Geophysical Research Letters* 37.5.

Wilcox, B., P. Lucey, and B. Hawke (2006). "Radiative transfer modeling of compositions of lunar pyroclastic deposits." In: *Journal of Geophysical Research: Planets* 111.E9.

Wöhler, C., M. Bhatt, M. Arnaut, S. Ganesh, K. Aravind, and A. Bhardwaj (2023). "Spectropolarimetric Properties of the Lunar Swirl Reiner Gamma and Western Oceanus Procellarum." In: *LPI Contributions* 2806, p. 1609.

Wöhler, C., A. Grumpe, M. Bhatt, A. Berezhnoy, V. Shevchenko, and A. Bhardwaj (2019). "Detection of an excessively strong 3-μm absorption near the lunar highland crater Dufay." In: *Astronomy & Astrophysics* 630, p. L7.

Wöhler, C., A. A. Berezhnoy, A. Grumpe, and V. V. Shevchenko (2018). "Correlation Between Lunar Soil Composition and Weakly Bounded Surficial OH/H_2O Component." In: *European Lunar Symposium*. Toulouse, Abstract #033.

Wöhler, C., A. Grumpe, A. Berezhnoy, M. U. Bhatt, and U. Mall (2014). "Integrated topographic, photometric and spectral analysis of the lunar surface: Application to impact melt flows and ponds." In: *Icarus* 235, pp. 86–122.

Wöhler, C., A. Grumpe, A. A. Berezhnoy, E. A. Feoktistova, N. A. Evdokimova, K. Kapoor, and V. V. Shevchenko (Feb. 2017a). "Temperature regime and water/hydroxyl behavior in the crater Boguslawsky on the Moon." In: *Icarus* 285, pp. 118–136. ISSN: 0019-1035.

Wöhler, C., A. Grumpe, A. A. Berezhnoy, and V. V. Shevchenko (Nov. 2017b). "Time-of-day–dependent global distribution of lunar surficial water/hydroxyl." In: *Science Advances* 3, e1701286.

Wöhler, C., A. Grumpe, A. A. Berezhnoy, and V. V. Shevchenko (Dec. 2021). *Global maps of the lunar 3-μm absorption band*. Zenodo. DOI: 10.5281/zenodo.5773293. URL: https://doi.org/10.5281/zenodo.5773293.

Wohlfarth, K., C. Wöhler, H. Hiesinger, and J. Helbert (2023). "An advanced thermal roughness model for airless planetary bodies-Implications for global variations of lunar hydration and mineralogical mapping of Mercury with the MERTIS spectrometer." In: *Astronomy & Astrophysics* 674, A69.

Wohlfarth, K. S., C. Wöhler, and A. Grumpe (2019). "Space Weathering and Lunar OH/H_2O Insights from Ab Initio Mie Modeling of Submicroscopic Iron." In: *The Astronomical Journal* 158.2, p. 80.

Wu, Y. and B. Hapke (2018). "Spectroscopic observations of the Moon at the lunar surface." In: *Earth and Planetary Science Letters* 484, pp. 145–153.

Xu, J., M. Wang, H. Lin, X. Xu, B. Liu, W. Yan, Y. Yang, R. Wang, C. Liu, R. Xu, et al. (2022). "In-Situ Photometric Properties of Lunar Regolith Revealed by Lunar Mineralogical Spectrometer on Board Chang'E-5 Lander." In: *Geophysical Research Letters* 49.4, e2021GL096876.

Xu, X., J. Liu, D. Liu, B. Liu, and R. Shu (2020). "Photometric correction of chang'e-1 interference imaging spectrometer's (Iim) limited observing geometries data with hapke model." In: *Remote Sensing* 12.22, p. 3676.

Yamamoto, S. et al. (2013). "A new type of pyroclastic deposit on the Moon containing Fe-spinel and chromite." In: *Geophysical Research Letters* 40.17, pp. 4549–4554.

Yamamoto, S., R. Nakamura, T. Matsunaga, Y. Ogawa, Y. Ishihara, T. Morota, N. Hirata, M. Ohtake, T. Hiroi, Y. Yokota, et al. (2015). "Featureless spectra on the Moon as evidence of residual lunar primordial crust." In: *Journal of Geophysical Research: Planets* 120.12, pp. 2190–2205.

Zhang, H., C. Li, J. You, X. Zhang, Y. Wang, L. Chen, Q. Fu, B. Zhang, and Y. Wang (2022). "The Investigation of Plume-Regolith Interaction and Dust Dispersal during Chang'E-5 Descent Stage." In: *Aerospace* 9.7, p. 358.

Zhang, X., B. Lu, R. Li, C. Fan, Z. Liang, and P. Han (2015). "Structural, electronic and optical properties of ilmenite $ATiO_3$ (A= Fe, Co, Ni)." In: *Materials Science in Semiconductor Processing* 39, pp. 6–16.

Zhang, Y., E. M. Stolper, and G. Wasserburg (1991). "Diffusion of water in rhyolitic glasses." In: *Geochimica et Cosmochimica Acta* 55.2, pp. 441–456.

Zhou, C., Y. Jia, J. Liu, H. Li, Y. Fan, Z. Zhang, Y. Liu, Y. Jiang, B. Zhou, Z. He, et al. (2022). "Scientific objectives and payloads of the lunar sample return mission—Chang'e-5." In: *Advances in Space Research* 69.1, pp. 823–836.

Zhuravlev, L. (2000). "The surface chemistry of amorphous silica. Zhuravlev model." In: *Colloids and Surfaces A: Physicochemical and Engineering Aspects* 173.1, pp. 1–38. ISSN: 0927-7757.